

Plasmonic porous ceramics for molecule detection via surface-enhanced Raman scattering

Vom Fachbereich Produktionstechnik

Der

UNIVERSITÄT BREMEN

Zur Erlangung des Grades

Doktor der Ingenieurwissenschaften (Dr.-Ing)

genehmigte

Dissertation

Von

M. Sc. Tongwei Guo

Gutachter:

Prof. Dr. -Ing. Kurosch Rezwan

Prof. Dr. -Ing. Johannes Kiefer

Tag der mündlichen Prüfung: 23.01.2024

Acknowledgments

First and foremost, I would like to express my deepest gratitude to Prof. Dr. -Ing. Kurosch Rezwan for the opportunity to pursue my Ph.D. studies at the Advanced Ceramics institute. His expertise, wisdom and feedback have been invaluable in shaping my research and helping me to refine my ideas. I am very grateful to him and my supervisor PD Dr. Michael Maas for their unwavering support, guidance and encouragement throughout my doctoral studies. I would like to thank them for the patience, understanding and constant support, which has been a source of strength and motivation for me.

I would also like to thank Prof. Dr. -Ing. Johannes Kiefer for supporting me as the second examiner of this work, as well as the members of my dissertation committee, for their invaluable feedback and contributions to my research. Their constructive criticism and insightful comments have helped me to sharpen my arguments and refine my research methods.

I am also grateful that I worked with so many kind and supportive colleagues for their encouragement and support during my doctoral journey. I would like to thank the technical staff (Tina Kühn, Cristian Nuortila, Jürgen Horvath and Christian Ellenberg) for their expertise and assistance, my fellow Ph.D. and postdoc colleagues (Tanja Link, Nurul Karim, Pedro H.d.R Braun, Natalia Fontão and Vicente Durán Toro) for their moral support, friendship and nice conversations.

I would like to especially thank MIMENIMA colleagues for scientific exchange and communications, and fruitful events. Their insights, suggestions and feedback have been instrumental in shaping my research and helping me to navigate the challenges of graduate school.

Finally, I owe special thanks to my family, especially my parents for their unconditional love, encouragement and support throughout my academic career. Their unwavering belief in my abilities and their constant encouragement has been a source of inspiration for me.

In conclusion, I am extremely grateful to all those who have supported and encouraged me throughout my doctoral journey. Without their support and guidance, this dissertation would not have been possible. Thank you all from the bottom of my heart!

Tongwei

Table of Contents

Acknowledgments.....	iii
Table of Contents	v
Abstract	ix
Kurzfassung.....	xiii
List of abbreviations and symbols	xvii
1. Introduction.....	1
1.1 State of art.....	1
1.2 Goals.....	4
2. Theoretical background.....	5
2.1 Light propagation	5
2.1.1 Scattering.....	6
2.1.2 Light propagation in porous medium	8
2.2 Plasmonic Materials.....	12
2.2.1 Metallic materials	13
2.2.2 Metallic core-shell nanoparticles	16
2.3 Surface-enhanced Raman scattering	17
2.3.1 Electromagnetic enhancement.....	17
2.3.2 Chemical enhancement.....	18
2.3.3 Plasmonic hot spots	19
2.4 Bioceramics.....	20
3. Methodology.....	25
3.1 Macro-porous ceramic processing	25
3.2 Synthesis of nanoparticles.....	27
3.2.1 Synthesis of metallic nanoparticles.....	27
3.2.2 Synthesis of metallic core-shell nanoparticles	32
3.3 Surface-enhanced Raman spectroscopy	34
3.3.1 Influence of hot spots on Raman enhancement factors	34
3.3.2 Choosing the excitation wavelength during SERS measurements.....	35
3.3.3 Fabrication of SERS substrates	37
3.3.4 Interpretation of SERS shifts using density functional theory.....	44
3.4 UV-vis spectroscopy.....	46
3.5 Integrating sphere	46
3.6 Electron microscopy	47
3.7 X-ray micro computed tomography	48
4. Concept of plasmonic porous ceramics.....	50

4.1 Materials	50
4.2 Methods.....	51
4.2.1 Fabrication of porous ZTA ceramics.....	51
4.2.2 Fabrication of dense ZTA ceramic pellets.....	52
4.2.3 Fabrication of ZTA ceramic thin rods.....	52
4.2.4 Deposition of Ag nanoparticles onto the ceramic surface	53
4.2.5 Determination of pore size and strut thickness	54
4.2.6 Scanning electron microscopy (SEM) and nanoparticle coverage determination ..	55
4.2.7 Raman scattering of the plasmonic ceramics.....	55
4.3 Results and discussion	56
4.3.1 Preparation of porous ceramics.....	56
4.3.2 Ag nanoparticle coverage on ceramic surface	57
4.3.3 Characterization of plasmonic properties as a function of particle coverage	59
4.3.4 Plasmonic porous ceramics with different pore sizes	61
4.3.5 Influence of strut size and surface curvature of the porous structure.....	63
4.3.6 Influence of the porous structure on Raman enhancement effect	64
4.4 Conclusions.....	65
5. Plasmonic porous ceramics for <i>in situ</i> catalytic reaction monitoring.....	67
5.1 Materials	68
5.2 Methods.....	68
5.2.1 Functionalization of the ZTA ceramics with metallic core-shell nanoparticles	68
5.2.2 Characterization.....	69
5.3 Results and discussion	69
5.3.1 Molecule detection via SERS.....	73
5.3.2 Catalytic function of the plasmonic porous ceramics	76
5.3.3 Comparing porous and dense ceramic substrates.....	81
5.3.4 <i>In situ</i> reaction monitoring via SERS	83
5.4 conclusions	85
6. Plasmonic porous ceramics for biomedical applications.....	86
6.1 Materials	87
6.2 Methods.....	88
6.2.1 Synthesis of 45S5 Bioglass powder	88
6.2.2 Synthesis of porous and dense Bioglass substrates.....	88
6.2.3 Deposition of Au nanoparticles.....	89
6.2.4 Characterization.....	90
6.3 Results and discussion	90

6.3.1 Ceramic substrate characterisation	90
6.3.2 Functionalization of bioceramics with plasmonic nanoparticles	92
6.3.3 Raman enhancement of porous Bioglass under simulated biological conditions...	97
6.3.4 Stability of plasmonic porous Bioglass in biological media	99
6.4 Conclusions.....	104
7. Conclusion.....	105
8. Outlook.....	107
9. References	109
Curriculum vitae	131
List of publications and oral presentations.....	132
List of student projects	133

Abstract

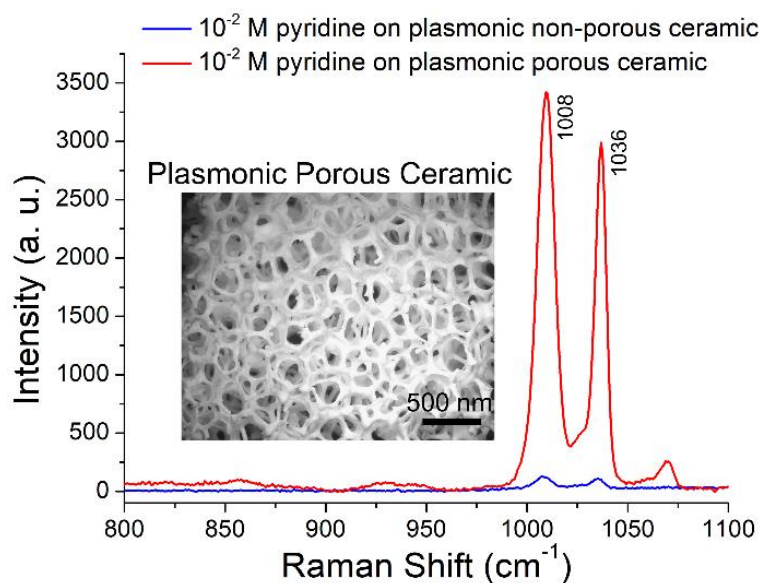
Abstract has been partially adapted from [1–3] with permission from *Elsevier* and *Wiley*, respectively.

A plasmonic porous ceramic can be defined as a three-dimensional porous ceramic matrix with embedded plasmonic nanoparticles. Like regular ceramics, this material class shows advantages like high temperature and pressure stability, chemically inertness, along with dielectric properties. Plasmonic porous ceramics have a high potential for a broad range of applications in various fields, for example ultrasensitive chemical detection under high-temperature/high-pressure conditions, for biomarker detection in biological systems or for highly efficient energy generation through plasmonic photothermal heating.

In general, plasmonic materials are developed because of their ability of confining and manipulating electromagnetic radiation, which enables highly sensitive and rapid detection of molecules, for example via surface-enhanced Raman spectroscopy (SERS). Typical plasmonic nanoparticles used for SERS are gold and silver nanoparticles. Because of the high density of mobile electrons, plasmonic nanoparticles (Au, Ag nanoparticles) can couple with the electromagnetic radiation of wavelengths that are far larger than the nanoparticles themselves. Light absorption and scattering by plasmonic nanoparticles can be tailored by varying their size, geometry and relative positions.

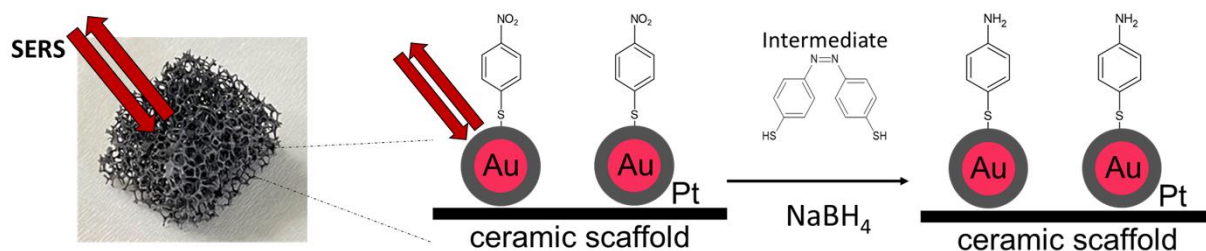
This thesis aims to present the new concept of plasmonic porous ceramic by introducing plasmonic nanostructures in open-cell foam ceramics and to investigate application possibilities of this substrate due to its advanced optical properties. These optical properties of the plasmonic porous ceramic lead to significant magnification of the Raman scattering signal, that enables this substrate serving as SERS substrate and providing molecule “fingerprint” for sensitive and real-time detection.

Therefore, the first cornerstone of this work is proof-of-principle of plasmonic porous ceramics. Open porous ceramic structures based on zirconia-toughened alumina (ZTA) were processed, sintered and functionalized with silver nanoparticles. The Raman enhancement of the plasmonic structures was analyzed as a function of the amount of deposited silver nanoparticles, pore diameter and strut diameter of the ceramic structure using the probe molecule pyridine. Flat substrates of the same chemical composition and non-porous fragments of the porous structure were used for comparison. The Raman signal is found to be significantly augmented by the porous structure compared to that collected on flat substrates with similar composition. Accordingly, the plasmonic porous ceramics were supposed to be well suited as 3D SERS substrates, allowing real-time Raman sensing of trace amounts of molecules.



Graphical abstract 1 Raman spectra of pyridine adsorbed on plasmonic non-porous pellet and porous ZTA ceramic respectively.

To investigate the application possibility of the plasmonic porous ceramics, porous ZTA ceramics functionalized with bifunctional metallic Au@Pd or Au@Pt core-shell nanoparticles were designed, synthesized and tested for *in situ* monitoring of catalytic reactions via surface-enhanced Raman scattering (SERS). The SERS enhancement ability was augmented by the open cell foam structure of the ceramic support. Meanwhile, the porous ceramic enables efficient light-trapping and propagation onto the coated surface, which provides good accessibility of the catalyst, while the core-shell particles are equipped with a catalytically active shell and a plasmonic core which enables SERS sensing. The metallic core-shell nanoparticles were synthesized by the Au-seed mediated growth method and colloiddally deposited onto the open porous ceramic matrix prepared via the polymer replica method. The Au@Pt nanoparticle functionalized porous ceramic showed a Raman enhancement factor (EF) up to 10^6 , which is significantly higher than that of non-porous samples. *In situ* reaction monitoring via SERS was demonstrated by the Pt-catalyzed reduction of 4-nitrothiophenol (4-NTP) to 4-aminothiophenol (4-ATP), showing high specificity for analysis of reactants and products. This multifunctional material concept featuring ceramics-augmented SERS and catalytic activity could be extended beyond real-time, sensitive reaction monitoring towards high temperature reactions, photothermal catalysis, bioprocessing and -sensing, green energy conversion and related applications.

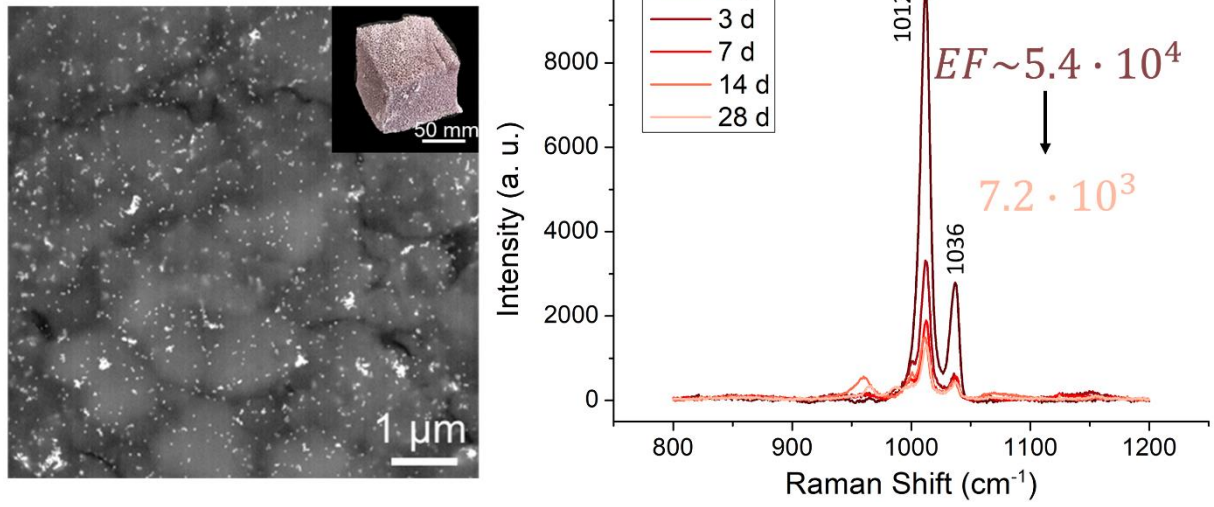


Graphical abstract 2 ZTA based plasmonic porous ceramic functionalized with 48 nm Au@Pt nanoparticles for *in situ* reaction monitoring of the Pt-catalyzed reduction of 4-NTP to 4-ATP via SERS.

Furthermore, the application of plasmonic porous ceramics was developed in the biomedical field by employing bioceramic material. Open cell foams of Bioglass45S5, the commercial hydroxyapatite-based product Bio-Oss[®] and bio-inert ZTA were coated with Au nanoparticles via colloidal deposition to introduce plasmonic effects. The ability of these plasmonic porous bioceramics to detect molecules was analyzed *in situ* in various biological media. Pyridine (Py) was used as a model molecule to test the detection enhancement. Depending on the pore size, gold-functionalized plasmonic porous Bioglass showed Raman EFs up to $5.4 \cdot 10^4$, while depositing gold nanoparticles on Bio-Oss[®] and porous ZTA resulted in EFs of $1.1 \cdot 10^4$ and $2.4 \cdot 10^5$, respectively. The performance of the plasmonic porous bioceramics under simulated biological conditions was examined in the biological media fetal bovine serum (FBS) and simulated body fluid (SBF). Bioglass showed moderately reduced EFs of $1.9 \cdot 10^4$ for FBS and $1.6 \cdot 10^4$ for SBF, while Bio-Oss[®] and ZTA showed hardly any decrease.

Furthermore, the plasmonic porous bioceramics were tested during extended incubation in mineralizing Simulated Body Fluid (SBF). The plasmonic porous Bioglass still delivered a Raman EF around $7.2 \cdot 10^3$ after 28 days of incubation, indicating a promising stability in simulated biological conditions. Bio-Oss[®] showed a strong reduction of Raman enhancement after 14 days with barely any enhancement after 28 days, while the bioinert ZTA exhibited very stable EFs after an initial decline to $9.0 \cdot 10^4$. No significant difference of Bioglass in terms of SBF-bioactivity after 14 days was noted by the Au-deposition. The presented material concept of plasmonic porous bioceramics is shown to be very robust and could be further developed for sensing of specific biomarkers, e.g., in the context of osseointegration of bone replacement materials. In conclusion, we were able to demonstrate that the plasmonically-enhanced porous bioceramics offer the possibility of real-time and sensitive molecule detection at SBF and FBS conditions. Beyond the biomedical application the plasmonically-enhanced ceramics can be used for biotechnological applications where within porous reactors molecule turn-over rates can be monitored.

Plasmonic Porous Bioglass



Graphical abstract 3 Plasmonic porous Bioglass showed Raman EF of $5.4 \cdot 10^4$, which only moderately decreased to $7.2 \cdot 10^3$ after 28 days of incubation in SBF.

Kurzfassung

Teile dieser Kurzfassung werden mit Genehmigung der Herausgeber *Elsevier* [1] und *Wiley* [2,3] adaptiert.

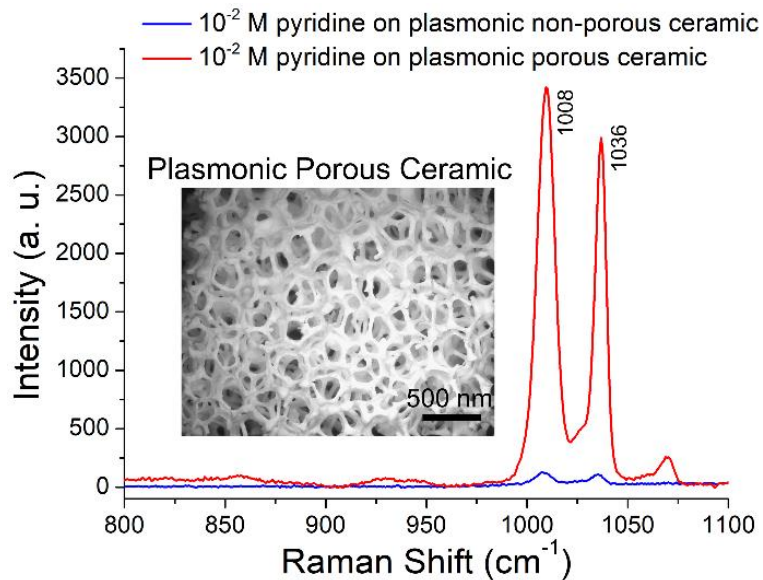
Eine plasmonische poröse Keramik kann als dreidimensionale poröse Keramikmatrix mit eingebetteten plasmonischen Nanopartikeln definiert werden. Wie normale Keramiken besitzt diese Materialklasse einige Vorteile, wie eine hohe Temperatur- und Druckstabilität, chemische Inertheit sowie dielektrische Eigenschaften. Plasmonische poröse Keramiken haben ein hohes Potenzial für eine breite Palette von Anwendungen in verschiedenen Bereichen, wie z.B. ultrasensitive chemische Detektion unter Hochtemperatur-/Hochdruckbedingungen, für Biomarker-Detektion in biologischen Systemen oder für hoch-effiziente Energieerzeugung durch plasmonische photothermische Erwärmung.

Im Allgemeinen werden plasmonische Materialien aufgrund ihrer Fähigkeit entwickelt, elektromagnetische Strahlung zu begrenzen und zu manipulieren, was eine hochempfindliche und schnelle Detektion von Molekülen ermöglicht, zum Beispiel mittels oberflächenverstärkter Raman-Spektroskopie (SERS). Typische plasmonische Nanopartikel, die für SERS verwendet werden, sind Gold- und Silbernanopartikel. Aufgrund der hohen Dichte an beweglichen Elektronen können plasmonische Nanopartikel (Au-, Ag-Nanopartikel) mit der elektromagnetischen Strahlung von Wellenlängen koppeln, die weit größer sind als die Nanopartikel selbst. Lichtabsorption und Streuung durch plasmonische Nanopartikel können durch Variation ihrer Größe, Geometrie und relativen Positionen angepasst werden.

Diese Arbeit zielt darauf ab, das neue Konzept der plasmonischen porösen Keramik vorzustellen, indem plasmonische Nanostrukturen in offenzelligen Schaumkeramiken eingeführt werden, und die Anwendungsmöglichkeiten dieses Substrats aufgrund seiner fortschrittlichen optischen Eigenschaften zu untersuchen. Diese optischen Eigenschaften der plasmonischen porösen Keramik führen zu einer signifikanten Verstärkung des Raman-Streusignals, wodurch dieses Substrat als SERS-Substrat dienen und ein Molekül-"Fingerabdruck" für eine empfindliche und Echtzeit-Detektion bereitstellen kann.

Daher ist der erste Eckpfeiler dieser Arbeit der Nachweis des Prinzips der plasmonischen porösen Keramiken. Offenporige Keramikstrukturen auf der Basis von Zirkonia-verstärktem Aluminiumoxid (ZTA) wurden verarbeitet, gesintert und mit Silbernanopartikeln funktionalisiert. Die Raman-Verstärkung der plasmonischen Strukturen wurde in Abhängigkeit von der Menge der abgeschiedenen Silbernanopartikel, dem Porendurchmesser und dem Steg-Durchmesser der Keramikstruktur mit dem Probenmolekül Pyridin analysiert. Flache Substrate mit derselben chemischen Zusammensetzung sowie nicht-poröse Fragmente der porösen Struktur wurden

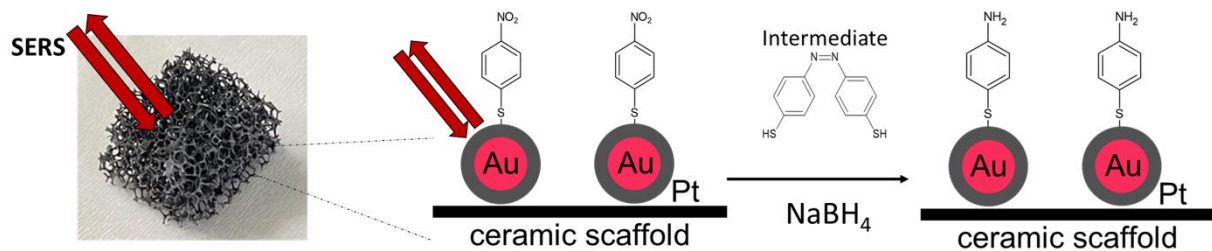
zum Vergleich verwendet. Das Raman-Signal wurde im Vergleich zu auf flachen Substraten mit ähnlicher Zusammensetzung gesammelten Signalen durch die poröse Struktur signifikant verstärkt. Demzufolge eignen sich plasmonische poröse Keramiken als 3D SERS-Substrate, um geringe Mengen von Molekülen in Echtzeit zu detektieren.



Grafische Zusammenfassung 1: Raman-Spektren von Pyridin, das jeweils auf einem plasmonischen nicht-porösen Pellet und einer porösen ZTA-Keramik adsorbiert wurde.

Um die Anwendungsmöglichkeiten der plasmonischen porösen Keramik zu untersuchen, wurden poröse ZTA-Keramiken mit bifunktionalen metallischen Au@Pd- oder Au@Pt-Kern-Schale-Nanopartikeln funktionalisiert, synthetisiert und für die in-situ-Überwachung von katalytischen Reaktionen mittels oberflächenverstärkter Raman-Streuung (SERS) getestet. Die SERS-Verstärkungsfähigkeit wurde durch die offenzellige Schaumstruktur des keramischen Trägers verbessert. Gleichzeitig ermöglicht die poröse Keramik eine effiziente Lichttrapping und -propagation auf der beschichteten Oberfläche, was eine gute Zugänglichkeit des Katalysators gewährleistet, während die Kern-Schale-Partikel mit einer katalytisch aktiven Schale und einem plasmonischen Kern ausgestattet sind, der eine SERS-Sensorik ermöglicht. Die metallischen Kern-Schale-Nanopartikel wurden durch die Au-Samen-vermittelte Wachstumsmethode synthetisiert und kolloidal auf die offene poröse keramische Matrix aufgebracht, die mittels der Polymer-Replikationsmethode hergestellt wurde. Die mit Au@Pt-Nanopartikeln funktionalisierte poröse Keramik zeigte einen Raman-Verstärkungsfaktor (EF) von bis zu 106, der deutlich höher ist als der von nicht-porösen Proben. Die in-situ-Überwachung von Reaktionen mittels SERS wurde durch die Pt-katalysierte Reduktion von 4-Nitrothiophenol (4-NTP) zu 4-Aminothiophenol (4-ATP) demonstriert und

zeigte eine hohe Spezifität für die Analyse von Reaktionspartnern und Produkten. Dieses multifunktionale Materialkonzept, das keramik-augmentierte SERS und katalytische Aktivität kombiniert, könnte über die Echtzeitüberwachung empfindlicher Reaktionen hinaus erweitert werden und Anwendungen in Bereichen wie Hochtemperaturreaktionen, photothermaler Katalyse, Bioprozessierung und -sensorik, grüne Energieumwandlung und verwandten Bereichen finden.



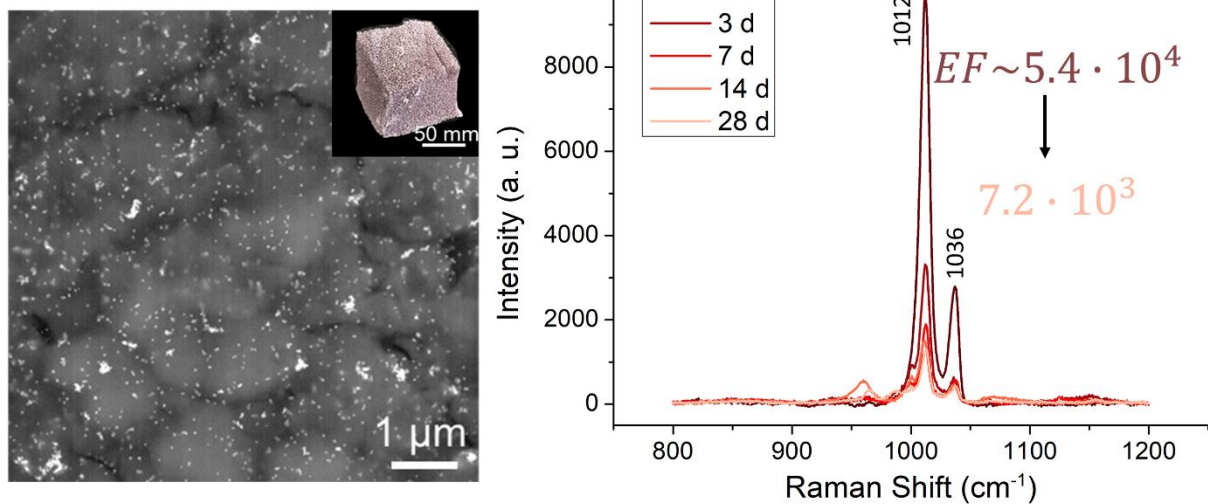
Grafikzusammenfassung 2: ZTA-basierte plasmonische poröse Keramik, funktionalisiert mit 48 nm Au@Pt-Nanopartikeln, zur in-situ-Reaktionsüberwachung der Pt-katalysierten Reduktion von 4-NTP zu 4-ATP über SERS.

Darüber hinaus wurde die Anwendung von plasmonischen porösen Keramiken im biomedizinischen Bereich durch die Verwendung von Biokeramikmaterialien entwickelt. Offenporige Schäume von Bioglass45S5, dem kommerziellen hydroxyapatitbasierten Produkt Bio-Oss[®] und bioinerten ZTA wurden mittels kolloidaler Abscheidung mit Goldnanopartikeln beschichtet, um plasmonische Effekte einzuführen. Die Fähigkeit dieser plasmonischen porösen Biokeramiken zur Moleküldetektion wurde in situ in verschiedenen biologischen Medien analysiert. Pyridin (Py) wurde als Modellmolekül zur Testung der Detektionsverstärkung verwendet. Abhängig von der Porengröße zeigte plasmonisch funktionalisiertes Bioglass Raman-Verstärkungsfaktoren von bis zu $5.4 \cdot 10^4$, während die Abscheidung von Goldnanopartikeln auf Bio-Oss[®] und porösem ZTA zu EFs von $1.1 \cdot 10^4$ bzw. $2.4 \cdot 10^4$ führte. Die Leistungsfähigkeit der plasmonischen porösen Biokeramiken unter simulierten biologischen Bedingungen wurde in den biologischen Medien fötalem Kälberserum (FBS) und simulierter Körperflüssigkeit (SBF) untersucht. Bioglas zeigte mäßig reduzierte EFs von $1.9 \cdot 10^4$ für FBS und $1.6 \cdot 10^4$ für SBF, während Bio-Oss[®] und ZTA kaum eine Abnahme aufwiesen.

Darüber hinaus wurden die plasmonischen porösen Biokeramiken während einer langen Inkubationszeit in mineralisierender simulierter Körperflüssigkeit (SBF) getestet. Das plasmonische poröse Bioglas lieferte auch nach 28 Tagen Inkubation immer noch einen Raman-Verstärkungsfaktor von etwa $7.2 \cdot 10^3$, was auf eine vielversprechende Stabilität unter simulierten biologischen Bedingungen hinweist. Bio-Oss[®] zeigte eine starke Reduktion der

Raman-Verstärkung nach 14 Tagen und kaum noch Verstärkung nach 28 Tagen, während das bioinerte ZTA nach einem anfänglichen Rückgang auf $9.0 \cdot 10^4$ sehr stabile EFs zeigte. Es wurde keine signifikanten Unterschiede für Bioglass in Bezug auf SBF-Bioaktivität nach 14 Tagen durch die Au-Deposition festgestellt. Das vorgestellte Materialkonzept plasmonischer poröser Biokeramiken hat sich als sehr robust erwiesen und könnte für die Erkennung spezifischer Biomarker, z.B. im Kontext der Osseointegration von Knochenersatzmaterialien, weiterentwickelt werden. Zusammenfassend konnten wir zeigen, dass die plasmonisch verstärkten porösen Biokeramiken die Möglichkeit bieten, Moleküle in Echtzeit und mit hoher Empfindlichkeit unter SBF- und FBS-Bedingungen zu detektieren. Über die biomedizinische Anwendung hinaus können die plasmonisch verstärkten Keramiken für biotechnologische Anwendungen eingesetzt werden, bei denen in porösen Reaktoren die Molekülumsatzraten überwacht werden können.

Plasmonic Porous Bioglass



Grafische Zusammenfassung 3 Das plasmonisch-poröse Bioglas zeigte einen Raman-Verstärkungsfaktor (EF) von $5.4 \cdot 10^4$, der nach 28-tägiger Inkubation in SBF nur mäßig auf $7.2 \cdot 10^3$ abnahm.

List of abbreviations and symbols

AAO	Anodic aluminum oxide
Ag	Silver
Al	Aluminum
Au	Gold
A	Absorption intensity
a	Radius
BPE	<i>trans</i> -1,2-bis(4-pyridyl)-ethylene
BSE-SEM	Scanning electron microscope using backscattered electron
b	Sample thickness
β_λ	Spectral extinction coefficient
Co	Cobalt
CT	Charge transfer
CTAB	cetyltrimethylammonium bromide
Cu	Copper
CV	Cyclic voltammetry
C	Sample concentration
c	Speed of light in vacuum
C_{Normal}	Sample concentration during Raman scattering
C_{SERS}	Sample concentration during SERS
DFT	Density functional theory
DSPD	Double-step potential deposition
D	Particle diameter
d	Distance, gap
d_{cs}	Cross-sectional diameter of the ceramic strut
ED	Electrochemical deposition
EF	Enhancement factor
ER	Electrochemical roughening
e	Charge
$E_{Loc}(\omega_L)$	Local electric field experienced by the probe molecule
$E(\omega_L)$	External electric field oscillating at frequency ω_L
E_0	External electric field

ε	Dielectric constant of the metal particle
ε_{ab}	Molar absorption coefficient
ε_d	Dielectric constant of the medium surrounding the nanoparticle
$E_{Loc}(\omega_L)$	Local electric field experienced by the probe molecule
$\varepsilon(\omega)$	Dielectric constant of a material when interacting with an external electromagnetic field
$\varepsilon'(\omega)$	Polarization effect caused by the external field on the material
$\varepsilon''(\omega)$	Loss caused during the polarization process
ε_0	Relative permittivity of free space
ΔE_i	Incident light energy
$\Delta E_{Rayleigh}$	Rayleigh scattered light energy
ΔE_{Stokes}	Stokes scattered light energy
ΔE_v	Scattered light energy
FBS	Fetal bovine serum
Fe	Iron
G_{SERS}	Total SERS enhancement factor
G_{SERS}^{Em}	Electromagnetic enhancement factor
G_{SERS}^{Chem}	Chemical enhancement factor
h	Planck's constant
HCA	Hydroxy carbonate apatite
I	Laser intensity
I_{trans}	Transmitted light intensity
I_0	Incident light intensity
IB	Interband
IR	Infrared
I_λ	Spectral radiation
K	Fraction of the detected to emitted photons during Raman scattering
k	Wavevector
k_B	Boltzmann constant
κ_λ	Spectral absorption coefficient

LSP	Localized surface plasmon
LSPR	Localized surface plasmon resonance
l_{cs}	Cross-sectional edge length of the strut
l_{β}	Possible transfer distance
M	Metal
m	Mass
m^*	Effective optical mass
MCRT	Monte Carlo ray-tracing
Mg	Magnesium
$M_{Loc}^Z(\omega_L)$	Local field enhancement with polarization of the incident laser along the Z axis
M_{Rad}	re-radiation enhancement
N	Number of the illuminated molecules
NIR	Near-infrared
n	Number density of mobile charge carriers
$n_{a,alumina}$	Refractive index of alumina
$n_{a,zirconia}$	Refractive index of zirconia
n_e	Conduction electron density
n_{eff}	Effective refractive index
n_{solid}	Refractive index of ceramic strut solid
n_{void}	Refractive index of the void phase
Pd	Palladium
PDLLA	poly (D, L-lactide)
PE	Polyethylene
PEG	polyethylene glycol
PMMA	Pyramid polymethyl methacrylate
PPI	Pore per inch
Pt	Platinum
PU	Polyurethane
PVA	Poly(vinyl alcohol)
Py	Pyridine
P	Macro-porosity of the ceramic structure
P_{Normal}	Raman intensity measured by the detector
P_{Rad}	Radiation power by a dipole placed in an inhomogeneous environment

P_{Raman}	Intensity of Raman scattered light
P_0	Radiation power in vacuum
$Q_{Abs}(\omega)$	Absorption efficiency
$Q_{Ext}(\omega)$	Extinction efficiency
Q_{LSP}	Plasmonic quality factor
$Q_{max.LSP}$	Maximum quality localized surface frequency
$Q_{max.LSP,Au}$	Maximum quality localized surface frequency of gold
$Q_{max.LSP,Pd}$	Maximum quality localized surface frequency of palladium
$Q_{max.LSP,Pt}$	Maximum quality localized surface frequency of platinum
$Q_{NF}(\omega)$	Local field efficiency
$Q_{Sca}(\omega)$	Scattering efficiency
R	Alkyl group
REM	Reflection electro microscope
RH	Relative humidity
RIE	Reactive ion etching
RTE	Radiative transfer equation
\vec{r}	Position vector
SNR	Signal-to-noise ratio
SPR	Surface plasmon resonance
SBF	Simulated body fluid
SEM	Scanning electron microscope
SERS	Surface-enhanced Raman scattering
SESORS	Surface-enhanced spatially offset Raman scattering
SORS	Spatially offset Raman scattering
STM	Scanning tunneling microscope
\vec{s}	Incident direction vector
S	Interparticle spacing
S_{cc}	Cross-sectional area of the ceramic solid
S_{ch}	Cross-sectional area of the hollowness
\vec{S}_{in}	Direction of the incident light beam
\vec{S}_{out}	Direction of the leaving light beam

T	Temperature
TAED	Template assisted electrochemical deposition
TEM	Transmission electron microscope
TEOS	Tetraethyl orthosilicate
<i>trans</i> -DMAB	4,4-dimercaptoazobenzene
TSC	Trisodium citrate
UV-vis	Ultraviolet-visible
V_{pore}	Volume of the pores
V_{solid}	Volume of the solid part
V_{total}	Total volume
ν_0	Frequency of the incident light
ν_ν	Frequency of the scattered light
$\widetilde{\nu}_0$	Excitation laser wavenumber
$\widetilde{\nu}_k$	Raman shift of the k -th vibrational mode
W	Interparticle gap
ω_{Inter}	Onset of the interband transitions
ω_L	Laser angular frequency
ω_p	Plasmon frequency
ω_{solid}	Scattering albedo of the ceramic solid material
X	H or alkyl groups
ZTA	Zirconia-toughened-alumina
σ_{Abs}	Absorption cross-section
σ_k^{ads}	Raman cross-section of the vibrational mode k of the adsorbed molecule
σ_{Ext}	Extinction cross-section
σ_k^{free}	Raman cross-section of the vibrational mode k of the free molecule
σ_k	Raman cross-section
σ_{Sca}	Scattering cross-section
σ_{Solid}	Scattering coefficient of ceramic strut solid
$\sigma_{s\lambda}$	Spectral scattering coefficient
Φ, Φ_λ	Scattering phase function
Ω	Solid angle

ξ	Position of the incident light beam on the ceramic strut
ξ_β	Random number between 0 and 1
ξ_ρ	Random number between 0 and 1
ξ_ω	Random number
$\rho_k^{anti-Stoke/Stoke}$	Cross-section ratio between anti-Stokes and Stokes band of the k -th vibrational mode
$\rho(\theta_{in}, \theta_t)$	Local specular reflectivity between the void and solid phase
θ_{in}	Local incident ray angle
θ_r	Local reflection angle
θ_t	Local refractive angle
γ	Damping ratio
λ	Wavelength
λ_{Exc}	Wavelength of the extinction laser
Γ	Total damping rate
μ -CT	X-ray micro computed tomography
2D	Two-dimensional
3D	Three-dimensional
4-ATP	4-aminothiophenol
4-NTP	4-nitrothiophenol

1. Introduction

Chapter 1 has been partially adapted from [1] with permission from *Elsevier* and from [2,3] with permission from *Wiley*.

1.1 State of art

Plasmonic materials are well known for their ability of confining and manipulating electromagnetic radiation, which enables highly sensitive and rapid detection of molecules via surface-enhanced Raman scattering (SERS) [4–9]. However, most of the present plasmonic materials are based on two-dimensional assemblies of plasmonic nanoparticles, which cannot be easily scaled for the production of more complex three-dimensional architectures. An alternative strategy that holds the promise to leave the chip-based paradigm behind is the inclusion of plasmonic nanoparticles in porous structures which would enable SERS sensing from all directions. In this regard, experiments on plasmonic SERS substrates based on three-dimensional porous materials have been conducted by several research groups [10–12]. For example, a porous alumina aerogel has been designed for ultrasensitive dye molecule detection via SERS with an enhancement factor of $3.4 \cdot 10^7$ [11]. Gold-polymer nanocomposites have been realized via physical vapor deposition of gold metal onto pliable polydimethylsiloxane, which exhibited higher Raman signals than that on gold-glass composites [12]. The reported porous plasmonic materials were well suited for SERS sensing and other applications like plasmonic heating or photothermal therapy [10–15].

SERS has been developed since the enhancement of Raman signals by nanoparticles with localized plasmon resonance was first observed by Fleischmann *et al.* in 1974 [16]. This technology has drawn increasing interest in various research fields, such as chemistry, biology, medicine and environmental science since it allows the detection of extremely small amounts of Raman-active molecules with high specificity [13,15,17–22]. Metallic particles of 10-150 nm diameters show the most intensive surface plasmon resonance band [23], which leads to the strongest enhancement of the electromagnetic field near the plasmonic nanostructure. Accordingly, group 11 metals (Au, Ag, Cu) [24–26] and particularly silver nanoparticles are suitable plasmonic materials for SERS [27–32]. Light absorption and scattering by plasmonic nanoparticles can furthermore be tailored by varying their size, geometry and relative positions [33,34,34–40]. The distance of the Raman-active probe molecules to the plasmonic particles plays an important role for the Raman enhancement effect, as well. The closer the analyte is to the plasmonic particle, the stronger is the Raman enhancement effect [33,34]. The strongest enhancement effect is observed when the probe molecule is in close proximity to several plasmonic particles at once, which is referred to as a plasmonic hot spot leading to

enhancement factors of up to 10^9 under ideal conditions. Many of the described plasmonic materials are reported with Raman factors in the range on 10^3 - 10^6 , which is still well suited for sensitive detection of Raman probes [23]. Such materials could exhibit a combination of isolated plasmonic particles and plasmonic hotspots with the hotspots contributing to the majority of the SERS enhancement.

For applications of SERS under extreme conditions, such as high temperature/pressure environments, the development of plasmonic ceramic materials is of crucial importance. Ceramics are known for their exceptional features, including stability at extreme temperatures and pressures, chemical inertness, dielectric properties and biocompatibility [41–45]. Open porous ceramics are often used as flow reactors [46], especially in high-temperature and high-pressure applications [47]. For instance, porous ceramic filters are utilized in the processing of nuclear waste to trap radioactive nuclides [48], or as water/hot gas/molten metal filters [49]. Therefore, it would be of great advantage to equip porous ceramics with SERS-sensing properties to enable online process analysis in harsh environments or *in-vivo* biomarker sensing.

Several research groups have designed and investigated on three-dimensional (3D) plasmonic SERS substrates. Li *et al.* have presented 3D plasmonic nanostructures as high-quantum-efficiency UV photodetectors based on anodic aluminum oxide (AAO) matrix substrates, where the light confinement was spatially extended from 2D to 3D. It was reported that the incident light is concentrated by the gold nanostructures and the strong optical interference within the AAO matrix, leading to light-trapping followed by a high Raman enhancement factor (EF) [50]. Polymeric materials were also reported as 3D SERS substrates. For example, 3D pyramid polymethyl methacrylate (PMMA) functionalized with Ag nanoparticles exhibited EFs up to 10^8 [20]. Ag nanoparticles@MoS₂/PMMA polymer composites showed a detection limit of 10^{-10} M of the melamine standard solution [51]. Other examples include plasmonic 3D photonic crystals, 3D plasmonic nanoantenna based on multielectrode arrays, 3D plasmonic nanorod forests on paper or 3D SERS substrates based on graphene [52–55]. Although there have been a number of studies on light propagation and scattering inside ceramic structures [56–63], little is known about the influence of porous ceramics on the Raman enhancement effect [51,64].

In the context of application possibilities, the plasmonic porous ceramics can be developed for *in situ* reaction monitoring, through introducing multifunctional metallic alloy nanoparticles in the open porous ceramic matrix. *In situ* metal-catalyzed reaction monitoring has been realized via various techniques, such as UV-vis absorption spectroscopy, infrared (IR) spectroscopy and SERS [9–13]. While UV-vis absorption spectroscopy provides only limited chemical information, IR spectroscopy functions inefficiently in aqueous systems due to strong IR absorption of water. On the other hand, Raman spectroscopy, especially SERS allows

monitoring and investigation of reaction processes by detecting specific molecular vibrational modes of reactants, intermediates and products at different reaction time spots, providing direct information of the chemistry of the analysed reaction [14–16]. SERS uses plasmonic nanostructures to excite the localized plasmon resonance in metallic nanoparticles, which leads to significantly increased Raman intensity [17]. However, most of the reported SERS substrates are based on two-dimensional (2D) assemblies, which have been demonstrated to provide very high Raman enhancement, but are difficult to adapt to more complex setups.

While being able to catalyze a wide range of chemical reactions, the group VIII B transition metals palladium (Pd) and platinum (Pt) exhibit a high imaginary part of the complex permittivity and therefore only generate weak SERS EFs due to dampening of the plasmonic oscillation.^[28] To make up for the weak EFs, Pd / Pt-based SERS substrates usually demand perfect ordering and uniform deposition with high surface coverage, that also consider the size, shape, geometry and position of the metallic nanostructures [29–34]. Conversely, while conventionally used as excellent SERS-active metals, Au NPs have a size limit of around 5 nm for efficient catalytic activity, which is too small for SERS-activity [65,66]. In this context, the design of metallic hybrid nanostructures which enable the combination of various properties of the different metals in one structural unit were reported [12,13,35–40]. Particularly, metallic alloy nanoparticles consisting of Au in combination with Pd or Pt can lead to both plasmonic and catalytic activity in a single core-shell particle. For example, Hu *et al.* prepared Au core / Pd shell (Au@Pd) nanoparticles with a size from 35 to 100 nm by the Au-seed mediated method. The Au@Pd nanoparticles distributed on a Pt electrode surface showed Raman EF up to $2.7 \cdot 10^3$ [35]. Xie *et al.* presented the synthesis of bifunctional Au / Pt / Au nanoraspberries for *in situ* monitoring of platinum-catalyzed reactions [13]. The synthesized raspberry-like Au / Pt bimetallic nanoparticles have two exposed metal surfaces, resulting in both SERS and catalytic activity in a single bifunctional unit. However, most of the current research on metallic alloy nanoparticles for molecule detection and reaction monitoring via SERS focused on synthesis, characterisation and dispersions of metallic alloy nanoparticles [12,13,35–39].

Meanwhile, through employing bioceramics as substrate, plasmonic porous ceramics can be applied in biomedical field. Current research on SERS biosensing focuses mostly on the synthesis of plasmonic nanostructures and evaluation of these materials in a particular biological context [67–69]. For the analysis of biomarkers, there are two major approaches: label-free and label-aided SERS. For label-free SERS, no reporter molecule is required. However, in the biological context, multiple types of biomolecules can contribute similar Raman signals, which results in very complex readouts that are difficult to interpret [68]. Label-aided SERS is an indirect sensing of the analyte by monitoring the Raman spectrum of the SERS

tags, which consist of plasmonic nanoparticles that are functionalized with Raman reporter molecules as label and further targeting molecules [67,70].

Recently, measuring in or through biological tissue has been made possible via surface-enhanced spatially offset Raman spectroscopy (SESORS) [71–74]. In spatially offset Raman spectroscopy (SORS), Raman scattered light is collected from regions offset from the point of laser excitation at the sample, which allows a preferential collection of the sub-surface spectra [75]. Using the SESORS method, Stone *et al.* have reported successful detection of Raman signals after injection of encapsulated SERS nanoparticles into a porcine tissue block with a thickness of 20 mm [74]. The SERS nanoparticles used in these experiments were Au nanoparticles coated with reporter molecules and encapsulated in a silica shell. Later, SERSORS measurements through 3-8 mm thick bone using commercial SERS nanotags have been performed [72].

1.2 Goals

The current research on 3D plasmonic SERS substrates mainly focuses mostly on the nano scale structure of the plasmonic particles and their supports [76,77], not on macroscopic technical materials. This work aims to introduce the concept of a macro-scaled 3D plasmonic porous ceramics. By employing a macro-porous open-cell foam ceramic as substrate, the advanced optical properties of plasmonic materials can be combined with advantages of porous ceramics, featuring a high surface accessibility and possibility as SERS substrate for real-time and sensitive molecule detection. Meanwhile, after proof-of-principle of plasmonic porous ceramics, the application of this substrate should be investigated in different directions. The content of this thesis is organized into 8 chapters, starting with the introduction in Chapter 1, which briefly introduced the state of art and the goal of this work. Chapter 2 explained the theoretical background of the related scientific terms, from light propagation (Chapter 2.1), plasmonic materials (Chapter 2.2) to bioceramics (Chapter 2.3). The fundamental principles of the applied methods were described in Chapter 3. Chapter 4 introduced the proven-of-principle of the plasmonic porous ceramics and the feasibility of the sample as SERS substrate. Chapter 5 depicted the plasmonic porous ceramic functionalized with multifunctional metallic core-shell nanoparticles and its application for *in situ* catalytic reaction monitoring. Chapter 6 pointed out further application possibility of the adapted plasmonic porous bioceramics for biomedical use. Chapter 7 described the conclusion of the presented results. A general outlook is given in Chapter 8.

2. Theoretical background

2.1 Light propagation

Light propagation refers to the manner that an electromagnetic wave transfers energy from one point to another. When light travels from between boundaries from one medium to another, different processes can happen, namely transmission, absorption, reflection and refraction. Light transmission is determined by the amount of light that can pass through different material boundaries. Absorption happens, when the electromagnetic radiation is converted to internal energy. While, reflection takes place, when electromagnetic radiation is returned either at the boundary of two different media (surface reflection), or within a medium (volume reflection). Refraction refers to the light bending when entering a medium with a different speed. The refractive index indicates the light bending ability of the material.

The Fresnel equations describe the behavior of the s and p polarization incident waves at the interface. The s polarization is the polarization with wave's electric field normal to the plane of incidence, while the p polarization with electric field perpendicular to the plane of incidence. The plane of incidence refers to the plane that contains the incident radiation's propagation vector and the normal vector of the surface.

The Fresnel equations reveal the relation between reflection coefficients ($r_{i,j}$), transmissions coefficient ($t_{i,j}$), angle of incidence (θ_{in}), angle of refraction (θ_j), and refractive index (n_i, n_j) of media (incident medium i , transmitted medium j) by applying Maxwell's equations and Snell's law. Fresnel equations for s and p polarization are shown respectively:[78]

P polarization:

$$r_{i,j} = \frac{n_j \cos \theta_{in} - n_i \cos \theta_j}{n_j \cos \theta_{in} + n_i \cos \theta_j} \quad (\text{Equation 2.1.1})$$

$$t_{i,j} = \frac{2n_i \cos \theta_{in}}{n_j \cos \theta_{in} + n_i \cos \theta_j} \quad (\text{Equation 2.1.2})$$

S polarization:

$$r_{i,j} = \frac{n_i \cos \theta_{in} - n_j \cos \theta_j}{n_i \cos \theta_{in} + n_j \cos \theta_j} \quad (\text{Equation 2.1.3})$$

$$t_{i,j} = \frac{2n_i \cos \theta_{in} - n_i \cos \theta_j}{n_i \cos \theta_{in} + n_j \cos \theta_j} \quad (\text{Equation 2.1.4})$$

where θ_{in} and θ_j are the angles of the incident and refraction.

A typical application of Fresnel theory is UV-vis photometry, which measures the UV-vis light absorbed by or transmitted through a sample.

2.1.1 Scattering

Reflections of radiation can be classified as diffuse reflections or specular reflections. Diffuse reflection refers to the electromagnetic waves that undergo scattering. Radiation scattered by only one scattering center is called single scattering. While, multiple scattering happens when multiple scattering centers exist [79].

When light interacts with particles of much smaller size than the wavelength of the incident light, most of the light gets scattered elastically. The elastically scattered light is called as Rayleigh scattering [80,81], referring to the scattered light having the same frequency/energy as the incident light:

$$|\Delta E_i| = |\Delta E_{Rayleigh}| \quad (\text{Equation 2.1.1.1})$$

Only small portion of the light is scattered inelastically, which is referred as Raman scattering [82]. By Raman scattering, the scattered light has different frequency/energy as the incident light. Raman scattering can be sorted into two different kinds: Stokes scattering and anti-Stokes scattering. Stokes scattering refers to the scattering, that has less energy than the incident light:

$$|\Delta E_i| > |\Delta E_{Rayleigh}| \quad (\text{Equation 2.1.1.2})$$

Anti-Stokes scattering is the opposite, which refers to the scattering with more energy than the incident light:

$$|\Delta E_i| < |\Delta E_{Rayleigh}| \quad (\text{Equation 2.1.1.3})$$

Figure 2.1.1.1 illustrates the detailed energy change of the Rayleigh scattering, Stokes scattering and anti-Stokes scattering respectively. The molecule gets excited to a virtual energy level by incident photon. The re-emission of the photon leads to Rayleigh or Raman scattering. The energy change of Raman scattering contributes to the molecule vibration mode. Therefore, the Raman scattered photon can deliver information of the molecule vibrational modes. Since the molecule vibrational modes are unique like a fingerprint for each single molecule, molecules can be distinguished according to their Raman scattering spectra. Raman spectrum records usually Stokes bands, because Stokes bands are significantly more intensive than anti-Stokes bands.

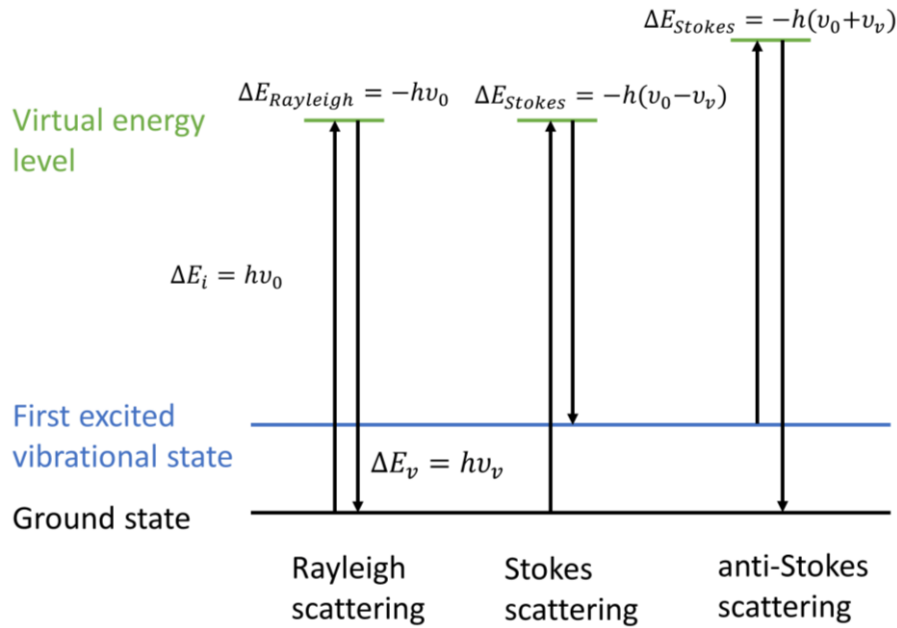


Figure 2.1.1.1 Illustration of the excitation energy change of Rayleigh scattering, Stokes scattering and anti-Stokes scattering respectively.

Raman scattering is an extremely weak phenomenon. The intensity of Raman scattered light depends on the Raman cross-section σ_k :

$$P_{Raman} = KN\sigma_k I \quad (\text{Equation 2.1.1.4})$$

with K representing the factor indicating the fraction of the detected to emitted photons, N number of the illuminated molecules, I laser intensity.

It is worth noticing that Raman scattering has extremely low intensity compared to fluorescence. The cross-sections of fluorescence are typical around $\sim 10^{-16}$ cm²/molecule, while the Stokes Raman cross-section are $\sim 10^{-29}$ cm²/molecule [83–85]. The anti-Stokes cross-section is significantly weaker than that of Stokes. The cross-section ratio between anti-Stokes and Stokes bands of the k -th vibrational mode can be written as:

$$\rho_k^{anti-Stoke/Stoke} = \frac{\sigma_k^{anti-Stoke}}{\sigma_k^{Stoke}} = \left(\frac{\tilde{\nu}_0 + \tilde{\nu}_k}{\tilde{\nu}_0 - \tilde{\nu}_k} \right)^3 e^{-\frac{hc\tilde{\nu}_k}{k_B T}} \quad (\text{Equation 2.1.1.5})$$

with h presenting the Planck constant, c the speed of light in vacuum, k_B the Boltzmann constant, T the temperature, $\tilde{\nu}_0$ the excitation laser wavenumber, $\tilde{\nu}_k$ the Raman shift of the k -th vibrational mode.

Since the intensity of Stokes bands are significantly higher than that of anti-Stokes bands, Raman spectra normally record Stokes band. The intrinsic low efficiency of Raman scattering can be intensively amplified, by placing probe molecule near the surface certain

nanostructures, which is the so-called surface-enhanced Raman scattering. The SERS signal can be expressed as:[23]

$$P_{SERS} = G_{SERS}P_{Normal} \quad (\text{Equation 2.1.1.6})$$

where G_{SERS} is the (total) SERS enhancement factor (EF), P_{Normal} represents the Raman power measured by the detector, which is proportional to the Raman cross-section, the incident laser intensity, the illuminated molecules and the fraction of the emitted photons [86].

2.1.2 Light propagation in porous medium

Porous medium has wide application demands in various technical fields such aviation, automobile, solar energy conversion, combustion or catalysis [87–92]. Therefore, investigation of light electromagnetic radiation within porous media is of great importance. This investigation of light transfer within porous media can be conducted based on different theories: macro scale method based on the volume average theory, pore size scale method by solving radiative transfer equation (RTE) based on geometrical optic and diffraction theory and pore size scale method by solving Maxwell equations based on electromagnetic radiation theory [93]. Among all the theories and solving methods, Monte Carlo ray-tracing (MCRT) method is the one suitable for complex random pore structure, when the wavelength of the incident light is much smaller than the pore sizes. Figure 2.1.2.1 shows the schematic presentation of a typical random porous structure with irregular strut. Due to the irregular struts with rough surfaces that form the structure of the porous media, computing the light propagating using classical electromagnetic wave theory is impossible [94]. Hence, the light behavior within porous media is mostly determined by the incoming and outgoing directions, material, temperature and wavelength of the incident light. The relationship between the optical constants absorbance, reflectance and transmittance of a porous medium can be expressed as: [95–98]

$$\text{Absorbance} + \text{Reflectance} + \text{Transmittance} = 1 \quad (\text{Equation 2.1.2.1})$$

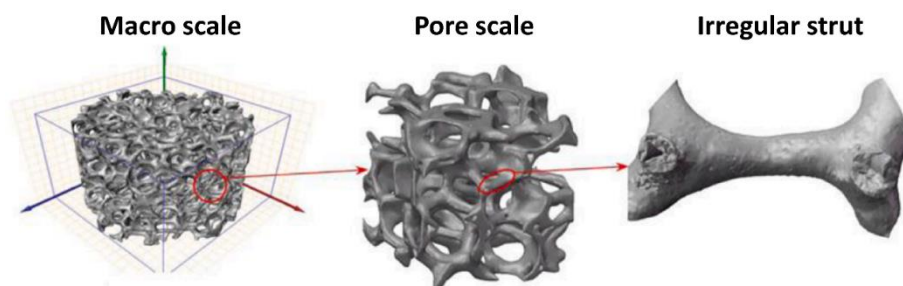


Figure 2.1.2.1 Schematic presentation of typical macro scale and pore scale of porous medium with irregular struts. Reproduced with permission from [93]. Copy right (2022), *Applied Thermal Engineering*.

To investigate the light propagation within an open-cell ceramic foam, a ceramic strut was cut open and illustrated in Figure 2.1.2.2. It is worth noticing that the strut thickness and hollowness varied along the strut length. And the cross-sectional thickness increased from the strut middle to the extremities. Figure 2.1.2.2 (c) showed the quantitative analysis of the ceramic strut, with d_{cs} representing the cross-sectional diameter of the strut, l_{cs} the cross-sectional edge length of the strut, l_{ch} the cross-sectional edge length of the hollowness, S_{ch} the cross-sectional area of the hollowness, S_{cc} the cross-sectional area of the ceramic solid.

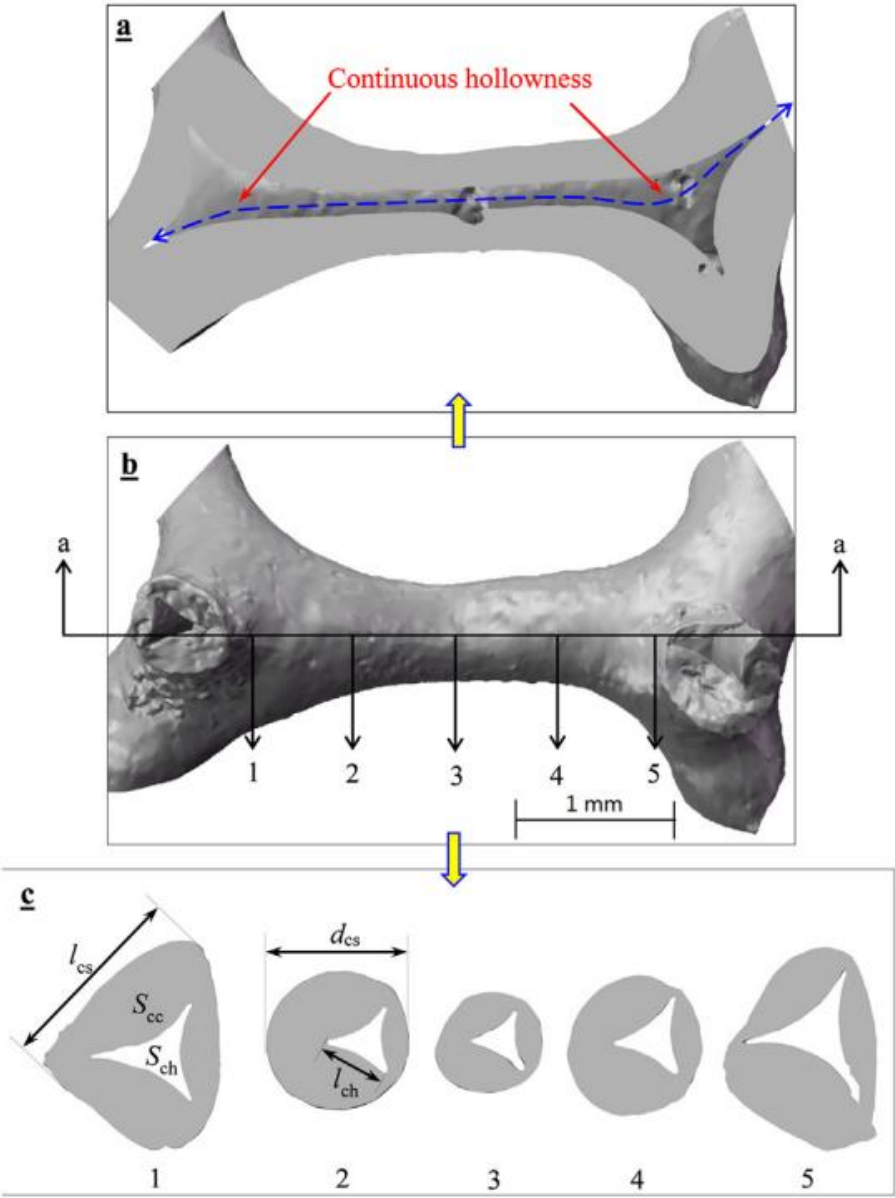


Figure 2.1.2.2 Illustration of the structure of an open-cell ceramic foam: (a) continuous hollowness; (b) overall view; (c) cross-sectional view. Adapted with permission from [99]. Copyright (2018), Elsevier.

To simulate the light propagation of this ceramic foam, the following assumptions were made [99]:

- The ceramic foam is considered isothermal. Hence, the light radiative heat transfer due to self-emission is insignificant and not considered.
- The ceramic surface is considered as smooth.
- The light radiation interaction is restricted to geometric optics approximation (GOA). Diffractions and interferences are not considered.
- The void phase is assumed as transparent.

With these assumptions, the light radiation inside the ceramic foam can be expressed using Radiative Transfer Equation (RTE):

$$\vec{s} \cdot \nabla I_\lambda(\vec{r}, \vec{s}) = \kappa_\lambda(\vec{r}) I_{b\lambda}(\vec{r}) - \beta_\lambda(\vec{r}) I_\lambda(\vec{r}, \vec{s}) + \sigma_{s\lambda}(\vec{r}) / (4\pi) \int_{4\pi}^0 I_\lambda(\vec{r}, \vec{s}') \Phi_\lambda(\vec{r}, \vec{s}', \vec{s}) d\Omega$$

(Equation 2.1.2.2)

with \vec{r} representing the position vector, \vec{s} the propagation direction vector, \vec{s}' the incident direction vector, Φ_λ the scattering phase function, Ω the solid angle, I_λ the spectral radiation intensity, κ_λ the spectral absorption coefficient, $\sigma_{s\lambda}$ the spectral scattering coefficient and β_λ the spectral extinction coefficient.

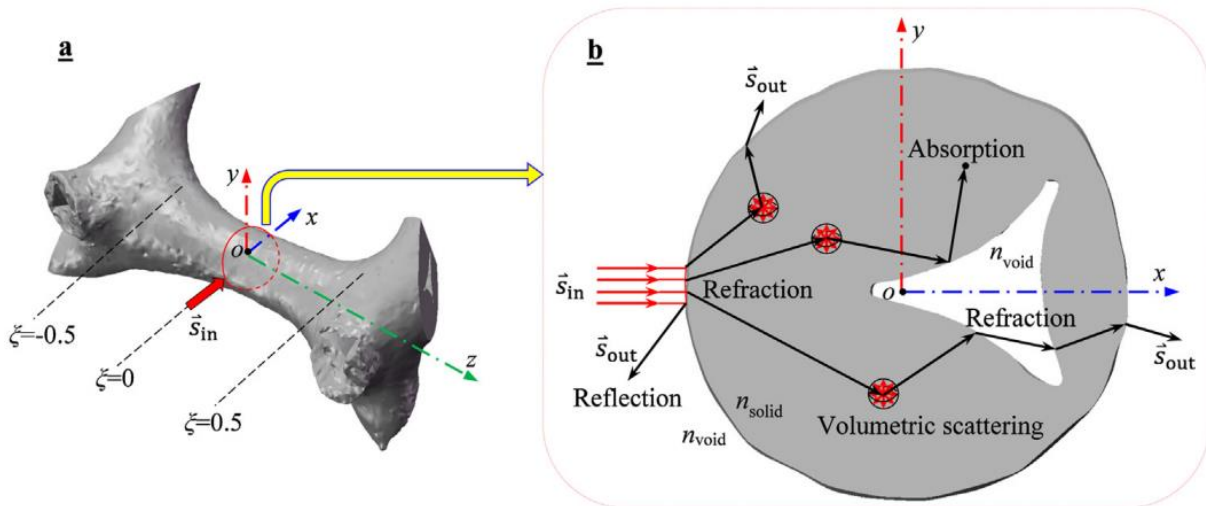


Figure 2.1.2.3 Schematic presentation of light radiative behavior modeling of a random ceramic single strut: (a) 3D overall view of the physical model; (b) 2D view of the cross-section of typical ray paths at the modeled coordinate origin. Adapted with permission from [99]. Copyright (2018), Elsevier.

In the case of a single ceramic strut, the incident light beam with direction \vec{s}_{in} reaches the ceramic strut and irradiates uniformly at position ξ . To model this process, a local coordinate system with the strut length direction as z axis and the strut center as coordinate origin is established and illustrated in Figure 2.1.2.3.

To model the light propagation, specular reflection and Snell's refraction at the solid-void interface, and the volumetric light propagation inside the solid strut must be considered [100]. Reflection and refraction occur (Figure 2.1.2.2 (b)), when the refractive index of strut solid phase n_{solid} is different from that of the void phase n_{void} . The MCRT method utilizes Fresnel's law and Snell's law to calculate reflection and refraction at the solid-void interface, respectively.

According to Fresnel's law, the local specular reflectivity can be expressed as [100]:

$$\rho(\theta_{in}, \theta_t) = \frac{1}{2} \left[\frac{\tan^2 \theta_{in} - \theta_t}{\tan^2 \theta_{in} + \theta_t} + \frac{\sin^2 \theta_{in} - \theta_t}{\sin^2 \theta_{in} + \theta_t} \right] \quad (\text{Equation 2.1.2.3})$$

with θ_{in} referring the local incident ray angle and θ_t the local refractive angle.

The local refractive angle θ_t can be calculated using the Snell refraction equation [100]:

$$\frac{\sin \theta_{in}}{\sin \theta_t} = \frac{n_2}{n_1} \quad (\text{Equation 2.1.2.4})$$

where n_1 equals n_{void} , and n_2 equals n_{solid} , if the ray reaches the interface from the void phase.

In MCRT method, a random number $\xi_\rho \in (0,1)$ is generated to determine whether a ray is reflected or refracted:

$$\xi_\rho < \rho(\theta_{in}, \theta_t), \text{ reflected} \quad (\text{Equation 2.1.2.5})$$

when reflected, the local reflection direction θ_r calculated based on the local incident direction and the local facet normal:

$$\theta_r = \theta_t \quad (\text{Equation 2.1.2.6})$$

The ray determined to be refracted:

$$\xi_\rho > \rho(\theta_{in}, \theta_t), \text{ refracted} \quad (\text{Equation 2.1.2.7})$$

when refracted, the refraction direction can be computed by Equation 2.1.2.2.

As soon as the ray reaches the solid phase, the transmission, absorption and scattering can be investigated through the media radiation transfer theory [100]. The possible transfer distance l_β can be determined using probability equation as:

$$l_\beta = -\ln(1 - \xi_\beta) / \beta_{solid} \quad (\text{Equation 2.1.2.8})$$

with ξ_β referring to a random number from 0 to 1, β_{solid} the extinction coefficient of the ceramic solid material.

After the travel distance l_β is reached, random number ξ_ω is established to determine if the ray is scattered or absorbed:

$$\xi_\omega < \omega_{solid}, \text{ scattered} \quad (\text{Equation 2.1.2.9})$$

$$\xi_\omega > \omega_{solid}, \text{ absorbed} \quad (\text{Equation 2.1.2.10})$$

with ω_{solid} referring to the scattering albedo of the ceramic solid material.

$$\omega_{solid} = \sigma_{solid} / \beta_{solid} \quad (\text{Equation 2.1.2.11})$$

where σ_{solid} is the scattering coefficient of ceramic strut solid phase.

Furthermore, after scattering, the ray continues to travel into a new direction, which can be determined by the isotropic scattering phase function $\Phi = 1$. Or after absorbing, a new ray is emitted. The rays inside the porous structure keep traveling until either absorbed by the structure or reaching the solid-void interface, that the MCRT method can be applied to determine reflection or refraction (circulating from Equation 2.1.2.3).

In conclusion, multiple reflection-refraction-absorption-scattering events happen to the rays inside a porous medium, until the rays leave the strut borders (\vec{S}_{out} in Figure 2.1.2.2), or they are absorbed by the strut of the porous structure [99].

2.2 Plasmonic Materials

Plasmons are defined as resonant modes that involve interaction between free charges and light. Plasma refers to medium that processes freely mobile charges, for instance, ionosphere and metals. For a bulk plasma material, the plasmon frequency ω_p can be expressed as [6]:

$$\omega_p^2 = \frac{ne^2}{\epsilon_0 m} \quad (\text{Equation 2.2.1})$$

with n referring to the number density of mobile charge carriers, e their charge, m their mass and ϵ_0 the relative permittivity of free space.

Plasmonic materials have drawn increasing attention due to their ability of confining and manipulating electromagnetic radiation. Research on plasmonics mostly focus on optics and nanoelectronics by confining light with relatively higher wavelength than the plasmonic nanostructure itself, which leads to numerous novel devices. Conventional plasmonic particles are noble metal nanoparticles, such as gold (Au) and silver (Ag), because of their oxidation

resistance and pronounced plasmon resonance. The surface plasmon resonance (SPR) refers to the coherent collective oscillation of electrons at the metal surface. While, localized surface plasmon resonance (LSPR) is the confinement of the surface plasmon resonance in a nanostructure, which is usually smaller or comparable to the wavelength of the incident light (seen Chapter 2.2.1). Recently, researches on unconventional plasmonic nanoparticles have been conducted as well. Nanostructured metal oxides and metal nitrides have been reported functioning as plasmonic materials, such as TiO₂ nanoparticles [101], CuO nanocrystals [102], MoO₂ nanospheres [103], WO_{2.83} nanorods [104], and TiN / ZrN / TaN / HfN thin films [105,106]. However, these unconventional plasmonic nanostructures have high requirements on processing methods and limited optic properties. In this work, we focused on metallic and metallic core-shell nanoparticles as plasmonic materials.

2.2.1 Metallic materials

When light of a certain wavelength interacts with plasmonic nanostructures, the conduction electrons get displaced with respect to the positive ions, inducing a polarization of the system. The coulombic attraction between the negative and positive works as a restoring force, which results in coherent oscillation of the conduction electrons in the metallic nanoparticle. This coherent oscillation is the so-called localized surface plasmon resonance (LSPR) [107]. Figure 2.2.1.1 illustrates the collective oscillations of electrons in metallic nanoparticles when interact with light.

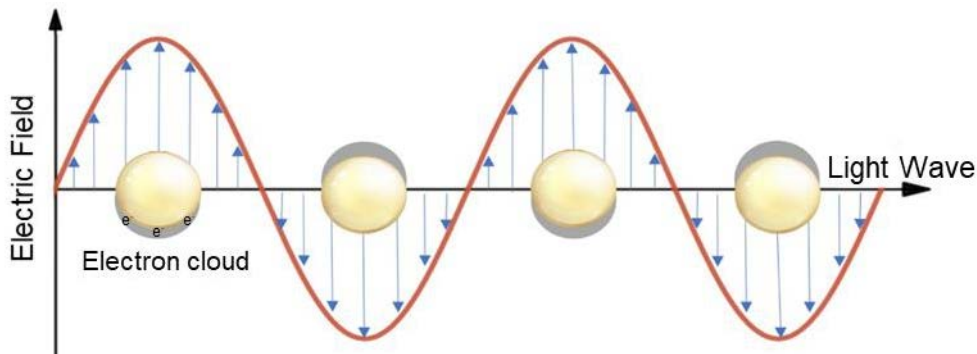


Figure 2.2.1.1 collective oscillation of conduction electrons on metallic nanoparticle surface.

The absorption (σ_{Abs}), scattering (σ_{Sca}) and extinction cross-section (σ_{Ext}) of a single metallic nanoparticle can be calculated respectively as [23]:

$$\sigma_{Abs}(\omega) = 4\pi k a^3 \text{Im} \left[\frac{\varepsilon(\omega) - \varepsilon_d}{\varepsilon(\omega) + 2\varepsilon_d} \right] \quad (\text{Equation 2.2.1.1})$$

$$\sigma_{Sca}(\omega) = \frac{8\pi}{3} k^4 a^6 \left| \frac{\varepsilon(\omega) - \varepsilon_d}{\varepsilon(\omega) + 2\varepsilon_d} \right|^2 \quad (\text{Equation 2.2.1.2})$$

$$\sigma_{Ext}(\omega) = \sigma_{Abs}(\omega) + \sigma_{Sca}(\omega) \quad (\text{Equation 2.2.1.3})$$

with k representing the wavevector, a the radius of the nanoparticle, ε the dielectric constant of the metal particle, ε_d the dielectric constant of the medium surrounding the nanoparticle, $\varepsilon(\omega)$ the dielectric constant of a material when interacting with an external electromagnetic field.

$\varepsilon(\omega)$ consists of two parts:

$$\varepsilon(\omega) = \varepsilon'(\omega) + i\varepsilon''(\omega) \quad (\text{Equation 2.2.1.4})$$

with $\varepsilon'(\omega)$ showing the polarization effect of the external field on the material, $\varepsilon''(\omega)$ the loss caused during the polarization process.

When the metallic nanoparticle is much smaller than the wavelength of the light, the electric field distribution along the whole nanoparticle volume can be considered homogenous. The localized surface plasmon (LSP) intensity can be quantified by the plasmonic quality factor Q_{LSP} : [108]

$$Q_{LSP} = -\frac{\varepsilon'(\omega)}{\varepsilon''(\omega)} \quad (\text{Equation 2.2.1.5})$$

The quality factor can be re-written by substituting the Drudel model: [109]

$$Q_{LSP}^{max} = \frac{2(\omega_p^2 - \gamma^2)^{3/2}}{3\gamma\omega_p^2\sqrt{3}} \quad (\text{Equation 2.2.1.6})$$

where ω_p is the plasma frequency, γ the damping ratio.

Under the so-called resonance condition, the absorption, scattering and extinction get a maximized value, when:

$$\varepsilon(\omega) + 2\varepsilon_d \cong 0 \quad (\text{Equation 2.2.1.7})$$

Therefore, the local field E_{in} inside the nanoparticle can be expressed as a function of the incident one E_0 :

$$E_{in} = \frac{3\varepsilon_d}{\varepsilon(\omega) + 2\varepsilon_d} E_0 \quad (\text{Equation 2.2.1.8})$$

Messinger *et al.* calculated the scattering, absorption, extinction and local field efficiencies ($Q_{Sca}(\omega)$, $Q_{Abs}(\omega)$, $Q_{Ext}(\omega)$, $Q_{NF}(\omega)$ respectively) for a silver nanoparticle with a radius of 22 nm in water, showing proportional relation to the corresponding cross-sections σ [110].

To be more specific, the polarization induced on the metallic nanoparticle surface by the field can be seen as equal to a point dipole located at the centre of the sphere. The field caused by the oscillating dipole adds up to the external field, resulting in a stronger field ($|E_{in}| > |E_0|$). Therefore, the resonance condition improves the scattering, absorption, extinction and local field.

According to the Drude model, the dielectric constant of metals can be expressed as [8]:

$$\varepsilon(\omega) = \left[1 - \frac{\omega_p^2}{\omega^2 + \Gamma^2}\right] + i \left[\frac{\omega_p^2 \Gamma}{\omega(\omega^2 + \Gamma^2)}\right] \quad (\text{Equation 2.2.1.9})$$

with ω_p representing the plasma oscillation frequency (Equation 2.2.1), Γ the total damping rate.

In bulk noble metal material, the valence d-band and conduction s-band are energetically close. While, noble metal atoms have closed shell d levels. In the case of clusters, the emerging of the surface plasmon resonance occurs easily and can be influenced by the d electrons [111]. For instance, the threshold of interband (IB) transitions ω_{Inter} in Ag bulk material is around 4 eV (310 nm). A red-shift of the plasmon frequency ω_p towards the near UV range takes place under the influence of the screening induced by the d electrons [112,113].

The plasmon frequency ω_p of Au, Ag, Al and Cu lies at 139 nm, 135 nm, 98 nm and 142 nm respectively, while the threshold of the IB transitions ω_{Inter} lies at 620 nm, 310 nm, 886 nm and 620 nm respectively [23]. For the above-listed metals, the real part of the dielectric constant is negative at optical frequencies, indicating the electrons do not oscillate with the external field within the spring-mass model, since the electrons cannot move fast enough to follow the oscillation caused by the external radiation [23,107]. At frequencies higher than the IB transition ω_{Inter} , losses generated during the polarization process increase significantly. The IB contribution dominates.

Through analysing of the real and imaginary part of the dielectric constant of different metals (Au, Cu, Ag and Al) [23,86,114], it can be concluded, that the resonance condition is fulfilled in the optical wavelength range between 200 to 1200 nm. Ag shows the lowest loss in the visible wavelength range, indicating that Ag could provide the highest enhancement in the corresponding region. In the near-infrared range, Ag, Au and Cu exhibit little difference, meaning that these three metals should have similar plasmonic properties in this range. Although Al shows the threshold of the IB transition at around 880 nm, the losses are quite low in the ultra-violet (UV) region, therefore, Al should be efficiently plasmonic-active in the UV range.

Different metals have been researched for their plasmonic properties and hence as SERS substrates. Gold is often employed in the case of medical and biological applications, due to its superior chemical stability and low toxicity [115–118]. Silver can get oxidized or sulfidated in the atmosphere [119–122]. Likewise, copper and alumina can easily form oxide layers in air [123,124]. The presence of the oxide layer can prohibit the plasmonic activity of the metal, since the analyte loses the direct contact with the metal surface.

2.2.2 Metallic core-shell nanoparticles

Like other transition (group VIII B) metals, palladium (Pd) and platinum (Pt) are not sufficiently plasmonic-active. To fabricate SERS substrates based on transition metals, perfect ordering/uniform deposition and high surface coverage of the metallic nanostructure are usually demanded [125–130]. Through alloying noble metals with transition metals, the band structure of the metallic alloy material can be engineered. The optical and plasmonic properties of the metallic alloys can be modified, since the plasma frequency ω_p and the threshold of the IB transitions can be shifted by the transition metal.

There are relatively few elements with excellent plasmonic properties, other than Au, Ag and Al. Because of the probability of low-frequency IB transitions and consequent increase of the SPR relaxation frequency, metals with partially occupied d-orbital function less efficiently as plasmonic materials. Therefore, alloys are mostly designed for combination of the plasmonic properties with other properties, such as magnetism or catalytic activity [131,132]. For example, metallic alloy nanostructure consisting Au and Pd can lead to both plasmonic- and catalytic-activity in a single entity. Likewise, metallic alloy of Au and Mg can result in plasmonic- and magnetic-activity in a single configuration.

The plasmon response of the metal alloy is dominated by the metal with IB transitions at lower frequency [133]. Since the frequencies of the maximum local surface plasmon quality factor Q_{LSP} of Cu, Pd and Pt are significantly lower than that of Au [108], the dominating metal in Au-Cu, Au-Pd and Au-Pt metallic alloy materials would be Cu, Pd and Pt respectively. In the case of Au-Fe alloy, a SPR damping and blueshift was observed by the sample of 11 % atomic fraction of Fe. When the atomic fraction of Fe increased to 13 %, the local-field enhancement was reduced by around 20 times [134]. The IB transitions in Ag are at a shorter wavelength than in Au, which leads to larger $\epsilon'(\omega)$ and smaller $\epsilon''(\omega)$ of the Au-Ag alloys, and hence, a higher Q_{LSP} [108].

Meanwhile, metallic bimetallic nanostructures have drawn increasing attentions by various research groups [135–139]. Hu *et al.* prepared Au core Pd shell (Au@Pd) nanoparticles with a size varying from 35 to 100 nm and Pt electrode functionalized with the Au@Pd

nanoparticles as SERS substrate [137]. The Au core has a size of 12 nm with the Pd shell of different thicknesses. The Pt electrode functionalized on the surface with Au@Pd nanoparticles can realize Raman EFs up to $2.7 \cdot 10^3$. Xie *et al.* reported their research on bifunctional Au/Pt/Au nanoraspberries for in situ monitoring Pt-catalyzed reactions [138]. The synthesized raspberry-like Au/Pt bimetallic nanoparticles have two exposed metal surfaces of Au and Pt, resulting in both plasmonic- and catalytic-activity into a single unit. However, the EFs of these bimetallic nanoraspberries were not calculated, due to the complex nanostructure.

2.3 Surface-enhanced Raman scattering

Surface-enhanced Raman scattering refers to the phenomenon that Raman scattering by probe molecules is significantly enhanced when the molecules are adsorbed on the surface of plasmonic nanostructures. This phenomenon was firstly observed in 1974 by Fleischmann *et al.* [16]. The Raman intensity of a probe molecule on a plasmonic nanostructure can be enhanced by different mechanisms: the electromagnetic enhancement and the chemical enhancement. Therefore, the total SERS enhancement factor G_{SERS} can be written as:

$$G_{SERS} = G_{SERS}^{Em} G_{SERS}^{Chem} \quad (\text{Equation 2.3.1})$$

where G_{SERS}^{Em} is the electromagnetic EF and G_{SERS}^{Chem} the chemical EF.

2.3.1 Electromagnetic enhancement

Electromagnetic enhancement refers to the enhancement effect originates from the localization of the plasmon at the SERS substrate surface. Electromagnetic enhancement depends on the feature of the SERS substrate entirely, and type of the probe molecule is irrelevant here.

Electromagnetic enhancement consists of two contributions: the local field enhancement and the re-radiation enhancement. The local field enhancement refers to the phenomena, that the excitation of surface plasmons induces a strong localization in small spatial regions, causing spatial amplification of the laser light. The local field enhancement $M_{Loc}^Z(\omega_L)$ can be defined as:

$$M_{Loc}^Z(\omega_L) = \frac{|E_{Loc}(\omega_L)|^2}{|E(\omega_L)|^2} \quad (\text{Equation 2.3.1.1})$$

with $E(\omega_L)$ indicating the external electric field oscillating at the laser angular frequency ω_L , $E_{Loc}(\omega_L)$ the local electric field experienced by the probe molecule. Z refers to the polarization of the incident laser along the Z axis.

The re-radiation enhancement is caused by the presence of the structure adjacent to the molecule, since the radiated power by a dipole also depends on the environment. A molecule radiates differently if it is excited in vacuum or at the surface of different materials. When the molecule is placed in vacuum or a homogenous medium, the radiation diffuses along the typical emission pattern of a dipole. When the molecule is at an interface, the electromagnetic field irradiated by the dipole gets scattered at the interface and reflected to the dipole, causing a change of the dipole radiation. The re-radiation enhancement can be expressed as:

$$M_{Rad} = \frac{P_{Rad}}{P_0} \quad (\text{Equation 2.3.1.2})$$

where P_{Rad} is the radiation power by a dipole placed in an inhomogeneous environment, P_0 the radiation power in vacuum.

Comparing with chemical enhancement, electromagnetic enhancement is considered as a long-range effect, that the probe molecule should be placed near the plasmonic nanostructure (within a few nanometers range). Normally, electromagnetic enhancement can reach up to 10^8 over the substrate, and to 10^{10} in a hot spot [86].

Meanwhile, the electromagnetic enhancement is reported to be distance dependent [83]. The Raman enhancement at a spot with distance d to the spherical plasmonic nanoparticle with a radius of a can be expressed as:

$$\frac{G_{SERS}^{Em}(d)}{G_{SERS}^{Em}(0)} = \left[\frac{a}{a+d} \right]^{12} \quad (\text{Equation 2.3.1.3})$$

It is important to note that the distance dependency of the SERS signal P_{SERS} is different from the SERS EF G_{SERS} , because P_{SERS} also considers the number of the illuminated molecules. The number of the illuminated molecules depends on the surface area, therefore, the distance dependency of the Raman intensity can be written as:

$$\frac{P_{SERS}(d)}{P_{SERS}(0)} = \left[\frac{a}{a+d} \right]^{10} \quad (\text{Equation 2.3.1.4})$$

2.3.2 Chemical enhancement

Chemical enhancement refers to the enhancement effect from the modification of the polarizability of the probe molecule, which comes from the physic-chemical interaction between the probe molecule and the substrate surface. The chemical enhancement is normally much weaker than the electromagnetic enhancement and is around 10^2 - 10^4 depending on the respective mechanism. The adsorption of a molecule on a substrate surface can be classified as physisorption or chemisorption, depending on the strength of the interaction. Physisorption

is driven by Van der Waals force. While, chemical bond is formed during chemisorption. Nevertheless, the electronic and geometrical structure of the molecule is modified during the interaction with the substrate surface in both adsorption cases. Accordingly, the Raman cross-section of the molecular vibrational modes is altered [23]:

$$G_{SERS}^{Chem} = \frac{\sigma_k^{ads}}{\sigma_k^{free}} \quad (\text{Equation 2.3.2.1})$$

where σ_k^{ads} is the Raman cross-section of the vibrational mode k of the adsorbed molecule, σ_k^{free} the Raman cross-section of the vibrational mode k of the free molecule.

The chemical enhancement consists of two kinds of effect: non-resonant chemical effect and resonant charge transfer chemical effect [140]. The non-resonant chemical effect happens, when the molecule orbital energy is not close enough to the Fermi level the metallic nanostructure, so that a new electronic state is not formed. A new formation of the metal-molecule charge transfer (CT) state leads to the resonant CT chemical effect. Both non-resonant chemical effect and resonance charge transfer chemical effect can be interpreted by density functional theory (DFT) computational methods. The DFT methods can be applied for the explanation of three conditions: enhancement from chemical interaction between molecule and substrate surface at ground state, resonance Raman enhancement with excitation resonance with molecular transition, and CT resonance Raman enhancement with excitation resonance with metal-molecule CT transition [23,140]. Interpretation of Raman enhancement shifts based on DFT method is discussed in Chapter 3.1.3.

2.3.3 Plasmonic hot spots

The term plasmonic hotspot refers to the extremely inhomogeneous and predominantly concentrated distribution of the field enhancement on the surface of a plasmonic structure. These hot spots are often identified as sharp tips or nanogaps between plasmonic nanostructures. With nanogaps exhibiting significantly higher efficiency in amplifying optical signals compared to sharp tips, nanogaps are considered more effective in generating hot spots [23].

Figure 2.3.3.1 shows the schematic presentation of a plasmonic hot spot dimer assembled with two nanoparticles with a distance of d . Polarization of the external electric field along the main axis of the dimer is illustrated in Figure 2.3.3.1 (a), while polarization perpendicular to the dimer axis is exhibited in Figure 2.3.3.1 (b). The nanoparticles are polarized by the external electric field, creating an excess of positive and negative charges on the sides on the nanoparticles. With along-axis polarization, the separation between the induced surface

charges reduces, as the nanoparticles are brought closer to each other, which lead to an increase in the electric field between the two particles.

Furthermore, the polarization of the nanoparticle is influenced not only by the external electric field, but also by the induced dipole in the other nanoparticle. Both effects are present in configuration shown in Figure 2.3.3.1 (a). However, they are not observed in Figure 2.3.3.1 (b), since there is a certain distance between the negative and positive charges on different nanoparticles and the induced dipoles are not allowed for their mutual reinforcement upon the distance in-between.

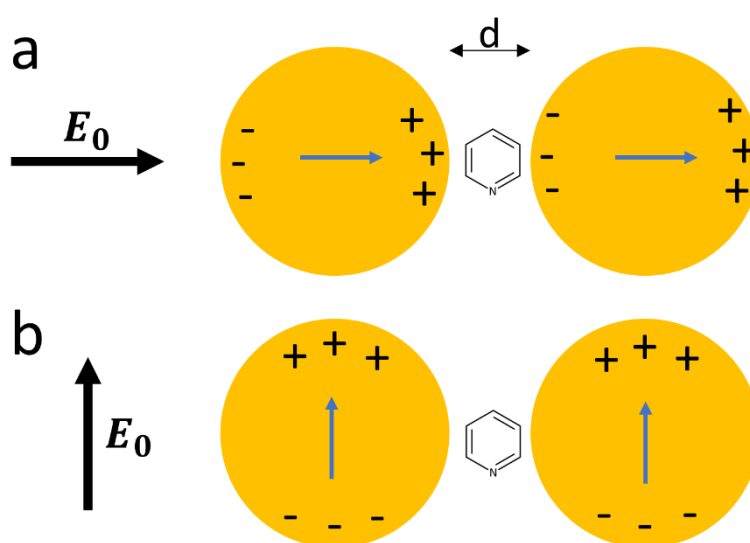


Figure 2.3.3.1 Schematic presentation of a dimer assembled with two nanoparticles with a distance of d . E_0 is the external electric field, pyridine as probe molecule is positioned in the middle between the two nanoparticles. E_0 can be polarized along the axis of the dimer (a), or perpendicularly to the dimer axis. Blue arrows refer to the induced dipoles. Reproduced with permission from [23]. Copyright (2019), *Multidisciplinary Digital Publishing Institute*.

2.4 Bioceramics

Bioceramics refer to ceramics utilized to repair and reconstruct damaged or diseased musculoskeletal components. These ceramics can possess different properties, such as bioinertness (alumina and zirconia); resorbability (tricalcium phosphate); bioactivity (hydroxyapatite and bioactive glass) [141].

Bone substitute materials are categorized into bone grafts and bone graft substitutes according to their composition [142]. Different bioceramic materials are utilized under different conditions, for example hydroxyapatite- or tricalcium phosphate-based ceramics resembling the natural bone mineral and bioactive glasses, such as 45S5 Bioglass can be used as bone substitute materials because of their bioactivity and resorbability, and zirconia-toughened alumina (ZTA)

can be applied as a dental implant material because of their mechanical properties. Both materials show excellent biocompatibility and osteoconductive properties [143,144]. They can be resorbed by the body over time, although bioactive glasses usually degrade significantly faster than hydroxyapatite-based implant material [145].

Hydroxyapatite-based ceramics as bone graft substitute is based on the fact that the inorganic phase of natural bone consists of hydroxyapatite mainly. Hydroxyapatite has a high stability within pH range from 4.2 to 8, and dissolves slowly in the body [143,144]. Alternatively, tricalcium phosphate-based ceramics can also be applied as bone substitute material, although its biodegradation rate is higher than the hydroxyapatite-based material and its mechanical properties is relatively poor. Biphasic calcium phosphates containing hydroxyapatite and tricalcium phosphate has been developed for a combination of mechanical support and proper rate of implant resorption [144].

Bioactive glasses refer to silica-based glasses, that usually also contain Na_2O , CaO and/or P_2O_5 . The exact composition of bioactive glass can vary from product to product. While the most widely investigated and used type is Bioglass 45S5 with a composition of 45 % SiO_2 , 24.5 % Na_2O , 24.5 % CaO and 5 % P_2O_5 . The material's bioactivity can be modified by altering the composition [146]. Figure 2.4.1 illustrates an overview of the influence of the bioactive glass composition on the respective bioactivity [147]. Region A refers to the compositions with bone bonding ability. Region S has additional ability of soft tissue bonding. As the content of silica increases, the glass network becomes denser, which leads to bioinert property (region B). Region C represents a high reactivity that the glass dissolves too quickly. When the silica content gets too low, no glass network can be forming (region D).

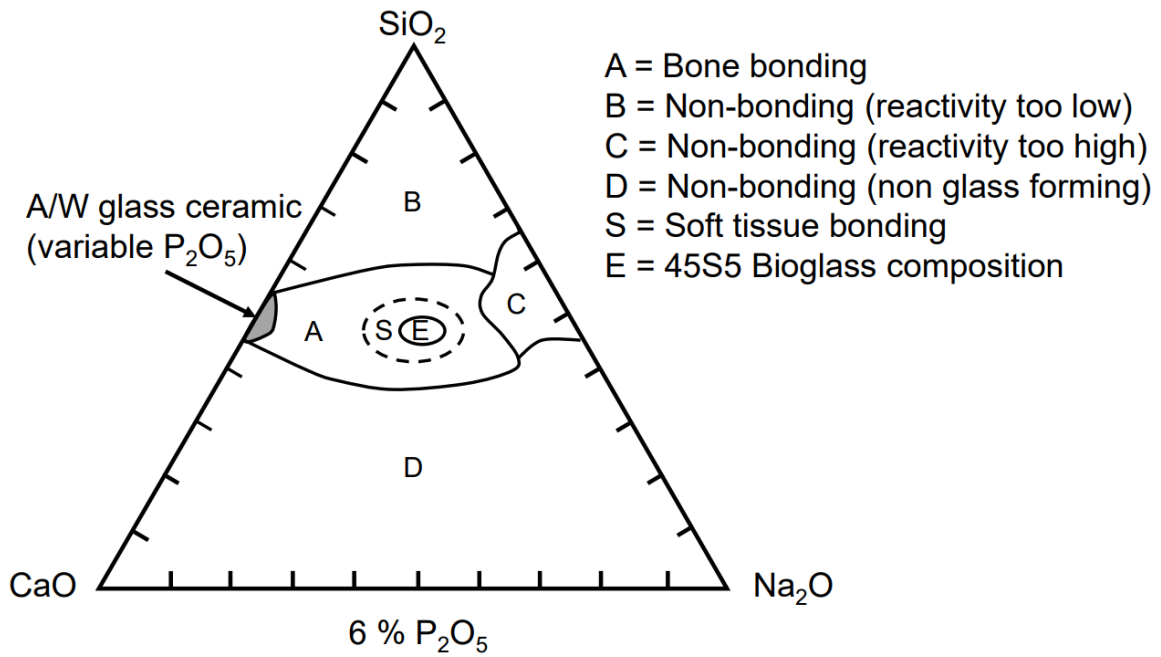


Figure 2.4.1 Influence of bioactive glass composition on tissue bonding. Adapted with permission from [141]. Copyright (1998), *the American Ceramic Society*.

Figure 2.4.2 shows the twelve reaction stages of the bone bonding reaction of bioactive glass [148]. The process is initialized by ion exchange between the bioactive glass and the surrounding body fluids, which leads to the glass network dissolution (stage 1 and 2). By stage 3, a hydrated silica gel forms on the bioactive glass surface, followed by formation and crystallization of a hydroxy carbonate apatite (HCA) layer (stage 4 and 5). Subsequently, growth factors start to adsorb on the HCA layer, which results in the formation of new bone with a bonding to the bioactive glass implant. Furthermore, Bioglass can promote bone growth further away from the material, since the release of silica and calcium ions triggers the deposition of bone matrix by osteogenic cells in the surrounding tissue [149].

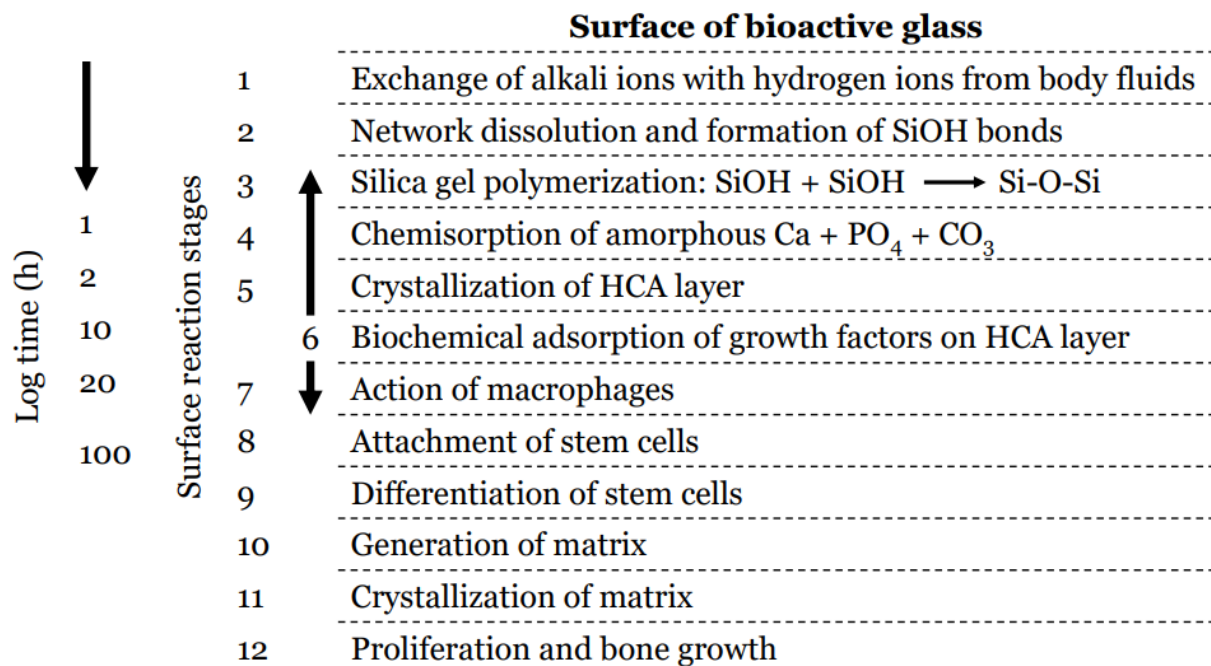


Figure 2.4.2 Sequence of the bonding process of bioactive glass. Adapted with permission from [141]. Copyright (1998), *the American Ceramic Society*.

For actual physiological applications, bone implants are typically designed to be porous to offer a scaffold for vascularization and bone ingrowth [143,144]. However, the limited mechanical strength and fracture toughness of bioactive glass can be disadvantageous when implemented as a porous scaffold [150]. Through altering the composition, synthesis methods and pore architecture, the mechanical properties of the bioactive glass can be tailored similar to cancellous or even cortical bone [151,152]. For instance, employing bioactive glass in the crystalline or semi-crystalline phase can enhance the mechanical properties. However, the biodegradation rate decreases with the increasing mechanical properties [153].

By adjusting the porosity of a bone implant, its mechanical properties can be tailored according to the required application [154]. The principle of determining the bone implant porosity is to possibly mimic the respective surrounding bone. For cortical bone, a porosity of 5-10 % is required, while, for cancellous bone, the porosity should be between 50-90 % [146]. Meanwhile, pore interconnectivity plays an important role, which allows fluid circulation for the transport of reactants and products and to increase the accessible surface for bone deposition [155–157]. A pore interconnectivity possible close to 100 % would be optimal [143]. Besides porosity and pore interconnectivity, pore size is important as well. Pore sizes between 1-10 μm allow a high specific surface area for cell attachment and osteointegration [158,159]. Larger pores in the range between 200 and 500 μm enable bone ingrowth and better vascularization, which promotes new bone tissue formation [160]. Generally, a pore size between 1 and 500 μm is acceptable. Baino *et al.* have pointed out that a scaffold with interconnected porous structure

should have a porosity above 90 % and pore size between 300 and 500 μm , which allows cell penetration, tissue ingrowth, vascularization and nutrient delivery [154].

A conventional synthesis method of bioactive glass powder is the melt-quench method. The respective oxides are melted at a high temperature and quenched in water or in a mold, which leads to a dense glass structure. Alternatively, sol-gel method can also be used. By sol-gel method, a sol containing a silicate-based gel precursor and modifiers is mixed and prepared to allow gel formation. The gel is aged, dried and calcinated to form a semi-crystalline glass-ceramic. This method allows an easier modification of the composition, which does not involve high temperatures, and results in higher purity and homogeneity of the sample [161]. Additionally, bioactive glass synthesized via the sol-gel method shows higher bioactivity and biodegradation rates compared to melt-derived bioactive glass, due to its inherent nanoporosity.

3. Methodology

3.1 Macro-porous ceramic processing

Processing of macro-porous ceramics with a porosity above 20 % has been well-established [162]. Most commonly applied processing methods can be classified into replica technique, sacrificial template method and direct foaming method (as shown in Figure 3.1.1).

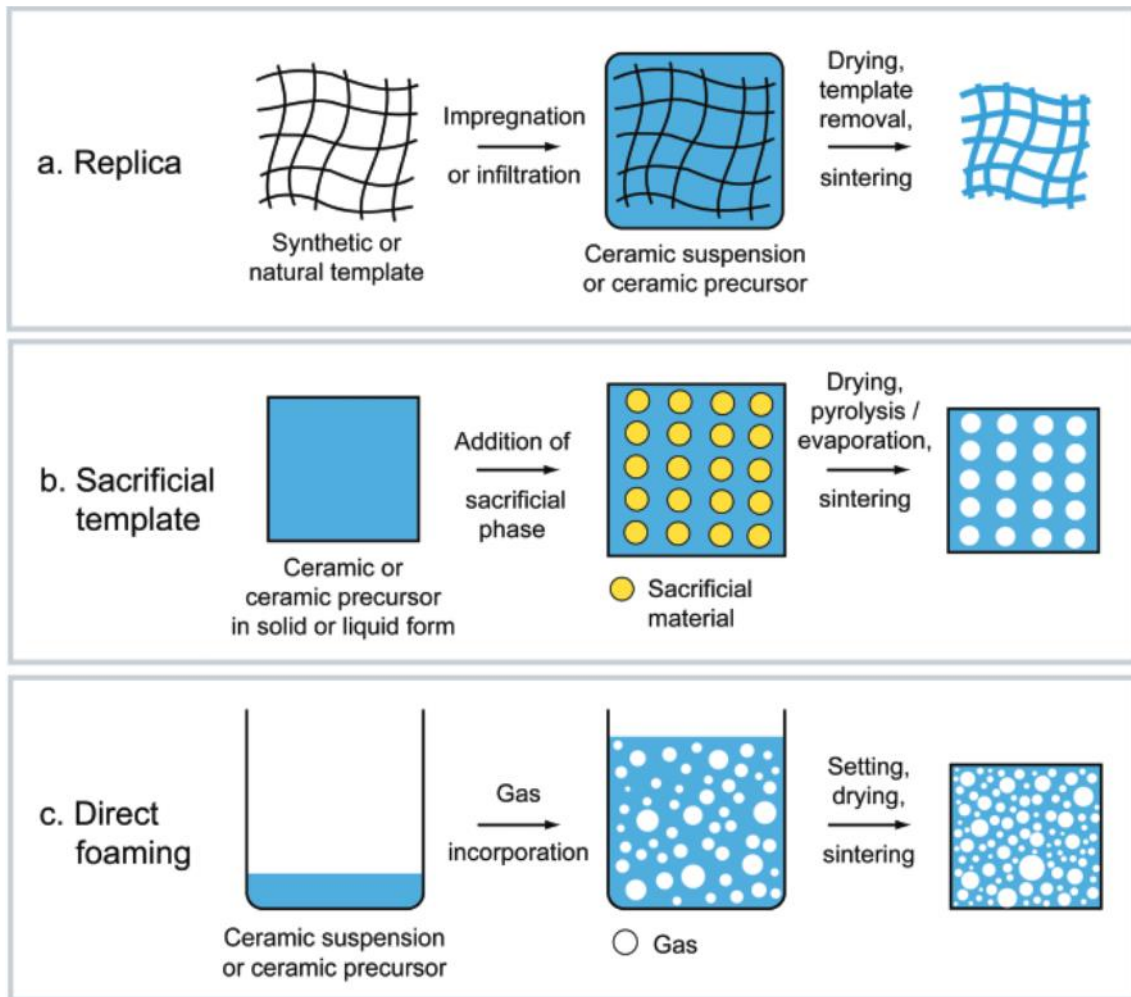


Figure 3.1.1 Schematic representation of (a) replica technique, (b) sacrificial template method, and (c) direct foaming method for macro-porous ceramic processing. Adapted with permission from [162]. Copyright (2006), the American Ceramic Society.

Replica technique

The replica technique involves impregnating a cellular structure with a ceramic suspension or precursor solution to create a macro-porous ceramic that mimics the morphology of the original porous material (as shown in Figure 3.1.1 (a)). Subsequently, the with ceramic slurry coated template is dried and burned out, leaving a macro-porous structured ceramic.

This technique can be applied to a wide range of synthetic and natural cellular structures. Typical synthetic templates are polymer foams, carbon foams, while natural templates are coral and wood. Meanwhile, this technique shows a high flexibility, since it can be applied to any ceramic material that can be appropriately made into a suspension. Porous ceramics produced with sponge replica technique can achieve an open-cell foam structure with porosity ranging from 40 % to 95 %. These structures exhibit a reticulated pattern of highly interconnected pores with sizes from 200 μm to 3 mm [162].

Sacrificial template method

The sacrificial template method involves creating a biphasic composite that comprises a continuous matrix of ceramic particles or precursors, and a dispersed sacrificial phase. The sacrificial phase is initially distributed uniformly throughout the template and eventually removed to create pores within the structure (Figure 3.1.1 (b)).

This method offers a significant advantage over other processing methods by allowing deliberate tailoring of the porosity, pore size distribution and pore morphology of the ceramic product, through which a wide range of porosity from 20 % to 90 % and pore size between 1 and 700 μm can be realized [162]. The sacrificial template method leads to a ceramic component that is the opposite of the original template, so that no flaws will be left in the structure by the removal of the sacrificial phase. As a result, the porous ceramics produced with this method have normally a remarkably higher mechanical strength.

Direct foaming method

By direct foaming method, air is firstly introduced in a suspension or liquid medium, which is then solidified to maintain the structure of the created air bubbles (Figure 3.1.1 (c)). A high sintering temperature is typically required to produce porous ceramics with a high mechanical strength. The porosity of the porous ceramics produced with this method can be tailored by controlling the incorporated gas, while the pore size is determined by the wet foam before setting.

Wet foams are thermodynamically unstable, since they experience ongoing Ostwald ripening and coalescence processes to reduce to overall free energy. These processes lead to an increase in the size of the incorporated bubbles, which results in large pores in the porous structure. Normally, the wet foams can be stabilized with surfactants or particles. The surfactant-based direct foaming is able to realize pore sizes ranging from 35 μm to 1.2 mm and a porosity between 40 % to 97 % [162].

3.2 Synthesis of nanoparticles

Nanoparticles are particles with a size between 1 and 100 nanometers. Compared to the respective particles at macro-scope, nanoparticles possess unique physical, chemical and biological properties at nano scale, because of their relatively higher surface area to volume ratio, increased reactivity (or stability) in chemical processes and other qualities [163].

In general, the synthesis of nanoparticles can be categorized into top-down or bottom-up method. Top-down approach describes the breaking down of the bulk material into nanosized structures. While, bottom-up approach refers to the build-up of the nanoparticles: atom by atom, molecule by molecule, or cluster by cluster. Compared to the top-down approach, the bottom-up approach shows advantages in tuning the nanoparticle shape and size [164].



Figure 3.2.1 Schematic representation of top-down and bottom-up approach for the nanoparticle synthesis.

3.2.1 Synthesis of metallic nanoparticles

For the synthesis of metallic nanoparticles, various physical and chemical methods are frequently employed, including electrochemical reaction, chemical reduction, and photochemical reduction [165,166]. Determining an appropriate method for preparing metallic nanoparticles is of great importance, since the interaction of metal ions with the reductant, the stabilizing agent and experimental related process significantly affect the morphology, stability and physicochemical properties of the metallic nanoparticles [167]. Various methods for metallic nanoparticle synthesis are listed in Table 3.2.1.1.

Mechanical milling

By mechanical milling, the particle size is decreased using high energy ball milling. This method involves adding bulk power to a container filled with heavy balls, which are subjected to high mechanical energy via high-speed rotating balls. By employing high-energy mills, such as attrition ball mill, planetary ball mill, or vibrating ball mill, the particle size reduction can be achieved. The efficiency of mechanical milling is influenced by the process variables and the milling power properties. This method is often used for preparation of intermetallic nanoparticles [168]. This method offers a possibility of cost effective and large-scale production of high purity nanoparticles. However, prolonged milling time and high energy is required.

Laser ablation

The laser ablation method utilizes laser irradiation to reduce the size of the particles to nano scale. During this method, a solid target is positioned beneath a thin layer and exposed to pulsed laser irradiation, which leads to fragmentation of the solid material into nanoparticles. The synthesized nanoparticles are dispersed in the surrounding liquid, resulting a colloidal solution. This method provides an effective option with a simple procedure [169].

Table 3.2.1.1 Methods for metallic nanoparticle synthesis. Adapted with permission from [169]. Copyright (2019), *Elsevier*.

No.	Top-down approach		Bottom-up approach	
	Method	Examples	Methods	Examples
1	Mechanical milling	Ball milling Mechanochemical method	Solid state method	Physical vapor deposition Chemical vapor deposition
2	Laser ablation		Liquid state method	Sol-gel method Chemical reduction Hydrothermal method Solvothermal method
3	Sputtering		Gas phase method	Spray pyrolysis Laser ablation Flame pyrolysis
4			Biological method	Bacteria Fungus Yeast Algae Plant extract
5			Other methods	Electrodeposition Microwave technique Supercritical fluid Precipitation process Ultra sound technique

Solid state methods

Solid state methods can be classified into physical vapor deposition and chemical vapor deposition. Physical deposition involves depositing material onto a surface in the form of either a thin film or nanoparticles. During the process, vaporization of the materials is realized through highly controlled vacuum techniques and later condensed on a substrate. This method is frequently employed to deposit metallic nanoparticles and thin films onto substrates [170], however, is limited due to high cost and generating low volume of the material.

By chemical vapor deposition, the thin film or nanoparticles are deposited on a surface through the chemical reaction of gaseous molecule containing required atoms. During this method, volatile molecules are released as precursors to interact with precursor fragments and substrate surface to form a thin film or nanoparticles [171].

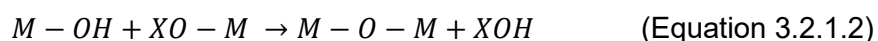
Liquid state methods

In the sol-gel process, the sol undergoes a gradual evolution towards the development of a gel-like network, which contains both liquid and solid phase. Normal sol-gel process has four steps: hydrolysis, condensation, aging and drying and calcination. Figure 3.2.1.1 shows the four steps of a sol-gel process to synthesize metal oxide nanoparticles [172]. The first step hydrolysis of precursors happens in liquid. The general chemical reaction during the hydrolysis can be expressed as:



with M representing metal and R alkyl group.

By the second step, condensation, the metal oxide linkages are formed, and a polymeric network grows to colloidal dimensions. Condensation consists of two processes: olation and oxolation. Olation refers to the process where a hydroxyl ($-OH-$) bridge is formed between two metal centers (metal-hydroxy-metal bond). While, oxolation describes the process where an oxo ($-O-$) bridge is formed between two metal centers (metal-oxo-metal bond). The condensation process can be described as:



with X representing H or alkyl groups.

Subsequently, an aging process takes place, during which polycondensation continues in the localized solution along with reprecipitation of the gel network, resulting an increase in thickness of the gel and decrease in the porosity. Thereafter, the drying process takes place. The relative humidity (RH) must be carefully controlled during drying, which could affect the

stability and performance of the synthesized nanoparticles. Finally, the sample undergoes a thermal treatment, to eliminate the water molecules from the sample.

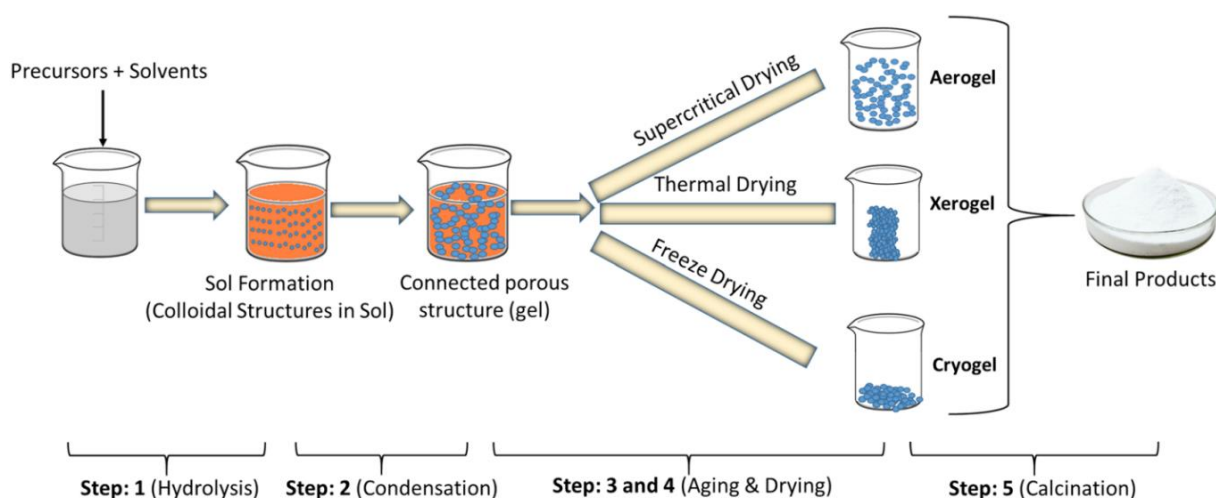


Figure 3.2.1.1 Schematic representation of a sol-gel process. Adapted with permission from [172]. Copyright (2020), Springer.

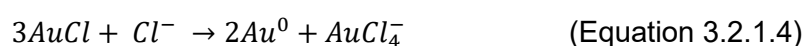
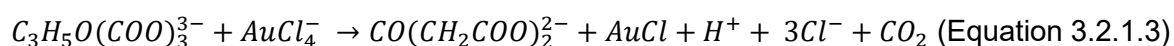
Typically used precursors for colloid synthesis are metal alkoxides and aloxysilanes. Metal alkoxides are organo-metallic precursor for different metals, such as aluminium and titanium [173–175]. The sol-gel method is a simple procedure technique, by which the particle size and morphology can be tuned by adjusting the reaction parameters.

Different from the sol-gel method, the chemical reduction method involves reducing an ionic salt in a suitable medium with the assistance of surfactants and reductants [176]. To synthesize noble nanoparticles, reductants such as sodium borohydrate, glucose, ethylene glycol, ethanol and sodium citrate are well-known. Besides the reductant, the action of a stabilizer in the solution phase synthesis plays an important role. For instance, trisodium citrate (TSC) is one of the most commonly used reductants, which can function as nanoparticle stabilizer as well. Amino acids can be employed for Au nanoparticle synthesis without any further surfactant. Ascorbic acid is often used for nanorod synthesis, where Au ions are complexed by surfactants, such as cetyltrimethylammonium bromide (CTAB) [177].

Among chemical reduction method using all different reductants, Turkevich method has been well investigated for synthesis of Au nanoparticles from 9 to 120 nm with defined size distribution [177,178]. Meanwhile, this method can be adapted for synthesis of transition metals, such as palladium (Pd) and platinum (Pt) [179–181]. Turkevich and Frens described the standard method for the chemical reduction synthesis method of Au nanoparticle using TSC as reductant. To initiate the reduction process, a solution of gold hydrochlorate is boiled

with TSC in a double-walled reactor, which enables a homogeneous temperature distribution within the reactor. After mixture of TSC and the gold hydrochlorate solution, Au nanoparticles are formed.

Large numbers of studies have investigated the particle growth mechanism using the Turkevich method [182–190]. The accepted mechanism of the Turkevich method for Au nanoparticle synthesis involves the initial redox reaction of Au^{3+} to Au^+ by citrate (Equation 3.3.1.3). Meanwhile, the citrate is oxidized to acetone dicarboxylate ($CO(CH_2COO)_2^{2-}$). The first redox reaction determines the reaction rate. While, the disproportionation reaction (Equation 3.3.1.4) occurs where the metal Au and Au^{3+} are produced.



Recently, Gao *et al.* challenged the conventional Turkevich mechanism for the Au nanoparticle synthesis using citrate as reductant and revealed the Turkevich mechanism consisting of two consecutive reduction steps (as shown in Figure 3.2.1.2), instead of the traditionally believed a reduction followed by a disproportionation reaction [191]. Acetone dicarboxylate ($CO(CH_2COO)_2^{2-}$) plays an important role as intermediate during these two-step process, as it showed remarkably higher reduction potential than citrate. Moreover, acetone dicarboxylate stabilizes the formed Au nanoparticles electrostatically through the coordination of the enol form.

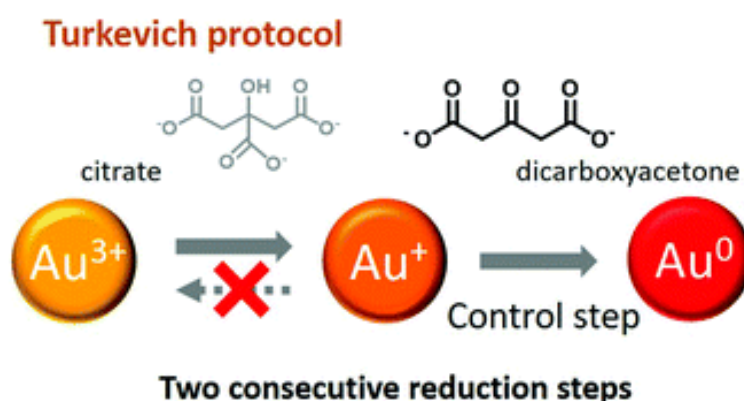


Figure 3.2.1.2 Schematic representation of the Turkevich mechanism consisting of two consecutive reduction steps. Adapted with permission from [191]. Copyright (2020), *Royal Society of Chemistry*.

The chemical reduction method is one of the simplest methods for metallic nanoparticle preparation, however, comes with limitations, such as toxicity or poor reducing ability of the reductant, high costs and possible impurities.

Gas phase methods

In the spray pyrolysis method, nanoparticle precursors are delivered in the form of small droplets form through a nebulizer into the hot reactor. Commonly used metal precursors are acetate, nitrate and chloride. The apparatus normally consists of three parts: a fluid nebulizer for atomization of metal precursor solution, a vertical tubular reactor which can be thermostatically controlled and a precipitator for collecting the synthesized metallic nanoparticles [192]. This method showed advantages in controllability of the particle size.

Laser pyrolysis utilizes laser as energy source to synthesize nanoparticles. The homogeneous nucleation of precursor is driven by the laser energy. Infrared CO₂ laser is one of the most commonly used lasers, which enables nanoparticle formation as soon as sufficient degree of the supersaturate product is reached in vapor phase [193].

3.2.2 Synthesis of metallic core-shell nanoparticles

The synthesis of metallic core-shell nanoparticles can be achieved through various methods, such as, galvanic replacement, seed-mediated growth, electrochemical deposition, sol-gel method, thermal evaporation and co-precipitation.

Galvanic replacement method

Galvanic replacement is a redox process that takes place when two metals come into contact in a solution phase. During this process, the ions of the second metal corrode the first metal, resulting in a core-shell structure. Two reactions are involved in this process, the corrosion of the first metal at the anode, and the reduction of the ions of the second metal, followed by subsequent deposition of the second metal. The driving force originates from the difference in reduction potentials between two different metals. The potential of the second metal must be higher than that of the first metal. This approach allows not only synthesis of bimetallic and hollow nanomaterials with ultrathin walls in a single reaction step, but also deposition of metallic nanostructures onto solid supports through wet-impregnation method [194,195].

Seed-mediated growth method

The concept of seed-mediated growth method is shown in Figure 3.2.2.1, where colloidal seeds serve as templates for atom deposition. During this synthesis process, a precursor solution is introduced into a vessel that contains seeds, reductant, capping agent and colloidal stabilizer. The metal precursor is reduced to form zero-valent metallic atoms and subsequently heterogeneously nucleate on the seed surface. As growth continues under controlled experimental conditions, well-defined nanostructures are formed. In the case of metal-metal core-shell nanoparticles, the seeds are the first metallic nanoparticles. These seeds can be

used in the original reaction solution or collected and dispersed into a new medium. Through carefully tuning the experimental conditions, such as reaction temperature and precursor concentration, the growth of the second metal on the seeds can be controlled, and therefore, result in nanostructures with desired chemical composition, size and shape [196].

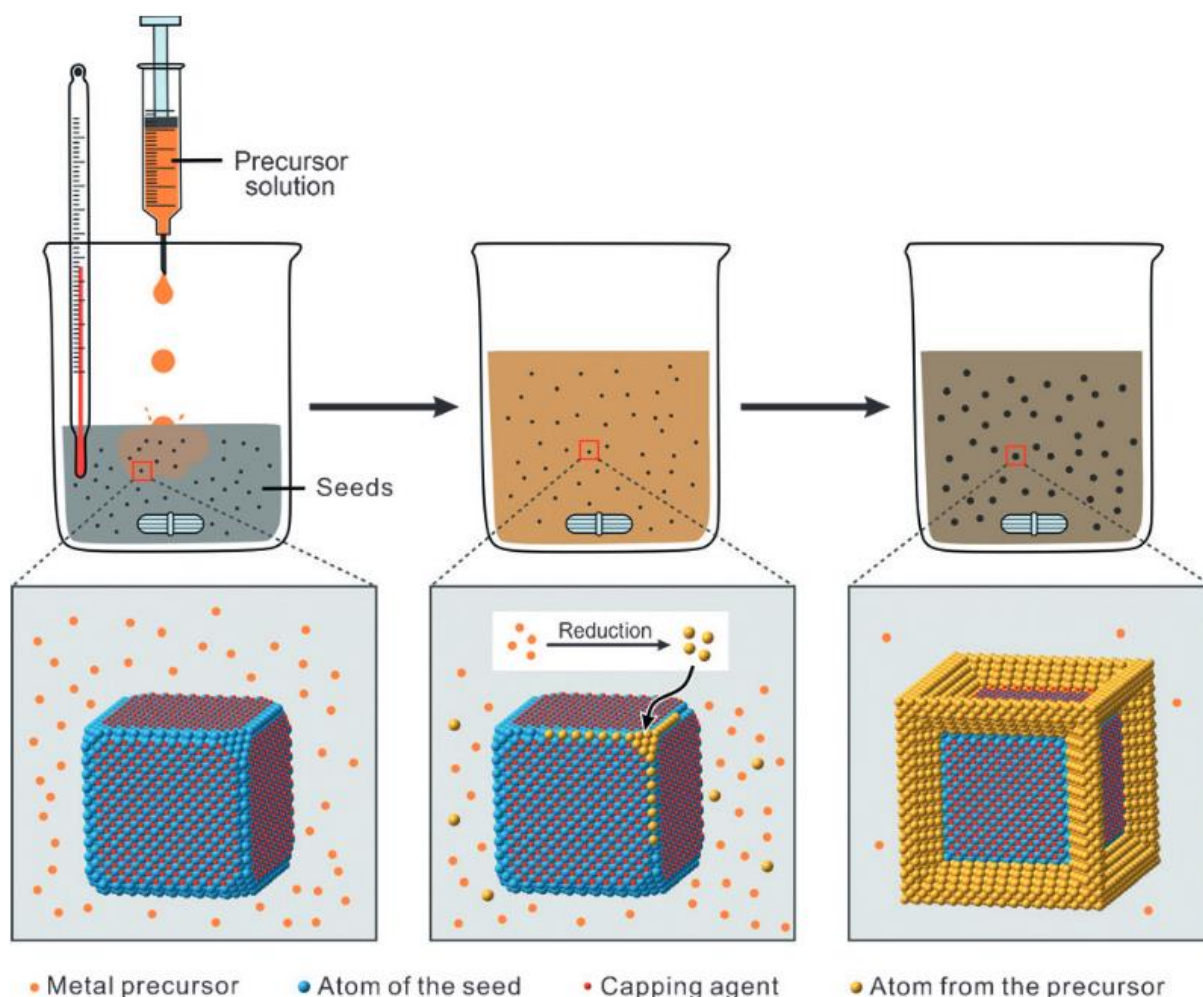


Figure 3.2.2.1 Schematic representation of the seed-mediated growth of colloidal metal nanocrystals. Adapted with permission from [196]. Copyright (2017), Wiley.

To synthesize bimetallic core-shell nanoparticles using seed-mediated growth method, the first metal is normally used as the seed, which serves as template for the deposition of the second metal atoms.

In the context of colloidal synthesis, nucleation is the initial step that atomic or molecular species must undergo before forming a nanostructure. Nucleation can occur either via homogeneous nucleation or heterogeneous nucleation. Homogeneous nucleation is also called self-nucleation, during which nuclei/seeds are generated. Heterogeneous nucleation involves the deposition of atoms on the surface of existing seeds. In both cases, the atoms are

required to overcome an energy barrier, which is unique to either nucleation mode. The energy barrier is usually lower during heterogeneous nucleation.

Thermal evaporation method

Thermal evaporation deposition belongs to the category of physical vapor deposition. This technology is widely used for producing thin films, where the materials is evaporated in a vacuum chamber to create gaseous atoms. These atoms then settle onto the substrate surface and form a thin film. Amorphous substrates such as carbon and glass can facilitate the agglomeration of Ag, Cu or other metal atoms into nanoparticles, due to the island growth mode [197].

The growth of bimetallic Ag-Cu nanoparticles was investigated using thermal evaporation method [198–200]. During the thermal evaporation method in vacuum, when Ag atoms were deposited on the Cu nanoparticles, the Ag atoms grew epitaxially and their lattices matched well. However, when Cu atoms were deposited on the Ag particles, a particular core-shell-like structure formed and disordered lattice was introduced.

3.3 Surface-enhanced Raman spectroscopy

Raman spectroscopy is a non-destructive method, that analyses the inelastic scattering energy shift due to unique vibrational modes of each single molecule. Surface-enhanced Raman scattering (SERS) uses plasmonic nanostructures to excite the localized plasmon resonance, which leads to significantly increased Raman intensity.

This technology allows rapid and sensitive detection of Raman-active molecules, and therefore, has drawn increasing interest in various research fields. Researches on SERS technique have been explored in various aspects, for instance, fundamental aspects regarding the enhancement mechanisms [36,201–205], single molecule detection [19,35,206,207], or the development of optimal SERS substrates [208–212].

3.3.1 Influence of hot spots on Raman enhancement factors

In Chapter 2.3.3, the concept of plasmonic hot spots was introduced and the theoretical background of the enhancement of the induced dipole was explained. The influence of hot spots on Raman EFs G_{SERS} was investigated qualitatively [23]. For instance, the dimer hot spot formed by two 50 nm sized Au nanoparticles with a gap d was studied [85]. During the measurement, the laser is polarized along the main axis of the dimer, with probe molecules placed at the surface of one of the Au particles, along the main axis. Compared with the limited

EF of around $2 \cdot 10^3$ offered by a single Au nanoparticle, the EF of the Au nanoparticle dimer hot spot reached $5 \cdot 10^5$ with the gap $d = 10 \text{ nm}$, and increased to $3 \cdot 10^9$, when the gap was reduced to 2 nm. The Raman EF is reported to be in relation with the gap in hot spot [213–215]:

$$G_{SERS} \sim \frac{1}{d^2} \quad (\text{Equation 3.3.1.1})$$

When the gap d reduced to less than 1 nm, the increase of the enhanced is limited, due to quantum mechanical properties [205,216].

3.3.2 Choosing the excitation wavelength during SERS measurements

To determine the appropriate light source for the SERS measurements, two factors must be taken into consideration. On the one hand, the SERS measurements should be conducted under experimental conditions that signal-to-noise ratio (SNR) is optimized [217]. This condition not only facilitates faster analysis but also helps to lower the limits of the detection. On the other hand, SERS spectra should be collected with excitation light source, which is within the optical window of the sample, especially for biomedical measurement. The light source should be able to propagate through the biological samples, such as skin, tissues and bones. Figure 3.1.4.1 shows the three optical windows of human skin, namely, first window between 650 and 950 nm (NIR-I), second window between 1000 and 1350 nm (NIR-II) and third window from 1500 to 1800 nm (NIR-III) [218]. In contrast to the other two windows, the first window between 650 and 950 nm exhibits a higher level of tissue auto-fluorescence, which contributes to the Raman signal as a broader background, and hence, leads to a reduction of the SNR.

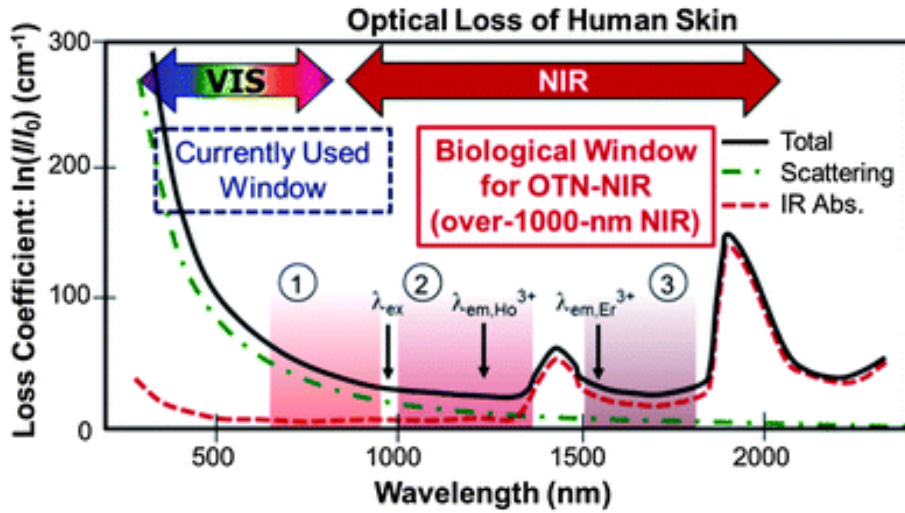


Figure 3.3.2.1 Absorption spectrum of human skin presenting the first, second and third biological optical window. Adapted with permission from [218]. Copyright (2013), *the Royal Society of Chemistry*.

Moreover, Raman spectra should be collected at the excitation wavelength at which a maximum SERS enhancement factor G_{SERS} can be reached. Normally, the SERS intensity is linear with the laser intensity. Therefore, the laser intensity can be increased, as soon as the photochemical or thermal process do not damage the probe molecule or the substrate.

The laser excitation also affects the Raman cross-section σ_k [23]:

$$\sigma_k \propto \tilde{\nu}_0 (\tilde{\nu}_0 - \tilde{\nu}_k)^3 \sim \tilde{\nu}_0^4 \quad (\text{Equation 3.3.2.1})$$

with $\tilde{\nu}_0$ referring to the excitation laser wavenumber, $\tilde{\nu}_k$ the Raman shift of the mode k and $\tilde{\nu}_0 - \tilde{\nu}_k$ the absolute (Stokes) Raman wavenumber.

This frequency dependence can be simplified as $\sim \tilde{\nu}_0^4$, in the case of small Raman shifts. Equation 3.1.2.4 indicates an increase in the amount of the scattered Raman photos, when the excitation laser is changed from near-infrared light to visible light. For instance [23],

$$\sigma(\lambda_{Exc} = 785 \text{ nm}) = 0.18 \cdot \sigma(\lambda_{Exc} = 514 \text{ nm}) \quad (\text{Equation 3.3.2.2})$$

Kleinman *et al.* investigated the correlation between the excitation laser wavelength and the Raman enhancement factor, based on the Raman signals from *trans*-1,2-bis(4-pyridyl)-ethylene (BPE) placed closely to a single gold dimer and encapsulated in a protective silica shell [219]. Eight lasers with different wavelengths were studied as excitation source. It is worth noticing, that the scattering spectrum peak (red spectrum) is strongly blue-shifted compared to the enhancement factor spectrum peak (blue spectrum, corresponding to the local field). The experimental result agreed with the calculation in the same paper and the theoretical results by Le Ru *et al* [85]. This result indicates the maximum enhancement of a dimer consisting of two nanoparticles is red-shifted compared to the single nanoparticle, however,

the enhancement provided by a dimer is exponentially increased. This results also implies that the choice of excitation wavelength for SERS substrates with plasmonic hot spots, such as dimers, should consider the red-shift of the local field enhancement maximum [23].



Figure 3.3.2.2 Diagram of scattering intensity (red) and enhancement factor (blue) measured on the single gold nanoparticle dimer encapsulated in a silica shell, with different excitation lasers. Adapted with permission from [219]. Copyright (2013), *American Chemical Society*.

3.3.3 Fabrication of SERS substrates

A perfect SERS substrate should possess the following features: high average enhancement, uniformity, reproducibility, large area, stability and ease of fabrication [210,220]. However, it is impossible to achieve all the qualities, a balance between the most desired qualities should be found. As a general rule, the high enhancement comes with the low uniformity / reproducibility [85,221].

High SERS enhancement factor G_{SERS} demands hot spot, where extremely small gaps (within few nanometers) are required. Such small gaps can be realized through nanoparticle assembly. However, the morphology is difficult to control. One may say, a controllable and reproducible morphology can be achieved by lithographic methods. However, the gaps by lithographic methods are limited to around 3 nm [222–224].

Conceptually, SERS detection can be conducted in two different ways: direct (label-free) and indirect (label-aided). With direct detection, the probe molecule is identified through its own Raman spectrum. This method is suitable for molecules with large cross-section, for example, pesticides and food dyes [225–228]. Indirect methods involve the engineering of a SERS label (also called SERS-tag) and a more complex detection spectrum. The SERS label normally consists of an efficient Raman reporter molecule, which can selectively bind to the probe molecule. The probe molecule is identified through the spectrum of the Raman reporter molecule.

Typical laboratory synthesis methods of SERS substrates for direct detection are catalogued and listed in Table 3.3.3.1.

Table 3.3.3.1 Summary of the typical laboratory synthesis methods of SERS substrates for direct detection. Reproduced with permission from [23]. Copyright (2019), *biosensors*.

Catalogue	Synthesis method
Aggregated nanoparticles in solution	Wet chemistry (nanoparticle synthesis) Laser ablation (nanoparticle synthesis) Molecular linkers (aggregating method) Laser tweezers (aggregating method)
Nanoparticle assembled on a surface	Electrochemical roughening / deposition Deposition on functionalized surface Ink-jet printing Screen printing Pen on paper Electrospinning Laser direct writing
Ordered array of nanoparticles	Anodic alumina template Electron beam lithography Interference lithography Soft lithography

Aggregated nanoparticles in solution

This method is an efficient and easy method, which involves aggregation of nanoparticles in colloidal solution. The plasmonic nanoparticles can be synthesized via various methods (described in Chapter 3.2). The aggregation of nanoparticles can be facilitated by adding a salt to the solution, which increases the ionic strength of the solution and reduces the screening of the stabilizing charges at the nanoparticle surface, leading to aggregation. Meanwhile, probe molecules equipped with certain functional groups, are able to displace the stabilizing ligands at the nanoparticle surface, which promotes the aggregation as well. Certainly, the experimental procedure of the colloidal nanoparticle plays an important role. For instance, a longer mixing time during the aggregation step of the silver colloids resulted in a better reproducibility of the SERS data, due to the reduced formation of random silver nanoparticle aggregates [229]. Also, it was reported that through the addition of KCl, the silver colloid can be aggregated and form a metastable state without precipitation of large clusters [230].

To tune the nanoparticle aggregation in solution, methods like molecular linker or laser tweezer can be applied. Molecular linker facilitates the dimer formation with extremely small gap [231–233]. While, laser tweezer method utilizes highly focused laser beam and the optical forces on the metal nanoparticles. When the excitation wavelength is longer than the surface plasmon resonance of the nanoparticle, the nanoparticle experiences two forces: a gradient attractive force towards the high intensity region of the laser beam and a radiation pressure force that moves the nanoparticle in the direction of the beam's propagation [234,235].

Nanoparticles assembled on a surface

The approach nanoparticles assembled on a surface can be achieved via different methods, such as electrochemical techniques, nanoparticles adsorbed on solid / soft surface, laser direct writing and other methods. Electrochemical techniques allow easy tuning of the experimental conditions, resulting the formation of a wide range of nanostructures with different sizes, shapes and morphologies. The two main approaches electrochemical roughening (ER) and electrochemical deposition (ED) can be both realized in a two- or three-electrode cell system. One of the most commonly used approach is the potentiostatic condition [236,237].

The electrochemical approach normally consists of a working electrode and a reference electrode. Electrochemical roughening involves short pulses (~ 20 ms) at a positive potential to prompt the dissolution of small areas of metal, followed by a second pulse at a less positive potential, so that the metal re-deposits on the electrode. Meanwhile, electrochemical roughening requires a carefully prepared deposition bath containing the metal salt, organic or inorganic ligands for controlling the shape and dimension of the formed nanoparticles, and an electrolyte for buffering the ionic conductivity [23].

The deposition of nanostructures is potential controlled, which can be realized in different ways, such as, cyclic voltammetry (CV) or double-step potential deposition (DSPD) [238]. To tune the shape and morphology of the formed nanostructure, the following experimental parameters can be adjusted: concentration of the metal salt precursor, working electrode, supporting electrolyte and solvent, the organic or inorganic ligands [239–243].

Besides electrochemical approach, the nanoparticles can be deposited on functionalized surface. For instance, the gold and silver nanoparticles self-assemble on silanized glass surface. The interaction between the pending $-NH_2$ groups and the nanoparticles helps preventing the nanoparticle coalescence, which would happen if the nanoparticles were simply drop-cast on the glass surface [244]. Nanoparticles can be deposited on a substrate surface through electrostatic force as well. For instance, the gold nanoparticles synthesized by the Turkevich method are stabilized with negatively-charged citrate, which can be electrostatically

adsorbed on positively-charged ceramic surface. The positively-charged ceramic surface can be achieved by adjusting the pH value of the reaction solution.

Ordered arrays of nanoparticles

The deposition of metal nanoparticles with controlled geometry can be realized through the template assisted electrochemical deposition (TAED), using inorganic ordered templates or polymeric template [245–247]. Ordered alumina membranes can be easily processed by anodization of an aluminum foil. Figure 3.3.3.1 illustrates the procedure to fabricate arrays of silver nanoparticles ordered by gaps on an anodic aluminum oxide (AAO) substrate [248]. The AAO nanochannel is accomplished by anodizing a finely polished aluminum foil (Figure 3.3.3.1 (a and b)). Etching in 5 % phosphoric acid results in widening of the pore sizes (Figure 3.3.3.1 (c)). The gap between the nanochannels can be tuned by carefully adjusting the etching process. Subsequently, silver nanoparticles are deposited into the nanochannels by electrodeposition and separated by the walls, as shown in Figure 3.3.3.1 (d). After the silver nanoparticle deposition, the walls between the nanoparticles are etched away, so that the silver nanoparticles can be exposed as much as possible. Figure 3.3.3.1 (f) shows the final geometry of the ordered array of silver nanoparticles on an AAO substrate, with S representing the interparticle spacing, D the particle diameter, W the interparticle gap.

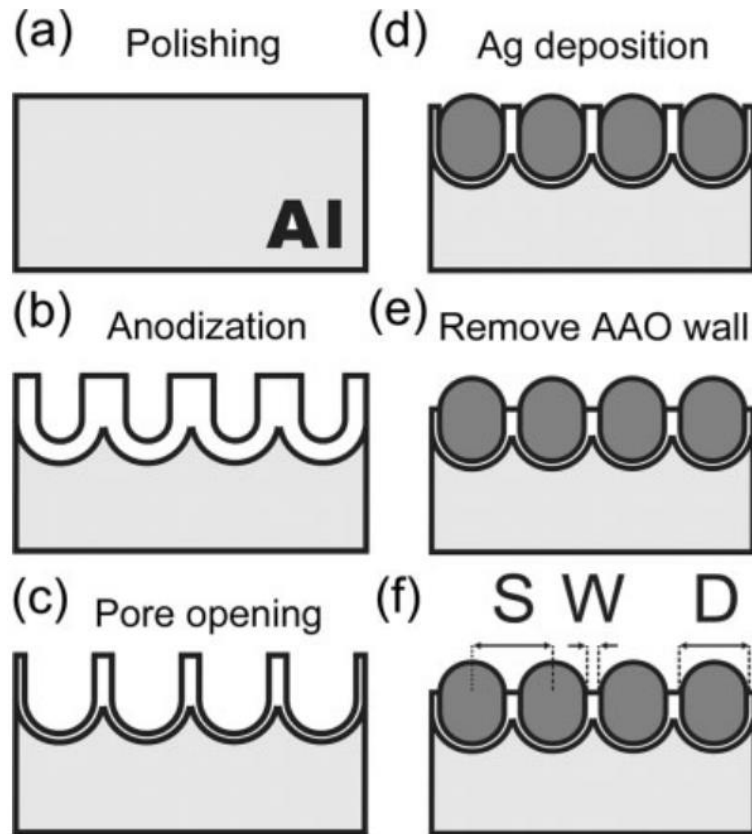


Figure 3.3.3.1 Schematic representation of the process for fabricating silver nanoparticle deposited anodic alumina substrates. Adapted with permission from [248]. Copyright (2006), Wiley.

Another approach to achieve ordered array of nanoparticles is lithography, such as electron beam lithography, interference lithography, or soft lithography.

Figure 3.3.3.2 shows the two different procedures of electron beam lithography: etching and lift-off [249]. Reactive ion etching (RIE) refers to the writing of a resist pattern (usually polymer) onto the substrate. During this method, the substrate is etched, the polymer is not. Subsequently, the polymer is removed, the metal evaporates. So that the whole surface is covered with metal. By lift-off method, the metal is deposited after the development stage, followed by the removal of the polymer.

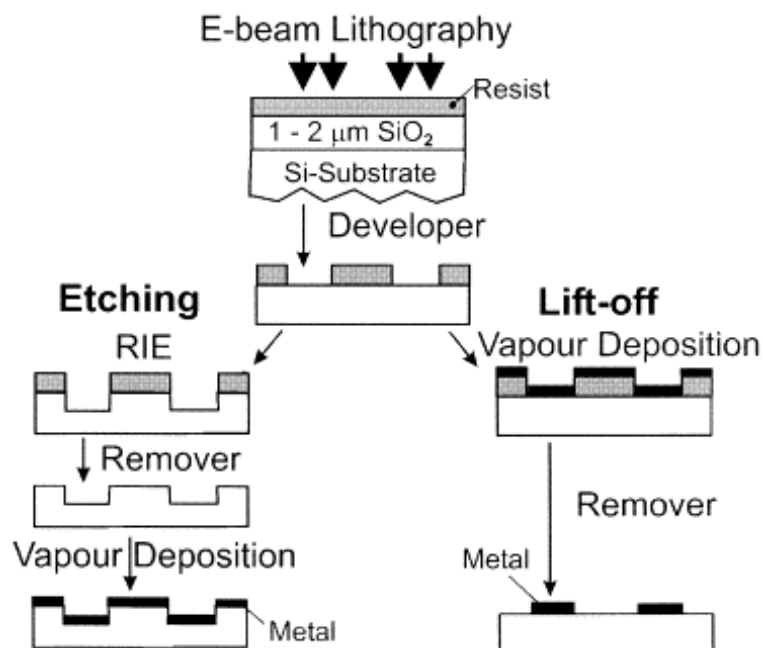


Figure 3.3.3.2 Schematic representation of etching and lift-off by electron beam lithography on an oxidized silicon substrate. Adapted with permission from [249]. Copyright (1998), Elsevier.

Interference lithography can be utilized to fabricate large area periodic patterns with a period of $\lambda/2$. This approach involves dividing a coherent laser beam into two parts. The interference between the two waves generates a pattern of light intensity minima and maxima, resulting in a periodic variation of solubility [250,251].

Soft lithography involves the use of a patterned elastomer as a mold. This method is much cost-efficient and easy applicable, compared to electron beam lithography [252–254]. Meanwhile, soft lithography facilitates the fabrication of large area substrates up to 1 cm² to serve as SERS substrates.

The above-described methods are all suited to prepare substrates for direct SERS detection. While the direct SERS detection is straightforward, it may be difficult under certain circumstances. For example, some biomolecules have small cross-section and are often buried in complex media, which can lead to intensive Raman noises and interferences of the Raman signals. Indirect SERS detection via SERS-tags could be the solution. Figure 3.3.3.3 depicts the general design and engineering of a biofunctionalized SERS-tag [255]. A typical SERS-tag consists of a metal nanoparticle core, adsorbed Raman reporter molecules (green stars in Figure 3.3.3.3) on the nanoparticle surface, targeting ligands (Biotin, NH₂, N₃ and COOH in Figure 3.3.3.3) and a shell encapsulating the metal nanoparticle and the adsorbed reporter molecules. The shell surface should be functionalized, in order to bond with probe molecule.

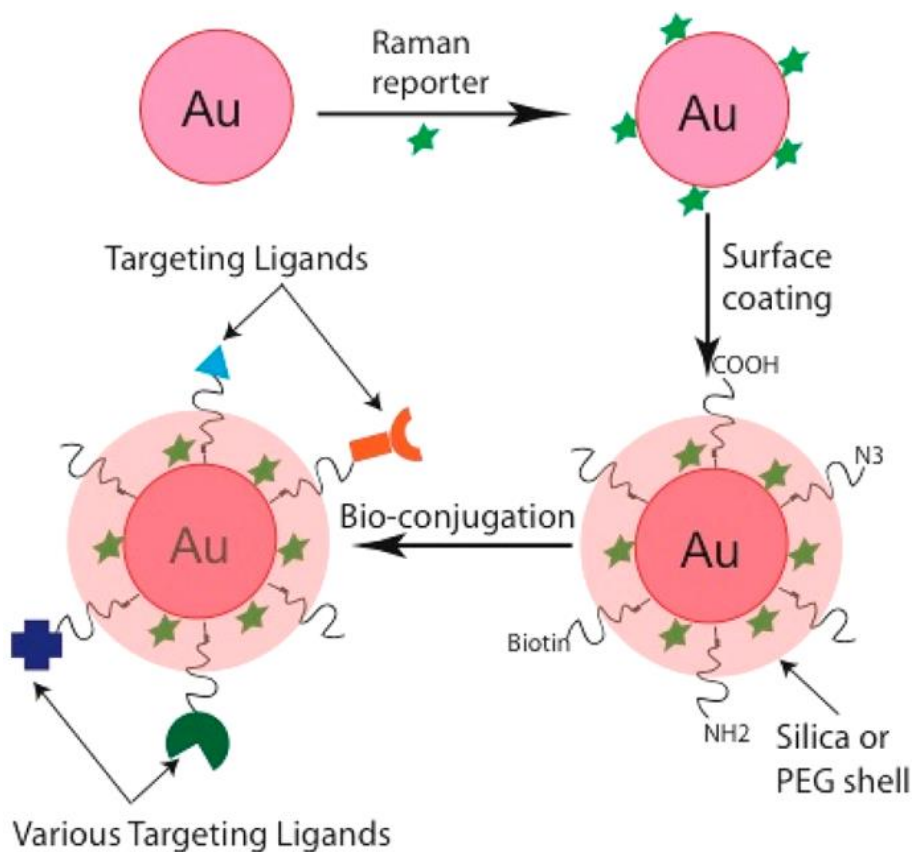


Figure 3.3.3.3 Schematic representation of a SERS-tag engineering. Adapted with permission from [255]. Copyright (2015), American Chemical Society.

The choice of the metallic nanoparticle core of a SERS-tag depends on the intended application. For example, gold nanoparticles should be chosen over silver nanoparticles for biomedical applications, since gold is nontoxic, while silver can be toxic to mammalian cells. Ideal Raman reporter molecule should have large Raman cross-section, such as malachite green, Rhodamine 6G, pyridine, crystal violet. Utilizing a dye molecule with an overlapping absorption spectrum with the excitation laser can trigger surface-enhanced resonance Raman scattering (SERRS), through which the Raman intensity can be further enhanced 10-100 fold [256].

Ligands refer to the functional groups that bind to a central metal atom to form a coordination complex. Different from the colloidal-stabilized metal nanoparticles, ligand-stabilized metal nanoparticles can aggregate or precipitate in biological fluids, due to the high ionic strength and presence of absorbing biomolecules. The selective adsorption of the probe molecules on the shell surface is facilitated through the corresponding ligand. The shell prevents the metal nanoparticles from aggregating. Most commonly used shell materials for SERS-tags are polyethylene glycol (PEG) and silica

3.3.4 Interpretation of SERS shifts using density functional theory

Density functional theory (DFT) is a computational method to investigate the electronic structure of multiple-body system, that has applications in various research fields, such as condensed matter physics, material science and chemistry. This theory is based on the concept of electron density instead of the wave function, which makes it computationally more efficient than other methods such as Hartree-Fock theory [257,258].

The SERS method has been established for a few decades. However, the assignment of the Raman signals to vibrational modes has always been unsatisfactory. The interpretation of DFT to vibrational modes assignment offers a new perspective. The SERS intensities of pyridine (Py) on transition metals (M) were investigated using the so-called 6-311+G**/LanL2DZ density functional method combined with B3LYP nonlocal exchange-correlation functionals [259], where the DFT B3LYP method is suitable for Py-M systems (Py-M, Py-M₂ and Py-M₅, with M=Fe, Co, Ni, Cu, Zn, Pd, Ag, Pt and Au), 6-311+G** basis set for C, N and H atoms and LanL2DZ basis functions for description of metal valence electrons [260,261]. The feasibility of the applied functionals was verified for free Py and adsorbed Py on noble metals [262–264]. Figure 3.3.4.1 shows the modeled Py-M complexes with labeled atoms.

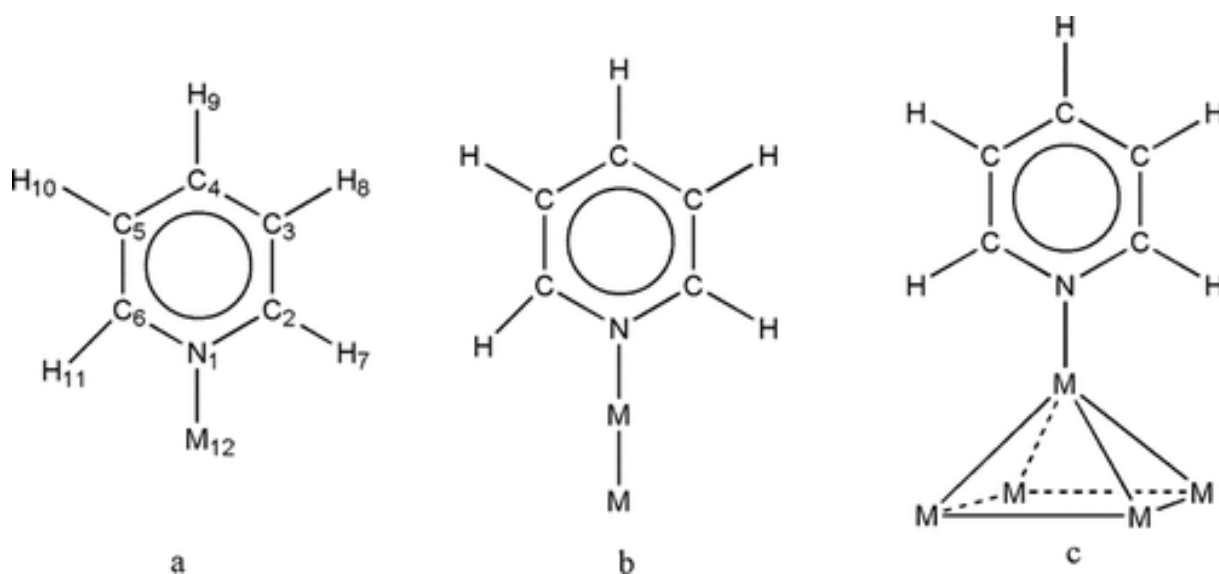


Figure 3.3.4.1 Modeling complexes with labeled atoms: (a) Py-M; (b) Py-M₂; (c) Py-M₅. Adapted with permission from [259]. Copyright (2006), Wiley.

The Raman intensities of these Py-M complexes can be determined after optimization of the geometries and electronic structures. The calculated C-C bond length had an error range within 0.004 Å of the experimental data. For C-H bond, the error between experimental and theoretical bond length is less than 0.002 Å. For all Py-M complexes, C-N bond are longer,

while two parallel C-C bond are shorter, due to the binding interaction. Comparing to free Py, with a C-C bond of 1.398 Å, Py-Fe₅, Py-Co₅, Py-Ni₅ have C-C bonds of 1.389 Å, Py-Pd₅ has a C-C bond of 1.391 Å, and Py-Pt₅ has C-C bond of 1.386 Å, due to the binding interaction changing the population of 2b₁ π-type orbital of the Py ring (Figure 3.3.4.2) [259].

The vibrational coupling between the internal modes of Py and the N-M stretching, results in a blue shift of the vibrational frequencies. This shift is dependent on the nature of the vibrational mode and the strength of the Py-M adsorption bond. For instance, in the case of free pyridine, the ring breathing mode ν_1 and symmetric ring deformation ν_{12} are located at 991 and 1027 cm⁻¹, respectively [265]. The vibrational frequencies show a blue shift after pyridine binds to metals.

Figure 3.3.4.2 illustrates the bonding orbitals of Py-M₅ (M=Ag, Au, Fe and Pt). Different from Ag and Au, the d orbital plays an important role when pyridine adsorbs on transition metals. Py-Ag₅ bonding is weakly formed, due to the interaction between the weak 5s-4d² hybridized orbital and the lone-pair orbital. Since there is a relatively big gap between 5s and 4d² orbital, the hybridization is weakly formed. The Py-Au₅ bond should be stronger, due to the smaller gap between the 6s and 5d orbitals. In the case of Py-Fe₅, a bonding interaction can take place in the unoccupied 3d₁ π-type orbital. While, the Py-Pt₅ bond is extremely strong, because of the low energy level and symmetry matching between the lone-pair and the Py ring. The accordingly changed electron cloud affects the C-N and C-C bond length significantly.

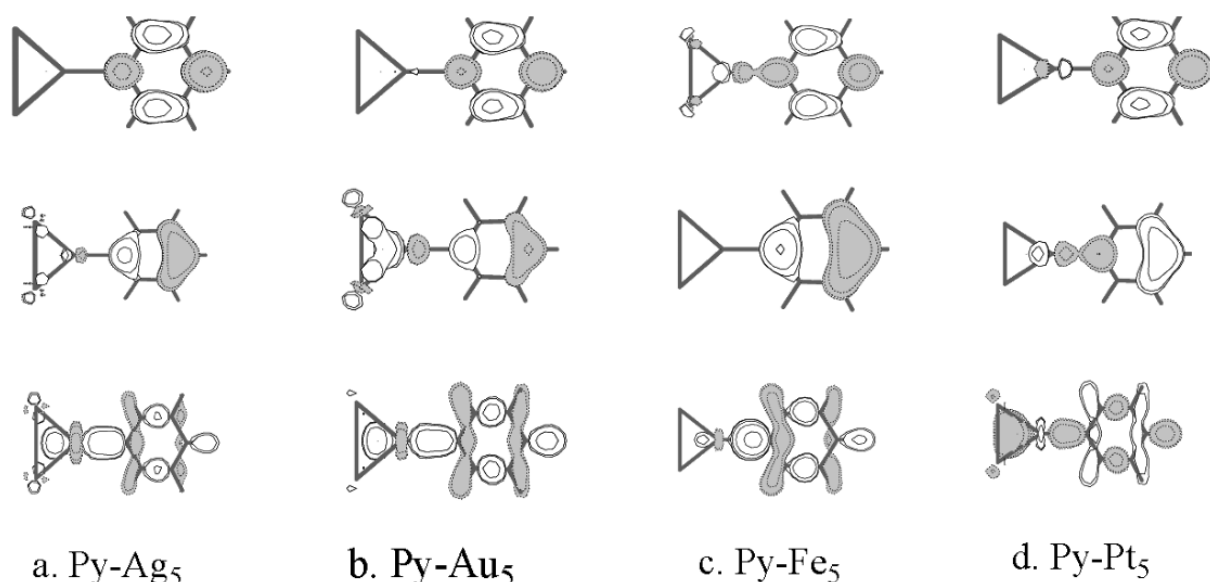


Figure 3.3.4.2 Schematic presentation of bonding orbitals π -type 3b₁ orbital (upper), π -type 3b₂ orbital (middle) and lone-pair orbital (bottom) in (a) Py-Ag₅; (b) Py-Au₅, (c) Py-Fe₅ and (d) Py-Pt₅. Adapted with permission from [259]. Copyright (2006), Wiley.

3.4 UV-vis spectroscopy

UV-vis spectroscopy is an analytical technique, which measures the UV-Vis light absorbed by or transmitted through a sample. Ultraviolet and visible light hit the surface of a matter and interact with the surface in different ways. Energy of light is proportional to its wavelength.

When light of a certain wavelength interacts with a matter, the matter absorbs part of the incident radiation of the light, electrons get excited from the initial state (ground state) to a higher energy level (excited state), which is detected as absorption. Electrons in different substances require different amounts of energy to get excited to higher energy level. Therefore, absorption of light radiation occurs in different substances at different wavelengths [266].

Beer-Lambert Law describes the intensity of an absorption in diluted homogenous medium [266,267]:

$$A = \varepsilon_{ab} bC = \log_{10} \left(\frac{I_0}{I_{trans}} \right) = \log_{10} \left(\frac{1}{T} \right) \quad (\text{Equation 3.4.1})$$

where ε_{ab} refers to the molar absorption coefficient, b the thickness of the sample, C concentration of the sample, I_0 the intensity of the incident light, I_{trans} the transmitted intensity and T transmittance. The Beer-Lambert law is commonly applied to obtain the concentration of a substance.

A UV-Vis spectrophotometer consists light source, wavelength selector, detector and computer for signal processing. A single xenon lamp is commonly used to emit high intensity light of a broad range of wavelengths. The wavelength selector selects light of certain wavelengths for analyse of the sample. Monochromator is one of the most commonly used wavelength selectors because of its versatility. Light of a certain wavelength passes through the sample and is collected by the detector. The detector converts the light signal into a computer-readable electronic signal.

3.5 Integrating sphere

Integrating sphere is a standard optical component used in optical and photometric measurements to determine the total amount of light emitted by a source or reflected from a surface. An integrating sphere contains a hollow spherical cavity with interior surface coated with a diffuse white reflective substrate. An integrating sphere consists of a light source, sample holder, integrating sphere, a baffle and a detector, and is usually combined with a UV-vis-IR spectrometer (Figure 3.5.1).

To examine the reflectance of a sample using an integrating sphere, the sample is placed at the sample port opposite the entrance port (as shown in Figure 3.5.1). The incident light ray

enters the integrating sphere through the entrance port, gets reflected multiple times by the highly reflective interior of the sphere and dispersed uniformly inside the sphere. Some of the light is absorbed by the sample and some is reflected back to the detector [268,269]. The measurement results of reflectance and transmittance using the integrating sphere are often presented spectrally, as a function of wavelength.

To measure the transmittance, the sample should be placed at the entrance port, while a reflectance standard should be placed at the sample port. After the reflectance and transmittance of the sample is obtained, the absorbance can be calculated using Equation 2.1.2.1.

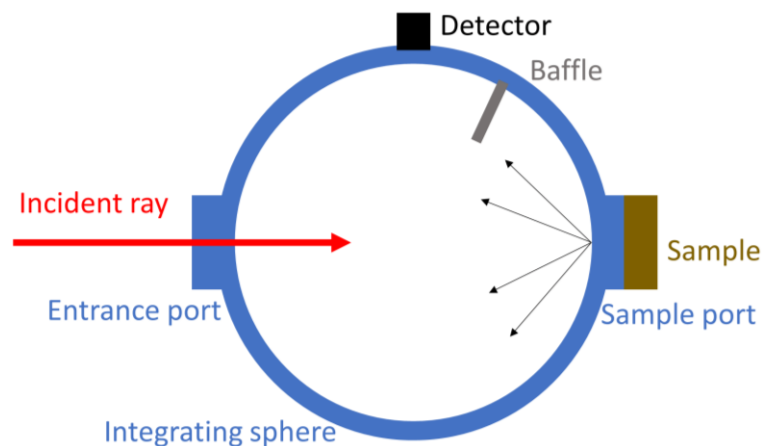


Figure 3.5.1 Schematic representation of an integrating sphere measuring the reflectance of a sample.

3.6 Electron microscopy

Electron microscopy refers to a technology to obtain high resolution images of specimens using a beam of accelerated electrons as light source. Nowadays, there have been invented different types of electron microscopes: transmission electron microscope (TEM), scanning electron microscope (SEM), reflection electron microscope (REM) and scanning tunneling microscope (STM).

Compared to most commonly used light microscopy, electron microscopy shows advantages at high image resolution. Most light microscopes have limits to $0.1 \mu\text{m}$ [270]. For light microscopes, the resolution limit is related to the visible light wavelength λ . Incident light by electron microscopy has shorter wavelength, and hence, can interact more strongly with the sample, which results in images with higher resolution [271–274].

Transmission electron microscopy has been an important method since it was first invented in 1931. A typical TEM instrument contains the following key components: electron source for generation of high-energy electron beam, electron lenses to focus the electron beam onto the

sample (including condenser lenses, objective lenses and projector lenses), sample holder, vacuum system, detector and computer. The TEM working principle can be described as follows: an electron beam is generated from an electron gun, functioning as light source. The emitted electrons interact with the sample, resulting in scattered, absorbed or transmitted electrons. By analyzing the transmitted electrons, a high-resolution image of the sample can be acquired [271,272].

Similar to TEM, a SEM instrument normally consists of an electron gun for high energy electron generation, a column as the electron travel path between electromagnetic lenses, a deflection system, a sample chamber and a computer system with a screen to present the scanned images. SEM involves the scanning of an electron beam on the sample surface and detecting the backscattered and secondary electrons. Backscattered electrons (BSE) refer to the electrons after elastic interactions between the incident ray and the sample, which originate from deeper regions of the sample. Secondary electrons originate from the sample surface. Therefore, SEM based on secondary electrons provides more detailed information on the sample topography. BSE SEM images offer high sensitivity according to atomic number. The higher the atomic number, the brighter the material shows in the images.

Furthermore, SEM can be used to obtain information about the elemental composition of the sample through energy-dispersive X-ray spectroscopy [273,275,276].

3.7 X-ray micro computed tomography

X-ray micro computed tomography (μ -CT) is a non-destructive 3D imaging technique using X-rays to visualize the interior of an object, slice by slice. μ -CT enables the preservation of the specimen for correlative analysis and offers a digital data format, which facilitates quantitative 3D architectural analysis. The basic design of μ -CT scanners comprises four components: an X-ray source, the specimen under examination, an imaging array that converts X-rays into electronic signals, and either a rotating specimen stage or a rotating scanner unit [277]. Figure 3.7.1 illustrates an overview of the operating principle of μ -CT using a commercial dice as specimen, along with the corresponding characteristic length scales of the current CT methods [278].

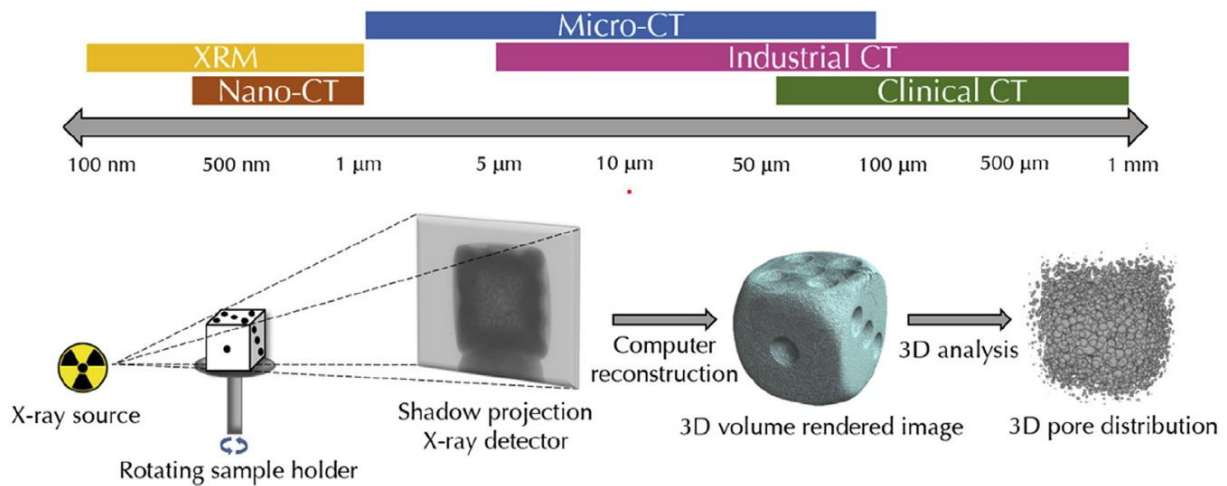


Figure 3.7.1. Schematic representation of μ -CT analysis of a commercial dice. Adapted with permission from [278]. Copyright (2020), Elsevier.

There are three approaches to achieve a higher μ -CT resolution, namely cone beam method, optical magnification method and Bragg diffraction method. By the cone beam method, a magnified X-ray image is projected onto a large-area X-ray imaging system. By optical magnification method, a non-magnified X-ray image is magnified by subsequent optical either by a lens or by a tapered fiber-optic coupling. While, by the Bragg diffraction method, a Bragg interferometer is used, which can magnify the images by virtue of photon wavelength-specific diffraction of photons [277].

CT imaging was conventionally utilized for medical purposes. As this technique became more widespread and refined, new applications emerged, such as food chemistry, dentistry, geoscience, life science, petroleum geology and scaffolds. μ -CT primarily provides information on the different in X-ray attenuation, which results in an absorption map (2D or 3D) that can be further enhanced through postprocessing. The 3D inner structure of the specimen, including the presence of pores, cracks can be investigated. This way, this technique can be seen as a qualitative diagnostic tool, through which the parameters, such as porosity, pore size distribution, pore connectivity can be determined [279].

4. Concept of plasmonic porous ceramics

Chapter 4 has been adapted with permission from *Elsevier* and is published in the *Journal Open Ceramics*, 2022, DOI: 10.1016/j.oceram.2022.100228

Besides the advantages of high mechanical strength, electrical resistance and minimal susceptibility to acids or caustics, a special feature of most ceramics is that they strongly scatter light, the reason being the high refractive index of oxidic ceramics ($n_{a,alumina} \sim 1.67$, $n_{a,zirconia} \sim 2.2$) and the presence of grain boundaries at which the light is scattered [56,280]. Moreover, the effective refractive index n_{eff} of a porous ceramic can be manipulated by varying the structure and porosity of the ceramic material [28,30,31]. This leads to shifted scattering coefficients, phenomena like forward scattering through the ceramic matrix [57], strong diffuse and subsurface scattering from rough ceramic surfaces [58,59] and disordered and enhanced scattering of porous ceramics [60]. Such features can potentially superimpose the optical properties of plasmonic materials which could lead to unexpected results, especially in the form of a 3D macro-porous ceramic substrate with an open-cell foam structure.

Therefore, the concept of plasmonic porous ceramics is introduced in this chapter. We define plasmonic porous ceramics as materials based on a 3D porous ceramic matrix functionalized with plasmonic Ag nanoparticles. Herein, porous ceramic substrates based on zirconia-toughened alumina with different pore diameters were processed by replicating polyurethane foams [281] and characterized using SEM and μ CT. Considering the distance dependency of the Raman enhancement effect, the plasmonic particles were introduced on the strut surface of the porous ceramic structure after the sintering process. Silver nanoparticles with diameters of 30 nm were deposited on the porous ceramic surface through chemical reduction of a silver nitrate solution. The synthesized silver nanoparticles were characterized with SEM and UV/vis spectroscopy. The plasmonic properties of the materials were evaluated by performing SERS with pyridine as Raman-active probe molecule. Next to analyzing porous ceramics with different pore diameters, the effect of strut diameter and curvature as well as of the surrounding porous matrix were analyzed independently, as well.

4.1 Materials

ZTA powder consists of 80 % alumina powder (Taimicron TM-DAR, KRAHN Chemie Deutschland GmbH, Germany) and 20 % yttria stabilized zirconia powder (TZ-3Y-E, Tosoh, Japan). Dispersant Dolapix CE64 was obtained from Zschimmer and Schwarz GmbH, Germany. Polyurethane foam was purchased from Modulor GmbH, Germany. Poly(vinyl alcohol) (PVA, Mw 31,000-50,000, 98-99% hydrolyzed, product no. 363138), trisodium citrate

dihydrate (TSC, ACS reagent, $\geq 99.0\%$, product no. S4641), silver nitrate (99.9999% trace metals basis, product no. 204390), stearic acid (product no. 175366) and pyridine (analytical standard, product no. 02486) were acquired from Sigma Aldrich, Germany. Beeswax (white, product no. 5825) was obtained from Carl Roth, Germany.

Deionized water (DI water, resistivity $> 18 \text{ M}\Omega \text{ cm}$, SynergyUltra Water System Millipore Corp., USA), decane (product no. D901, Honeywell, Germany) and *n*-hexane (product no. 24577, VWR Chemicals, Germany) were used for preparation of the slurries and solutions.

4.2 Methods

4.2.1 Fabrication of porous ZTA ceramics

The ZTA porous ceramics were prepared by the replica method with the recoating technique [281]. 20, 30 and 60 pore per inch (ppi) polyurethane foams were used as template. For the preparation of 100 g ZTA ceramic slurry, 80 g ZTA ceramic powder was dispersed in 18 g DI water with 0.8 g dispersant Dolapix CE64 and mixed with an overhead stirrer (IKA RW20 digital, IKA-Werke GmbH & Co. KG, Germany) at 1500 rpm for 15 min. Subsequently, 1.2 g PVA was added to the mixture and it was stirred for another 30 min. The mixture was degassed after stirring. PU foams were cut into small blocks (15 x 15 x 5 mm) and fully impregnated with the prepared ceramic slurry. Excess slurry in the PU foams was squeezed out manually. Blocked pores were carefully blown with compressed air. The thinly coated PU foams were dried for 24 h.

After the drying, the green bodies were coated with a less-concentrated ZTA slurry with 60wt % solid load. 100 g of the ZTA slurry for the recoating consists 60 g of ZTA powder, 0.6 g dispersant and 38.5 g DI water. After 15 min of vigorous mixing, 0.9 g PVA was added to the slurry. The slurry was mixed for another 30 min and degassed as during the first coating process. Subsequently, the green bodies were immersed in the recoating slurry and soaked for a few seconds. The blocked pores were cleared carefully with compressed air. The PU foams were dried for 24 h after the recoating. The green bodies were placed in a furnace (HT 04/17, Nabertherm GmbH, Germany) to burn out the PU templates with a heating rate of $1 \text{ }^\circ\text{C}/\text{min}$ with dwelling times of 2 h at $110 \text{ }^\circ\text{C}$, 3 h at $250 \text{ }^\circ\text{C}$ and 3 h at $600 \text{ }^\circ\text{C}$. The remaining porous structures were sintered at $1650 \text{ }^\circ\text{C}$ for 3 h with a heating rate of $3 \text{ }^\circ\text{C}/\text{min}$ and cooled to room temperature with a cooling rate of $3 \text{ }^\circ\text{C}/\text{min}$.

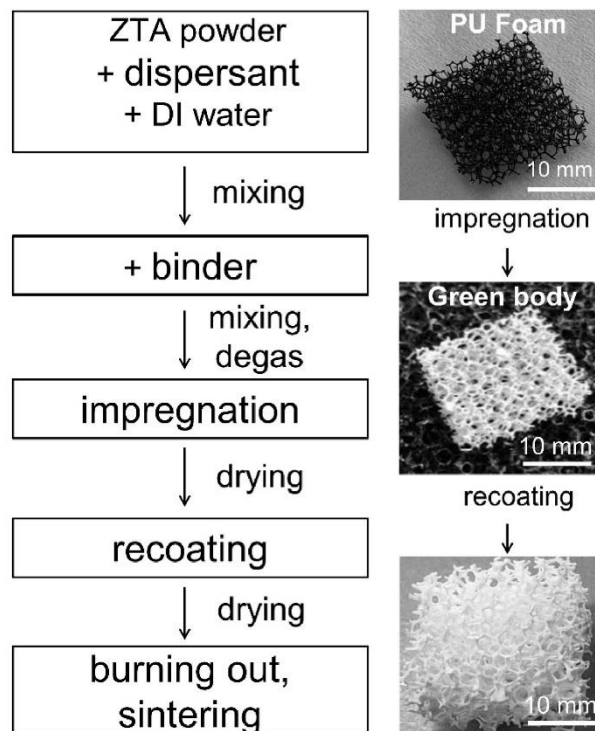


Figure 4.2.1.1 Flowchart of the processing procedures for preparing ZTA porous ceramics. Adapted with permission from [1]. Copyright (2022), Elsevier.

4.2.2 Fabrication of dense ZTA ceramic pellets

The dense ZTA pellets were fabricated with the uniaxial pressing method [282]. One pellet (\varnothing 2.0 cm) was pressed with 1.7 g ZTA ceramic powder at 10kN with a press (PW 40, Nr. W13972-495, Hawe GmbH, Germany). The ZTA pellets were sintered at 1650°C for 3 h with a heating and cooling rate of 3 °C/min.

4.2.3 Fabrication of ZTA ceramic thin rods

The ZTA ceramic thin rods were prepared by the extrusion method following the procedure described by Kroll *et al* [282]. In short, 0.29 g stearic acid was dissolved in 4.4 g decane at 80 °C and stirred with a magnetic stirrer. 4.4 g bees wax was added and stirred to dissolve. Subsequently, 3.08 g hexane and 25 g ceramic powder were added to the mixture. The ceramic slurry was ultra-sonicated for 10 min and stirred with an overhead stirrer (IKA RW20 digital, IKA-Werke GmbH & Co. KG, Germany) at high speed until it reached a sufficiently low viscosity. The ceramic slurry was filled into a temperature controlled double wall vessel of a custom-designed extruder (Advanced Ceramics, University of Bremen, Germany), closed with an adequate press ram and tempered to 35°C. The extruder was equipped with extrusion dies of sizes from 0.10 mm to 3.6 mm to obtain the desired green thin rods. The ceramic paste was pressed at around 2 kN through the extrusion dies of various diameters and cut into 2 cm long

thin rods. The green bodies were sintered at 1650 °C for 3 hours with a heating and cooling rate of 3 °C/min.

4.2.4 Deposition of Ag nanoparticles onto the ceramic surface

Figure 4.2.4.1 shows the deposition procedure of the plasmonic silver particles onto the ceramic surface. The reaction solution was obtained by dissolving 1.471 mg/3.676 mg/ 7.353 mg/14.705 mg/29.14 mg/147.05 mg trisodium citrate dihydrate in 45 mL DI water (resulting in molar ratios of Ag ion to TSC of 1:0.1/1:0.25/1:0.5/1:1/1:2/1:10). In a 100 ml 3-neck round flask, a porous ceramic sample was hung by a thin thread and immersed in 45 ml TSC reaction solution. The TSC solution was stirred with a magnetic stirrer and heated to 50 °C. The ceramic sample was impregnated in the TSC solution and incubated at 50 °C for 50 minutes at neutral pH (Figure 4.2.4.1 (a)), so that the negatively-charged citrate could adsorb onto the positively-charged ZTA ceramic surface through electrostatic force. Subsequently, the temperature was raised to 100 °C. 5 ml of 10 mM silver nitrate solution was added to the reaction solution drop by drop (Figure 4.2.4.1 (b)). After a few minutes, the colorless reaction solution turned yellow. The ceramic sample was taken out of the reaction solution, rinsed with DI water, dried and stored in an evacuated desiccator.

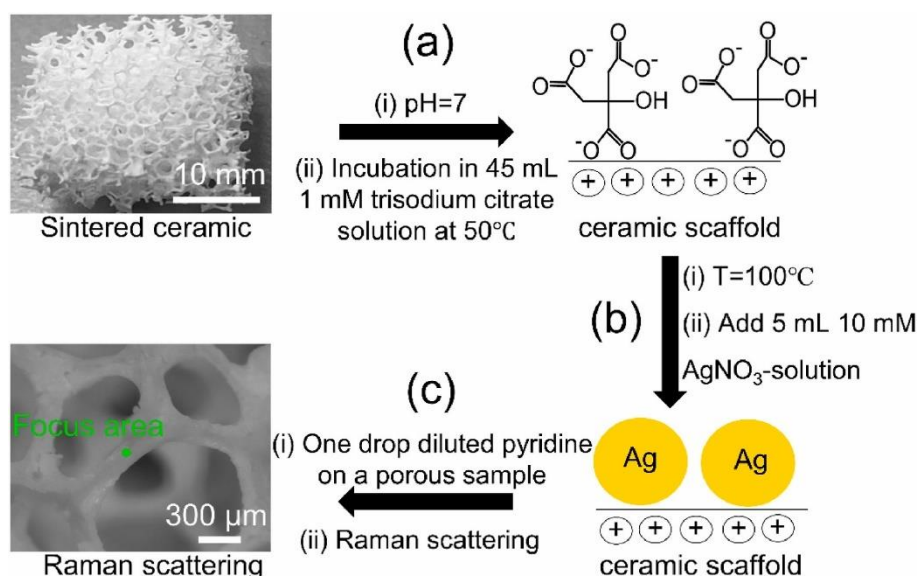


Figure 4.2.4.1 Schematic representation of deposition of the Ag particles onto the ceramic surface, followed by SERS measurements using the synthesized sample as substrate. Adapted with permission from [1]. Copyright (2022), Elsevier.

The deposition of Ag NPs on samples with different porosity, dense samples as well as thin rod samples were processed in the same way.

4.2.5 Determination of pore size and strut thickness

The porous ceramics were examined using X-ray micro-computed tomography (μ -CT). Samples were cut into sizes of 5 x 10 x 3 mm, glued on a clean sample holder and analyzed with a Xradia 520 Versa device (ZEISS, Germany). The 3D volumetric images were generated by the attenuation of X-rays passing through the specimen. Scanning voltage and X-ray radiation strength parameters are specified in Table 4.2.5.1.

Thereafter, a reconstruction algorithm based on the work of Katsevich *et al* [283] was applied to process the data. In the reconstructed image volume, 16-bit grayscale value was used for every voxel to denote a corresponding x-ray attenuation coefficient. Attenuation is directly related to the density and hence x-ray absorbance of the sample. Image processing software 3D slicer [284] and Fiji [285] were used for the calculation of pore morphological properties including pore size.

Table 4.2.5.1. X-ray μ -CT scanning parameters and specifications. Adapted with permission from [1]. Copyright (2022), Elsevier.

Scanning parameters	Specification
Radiographic field of vision [mm]	28×35
Number of display voxels	1050 X 1011
Detector pixel size [μ m]	140
Acquisition time [min]	45
Exposure time [s]	0.7
Energy of X-ray	70 kV (6000 mA)
Number of projections per revolution	2400
Total number of projections	1024
The angular step [$^{\circ}$]	0.15
Recorded data type	16-bit integer

For digital reconstruction of the μ -CT images, a binary image was generated using the Otsu multilevel filter to differentiate voids and matrix in the region of interest. The resulting binary pore images underwent a morphological filter to eliminate salt and pepper noise. The resolution was limited at 8 μ m, therefore, only pores with a size larger than 8 μ m were considered. The interconnected pores were separated by a distance transform filter, followed by the application of the 3D watershed algorithm. Since the ceramics in this work were dense sintered, the microporosity of the ceramic struts was not taken into consideration. The macro-porosity of the ceramic structure can be calculated as:

$$P = \frac{V_{pore}}{V_{total}} \quad (\text{Equation 4.2.5.1})$$

$$V_{total} = V_{solid} + V_{pore} \quad (\text{Equation 4.2.5.2})$$

where V_{solid} is the volume of the solid part and V_{pore} the volume of the pores.

The images of the porous structure struts were obtained by light microscope (Keyence digital microscope VHX-600, Keyence Deutschland GmbH, Germany) with magnification of 300-500. The acquired images were analyzed with ImageJ. For each sample, ten data points were collected for calculation of the average strut thickness.

4.2.6 Scanning electron microscopy (SEM) and nanoparticle coverage determination

The silver-NP-functionalized ceramic samples were cut into small fragments (porous sample: ≤ 2 mm, dense sample: ≤ 5 mm) and glued on a clean sample holder. The samples were analyzed with scanning electron microscopy (SEM, Supra 40, Carl Zeiss, Germany), at high voltage 1.00 kV with a working distance between 1.9-3.1 mm, magnification of 2k-5k. The samples for BSE measurements were vapor-coated with a carbon coater (Cressington 108 auto, Cressington Scientific Instruments Ltd, UK). For each experimental condition, three samples were analyzed and five SEM images were taken at different spots on each sample. Based on these images, the size and coverage area of the silver particles were determined with the software ImageJ.

4.2.7 Raman scattering of the plasmonic ceramics

SERS measurements were carried out using diluted pyridine as probe molecule. One droplet of 0.01 M pyridine in DI water was dropped on the plasmonic ceramic sample and collection of Raman spectra was immediately started. For each sample, ten measurements were conducted at different spots of the sample from various directions. Raman spectra were acquired using a 532 nm laser (Laser Quantum Ventus 532 with max power 50 mW) using a fully automated Raman confocal microscope (ARAMIS, Horiba Europe GmbH, Germany) followed by data processing with software Labspec 5.58.25. During the Raman measurement, a x10 objective (numerical aperture of 0.25) was used, providing a focal area diameter of 2.6 μm (Figure 4.2.4.1 (c)). The acquisition time was set to 10 s and 10 of such spectra were accumulated in one measurement.

The Raman spectrum of a pure pyridine sample was taken for the calculation of the Raman enhancement factor G_{SERS} using the following expression [286–288]:

$$G_{SERS} = \frac{P_{SERS}/N_{SERS}}{P_{Normal}/N_{Normal}} = \frac{P_{SERS}/c_{SERS}vNA}{P_{Normal}/c_{Normal}vNA} = \frac{P_{SERS}c_{Normal}}{P_{Normal}c_{SERS}} \quad (\text{Equation 4.2.7.1})$$

where P_{SERS} is the SERS intensity and P_{Normal} is the Raman intensity. In this work P_{SERS} refers to the integrated SERS intensity of the diluted pyridine sample on plasmonic ceramic substrate, while, P_{Normal} presents the integrated Raman intensity of the pure pyridine sample.

4.3 Results and discussion

4.3.1 Preparation of porous ceramics

Porous ceramics with three different pore sizes (20, 30 and 60 ppi) were processed using the replica technique with the recoating method (Figure 4.2.4.1). The replica technique uses a porous template, which is impregnated with ceramic suspension. After drying, the ceramic green body is recoated with a thinner ceramic slurry with less solid load, which leads to an increase in compressive strength of the final ceramic. After a final drying period, the template is burned out, leaving the porous ceramic as the product [162,289,290]. The fabricated ZTA porous ceramics are white, mechanically robust blocks with a size of 15 x 15 x 5 mm.

To evaluate the porous structure, the porous ceramics were examined using μ -CT with a voxel resolution of 8 μ m and the obtained data was digitally reconstructed for further analysis. Fig. 4.3.1 shows the 3D visualization of the porous ceramics. The average pore sizes of the 20, 30 and 60 ppi porous ceramics were 0.55 mm, 0.51 mm and 0.24 mm, respectively, as obtained by μ -CT reconstruction. The average strut thicknesses of the 20, 30 and 60 ppi porous ceramics were acquired by light microscopy, with values of 0.174 mm, 0.132 mm and 0.046 mm, respectively (Table 4.3.4.1).

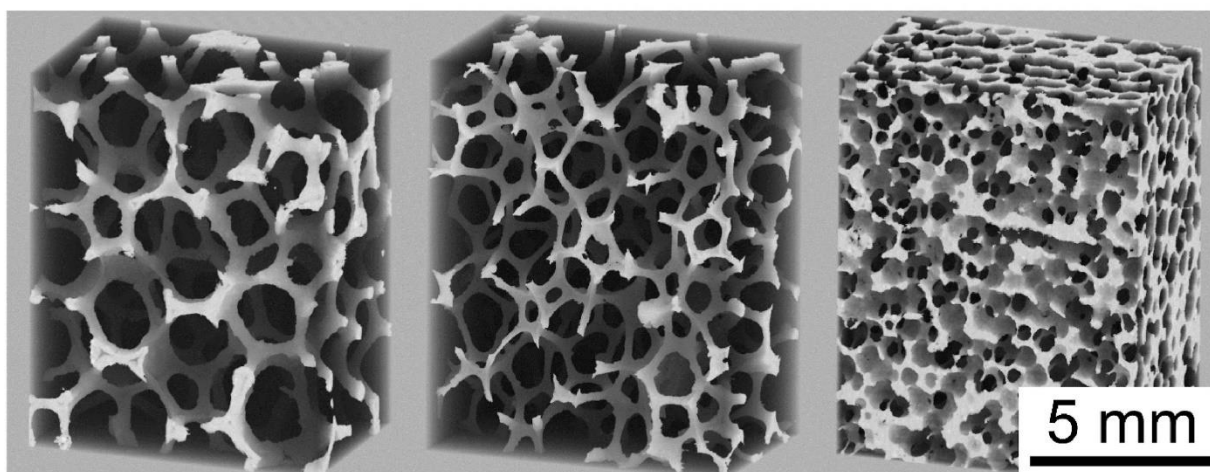


Figure 4.3.1 μ -CT 3D reconstruction (voxel resolution: 8 μ m) of the fabricated ZTA porous substrates, 20 ppi, 30 ppi and 60 ppi from left to right respectively. Adapted with permission from [1]. Copyright (2022), Elsevier.

4.3.2 Ag nanoparticle coverage on ceramic surface

The deposition of Ag NPs was realized by chemical reduction of silver ions to nucleate Ag NPs on the surface of the ceramic structures via heterogeneous nucleation [291–293]. In order to achieve a uniform silver particle size, trisodium citrate (TSC) was applied as reductant. To ensure the prevalence of heterogeneous nucleation on the material surface over homogenous nucleation in the solution and maintenance the balance between nucleation and grain growth, the concentrations the reactants were carefully chosen [294–299]. Accordingly, the density of the deposited Ag NPs (Ag NP coverage) on the ceramic surface changed in respect to the investigated molar ratio of Ag ions to TSC of 1:0.1, 1:0.25, 1:0.5, 1:1, 1:2 and 1:10. To enhance the material contrast in the images, Figure 4.3.2 (a and g) were obtained using the backscattered electron (BSE) detector of the SEM. Figure 4.3.2 (a) shows the non-functionalized ZTA ceramic surface, where the dark large grains are the alumina grains and the smaller bright grains can be assigned to the zirconia grains, which strengthen the ceramic structure. Figure 4.3.2 (g) shows the BSE image of the functionalized ZTA ceramic surface deposited with Ag NPs at molar ratio of Ag⁺ to TSC 1:2. The observed tiny bright nanoparticles are the deposited silver nanoparticles.

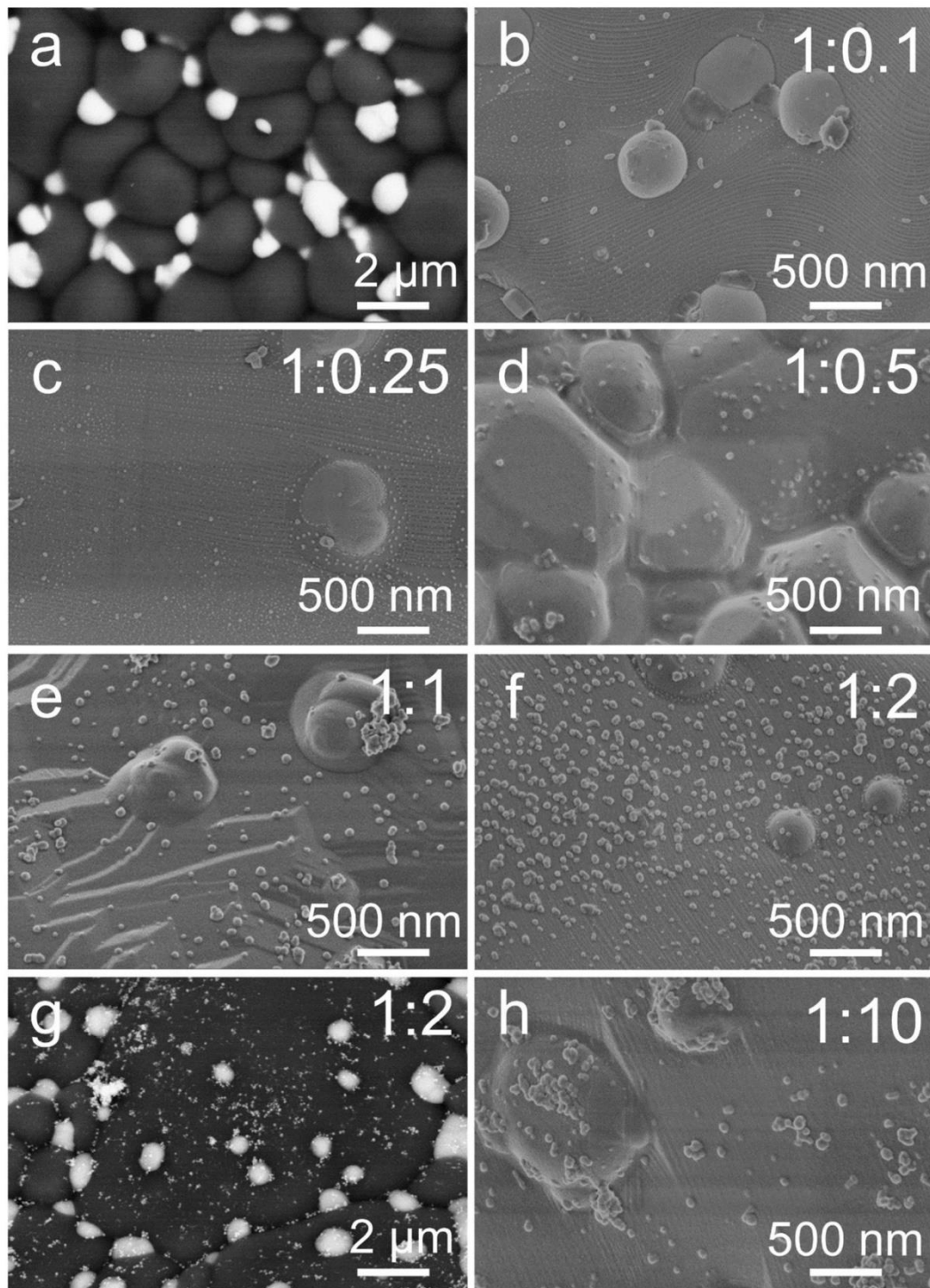


Figure 4.3.2 SEM-BSE images of 20 ppi porous ZTA ceramic surface before Ag nanoparticle deposition (a) and after Ag nanoparticle deposition at molar ratio 1:2 (g), SEM images of 20 ppi ZTA ceramic surface after Ag nanoparticle deposition at molar ratio 1:0.1 with a coverage of 1.7 % (b), at ratio 1:0.25 with a coverage of 2.7 % (c), at ratio 1:0.5 with a coverage of 3.2 % (d), at ratio 1:1 with a coverage of 4.9 % (e), at ratio 1:2 with a coverage of 12.2 % (f) and at ratio 1:10 with a coverage of 4.3 % (h). Adapted with permission from [1]. Copyright (2022), Elsevier.

Figure 4.3.2 (b, c, d, e, f and h) show representative SEM images (obtained with the regular secondary electron detector) of the Ag particle deposition on the 20 ppi ZTA porous ceramics

as a function of the amount of reductant. The particle coverage for each Ag/TSC ratio was determined from at least ten SEM images of each sample using the software ImageJ. The investigated Ag nanoparticle coverages are presented in Table 4.3.2.1.

Table 4.3.2.1 Ag nanoparticle coverage on ceramic surface under different molar ratios of Ag ion to TSC. Adapted with permission from [1]. Copyright (2022), *Elsevier*.

Molar ratio of Ag ion to TSC	1:0.1	1:0.25	1:0.5	1:1	1:2	1:10
Ag nanoparticle coverage on 20 ppi porous ceramic (%)	1.7 ± 0.7	2.7 ± 0.9	3.2 ± 0.9	4.9 ± 0.8	12.2 ± 5.7	4.3 ± 2.1
Ag nanoparticle coverage on dense ceramic pellet (%)	2.9 ± 1.0	3.2 ± 1.4	4.3 ± 3.0	4.4 ± 1.2	10.3 ± 2.2	6.3 ± 4.8

The Ag particle coverage increased from 1.7 ± 0.7 % to 12.2 ± 5.7 %, when the molar ratio of Ag ion to TSC increased from 1:0.1 to 1:2. However, the Ag NP coverage decreased again at the molar ratio of 1:10. Most likely the balance between heterogenous nucleation and homogenous nucleation in this case shifted towards favoring homogenous nucleation, resulting in the formation of a large number of particles in solution with low tendency to adsorb on the surface because of the colloidal stabilization effect of the TSC.

The Ag NP coverage on flat and dense ceramic substrates was comparable (4.4 ± 1.2 % at the molar ratio of 1:1) and indicated a similar trend as on the 20 ppi porous ceramic substrates, which is at first increasing until a ratio of 1:2, followed by decreasing density.

4.3.3 Characterization of plasmonic properties as a function of particle coverage

The Raman spectra of bare porous ZTA substrate before nanoparticle functionalized (a) and after nanoparticle functionalized (b) were shown in Figure 4.3.3.1. Porous ZTA substrate before and after nanoparticle functionalization shows a similar Raman spectrum, with two pronounced Raman shift at 1370 and 1400 cm^{-1} , which can be assigned to alpha-alumina. This indicated that the metal nanoparticle deposition alone does not have influence on the background spectrum.

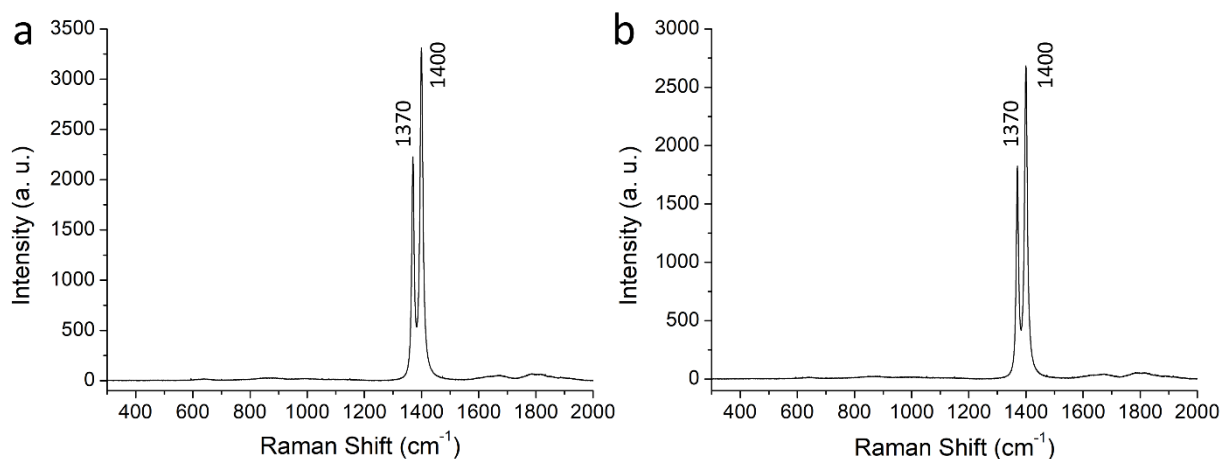


Figure 4.3.3.1 Raman spectra of bare porous ZTA substrate before nanoparticle functionalization (a) and after Ag nanoparticle functionalization (b). Adapted with permission from [1]. Copyright (2022), Elsevier.

Raman spectra of diluted pyridine adsorbed on the non-functionalized porous ceramics and on the Ag NP-functionalized plasmonic porous ceramics are shown in Figure 4.3.3.2 (a). Figure 4.3.3.2 (b and c) show Raman spectra of diluted pyridine measured using the 20 ppi porous ceramic with various molar ratios of Ag ions to TSC from 1:0.1 to 1:10. For comparison, the same measurements were performed with dense and flat ceramic pellets. SERS enhancement factors were calculated from the characteristic peak at 1008 cm⁻¹ and are summarized in Figure 4.3.3.2 (d). The calculation of the EFs followed Equation 4.2.7.1. The Raman intensity of pure pyridine was used as reference from which the EF was calculated based on the known concentration of the diluted pyridine solution that was used on the SERS substrates. Following the trend of the Ag NP coverage, the Raman signals of both porous and dense substrates first increased and then decreased with increasing amount of TSC (Figure 4.3.3.2 (b and c)). The Raman signal was the strongest at the molar ratio of 1:2. As shown on Figure 4.3.3.2 (d), the porous substrates had significantly higher Raman enhancement factors than the dense substrates. In the case of deposition at the molar ratio of 1:1, the EF of the 20 ppi porous sample reached $(2.1 \pm 0.5) \cdot 10^4$, while the EF of the dense sample was $(6.6 \pm 3.3) \cdot 10^3$. Moreover, the standard deviation of the EF values of the porous sample was lower (Figure 4.3.3.2 (d), and Table 4.3.4.1), which indicated that the enhancement effect of the porous samples was more evenly distributed over the sample surface than on the dense sample. EF values for the dense samples deposited at the ratios of 1:0.1 and 1:0.25 showed no significant Raman peaks for pyridine (Figure 4.3.3.2 (d)).

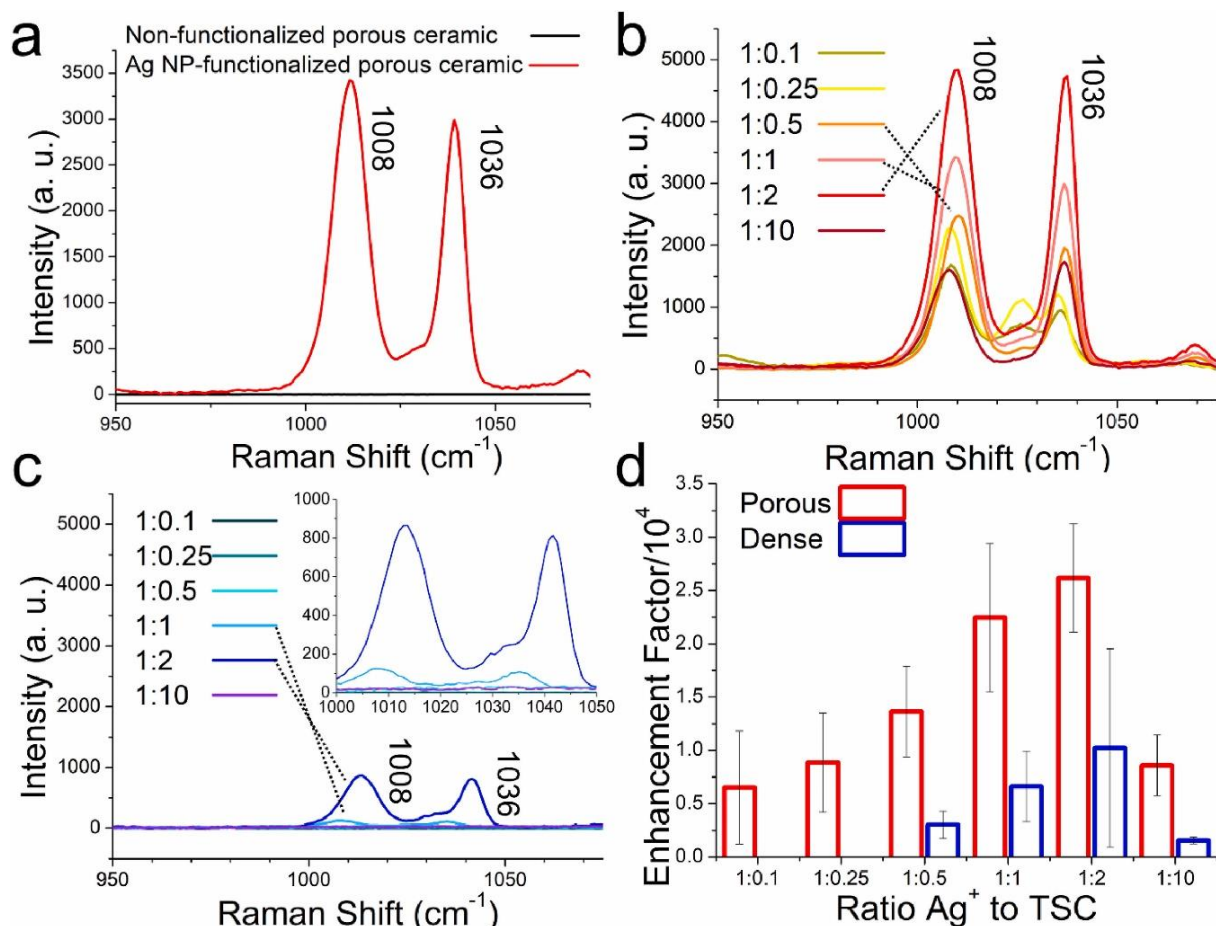


Figure 4.3.3.2 (a) Raman spectra of pyridine adsorbed on non-functionalized ZTA porous ceramic and Ag nanoparticle functionalized-sample; Raman spectra of pyridine using 20 ppi porous (b) and dense (c) ceramic as SERS substrate with Ag nanoparticles deposited at different molar ratios of Ag ions to TSC; (d) Raman enhancement factor as a function of the molar ratio of Ag ions to TSC. Adapted with permission from [1]. Copyright (2022), Elsevier.

In comparison to optimized flat substrates with more regularly spaced particles as reported in the literature, the observed EF in the order of 10^4 is in the lower range compared to literature values in the range of $10^4 \sim 10^8$ [11,300,301]. For example, AAO-based SERS substrates were reported with EF from 10^4 to 10^7 [302–305]. However, considering that in this work the Ag particles are randomly deposited with a fairly low surface coverage of around 5%, the EF of the porous ceramics is significant and already useable for sensitive detection of Raman-active molecules. Further optimization of particle distribution, packing and morphology should offer ample potential to further improve this value.

4.3.4 Plasmonic porous ceramics with different pore sizes

In order to study the effect of the pore size on the EF of the plasmonic porous ceramics, substrates with different pore sizes were deposited with Ag nanoparticles under the identical experimental conditions using TSC as reductant. Again, flat and dense substrates of the same

composition were used as reference. The parameters of the prepared porous ceramics with different pore sizes are listed in Table 4.3.4.1. The pore sizes of the porous ceramic samples were obtained by μ -CT 3D reconstruction, while the thicknesses at the mid-point of the struts of the porous structure were determined by light microscopy.

Table 4.3.4.1 Raman enhancement factors of porous ceramics with different pore sizes and dense pellet deposited under molar ratio of Ag ion to TSC 1:1. * obtained by μ -CT 3D reconstruction; ** analyzed by light microscopy. Adapted with permission from [1]. Copyright (2022), Elsevier.

Porous substrate	Pore size* (mm)	Ave. thickness of the struts** (mm)	Ag nanoparticle coverage (%)	Enhancement factor (10^4)
20 ppi	0.55	0.174 ± 0.011	4.9 ± 0.8	2.1 ± 0.5
30 ppi	0.51	0.132 ± 0.012	4.5 ± 1.0	2.0 ± 0.5
60 ppi	0.24	0.046 ± 0.006	4.6 ± 0.9	1.4 ± 0.5
Dense substrate	/	/	4.4 ± 1.2	6.6 ± 3.3

Figure 4.3.4.1 (a) shows the Raman spectra of plasmonic porous ceramic substrates with different pore sizes and of the dense substrate. The Raman enhancement factors were calculated as described and are summarized in Figure 4.3.4.1 (b). Again, the porous ceramics have significantly higher enhancement factors than the dense ceramic. The enhancement factor decreased with decreasing pore size of the porous ceramics. The particle coverage is very similar for all samples (Table 4.3.4.1).

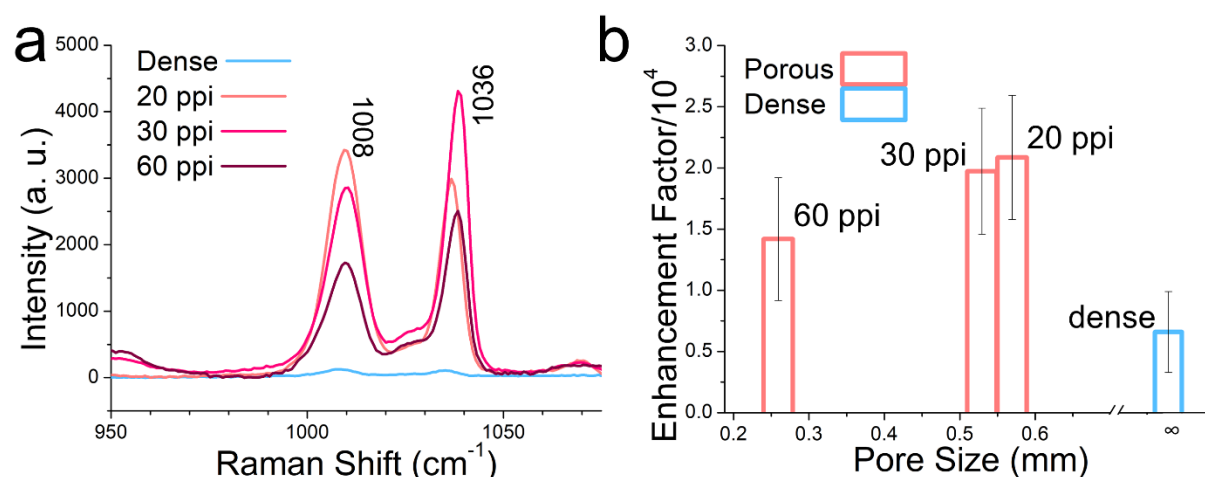


Figure 4.3.4.1 (a) Raman spectra of pyridine adsorbed on plasmonic porous ZTA substrates with different pore sizes and dense substrate under molar ratio of 1:1; (b) Plot of Raman EF against pore size of the ZTA ceramics. Adapted with permission from [1]. Copyright (2022), Elsevier.

4.3.5 Influence of strut size and surface curvature of the porous structure

Since the laser was focused on the strut of the porous structure during the SERS measurement (Figure 4.2.4.1 (c)), the observed variation of the enhancement factor could originate from the surface curvature of the struts [306]. To investigate the correlation between the surface curvature derived from the strut size of the porous ceramic substrate and the Raman enhancement effect, experiments with thin ceramic rods have been conducted. Thin rods of the same composition as the other substrates were extruded to various thicknesses after sintering from 0.08 mm to 3.0 mm. Raman spectra using thin rods as SERS substrates are shown in Figure 4.3.5.1 (a).

The Raman enhancement factors of the ceramic thin rods were calculated as before and are summarized in Figure 4.3.5.1 (b). The error bar represents the standard deviation between the ten measurements on each sample showing significant differences only between the values in the range of 0.46-1.5 and in the range of 1.85-2.35. The enhancement factors increased with the increasing thickness of the thin rods until the thickness reached 1.5 mm. When the ceramic thin rods became thicker, the enhancement factor decreased again. In comparison, the strut thickness of the porous ceramic substrates was below 0.2 mm. According to the result of the thin rods test, the enhancement factor slightly increases with increasing strut thickness. This result roughly corresponds with the trend observed on substrates with different pore sizes if the flat substrate is considered to be a porous ceramic with infinite pore size.

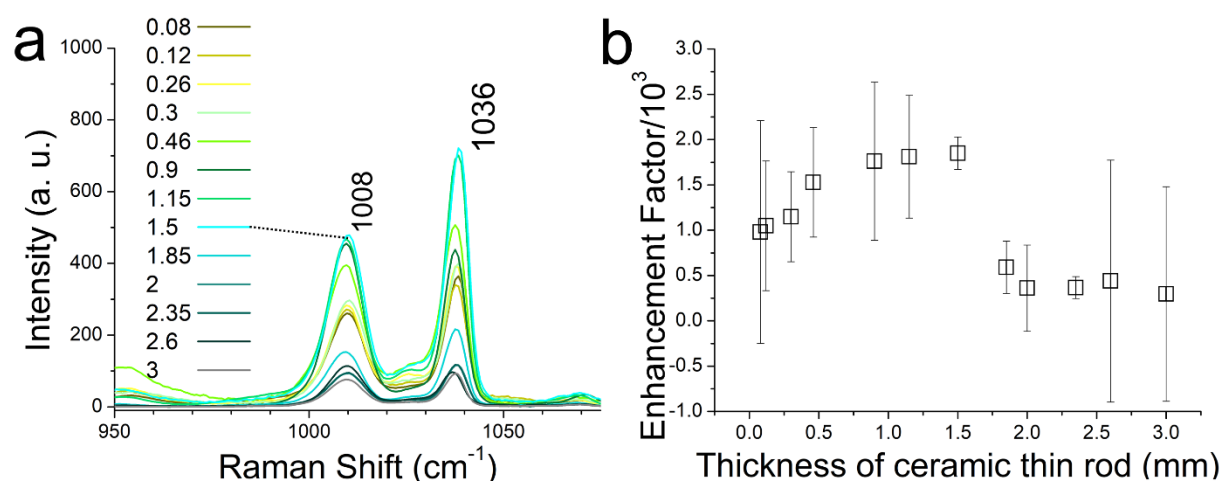


Figure 4.3.5.1 (a) Raman spectra of pyridine adsorbed on ceramic thin rods with different thicknesses (mm) functionalized with Ag nanoparticles at molar ratio of Ag ion to TSC 1:1; (b) Plot of Raman EF against thickness of the ceramic thin rods. Adapted with permission from [1]. Copyright (2022), Elsevier.

4.3.6 Influence of the porous structure on Raman enhancement effect

Comparing Figure 4.3.4.1 (b) with Figure 4.3.5.1 (b), it is obvious that the enhancement effect of the porous ceramic was much higher than that of the ceramic thin rods despite comparable surface coverage with Ag NPs. In fact, even though we observed a weak effect of surface curvature or strut size as described above, the EF of the thin rods is in the same low range than that of the dense substrate. Accordingly, the higher Raman enhancement effect of the porous samples may be directly caused by the three-dimensional porous structure.

In a simple experiment, isolated fragments of the plasmonic porous ceramics were analysed to assess the influence (or rather the effect of the absence) of the surrounding porous structure. The Raman spectra of the diluted pyridine molecule adsorbed on the porous structure and a fragment of the porous structure are demonstrated in Figure 4.3.6.1. It was observed that the Raman signal of the molecule adsorbed on the porous structure (intensity: 3528 ± 1293) was much more pronounced than that on a fragment (intensity: 796 ± 155). Hence, the calculated Raman EF of the porous structure ($(2.1 \pm 0.5) \cdot 10^4$) was significantly higher than that on a fragment ($(4.7 \pm 0.06) \cdot 10^3$).

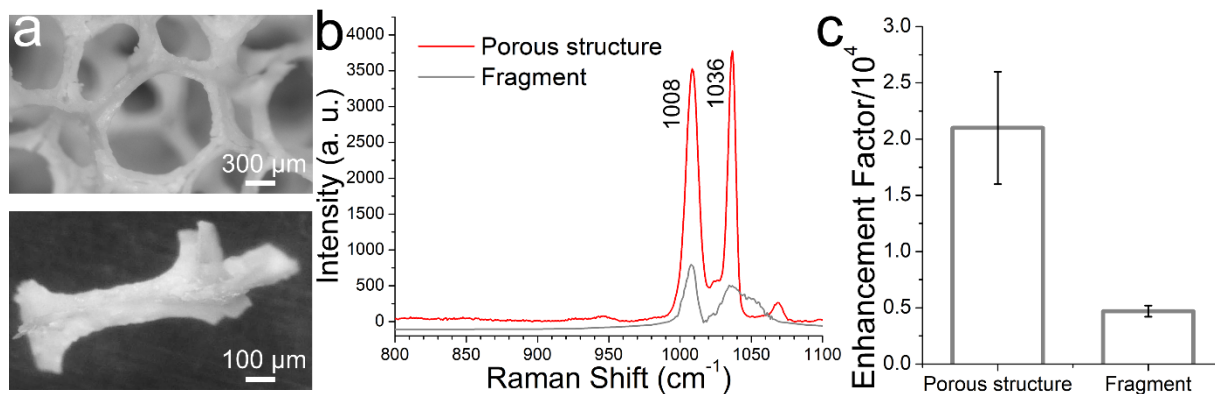


Figure 4.3.6.1 (a) Light microscopy image of a 20 ppi ceramic porous structure (upper) and a fragment piece of the 20 ppi ceramic (lower); (b) Raman spectra of pyridine adsorbed on the porous ceramic (red) and a on a fragment of a 20 ppi porous ceramic (grey); (c) Raman enhancement factor of the porous structure and of a single fragment. Adapted with permission from [1]. Copyright (2022), Elsevier.

Since the only real difference between the fragment and the full structure is the presence of the surrounding porous structure itself, this added enhancement is likely connected to the way light propagates inside the ceramic structure.

This leads us to hypothesize that the incident laser light might be scattered multiple times within the porous structure, increasing the possibility to excite a porous hotspot. Generally, the incident laser hits the molecules adsorbed on plasmonic particles on a fraction of the sample surface defined by the focal area of the laser (diameter of the focal area = 2.6 μm). In the case

of a non-porous fragment or a dense pellet sample, some of this light is scattered at the grain boundaries of the ceramic in all directions, but sufficient light is directly scattered back to the detector which records the Raman signal (Figure 4.3.6.2 left). However, when the incident laser hits the molecules adsorbed on a strut inside a plasmonic porous ceramic sample, the diffuse light might be scattered onto the neighbouring structures [56–63,99]. This way, the chance of the light hitting plasmonic NPs or even hotspots is increased. After multiple scattering events, some of the scattered light could also reach the detector including the incidences that were influenced by additional hotspots (Figure 4.3.6.2 right). This would explain why the porous ceramic samples show a higher Raman enhancement factor than the single fragment. Detailed experiments on light propagation including modeling of scattering inside the plasmonic porous ceramic need to be carried out to substantiate this tentative explanation, which would be of crucial importance for further studies.

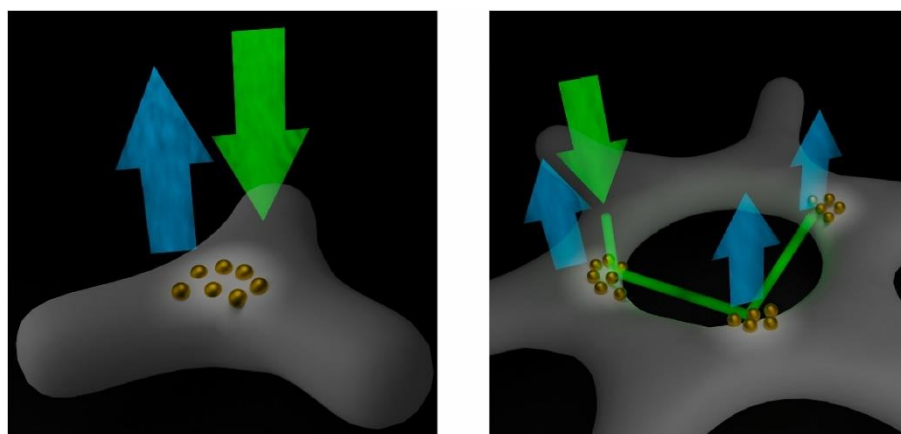


Figure 4.3.6.2 Schematic representation of the light path during Raman scattering on a fragment sample (left) and on a porous sample (right). Yellow dots present the Ag nanoparticles, green arrows indicate the incident light, blue arrows refer to the light, which is backscattered to the detector. Adapted with permission from [1]. Copyright (2022), Elsevier.

4.4 Conclusions

The results presented in this chapter introduced the concept of plasmonic porous ceramics for sensitive molecule detection via SERS. The synthesized plasmonic porous ZTA ceramics reached EFs of approximately 10^4 , which is around five times higher than that of a comparable non-porous structure. The EF could potentially be further improved by optimizing the deposition technique to achieve more plasmonic hotspots, as suggested by the simple deposition method employed here. The plasmonic nanoparticle surface coverage can be manipulated by varying the relative amount of the reactants. Meanwhile, pore size of the porous ceramic structure demonstrated a relatively weak effect on the enhancement effect. Notably, the Raman EF seemed to increase with pore and strut size until a certain point, at which the material was

assumed the properties of the non-porous dense sample. Importantly, the plasmonic porous ceramics have shown a higher Raman enhancement effect than both dense sample and a single fragment. This could be due to multiple light scattering / light-trapping within the porous structure, increasing the possibility of exciting probe molecules adsorbed on plasmonic nanoparticles or plasmonic hotspots.

The designed and processed plasmonic porous ZTA ceramics show promise for use in real-time and sensitive molecule detection via SERS under high pressure / temperature conditions. The maximum estimated working temperature is around 900 °C, limited by the melting point of the silver particles. To improve the working temperature of the plasmonic porous ceramics, refractory plasmonic particles, such as W, TiN, ZrN or Mo could be utilized for the processing procedure [307,308]. Multifunctional particles can be introduced in the plasmonic porous ceramics, in order to bring new function possibilities [309–311]. To assess the application of the plasmonic porous ceramics for biomedical applications, bioceramic materials such as hydroxyapatite, bioactive powder, could be used instead of bioinert ZTA ceramics [312–314].

5. Plasmonic porous ceramics for *in situ* catalytic reaction monitoring

Chapter 5 has been adapted with permission from *Wiley* and is published in the Journal *Advanced Materials Interfaces*, 2023, DOI: 10.1002/admi.202300207

Porous ceramics are well-established as supports for metal nanoparticle catalysts, where they are required to maintain spatial distribution and to facilitate product separation from the catalytic nanoparticles [315–318]. However, ceramic catalyst carriers usually complicate *in situ* reaction monitoring, because they block and/or scatter electromagnetic radiation at a wide range of wavelengths. This problem could be solved by specifically designing the porous support [1,319], so that it can utilize scattering processes to enable or even enhance Raman scattering-based sensing of reactants.

Ideal substrates for metal nanoparticle catalysts should feature chemical and thermal stability, high surface area and large open porosity providing high accessibility of the substrates. In this context, ceramics have obvious advantages over metal- and polymer-based materials in terms of mechanical and thermal stability, resistance against corrosion and chemical erosion. Additionally, ceramics can be processed with a wide range of porous structures with low density, high mechanical stability and high specific surface area for three-dimensional (3D) catalyst impregnation. In some instances, ceramics like alumina can act not only as a support, but also as a catalyst for reactions such as isomerization, alkylation, catalytic cracking and hydroforming [320]. Of different crystal structural phases (e. g., alpha, beta and gamma), alpha-alumina has the lowest catalytic activity and is mostly processed with a relatively low specific surface area as opposed to the “activated” alumina phases that exhibit meso- and microporosity along with a high abundance of active sites [321]. Here, this work focuses on passive alpha alumina supports structured as macro-porous open cell foams.

In Chapter 4, the concept of plasmonic porous ceramics was introduced, which is based on ZTA ceramics functionalized with Ag nanoparticles that combine the optical properties of plasmonic nanostructures with advantages of ceramics [41–45]. In this chapter, the concept of plasmonic porous ceramics was realized by preparing functionalized ceramic open cell foams with metallic core-shell nanoparticles (Au@Pd, Au@Pt). The core-shell nanoparticles are designed to exhibit a highly SERS-active Au core and a catalytically active Pd / Pt shell with a large surface area. The particles are prepared with various shell thicknesses via the Au-seed mediated method [322] and colloiddally deposited on the ceramic matrix after particle synthesis. The zirconia-stabilized alumina matrix of the porous ceramic acts as the catalyst support, which is designed to augment the SERS-based reaction monitoring through light-trapping and

scattering which is characterized by the diffuse reflectivity of the sample. The general material concept was tested by analyzing the well-known reaction of 4-nitrothiophenol (4-NTP) to 4-aminothiophenol (4-ATP).

5.1 Materials

Gold(III) chloride hydrate (99.995 % trace metals basis, product no. 254169), potassium tetrachloropalladate(II) (99.99 % trace metal basis, product no. 379816), chloroplatinic acid solution (8wt. % in H₂O, product no. 262587), L-Ascorbic acid (99 %, product no. A92902), sodium borohydride (99 %, product no. 213462) were purchased from Sigma Aldrich, Germany. 4-nitrothiophenol (product no. H59240) was obtained from Alfa Aesar, Germany.

5.2 Methods

5.2.1 Functionalization of the ZTA ceramics with metallic core-shell nanoparticles

The processing of 30 ppi ZTA porous ceramics and dense pellets followed the procedure described in section 4.2.1. The coating of the metallic core-shell nanoparticles was achieved through chemical reduction of noble metal ions. In a 100 ml 3-neck round flask filled with 14.705 mg 45 ml TSC solution, the ceramic sample was hung with a thin thread and submerged in the solution. The reaction solution was stirred with a magnetic stirrer and heated in oil bath to 100 °C. Subsequently, 5 ml 10 mM chloroauric acid was added dropwise to the reaction solution. The reaction solution turned ruby red, indicating the formation of the Au core. To coat the Au seed with a Pd shell, yielding Au@Pd nanoparticles, after 10 min stirring, 1.632/3.264/13.057/16.322 mg potassium tetrachloropalladate were added to the reaction solution (corresponding to K₂PdCl₄ reaction concentration 0.1 mM, 0.2 mM, 0.8 mM and 1 mM) respectively. The reaction solution was stirred and kept at 100 °C until the color changed from ruby red to dark grey [137,323,324].

To functionalize the Au particles with a Pt shell, yielding Au@Pt nanoparticles, after 10 min stirring followed by the formation of Au nanoparticles, 24.39/48.79/195.12/243.93 µl 8wt. % chloroplatinic acid solution was added to the reaction solution (corresponding to H₂PtCl₆ reaction solution concentration 0.1 mM, 0.2 mM, 0.8 mM and 1 mM) respectively.

5.2.2 Characterization

The SEM measurements followed the procedures described in Chapter 4.2.6. The metallic core-shell nanoparticle suspensions were analyzed by first diluting them heavily and then drying on a copper Formvar coated film. The dried nanoparticles were examined using a TEM instrument (EM 900, ZEISS, Germany). ImageJ was used to analyze the TEM images and determine the size of the nanoparticles. The polydispersity of the nanoparticles was assessed by a Gaussian fitting of the nanoparticle size distribution.

UV-Vis spectra were acquired using a Multiskan GO microplate spectrophotometer (Thermo Scientific GmbH, Germany). To obtain the absorption spectra of the metallic core-shell nanoparticles, suspensions were collected from the reaction solution after the deposition of the core-shell nanoparticles. Plasmonic porous ceramics were submerged in 5 ml of 0.5 mM 4-NTP to monitor the reduction process. A timer was started upon addition of 5 ml of 2.5 mM NaBH₄ to the 4-NTP solution. UV-vis spectra were recorded at different reaction time points.

Raman spectra were collected using the identical device described in Chapter 4.2.7. A laser working at 633 nm and less than 20 mW was used as light source. Raman spectra were recorded in the range of 800 to 1200 cm⁻¹ for pyridine, 900 to 1300 cm⁻¹ and 1450 to 1700 cm⁻¹ for the reaction monitoring of 4-NTP reduction.

To obtain the hemispherical reflectance, a VERTEX 80v (Bruker GmbH, Germany) Fourier-transform infrared spectrometer (FTIR) was utilized, which is equipped with a white polytetrafluoroethylene sphere with a diameter of 7.5 cm and a Si-Diode 2.4 mm detector. The measurements were performed at ambient temperature and 2.5 mbar by taking three consecutive readings between 450-1100 nm and averaging them. The calibration of the reflectivity was performed against the Spectralon[®] Diffuse Reflectance Standard 99 % (Labsphere, Inc., US).

5.3 Results and discussion

Metallic core-shell nanoparticles composed of an Au core and a Pd or Pt shell have been synthesized and introduced in the open porous ceramic foams in this work. The Au core was synthesized using TSC to reduced HAuCl₄ chemically. In the next step, the Pd/Pt shell was reduced on the Au core surface by the remaining surface adsorbed TSC (with the addition of L-ascorbic acid in the case of Pt shell). This process is known as seed growth, where the Au seed likely plays a role in catalyzing the reduction of PdCl₄²⁻ / PtCl₆²⁻ ions by facilitating electron transfer from the reductant to the metal salt ions [325].

The bifunctional core-shell structure realized the combination of catalytic- and SERS-activity in a single unit. Figure 5.3.1 shows the Raman spectrum of pyridine using Au NP coated plasmonic porous ceramic as SERS substrate (a) and the absorption spectrum of the 4-NTP reduction process at initial point and after 30 min reaction time (b), respectively. The sample functionalized with 39 nm Au nanoparticles reached an outstanding Raman enhancement factor up to $3.3 \cdot 10^6$. However, the absorption spectrum of the reactant 4-NTP after 30 min reaction time still overlapped with the initial spectrum, indicating the 4-NTP concentration barely changed, which implied the inefficiency of the sample as catalytic substrate.

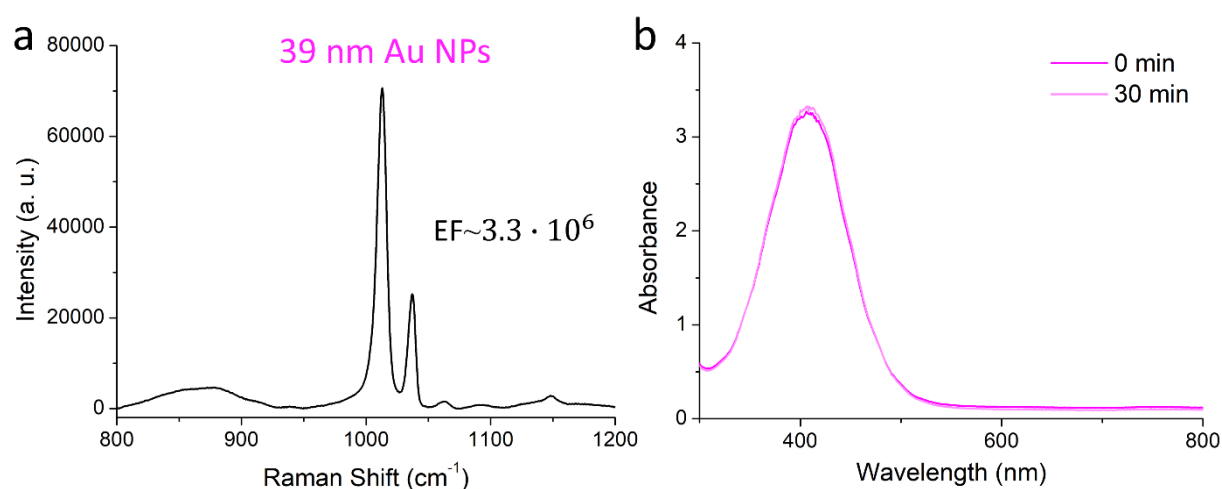


Figure 5.3.1 (a) Raman spectrum of pyridine on plasmonic porous ceramic functionalized with 39 nm Au nanoparticles; (b) Absorption spectrum of 4-NTP reduction process at initial time and after 30 min of reaction time. Adapted with permission from [2]. Copyright (2023), Wiley.

Figure 5.3.2 depicts BSE-SEM images of the ZTA ceramic surface functionalized with Au@Pd nanoparticles, as well as the insert TEM images of the Au@Pd nanoparticles synthesized with various concentrations of the palladate precursor. The TEM images demonstrate that the size of the core-shell particle increased with an increasing concentration of the palladate precursor. The diameters of the Au@Pd nanoparticles are 42.05 ± 3.29 nm, 54.01 ± 4.58 nm, 75.94 ± 3.28 nm and 93.18 ± 3.62 nm, respectively, for precursor concentrations of 0.1 mM, 0.2 mM, 0.8 mM and 1 mM. A rough shell is visible at the highest precursor concentration (as seen in the inset of Figure 5.3 (d)). Given that the prepared Au seed particles have a size of 39.1 ± 2.13 nm, the size change the core-shell particles implies a change in the shell thickness. In the SEM images, the dark background areas indicate alumina, while the lighter grey areas indicate zirconia grains that offer higher mechanical strength to the intricate porous ceramic structure [326]. The tiniest bright dots correspond to the metallic nanoparticles, reaching a total surface coverage of around 20 %.

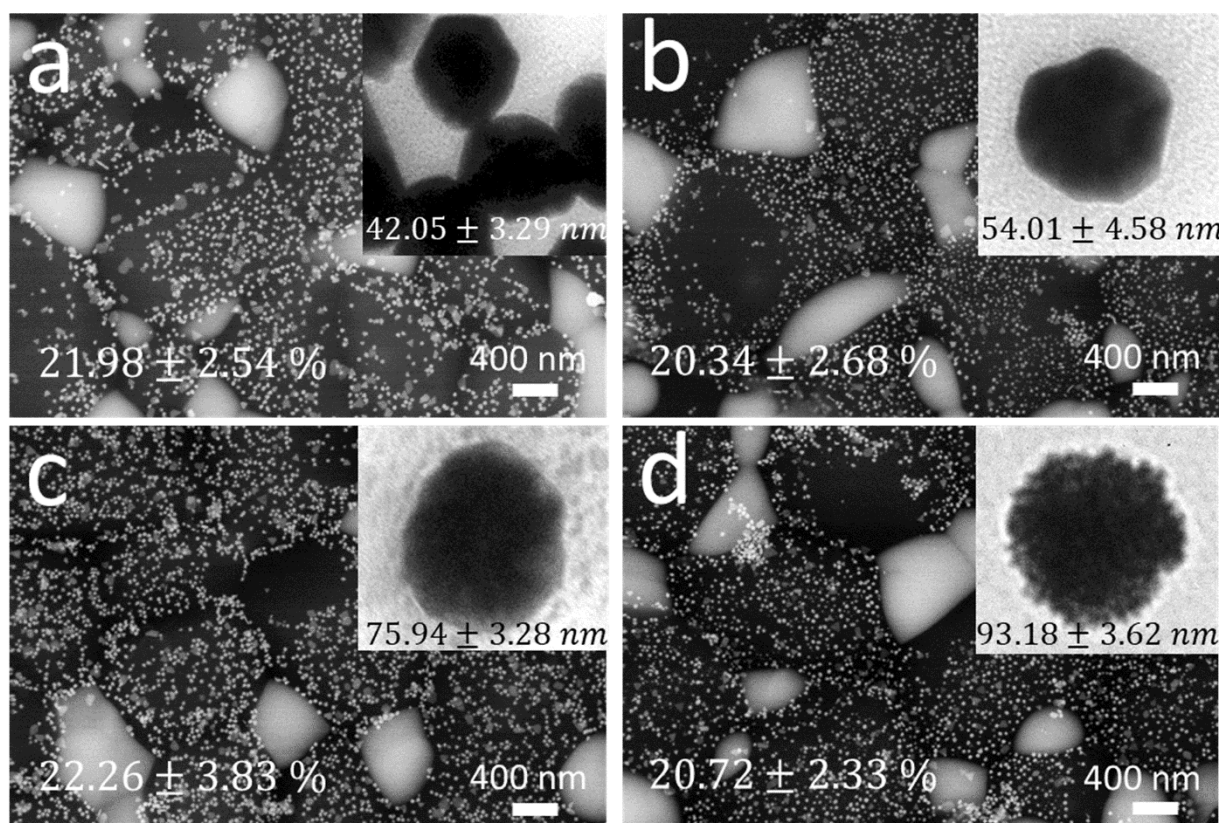


Figure 5.3.2 BSE-SEM images of porous ZTA ceramic surface functionalized with different sized Au@Pd core-shell nanoparticles synthesized with varying palladate concentration of (a) 0.1 mM, (b) 0.2 mM, (c) 0.8 mM and (d) 1 mM, respectively, with the nanoparticle coverage on the figures. Insets show the TEM images of the deposited core-shell nanoparticles with corresponding particle diameters. Adapted with permission from [2]. Copyright (2023), Wiley.

Similarly, SEM images of the synthesized and deposited Au@Pt core-shell nanoparticles are shown in Figure 5.3.3. The deposited Au@Pt nanoparticles exhibit diameter of 44.32 ± 0.57 nm, 48.11 ± 1.93 nm, 50.84 ± 4.7 nm and 70.78 ± 5.58 nm, corresponding to chloroplatinic acid reaction concentration of 0.1 mM, 0.2 mM, 0.8 mM and 1 mM, respectively. The rough shell structure can be observed obviously already at a platinic precursor concentration of 0.2 mM, as depicted in the inset of Figure 5.3.3 (b).

In general, the Pd shells on the surface of the Au core are thicker than the Pt shells under the same reaction conditions. This can be attributed to the higher reactivity of the PdCl_4^{2-} precursor, resulting in a slower rate for the Pt shell. This observation aligns with the postulated seed growth mechanism [325].

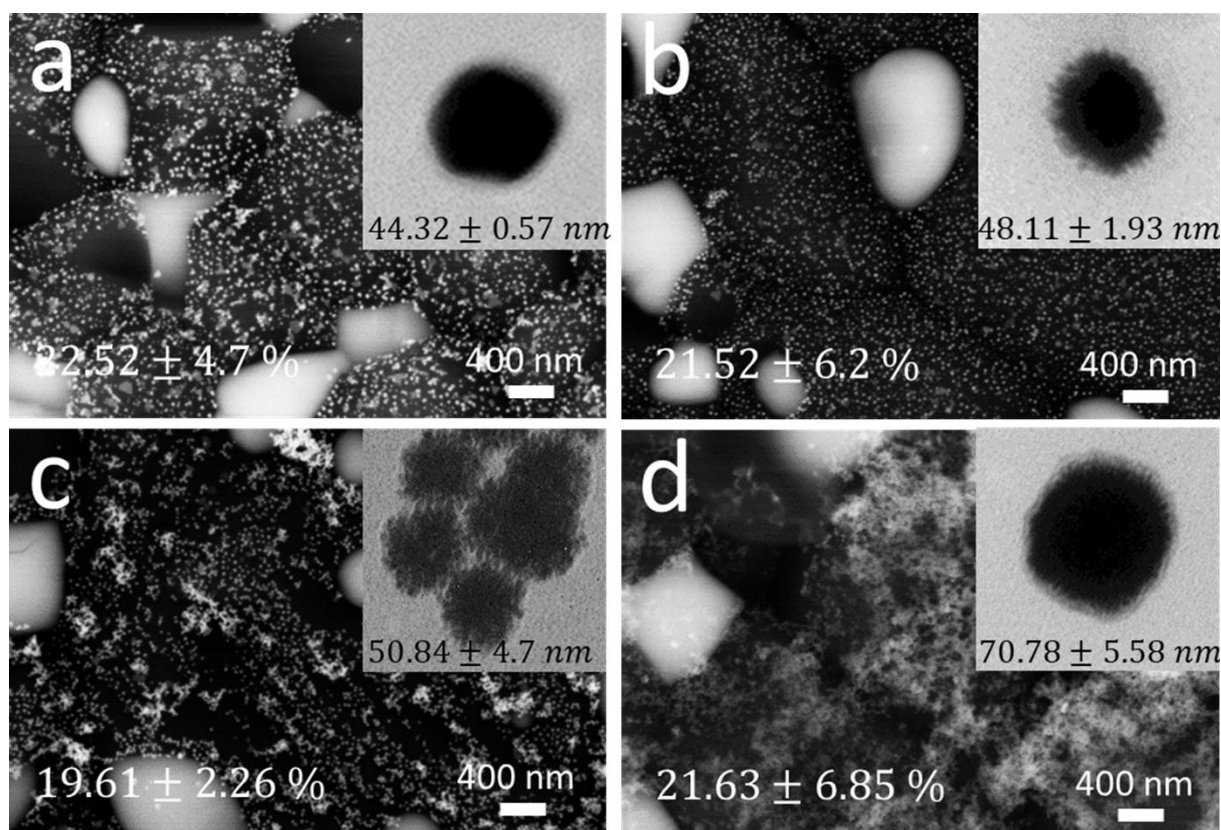


Figure 5.3.3 BSE-SEM images of porous ZTA ceramic surface functionalized with different sized Au@Pt core-shell nanoparticles synthesized with varying palladate concentration of (a) 0.1 mM, (b) 0.2 mM, (c) 0.8 mM and (d) 1 mM, respectively, with the nanoparticle coverage on the figures. Insets show the TEM images of the deposited core-shell nanoparticles with corresponding particle diameters. Adapted with permission from [2]. Copyright (2023), Wiley.

Figure 5.3.4 indicates the UV-vis absorption spectra of the suspensions the metallic core-shell nanoparticles, which exhibit a shift in intensity peaks towards higher wavelengths with increasing shell thickness. Compared with the reference spectrum of the 39 nm Au core nanoparticles with a sharp localized surface plasmon resonance (LSPR) peak at 526 nm, the suspensions of 42 and 54 nm Au@Pd nanoparticles exhibited LSPR peaks at 539 nm (Figure 5.3.3 (a)). As for the 76 nm sized Au@Pd particles, the LSPR peak shifted to 549 nm and became broader. The absorption peak of the 93 nm sized Au@Pd nanoparticles was observed at 561 nm and exhibited a flatter shape. This flattening of the LSPR peak suggested that the plasmon resonance of the core-shell nanoparticles is dominated by the damped plasmon oscillations in the Pd shell, which is consistent with previous report on similar particles [137].

The UV-vis absorption spectra of the Au@Pt core-shell nanoparticles are presented in Figure 5.3.4 (b). The LSPR peaks of the 44 nm, 48 nm, and 51 nm sized Au@Pd nanoparticles only exhibited a slight redshift at 529 nm, since the Pt shells were thinner. However, the LSPR peak for the 51 nm sized Au@Pt particles was more pronouncedly broadened. In contrast, the absorption curve of the 71 nm sized Au@Pt particles became much flatter and the resonance

peak disappeared, indicating that the damped plasmon resonance of the Pt shell dominates over the Au core now. Moreover, the width of the Au@Pt core-shell particle size distribution grew from 0.21 to 0.58 with the increasing size of the particle, which contributes to the broadening of the larger Au@Pt nanoparticle LSPR peak [327].

The localized surface plasmon resonance (LSPR) peaks of Au@Pd core-shell NPs were more pronouncedly redshifted than that of Au@Pt NPs. From the literature, the main resonance frequencies of the localized surface plasmon of Pd, Pt and Au are 0.10, 0.35 and 1.40 eV [108], respectively, corresponding to 12,398, 3,542 and 886 nm. The main resonance of Pd lies at a much higher wavelength than that of Pt, which leads to the more pronounced redshift of the Au@Pd LSPR peaks. In addition, the Pd shell was significantly thicker than the Pt shell, so the damped plasmon oscillations in the Pd shell should more pronounced.

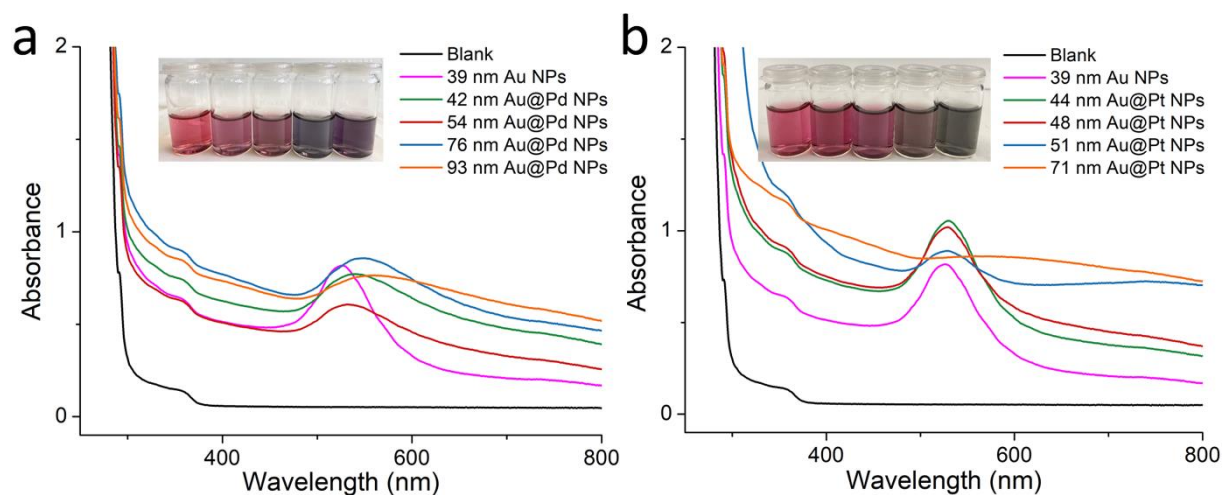


Figure 5.3.4 (a) Absorption spectra of nanoparticle suspensions of 39 nm Au core (purple), as well as 42 nm (green), 54 nm (red), 76 nm (blue) and 93 nm (orange) Au@Pd particles with inset showing the respective nanoparticle suspensions from left to right; (b) Absorption spectra of nanoparticle suspensions of 39 nm Au core (purple), as well as 44 nm (green), 48 nm (red), 51 nm (blue) and 71 nm (orange) Au@Pt particles with inset showing corresponding nanoparticle suspensions from left to right, respectively. Adapted with permission from [2]. Copyright (2023), Wiley.

5.3.1 Molecule detection via SERS

Similar to the substrates functionalized with Ag nanoparticles, the Au nanoparticles alone do not affect the Raman spectra of the ZTA substrate. Raman spectra of pure pyridine (Figure 5.3.1.1 (a)) on a bare ZTA substrate and of a 10^{-2} M pyridine droplet on porous ZTA functionalized with 39 nm Au nanoparticles (Figure 5.3.1.1 (b)) are presented here. The porous sample functionalized with 39 nm Au nanoparticles showed an EF around $3.3 \cdot 10^6$.

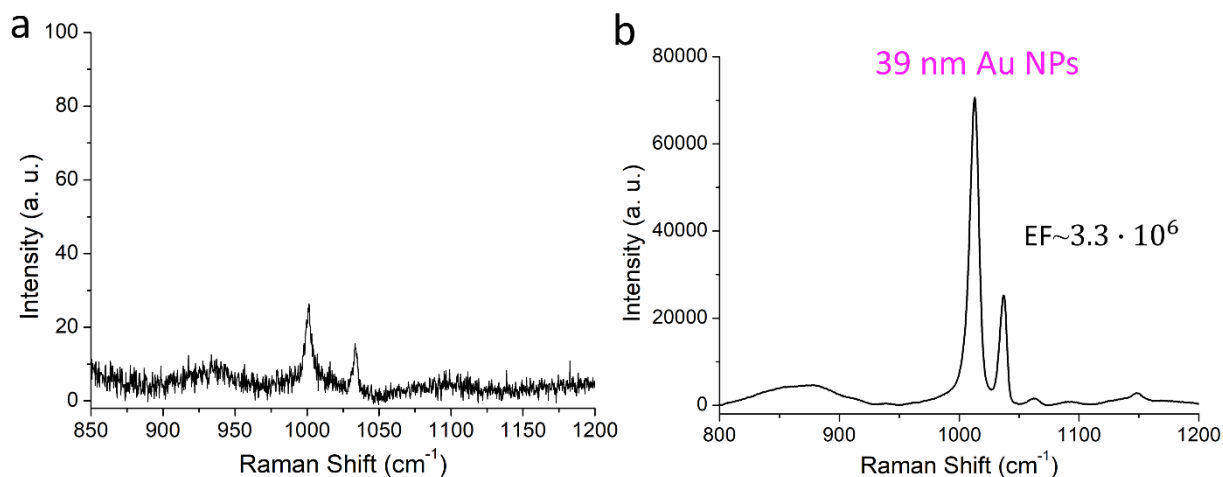


Figure 5.3.1.1 Raman spectra of pure pyridine on a bare ZTA substrate (a) and diluted pyridine droplet on 39 nm Au nanoparticle functionalized plasmonic porous ZTA substrate (b). Adapted with permission from [2]. Copyright (2023), Wiley.

The ability of metallic core-shell nanoparticles functionalized porous ceramics for real-time and sensitive molecule detection can be evaluated through SERS, using pyridine as the probe molecule. Figure 5.3.1.2 illustrates the Raman spectra of the probe molecule adsorbed on plasmonic porous ceramics functionalized with variously sized Au@Pd nanoparticles. The Raman shifts observed at 1012 and 1038 cm⁻¹ correspond to the pyridine ring breathing mode (ν_1) and symmetric ring deformation (ν_{12}), respectively, and are amplified by the localized plasmon resonance (LPR) of Au [328]. The peak intensity observed at 1026 cm⁻¹ is attributed to the symmetric ring deformation of pyridine adsorbed on Pd, which has previously been reported to occur between 1001-1005 cm⁻¹ [328]. The frequency shift of the pyridine symmetric ring deformation (ν_{12}) can be explained by the vibrational coupling effect [259,264,329–331]. The shift in vibration wavenumbers for the totally symmetric modes of pyridine can be linked to the strength of the adsorption bond between the probe molecule and the metal cluster. Density functional theory allows the modelling of pyridine adsorption on group VIII B metals as a pyridine metal complex (Py-M, Py-M₂, and Py-M₅), with the strength and distance of the bond dependent on the type of the metal cluster. Consequently, the vibrational mode of pyridine on the metal will change accordingly. For instance, Wu *et al.* calculated the Raman signal of the pyridine symmetric ring deformation (ν_{12}) at 1030 cm⁻¹ in the case of Py-Pd₂ [330], which correlates with the measured Raman signal at 1026 cm⁻¹ in this work. The slight shift between 1026 and 1030 cm⁻¹ can be interpreted by the quasi-harmonic nature of molecules at ambient temperature. Furthermore, Figure 5.3.1.2 (b) demonstrates the Raman of pyridine on plasmonic porous ceramic substrates functionalized with Au@Pt nanoparticles of different sizes. The Raman shift at 1015 cm⁻¹ is attributed to pyridine adsorbed on the Pt shell [328].

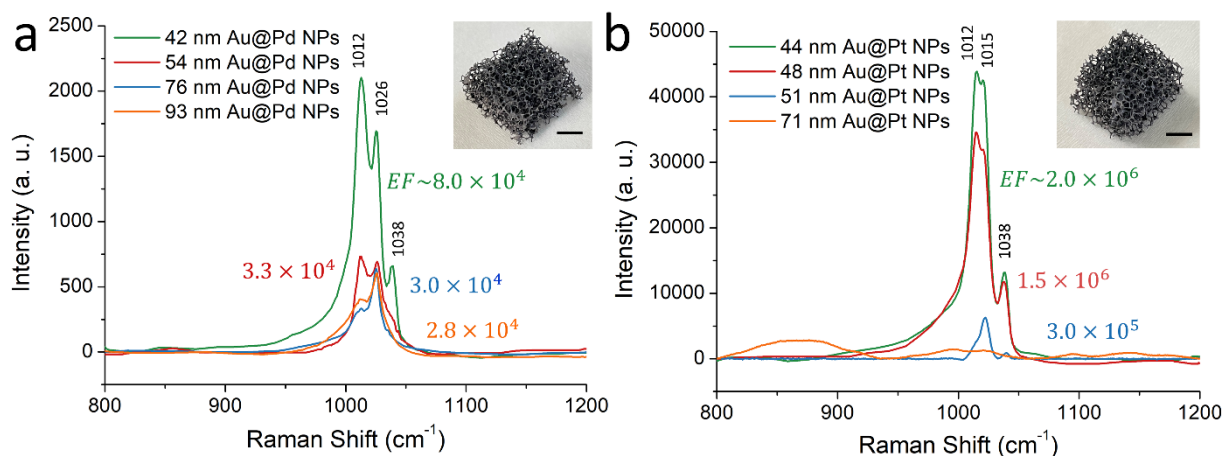


Figure 5.3.1.2 (a) Raman spectra of pyridine on plasmonic porous ceramics functionalized with Au@Pd nanoparticles (a) and Au@Pt nanoparticles (b) of different sizes. Insets show the corresponding sample in macroscopic scale, scale bar equals 5 mm. Adapted with permission from [2]. Copyright (2023), Wiley.

The Raman EFs were determined as described in Chapter 4.2.7, using the Raman intensity at 1026 and 1015 cm^{-1} for Au@Pd and Au@Pt nanoparticles functionalized samples, respectively. The Raman EFs exhibit a reducing trend with increasing shell thicknesses, consistent with the UV-vis spectra discussed above. The EFs of the substrates functionalized with Au@Pd nanoparticles decreased from $8.0 \cdot 10^4$ to $2.8 \cdot 10^4$ as the size of the core-shell particle increased from 42 to 93 nm. Nonetheless, the EFs remained in the same order of magnitude. In contrast, the EFs of the samples functionalized with Au@Pt nanoparticles dropped rapidly from $1.5 \cdot 10^6$ to $3.0 \cdot 10^5$ as the size of the particles increased from 48 to 51 nm. With a size of 71 nm, the sample no longer exhibited any characteristic Raman shifts of the probe molecule, indicating the loss of the Raman enhancement effect.

The SERS activity of pure transition metals was reported to be rather weak, which can be attributed to their limited plasmonic properties [328]. However, by depositing a thin layer of transition metal on top of a SERS-active Au core, the high SERS enhancement can still be achieved through the long-range effect of the electromagnetic field [332–335]. According to the electromagnetic mechanism of the Raman enhancement effect, the Raman enhancement increases as the probe molecule gets closer to the SERS-active nanostructure. Therefore, a thinner shell will place the probe molecule closer to the Au core, resulting in a higher Raman EF.

The porous substrates functionalized with Au@Pd nanoparticles exhibit Raman EFs in the order of 10^4 , while substrates functionalized with Au@Pt nanoparticles show much higher EFs, up to 10^6 . However, the effective permittivity of metallic core-shell particles is not solely determined by the size of the Au core, but also by the composition of the surrounding layer. When it comes to metallic nanoparticles, the plasmon response is mainly dominated by the

metal with interband electron transitions at lower frequency. Blaber *et al.* reported the frequencies of the maximum quality localized surface plasmon $Q_{max.LSP}$ of different metals. It was found that the frequencies of $Q_{max.LSP,Pd}$ and $Q_{max.LSP,Pt}$ are significantly lower than that of $Q_{max.LSP,Au}$, indicating that the Pd and Pt shells play a more dominant role in the plasmon response of the core-shell particle. Therefore, compared to conventional Au and Ag nanoparticles, core-shell particles Au@Pd and Au@Pt generally exhibit weaker SERS enhancement due to the dominance of Pd and Pt shell.

Meanwhile, Figure 5.3.1.3 shows the Raman spectrum of pyridine on plasmonic porous ceramic functionalized with 48 nm Au@Pt nanoparticles, measured with a 532 nm laser. The Raman EF is around $1.2 \cdot 10^4$. In comparison, the sample measured with the 633 nm laser (Figure 4b, red spectrum) showed an EF around $1.5 \cdot 10^6$. Although the Au@Pt core-shell particles exhibit an absorption peak around 529 nm, the 532 nm laser as excitation source provided weaker Raman EFs than the 633 nm laser. This phenomenon can be explained by the redshift of the local enhancement field caused by plasmonic hot spots, which has been experimentally demonstrated and theoretically calculated by several studies [23,85,219].

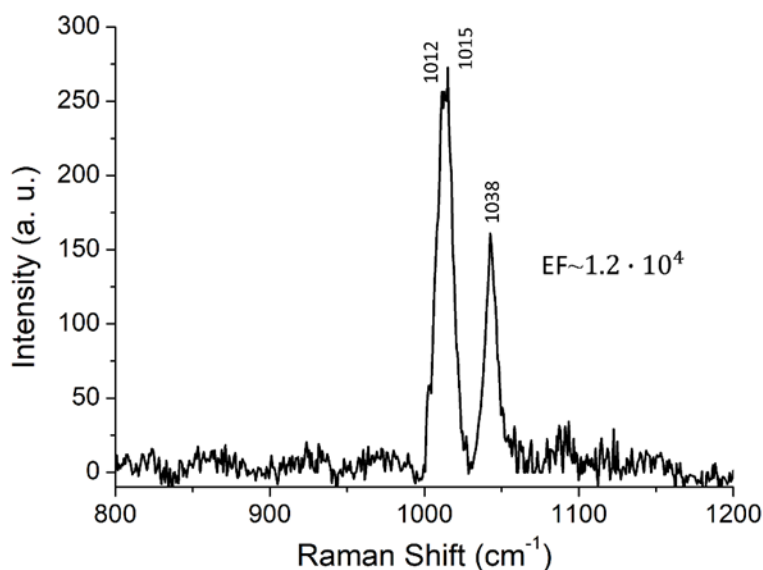


Figure 5.3.1.3 Raman spectrum of pyridine on plasmonic porous ceramic functionalized with 48 nm Au@Pt nanoparticles, measured with a 532 nm laser. Adapted with permission from [2]. Copyright (2023), Wiley.

5.3.2 Catalytic function of the plasmonic porous ceramics

The catalytic activity of the plasmonic porous ceramics functionalized with metallic core-shell nanoparticles was investigated by studying the reduction of 4-NTP using sodium borohydride (NaBH_4) as reductant to 4-ATP with 4,4-dimercaptoazobenzene (*trans*-DMAB) as intermediate

at room temperature (Figure 5.3.2.1). This reduction can be catalyzed by both Pd and Pt [66]. The reaction was analyzed using UV-vis spectroscopy, where the reactant 4-NTP exhibited an absorbance peak at around 412 nm, while the colorless product 4-ATP had no obvious absorbance peak. The change in intensity of the 412 nm absorbance peak allowed for the interpretation of the reduction process from 4-NTP to 4-ATP. It should be noted that the ZTA ceramic substrate was assumed to be completely inert and did not participate in the chemical reaction here [320].

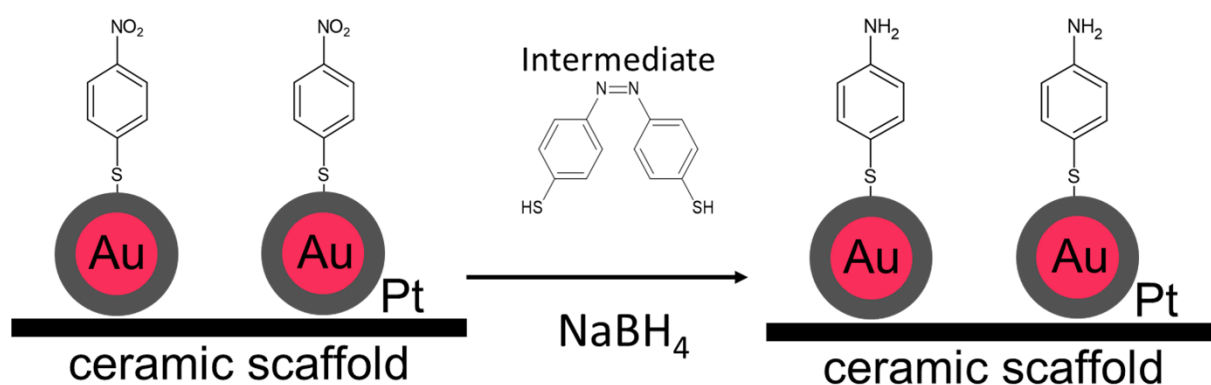


Figure 5.3.2.1 Schematic representation of 4-NTP reduced by NaBH_4 to 4-ATP on the 48 nm sized Au@Pt nanoparticles functionalized plasmonic porous ceramic. Adapted with permission from [2]. Copyright (2023), Wiley.

The absorption spectra of the reduction of 4-NTP on plasmonic porous ceramic functionalized with variously sized Au@Pd nanoparticles were shown in Figure 5.3.2.2. The absorbance peak of 4-NTP at 412 nm was still present after 30 min of reaction time, on the substrates functionalized with 42 and 54 nm Au@Pd nanoparticles, indicating incomplete reduction of 4-NTP. However, the absorbance peak at 412 nm disappeared after 2 min reaction time, implying a complete reduction to 4-ATP.

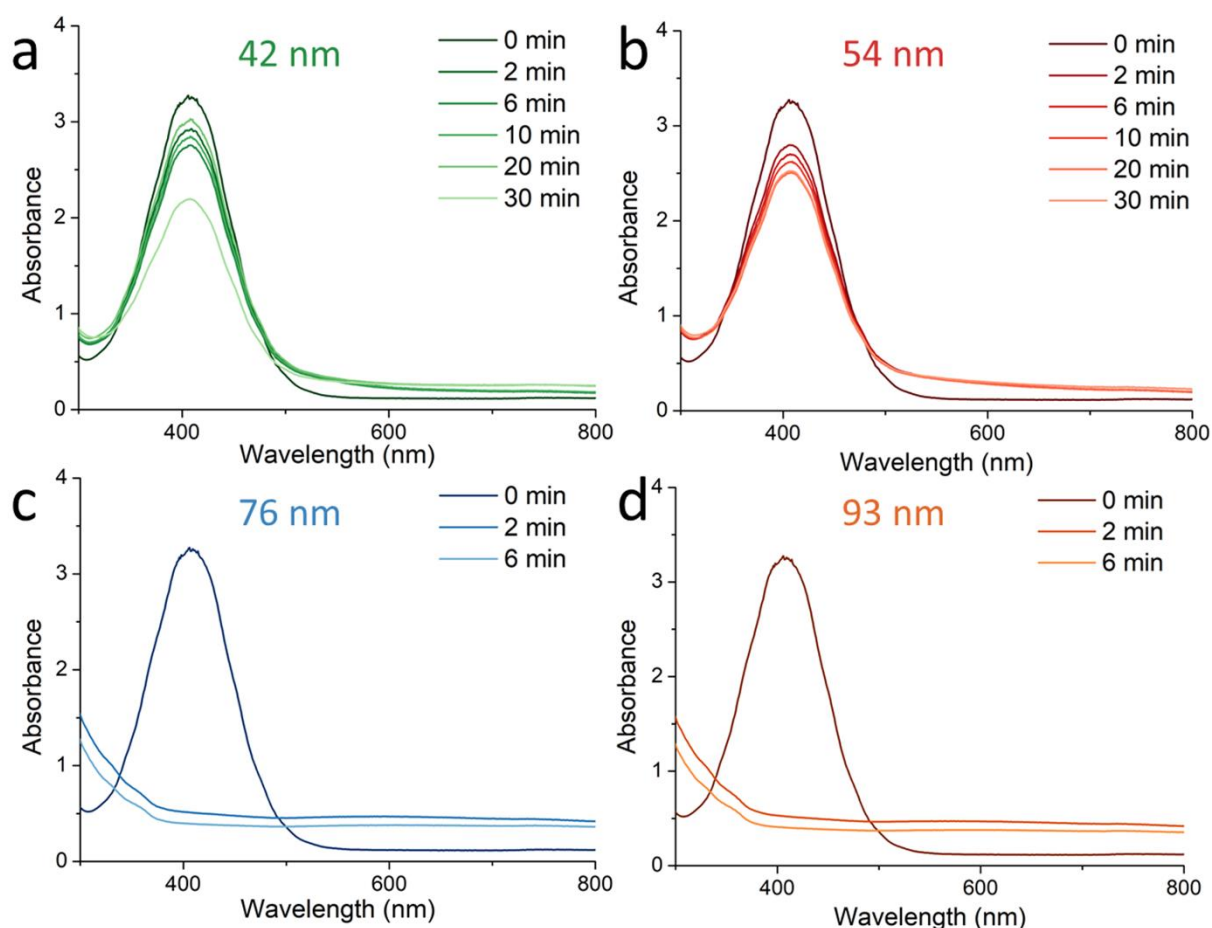


Figure 5.3.2.2 Absorption spectra during the reduction of 4-NTP at different reaction time on plasmonic porous ceramics functionalized with differently sized Au@Pd nanoparticles: (a) 42 nm; (b) 54 nm; (c) 76 nm; (d) 93 nm. Adapted with permission from [2]. Copyright (2023), Wiley.

It is worth noticing, that the substrate functionalized with 54 nm Au@Pd NPs showed a faster reaction rate than the substrate functionalized with 42 nm NPs within the first 20 min reaction time. Although the absorbance peak of the reactant 4-NTP seems to be weaker on the 54 nm functionalized sample after 30 min reaction time, the difference was not significant and within the standard deviation of the data (listed in Table 5.3.2.1).

Table 5.3.2.1 Absorbance value of 4-NTP during the reduction process using plasmonic porous ceramics functionalized with different sized Au@Pd and Au@Pt NPs. Adapted with permission from [2]. Copyright (2023), Wiley.

Au@Pd coated samples				
	42 nm	54 nm	76 nm	93 nm
2 min	3.03 ± 0.05	2.8 ± 0.01	0.52 ± 0.01	0.52 ± 0.01
6 min	2.93 ± 0.05	2.7 ± 0.03	0.4 ± 0.02	0.4 ± 0.01
10 min	2.85 ± 0.03	2.62 ± 0.03	0.3 ± 0.01	0.3 ± 0.01
20 min	2.76 ± 0.05	2.52 ± 0.02	/	/
30 min	2.2 ± 0.13	2.5 ± 0.32	/	/
Au@Pt coated samples				
	44 nm	48 nm	51 nm	71 nm
2 min	2.92 ± 0.01	2.8 ± 0.02	0.85 ± 0.01	0.68 ± 0.01
6 min	2.8 ± 0.02	2.75 ± 0.02	0.72 ± 0.01	0.6 ± 0.01
10 min	2.78 ± 0.01	2.73 ± 0.01	0.66 ± 0.01	0.59 ± 0.01
20 min	2.76 ± 0.02	2.6 ± 0.01	/	/
30 min	2.7 ± 0.02	2.36 ± 0.01	/	/

Likewise, the catalytic activity of the plasmonic porous ceramics functionalized with Au@Pt nanoparticles was shown in Figure 5.3.2.3, demonstrating a clearer trend. While the substrate functionalized with 44 nm Au@Pt nanoparticles exhibited only a minor decrease in the 412 nm peak intensity over 30 min of reaction time, indicating a slight decrease in the reactant 4-NTP concentration. The 48 nm sized particles functionalized sample showed a more noticeable decrease in the 4-NTP concentration. This suggested that the catalytic efficiency improved with an increase in the shell thickness of the core-shell nanoparticles. With an increase in the Au@Pt nanoparticles size to 51 nm, the reduction of 4-NTP was completed after 20 min. The substrate functionalized with 71 nm Au@Pt nanoparticles accelerated the reduction of 4-NTP, compared to the one functionalized with 51 nm particles. Both Au@Pd and Au@Pt nanoparticles on the porous ZTA surface showed a similar trend, indicating improved catalytic efficiency with an increased shell thickness of the core-shell nanoparticles. As the concentration of palladate / chloroplatinic precursor increased, the 39 nm Au core underwent partial coating and eventually a formation of a cohesive shell that became progressively rougher. This resulted in a larger surface area of the catalytically active metal being exposed, enabling more efficient catalysis.

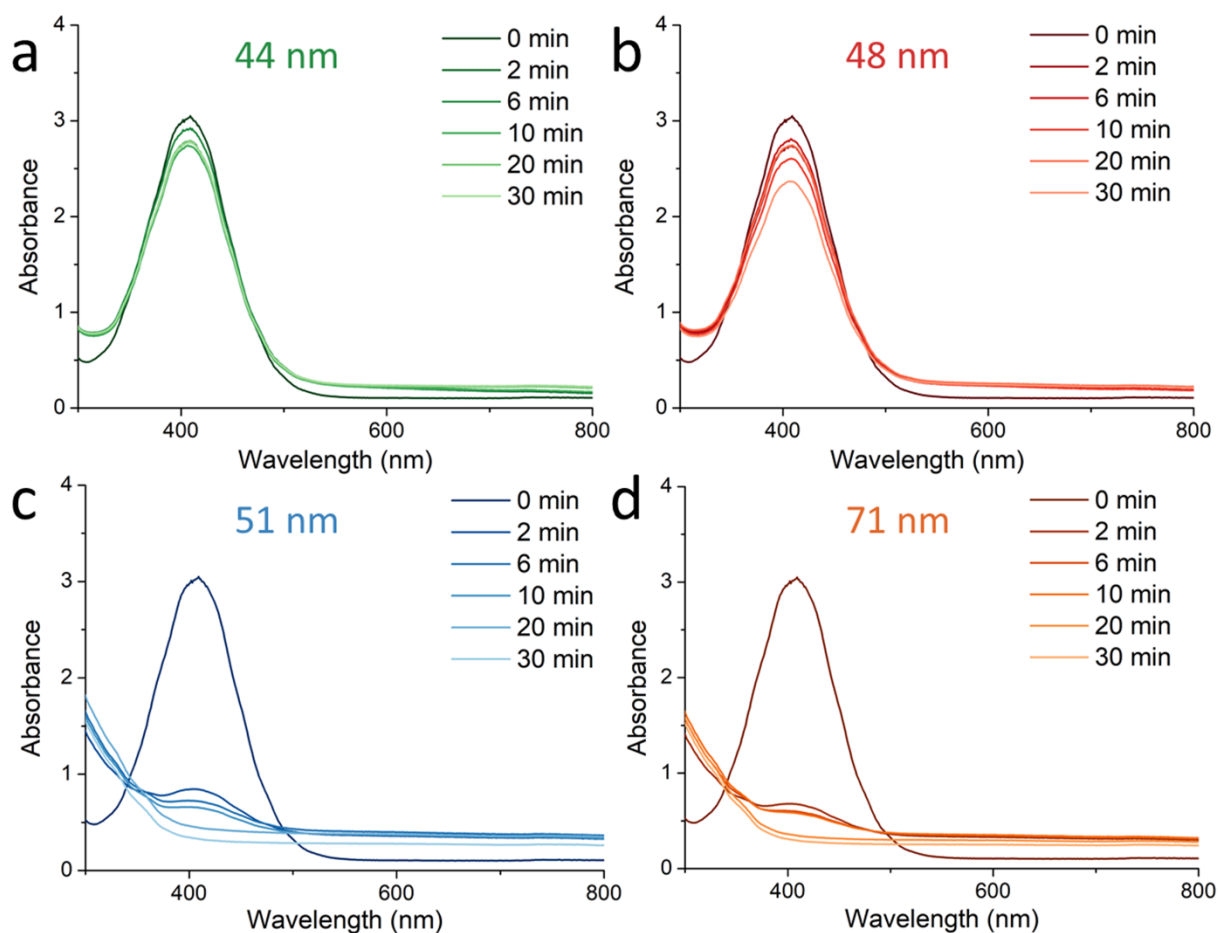


Figure 5.3.2.3 Absorption spectra during the reduction of 4-NTP at different reaction time on plasmonic porous ceramics functionalized with differently sized Au@Pt nanoparticles: (a) 44 nm; (b) 48 nm; (c) 51 nm; (d) 71 nm. Adapted with permission from [2]. Copyright (2023), Wiley.

Figure 5.3.2.4 shows the absorption spectra of the reduction of 4-NTP using Au nanoparticle functionalized sample as substrate at the initial point and after 30 min reaction time. After 30 min reaction time, the spectrum of the reactant 4-NTP was not significantly changed, which demonstrates that the bare Au-NPs do not show catalytic activity.

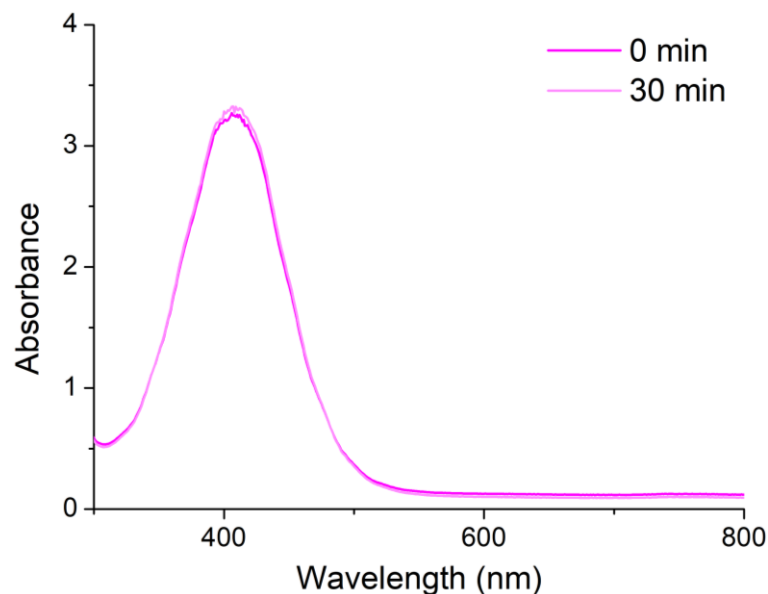


Figure 5.3.2.4 Absorption spectra of 4-NTP reduction catalyzed with 39 nm Au NP functionalized porous ZTA sample at initial time and after 30 min reaction time. Adapted with permission from [2]. Copyright (2023), Wiley.

5.3.3 Comparing porous and dense ceramic substrates

Similar to the results with Ag nanoparticles in Chapter 4.3.4, higher Raman EFs of the porous ceramic substrates functionalized with the core-shell nanoparticles were detected, comparing to dense substrates. Figure 5.3.3.1 (a) illustrates the remarkably higher Raman intensity provided by the porous structure, where Raman spectra of pyridine on both porous (red) and dense (grey) substrates both functionalized with identical core-shell particles are compared. The dense substrate had the same chemical composition and a similar nanoparticle surface coverage as the open porous ceramic substrate. Result here indicates that the porous sample provided approximately 7 times higher EF than the dense sample. Additionally, a nearly 10-fold increase in Raman EF was observed when using 4-NTP as probe molecule.

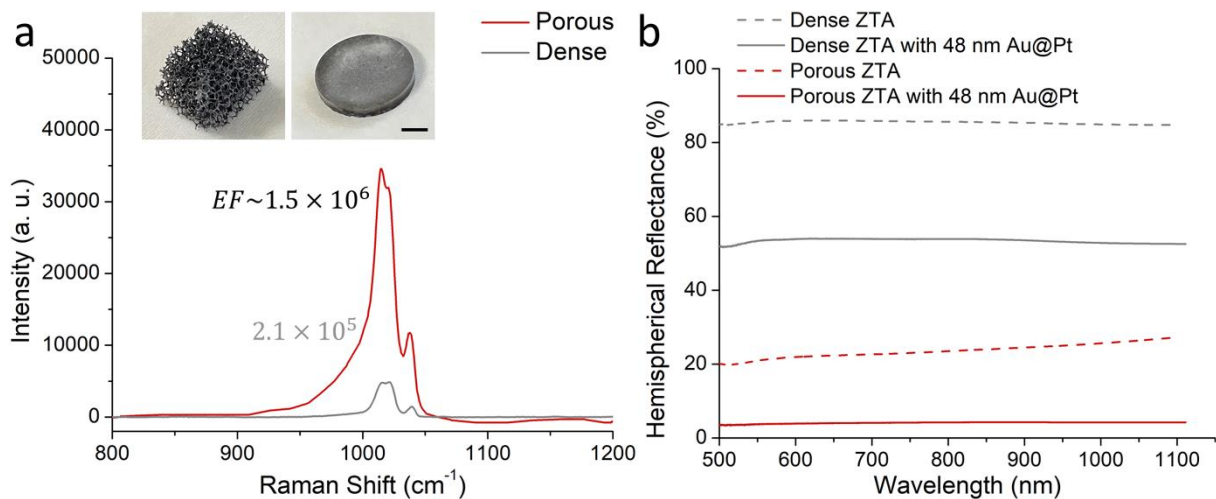


Figure 5.3.3.1 (a) Raman spectra of pyridine on plasmonic porous (red) and dense substrate (grey) functionalized with 48 nm Au@Pt nanoparticles. Inset photos illustrate the porous and dense substrate respectively, scale bar equals 5 mm; (b) Reflectance spectra of ZTA (dashed) and 48 nm Au@Pt nanoparticles functionalized ZTA ceramics (line) in dense and porous form respectively. Adapted with permission from [2]. Copyright (2023), Wiley.

In Figure 5.3.3.1 (b), the hemispherical reflectance of bare ZTA (dashed spectra) and 48 nm Au@Pt nanoparticles functionalized ZTA (line spectra) are demonstrated for both dense (grey) and porous (red) samples. The bright bare ZTA sample exhibited impressive reflectance properties between 20-30 % in the integrating sphere at wavelengths above 500 nm. The remaining light was either absorbed by the ceramic matrix, transmitted through the porous structure, or reflected towards the sides. By contrast, the total reflectivity of a bare dense ZTA pellet was around 85 %. It is worth noting that the bare porous ZTA sample showed growing reflectance as wavelength increased, which could be attributed to the behavior of light propagation inside the semi-transparent ceramic porous matrix. The phenomenon has been modeled by Li *et al.* using Monte Carlo ray tracing radiative transfer analysis of an alumina open-cell foam [99].

Functionalizing the open-cell porous ceramic foam with 48 nm sized Au@Pt nanoparticles resulted in a remarkable reduction in reflectance of approximately 80 %. The reflectance was around below 5 % over the entire measured wavelength range, which included the 633 nm wavelength of the incident laser during the SERS measurements. In comparison, the reflectivity of the dense pellet was reduced by only 40 %, indicating that the deposited nanoparticles effectively absorbed the previously reflected light within the ZTA porous structure. It is worth noting that the reflectivity spectra of the 48 nm sized Au@Pt nanoparticles functionalized sample did not exhibit any obvious feature at 529 nm, as these sized core-shell particles showed intensity peak on the adsorption spectrum (Figure 5.3.4 (b red spectrum)). This could suggest that the absorption spectra of the deposited core-shell nanoparticles on the

functionalized sample surface were broadened compared to the corresponding nanoparticle dispersions discussed above.

Likewise, the catalytic activity of dense ZTA pellets was compared to the porous substrates, which is shown in Figure S5, SI for ceramics functionalized with 48 nm Au@Pt NPs. During the first 20 min, the absorption spectra of 4-NTP catalyzed with the dense substrate overlapped, with hardly a change in reactant concentration. After 30 min, the absorption intensity of the reaction 4-NTP was decreased by 5.9 %, while it decreased by 22.5 % for the porous substrate. Accordingly, the functionalized porous substrate showed better catalytic activity, which agreed with our expectation, since the porous ceramic offered higher specific surface area for deposition of the core-shell particles.

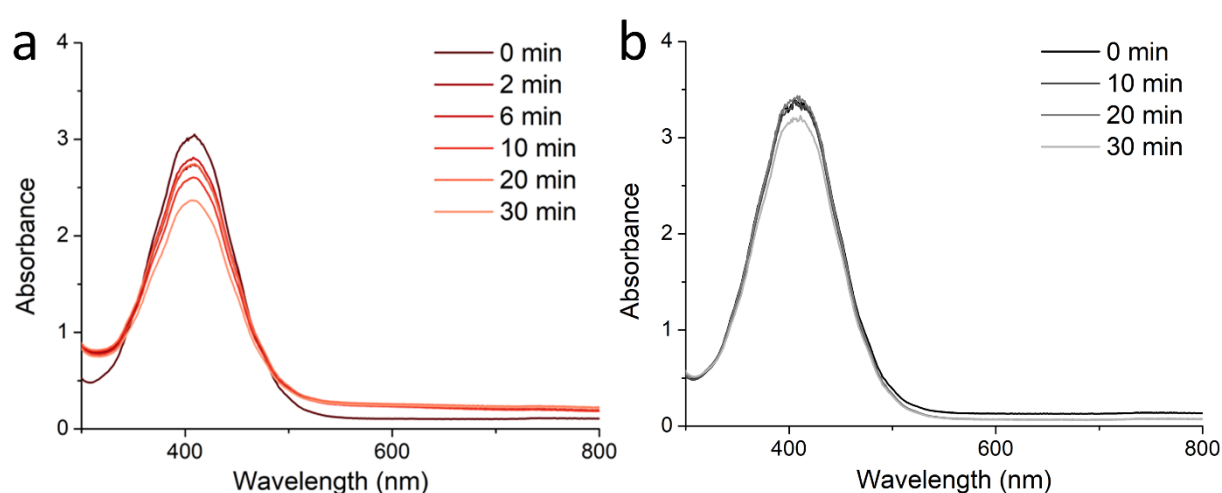


Figure 5.3.3.2 Absorption spectra of 4-NTP reduction reaction catalyzed with porous (a) and dense (b) substrate respectively, both functionalized with 48 nm Au@Pt nanoparticles. Adapted with permission from [2]. Copyright (2023), Wiley.

5.3.4 *In situ* reaction monitoring via SERS

Once the SERS enhancement and catalytic activity of the plasmonic porous ceramics have been examined, they can be combined for *in situ* reaction monitoring through SERS. Figure 5.3.4.1 illustrates the *in situ* reaction monitoring at various reaction time spots, utilizing plasmonic porous ceramic functionalized with 48 nm sized Au@Pt nanoparticles as a representative case.

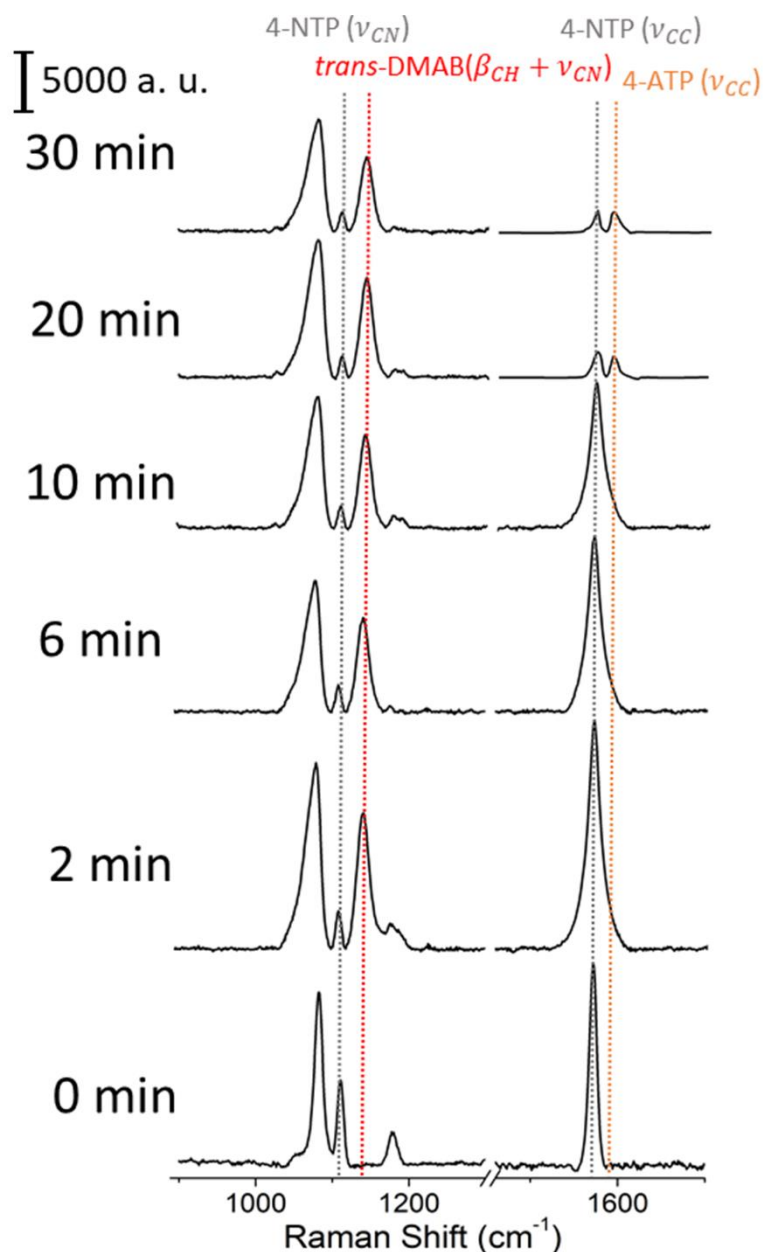


Figure 5.3.4.1 *In situ* reaction monitoring via SERS of the reduction of 4-NTP using the plasmonic porous ceramic functionalized with 48 nm sized Au@Pt NPs. Adapted with permission from [2]. Copyright (2023), Wiley.

The Raman shifts at 1108 and 1572 cm^{-1} (indicated by the grey dashed line) can be assigned with C-N stretching and phenyl-ring C-C stretching of the reactant 4-NTP, respectively, which could be observed on the spectrum at $t = 0 \text{ min}$. After 2 min of reaction, the appearance of the Raman peak at 1142 cm^{-1} suggested the formation of the reaction intermediate *trans*-DMAB (highlighted by the red dashed line). Moreover, the relative Raman intensity of the peak at 1108 cm^{-1} reduced significantly compared to that observed at $t = 0 \text{ min}$, indicating the decreased concentration of 4-NTP due to reduction reaction. At $t = 20 \text{ min}$, a new peak emerges at 1595 cm^{-1} , which can be attributed to the phenyl-ring C-C stretching of the reaction product 4-ATP (indicated by the orange dashed line). Thus, after 30 min, the simultaneous

decrease and increase in Raman intensity at 1572 and 1595 cm^{-1} respectively, can be interpreted as the decrease of 4-NTP concentration and increase of 4-ATP concentration, implying the reduction of 4-NTP to 4-ATP. The kinetics associated with the reaction can be further investigated by determining the differential Raman cross-section of the corresponding vibrational modes.

5.4 conclusions

This chapter involved the processing and analysis of the plasmonic porous ceramics functionalized with metallic core-shell nanoparticles using Au-seed mediated method and colloidal deposition. The substrates coated with Au@Pd nanoparticles demonstrated Raman EFs of around 10^4 , whereas the ones deposited with Au@Pt nanoparticles exhibited EFs up to 10^6 . The Raman enhancement effect of these substrates could be modulated by adjusting the Pd / Pt shell thickness through the amount of the corresponding metal salt precursors. As the Pd / Pt shell became thicker, the Raman EFs increased, owing to the dominant nature of the damped plasmon oscillations in the Pd / Pt shell. In contrast, the catalytic activity of the substrate improved as the Pd / Pt shell thickness increased, due to the higher surface area of the catalytically active Pd / Pt shell.

Meanwhile, the open-cell foam structure of the plasmonic porous ceramics offers easy access to the functionalized surface, which enables its potential use in complex 3D configurations and measuring in all direction. Additionally, the core-shell nanoparticles functionalized plasmonic porous ceramics demonstrated notably higher EFs compared to similar dense pellets, attributable to the efficient absorption and scattering of light within the porous ceramic structure.

As a result, the multifunctional plasmonic porous ceramics demonstrated in this chapter can be utilized for catalytic reaction monitoring via SERS. With Raman EFs reaching up to 10^6 , this approach enables high sensitivity through electromagnetic and chemical enhancement. Moreover, a high chemical septicity through detecting Raman active vibrational modes of each single molecule during the reaction can be realized.

6. Plasmonic porous ceramics for biomedical applications

Chapter 6 has been adapted with permission from *Wiley* and is published in the *Journal Advanced Engineering Materials*, 2023, DOI: 10.1002/adem.202300942

Besides application in *in situ* reaction monitoring described in Chapter 5, the application of plasmonic porous ceramics was explored with a focus on biomedical aspects. 45S5 Bioglass is one of the most widely investigated bioactive glass materials for bone substitute, which is capable of soft tissue bonding via collagen [147]. For biomedical applications, not only the composition of the bioactive glass, but also its structure matters. Bone implants are usually designed to be porous to offer a scaffold for vascularization and bone ingrowth [143,144]. Typical analysis methods of the synthetic bone substitute material are *in vitro* cell studies or *in vivo* using animal models [336–338]. Raman spectroscopy is one important method for medical research to detect the reactions and processes at the bone implant interface, since classical medical imaging methods only contain visual information. To enhance the weak Raman signal in biological conditions, SERS can be employed.

Porous bone replacement materials that enable surface-enhanced Raman scattering (SERS) have great potential for real-time non-destructive sensing of the chemical environment and tissue integration of the implant [336–338]. Besides SERS biosensing based on the plasmonic activity, including, for example, near-infrared (NIR) absorbing Au nanoparticles as sensing agents for cancer therapy [339]. Furthermore, Au nanoparticles are used as theranostic drug delivery carriers, for example in the form of colloidal capsules, that combine sensing with targeted drug delivery and other functional properties [340–343].

To achieve strong Raman resonance in the NIR, the Raman-active material usually needs to be specifically tailored to enhance the limited SERS signal in the biological environment. For example, Graham et al. investigated surface-enhanced resonance Raman scattering (SERRS) for application as a clinical tool, which offers equivalent detection limits to fluorescence labelled dyes with maximum tissue penetration depth of around 5 mm [344–347].

However, current research on bioceramics featuring SERS is limited. Related strategies that incorporate sensing into biomaterials are more strongly developed in the context of soft tissue engineering with polymers and related materials. For example, a hybrid biocompatible material consisting of an electrospun polymeric matrix and porous calcium carbonate coatings was reported as an effective substrate for SERS [348,349]. Graphene oxide/copper nanocomposite-decorated polylactide-co-glycolide / β -tricalcium phosphate scaffolds were presented for reconstruction of bacteria-contaminated bone defects, where the Graphene oxide/copper nanocomposite layer was responsible for the SERS effect [350]. Combinations

of plasmonic metallic nanoparticles with bioceramics were mostly reported for their photothermal effect [351,352].

The degradation of bioceramics during osseointegration must be taken into consideration as well, which could affect the performance of functionalized bioceramics significantly. In this context, Bioglass has been well established due to its high bioactivity and resorbability. When bioactive glass is placed in aqueous biological media, ion exchange between the bioactive glass and the biological media takes place, leading to glass network dissolution, which is followed by the formation of hydroxy carbonate apatite (HCA) on the Bioglass surface [148]. For instance, a 3D-printed bioactive glass scaffold doped with NIR-II (1000-1700 nm) ratiometric lanthanide-dye hybrid nanoprobe was presented as substrate for *in vivo* imaging, featuring *in situ* monitoring of implant degradation during mouse skull repair [353], or the degradation of Sm³⁺-doped bioactive glass fibers were investigated in simulated body fluid, where the degradation process was monitored by the luminescence sensing method [354].

In this chapter, the plasmonic porous ceramics concept introduced in Chapter 4 was adapted for biological use with established bioceramics. To this end, porous Bioglass was prepared and compared to the hydroxyapatite-based commercial product Bio-Oss[®], which is derived from cow bone, as well as the previously investigated ZTA open cell foam, which in this context is a bioinert ceramic. All these materials were functionalized with Au nanoparticles and the ability of the substrates to detect molecules was analyzed via SERS. For Bioglass, substrates with different pore sizes and comparable dense pellets were tested, as well. To assess the feasibility of this approach in the biological context, the molecule detection capability of the plasmonic bioceramics was investigated in the presence of the biological media fetal bovine serum (FBS) and simulated body fluid (SBF), including long-time studies that follow the degradation of the sensing properties during extended immersion in SBF.

6.1 Materials

Nitric acid (ACS reagent 70 %, product no. 438073), tetraethyl orthosilicate (TEOS, reagent grade 98 %, product no. 131903), triethyl phosphate (ReagentPlus 99.8 %, product no. 538728), calcium nitrate tetrahydrate (ACS reagent 99 %, product no. 237124), sodium nitrate (ACS reagent 99 %, product no. 221341), ethanol (absolute, 99.8 %, product no. 32205), poly(vinyl alcohol) (PVA, Mw 31,000-50,000, product no. 254169), hydrochloric acid (p. a., ACS reagent, 37 %, product no. 30721), aluminium chloride (reagent grade 98 %, product no. 206911), potassium chloride (p. a., 99.5-100%, product no. 31248), Trizma base (TRIS, BioXtra, 99.9 %, product no. T6791), pyridine (analytical standard, product no. 02486) and fetal bovine serum (FBS, product no. F9665) were acquired from Sigma Aldrich, Germany. Sodium bicarbonate (NaHCO₃, p. a., 99.5 %) was obtained from Honeywell Specialty Chemicals Seelze, Germany. Dipotassium phosphate (K₂PO₄·3H₂O, 99 %, product no.

12030250) was purchased from Grüssing GmbH, Germany. Magnesium chloride hexahydrate ($\text{MgCl}_2 \cdot 6\text{H}_2\text{O}$, p. a., ACS, 90 %) was obtained from Carl Roth, Germany. Bio-Oss[®] was acquired from Geistlich Pharma AG, Switzerland.

6.2 Methods

Porous ZTA ceramics were synthesized according to the process described in section 4.2. The synthesis of 45S5 Bioglass powder via sol-gel method and the porous Bioglass substrates, as well as the deposition process of the Au nanoparticles on Bioglass, Bio-Oss[®] and ZTA surface will be described in the following sections.

6.2.1 Synthesis of 45S5 Bioglass powder

The synthesis of 45S5 Bioglass powder via sol-gel method followed the protocol from Bahniuk *et al.* with adjusted amount of the chemicals [153]. For production of 20 g Bioglass powder, 33.92 ml tetraethyl orthosilicate was added in 50.44 ml 1M nitric acid solution, mixed and stirred with a magnetic stirrer at room temperature. After 15 min of stirring, 2.9 ml triethyl phosphate, 20.13 g calcium nitrate tetrahydrate and 13.52 g sodium nitrate were added to the mixture respectively. The mixing was continued for another 45 min. The sol was poured into a sealable polyethylene (PE) bottle and stored at room temperature for 5 days for gel formation. Subsequently, the gel was transferred into a glass breaker to dry at 70 °C for 24 h, at 120 °C for another 24 h and at 700 °C for another 24 h in an alumina crucible in furnace (Nabertherm L3/11/S27, Nabertherm GmbH, Germany). The calcinated sample was ball milled in a closed PE bottle with alumina balls (1:2 powder-to-ball weight ratio) and ethanol (1.2.5 powder-to-ethanol weight ratio) for 2 days. Afterwards, the powder was dried at 70 °C and stored at room temperature until it was used.

6.2.2 Synthesis of porous and dense Bioglass substrates

The porous Bioglass substrate processing is demonstrated in Figure 6.2.2.1. 100 g Bioglass slurry consists of 40 g Bioglass powder and 60 g 2 wt. % poly (vinyl alcohol) solution. After 30 min mixing at 1000 rpm, the slurry was ready for PU foam impregnation. Excess slurry was squeezed out manually. The with slurry coated PU foams were dried for 24 h at room temperature and again coated with a 30 wt. % Bioglass powder slurry. During the recoating process, the blocked pores were carefully blown with compressed air. Afterwards, the with slurry recoated PU foams were dried for another 24 h and sintered. By sintering, the temperature was heated with a rate of 1 °C/min from room temperature to 110 °C and held for

2 h, continuously to 250 °C and held for 3 h, to 400 °C and held for 3 h, to 600 °C and held for 3 h, finally to 1050 °C and held for 3 h. After the sintering, the temperature was cooled to room temperature with a rate of 1 °C/min.

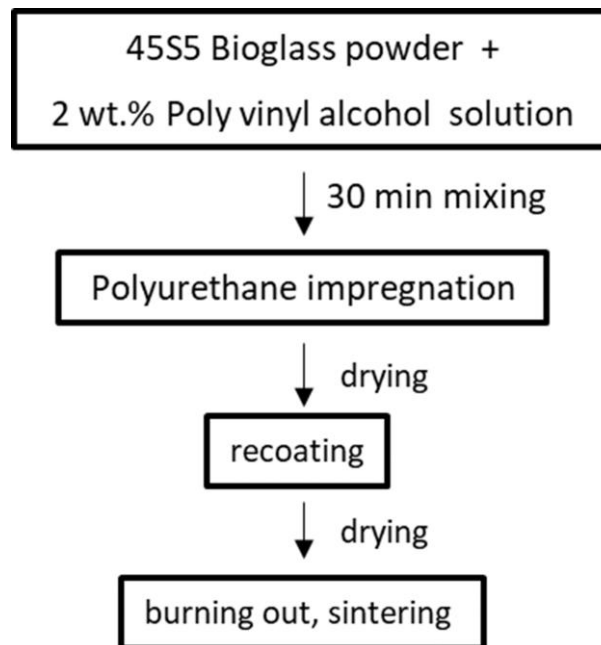


Figure 6.2.2.1 Flowchart of processing porous Bioglass via replica method with recoating. Adapted with permission from [3]. Copyright (2023), Wiley.

The dense Bioglass pellet was produced the similar way as ZTA dense pellet described in Chapter 4.2.2. Only the Bioglass pellets were produced with 1.2 g powder of each.

6.2.3 Deposition of Au nanoparticles

The deposition of Au nanoparticles on Bioglass and Bio-Oss[®] surface was realized through simple colloidal deposition. As pre-treatment, the Bioglass sample was submerged in 7.5 ml 2 mM AlCl₃ solution for 1 min, flushed with DI water and dried. In a 50 ml two-neck round flask, 25 ml 2 mM HAuCl₄ was added to 20 ml DI water, stirred and heated to 98 °C. 5 ml 10 mM TSC solution was added to the reaction solution, and heated to boiling point until colour changed to ruby red. The synthesized Au nanoparticle colloidal was cooled to room temperature and subsequently put in ultrasonic bath for 1 h. The porous Bioglass samples was hung and submerged in the Au nanoparticle colloidal under stirring for 30 s.

The Au nanoparticle deposition on Bio-Oss[®] surface was achieved without AlCl₃ pre-treatment and the submerging time was 2.5 min. After the submersion, the Bioglass and Bio-Oss[®] samples were dried and stored in an evacuated desiccator.

The deposition of Au nanoparticle on ZTA surface was similar to the reduction process described in Chapter 4.2.4. In short, the ZTA substrate was hung in a two-neck round flask and submerged in 25 ml 2 mM TSC solution. The reaction mixture was stirred and heated in a water bath to 90 °C, 25 ml 2 mM H₂AuCl₄ was added. After the temperature reached the boiling point and the colour changed, the ZTA substrate was kept in the reaction mixture for 20 min under stirring, taken out, dried and stored in an evacuated desiccator.

6.2.4 Characterization

The processed Bioglass and Bio-Oss[®] samples were analyzed with μ -CT measurements using a Xradia 520 Versa device (ZEISS, Germany) with detailed parameters and data processing procedures listed in Chapter 4.2.5.

SEM measurements were conducted using the same method and identical instrument as described in Chapter 4.2.6.

Raman spectra in air were collected as described in Chapter 4.2.7. Raman spectra in the presence of biological media were recorded as such: a droplet of the diluted pyridine was dropped on the sample surface. Subsequently, the sample was placed submerged in the respective biological media for measurement with Raman spectroscopy. Nine different spots on at least three samples of each material under each experimental condition were examined.

Simulated body fluid was prepared according to ISO standards and used for incubating the ceramics at 37 °C. During the incubation, the SBF was changed three times weekly to maintain the initial pH value. After incubation, the ceramics were removed from the SBF, dried at 70 °C for 48 h, and stored in an evacuated desiccator for further analysis.

6.3 Results and discussion

6.3.1 Ceramic substrate characterisation

The synthesized porous Bioglass substrates and Bio-Oss[®] were analysed via μ CT 3D reconstruction method. The images were shown in Figure 6.3.1.1.

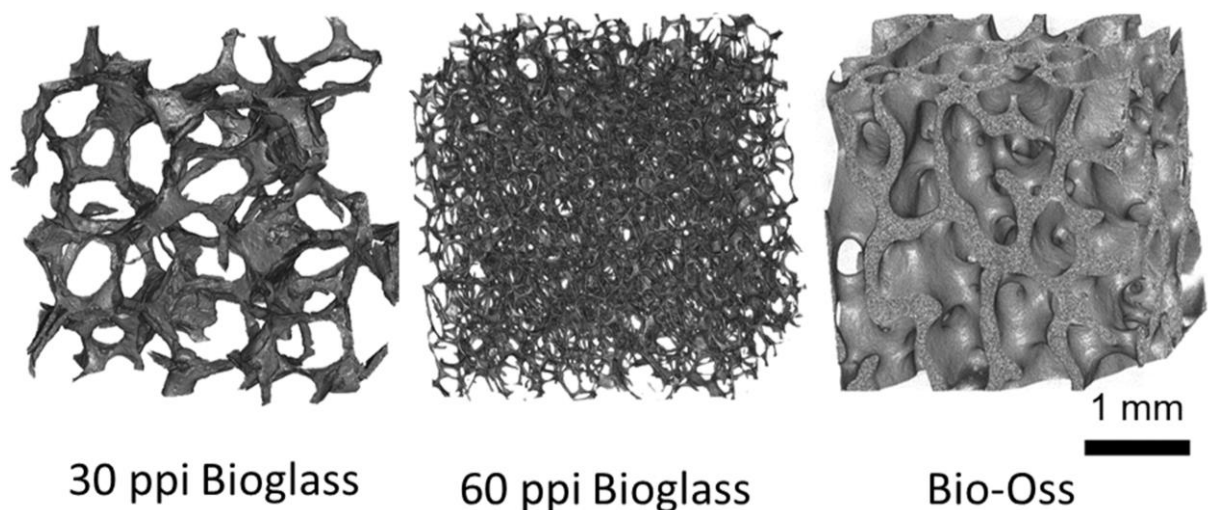


Figure 6.3.1.1 μ CT 3D reconstruction images of the synthesized 30 ppi, 60 ppi Bioglass and commercial product Bio-Oss[®] respectively. Adapted with permission from [3]. Copyright (2023), Wiley.

The CT models of the 30 ppi Bioglass substrate is visually similar to the 30 ppi ZTA substrate (Chapter 4.3.1). However, the 60 ppi Bioglass substrate has a finer network with thinner struts, which differs from the 60 ppi ZTA substrate. The parameters of the ceramics were listed in Table 6.3.1.1. In general, the porosity and pore size of the Bioglass substrates are higher than comparable ZTA samples, especially for the 60 ppi substrates, which is a surprise since all the porous ceramics were prepared with the identical PU foam as templates. Porous Bioglass has a porosity of 94 % using 30 ppi PU foam as template and a porosity of 93 % using 60 ppi as template. While, porous ZTA shows a porosity of 91 % and 76 % respectively. Bio-Oss[®] has the minimum porosity of 62 %. Nonetheless, this difference might be caused due to the shrinkage of the ceramic during the sintering. The shrinkage of porous and dense ZTA substrates is similar. While the shrinkage of the porous Bioglass reached 71.1 %, which is significantly higher than that of the porous ZTA with a shrinkage of 38 %. This high shrinkage of porous Bioglass can be explained by the remarkably increased viscous flowing of the Bioglass at high temperature [145]. The high shrinkage of the porous Bioglass substrate indicates an extremely high densification degree of the struts caused by viscous flowing. While in the case of porous ZTA, a hollow core remains in the strut after the polymer foam is burned out [355].

Investigating the parameters in Table 6.3.1.1, all porous samples fit in the required structure parameter range for a synthetic bone substitute. The porous Bioglass substrates with a porosity above 90 % are in the upper region as synthetic bone substitute. Among them, 60 ppi porous Bioglass shows the optimal architecture to serve as a bone substitute. For actual application, finer pore size might be more beneficial, considering the 60 ppi Bioglass with an

average pore size of 0.37 mm. Although, it is worth noticing, that the μ CT had a resolution of 6 μ m during the measurement. So that smaller pore cannot be detected and hence, can not be calculated for the mean pore size.

Table 6.3.1.1 Parameters of the synthesized Bioglass, commercial Bio-Oss[®] and ZTA ceramics. Adapted with permission from [3]. Copyright (2023), Wiley.

Material	Structure	Porosity (%)	Pore size (mm)	Specific surface area (mm ⁻¹)	Shrinkage (%)
Bioglass	30 ppi	94.2	0.83	2.28	71.1±4.7
	60 ppi	92.9	0.37	6.07	
	Dense pellet	/	/	/	14.9±1.9
Bio-Oss [®]	/	62.16	0.57	5.42	/
ZTA	30 ppi	91.02	0.51	5.37	38.0±1.8
	60 ppi	76.28	0.24	9.41	
	Dense pellet	/	/	/	43.8±1.0

6.3.2 Functionalization of bioceramics with plasmonic nanoparticles

The Au nanoparticles were deposited on the ZTA substrate surface through chemical reduction of gold ions on the ceramic surface via heterogeneous nucleation. While, deposition of Au nanoparticles on the Bioglass and Bio-Oss[®] surface was realized through colloidal deposition. Figure 6.3.2.1 shows the SEM-BSE images of the 60 ppi porous Bioglass, Bio-Oss[®] and 60 ppi ZTA surface before and after Au nanoparticle deposition respectively. The insert photo indicates the respective 60 ppi Bioglass sample with a scale bar of 50 mm. In Figure 6.3.2.1 (b, d and f), the tiny bright dots are the deposited Au nanoparticles. Comparing the three with Au nanoparticles functionalized samples, the Bio-Oss[®] sample has a higher nanoparticle coverage and more large agglomerates of nanoparticles. As discussed before, small agglomerates like dimer and trimer are beneficial for the Raman enhancement effect as hotspots are generated which results in exponentially increased enhancement effect. Such hotspots can be observed on the functionalized Bioglass and ZTA sample surface. However, when the size of the nanoparticle agglomerates increases to comparable to the wavelength of visible light, the plasmonic- and SERS-activity disappears, since the plasmons are not localized anymore and can propagate in all directions [356].

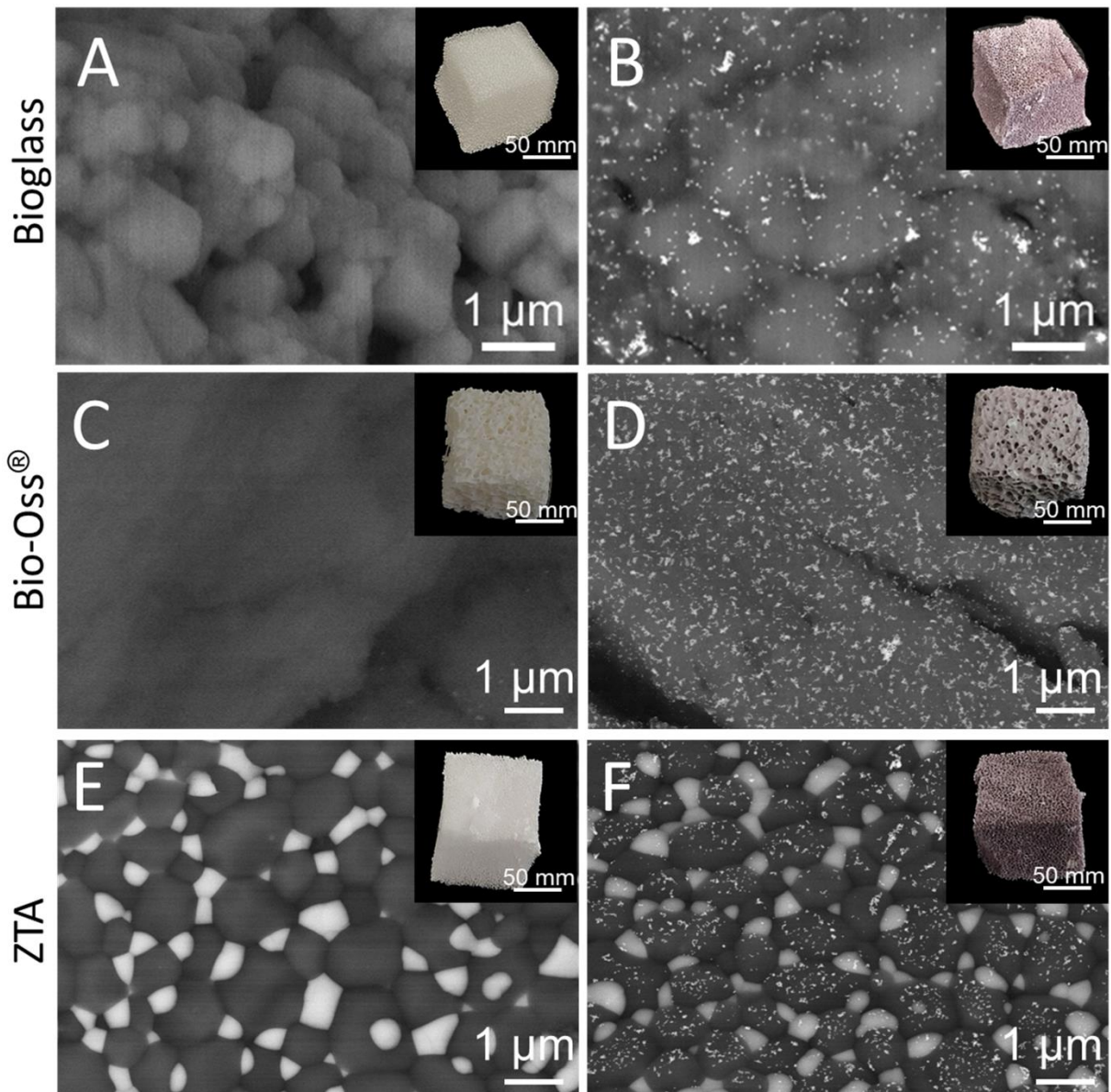


Figure 6.3.2.1 SEM-BSE images of 60 ppi porous Bioglass surface before (a) and after (b) Au nanoparticle deposition, with insert photo showing the corresponded sample. SEM-BSE images of Bio-Oss[®] surface before (c) and after (d) Au nanoparticle deposition, and 60 ppi porous ZTA surface before (e) and after (f) Au nanoparticle deposition. Adapted with permission from [3]. Copyright (2023), Wiley.

Raman spectra of the 60 ppi porous Bioglass before and after Au nanoparticle coating measured in air, in FBS and in SBF were illustrated in Figure 6.3.2.2 respectively. The spectra of Bioglass showed three main intensity peaks at 588, 966 and 989 cm^{-1} . The Raman shifts at 588 and 989 cm^{-1} can be associated with the stretching and rocking of the non-bonding silicon-oxygen bonds of the silica, while the peak at 966 cm^{-1} can be attributed to the phosphate groups in the bioactive glass [357,358]. Since the exact position of the silica Raman shift depends on the crystallization of the glass, the peak at 588 cm^{-1} indicates a partial crystallization of the Bioglass [359]. After the Au nanoparticle deposition on Bioglass surface, the Raman intensity was slightly enhanced (Figure 6.3.2.2 (b)). When measured in biological

media FBS and SBF, the intensities of Bioglass were significantly decreased. Meanwhile, there were more noises on the spectra, which originated from the contents in the biological media.

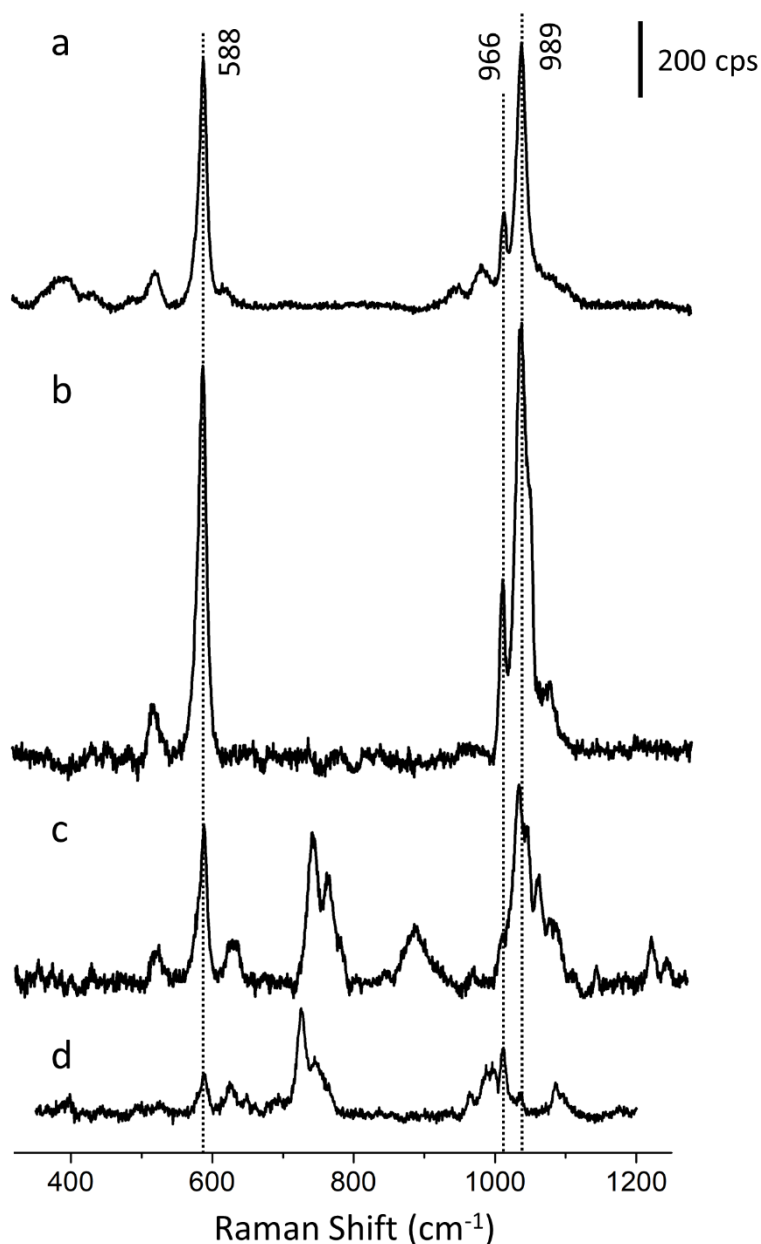


Figure 6.3.2.2 Raman spectra of 60 ppi porous Bioglass substrate before (a) and after Au nanoparticle deposition (b) measured in air, measured in FBS (c) and measured in SBF (d). Adapted with permission from [3]. Copyright (2023), Wiley.

The Bio-Oss® individual Raman spectrum (Figure 6.3.2.3 (a)) illustrates one main shift at 962 cm^{-1} and two weak peaks at 430 and 590 cm^{-1} , which can be related to the phosphate ions in the deproteinated bovine bone [360]. The porous ZTA substrate presented two main Raman shifts at 417 and 638 cm^{-1} , which correspond to alumina [361]. Similar to the Bioglass sample, Bio-Oss® and ZTA substrates showed slightly enhanced Raman intensity after the Au nanoparticle deposition, which should come from the backscattered signal right at the touching

point between the deposited Au nanoparticle and the ceramic surface, contributing enhanced Raman signal to the detector. The Raman spectra of the ceramic substrates themselves were considered as background spectra.

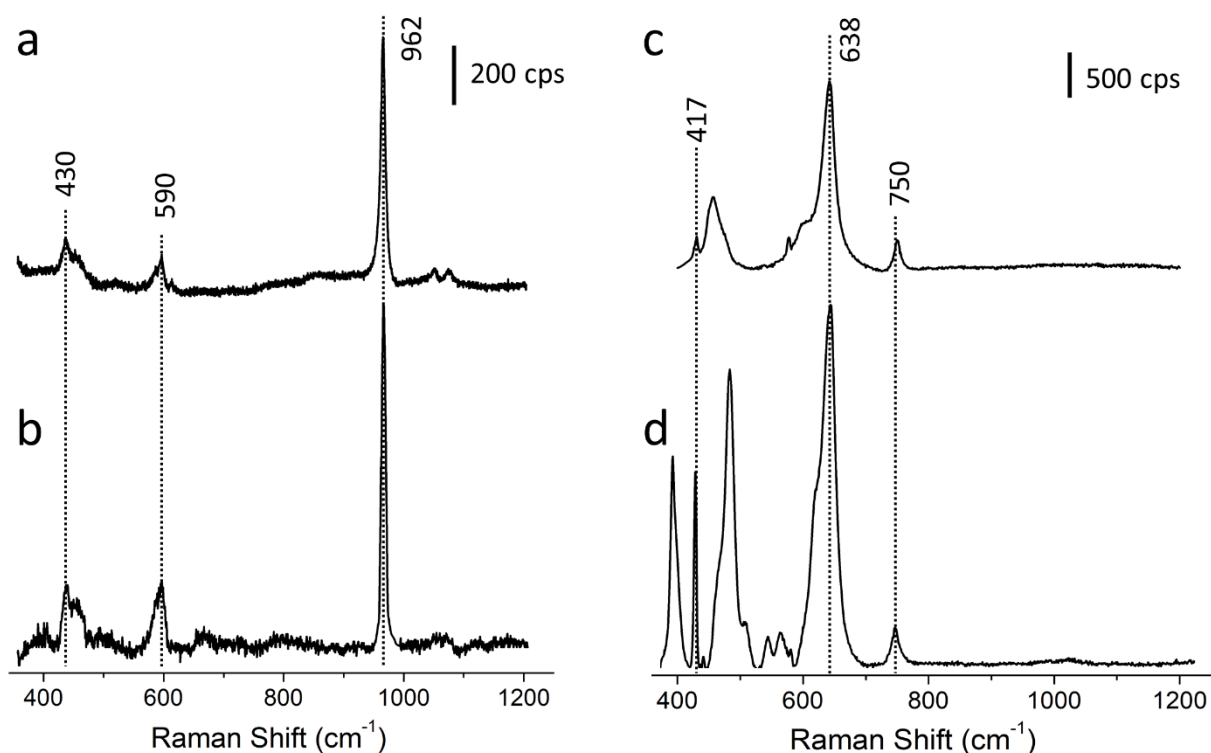


Figure 6.3.2.3 Raman spectra of Bio-Oss® substrate before (a) and after Au nanoparticle deposition (b), 60 ppi porous ZTA before (c) and after Au nanoparticle deposition (d) measured in air. Adapted with permission from [3]. Copyright (2023), Wiley.

The Raman enhancement ability of the substrates was analysed via SERS experiments with diluted pyridine (10^{-2} M) was reporter molecule. Figure 6.3.2.4 shows the Raman spectra of pyridine adsorbed on plasmonic Bioglass, Bio-Oss® and ZTA respectively. The observed two main Raman shifts at 1012 and 1036 cm^{-1} can be assigned to the ring breathing mode (ν_1) and the symmetric ring deformation (ν_{12}) of pyridine adsorbed on Au [328]. The intensity peak at 1012 cm^{-1} was used for Raman EF calculation.

Figure 6.3.2.4 (a) shows the Raman spectra of pyridine adsorbed on plasmonic 30 ppi, 60 ppi and dense pellet Bioglass substrates respectively. The dense pellet Bioglass presented slightly higher intensity. Nevertheless, all Bioglass substrates showed Raman EFs in the same order of magnitude (10^4), namely, from $3 \cdot 10^4$ to $5.6 \cdot 10^4$. In comparison to Bioglass and ZTA, Bio-Oss® performed the lowest Raman intensity. Furthermore, it is worth noticing that the Bio-Oss® background spectrum was more emphasized than that of the Bioglass and ZTA samples. Since the Raman intensity of the probe molecule was significantly enhanced, the background spectra

of Bioglass and ZTA substrates were too weak to be observed. Meanwhile, this indicates that the Raman intensity of the probe molecule is remarkably enhanced due to adsorption on the Au nanoparticle surface, while, the background spectra of the ceramics is only very slightly / barely enhanced. Raman spectra of different ZTA substrates were demonstrated in Figure 6.3.2.4 (c). The 30 ppi ZTA substrate showed the highest Raman intensity of the pyridine characteristic peaks. While, the dense pellet ZTA illustrated a significantly reduced Raman intensity. The Raman EFs of the Bioglass and ZTA substrates with different pore sizes were summarized in Figure 6.3.2.4 (d). The 30 ppi porous ZTA with an average pore size of 0.51 mm presented the highest Raman EF of $8.3 \cdot 10^5$. The 60 ppi porous sample with an average pore size of 0.24 mm showed a reduced EF of $2.4 \cdot 10^5$. While, the dense pellet ZTA showed a limited EF of $4.9 \cdot 10^4$. The porous ZTA samples reached at least 5 times higher EFs than the dense pellet. Meanwhile, the ZTA substrates showed an obvious trend that the Raman EFs decreased with the reducing pore size of porous ZTA ceramics. This result corresponds to the earlier findings of the Ag nanoparticles functionalized ZTA samples and metallic core-shell Au@Pt nanoparticles functionalized ZTA samples in Chapter 4 and 5 namely. However, the EFs of Bioglass substrates were pretty similar, regardless of the substrate pore size. Bioglass and ZTA have different refractive index, which might cause the different scattering behavior. The refractive index of Bioglass is reported between 1.54 to 1.59, while alumina has a higher refractive index around 1.77 to 1.86 [56,161,362]. Moreover, the fraction of yttria-stabilized zirconia increases the refractive index of the ZTA sample [363]. The difference in refractive index between Bioglass and ZTA substrates could lead to changed scattering behavior within the porous structure. Additionally, different grain sizes and interfacial roughness will affect the scattering behavior of the sample as well.

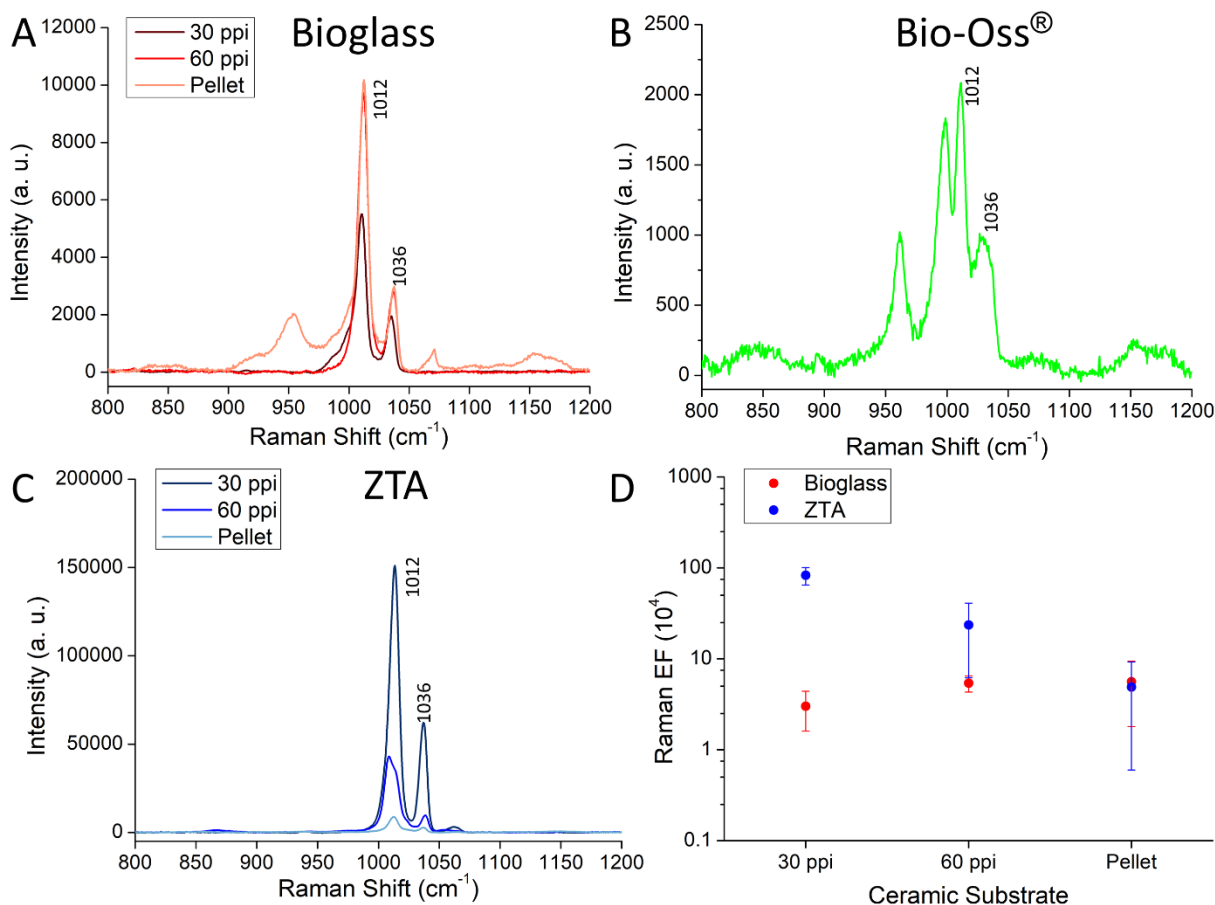


Figure 6.3.2.4 Raman spectra of pyridine adsorbed on Au-nanoparticle coated Bioglass (a), Bio-Oss[®] (b), and ZTA (c) respectively and summarized Raman enhancement factors of Bioglass and ZTA substrates with different pore sizes (d). Adapted with permission from [3]. Copyright (2023), Wiley.

6.3.3 Raman enhancement of porous Bioglass under simulated biological conditions

Based on the structure parameters of the 60 ppi porous Bioglass, this substrate is well suited as bone substitute as is well established in the literature [143,154–158,160]. Therefore, the plasmonic porous Bioglass in this work refers to the 60 ppi porous Bioglass substrate functionalized with Au nanoparticles from hereon. To test the feasibility of the plasmonic porous Bioglass for real-time molecule detection via SERS in biomedical applications, SERS measurements were conducted in simulated physiological conditions, namely in the presence of biological media, in FBS and in SBF. Figure 6.3.3.1 shows the Raman spectra of the pyridine on plasmonic porous Bioglass measured in air (red), in the presence of FBS (orange) and SBF (purple). When measured in air, the substrate reached the highest Raman EF up to $5.4 \cdot 10^4$. The EF showed a significant reduce to $1.9 \cdot 10^4$ and $1.6 \cdot 10^4$, when measured in FBS and SBF respectively. It is worth noticing that there were no obvious additional Raman shifts on the spectra in the presence of the biological media, although there were abundant proteins and

ions in the biological media. Regardless the remarkable decrease of the EF in biological media, selective and highly sensitive analysis of the probe molecule is still possible.

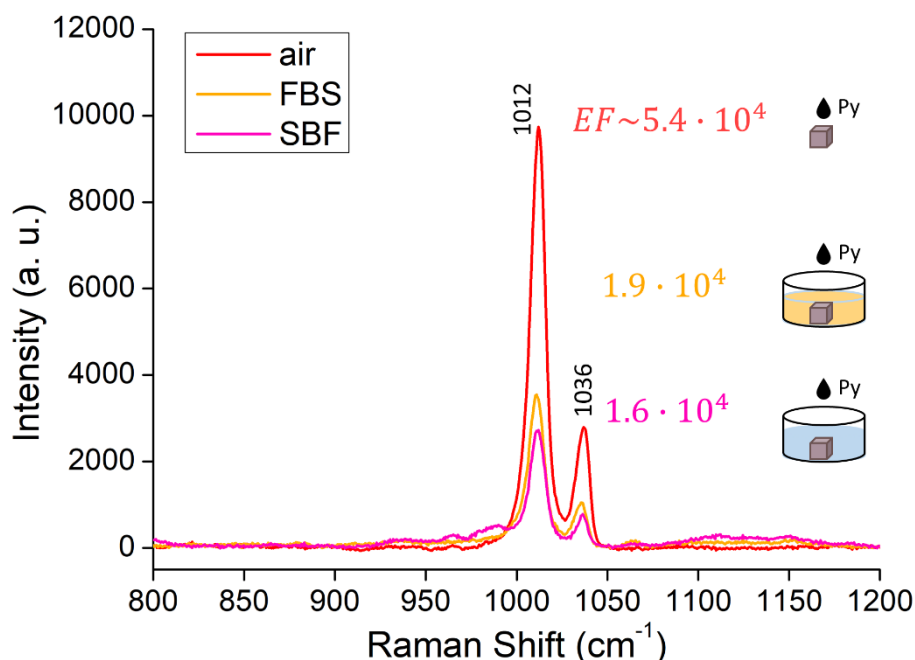


Figure 6.3.3.1 Raman spectra of pyridine adsorbed on porous Bioglass substrate measured in air, in the presence of the biological media FBS and SBF. Adapted with permission from [3]. Copyright (2023), Wiley.

The Raman EFs of the plasmonic porous Bioglass, Bio-Oss[®] and ZTA substrates were listed in Table 6.3.3.1. In contrast to Bioglass, Raman EFs of Bio-Oss[®] and ZTA did not decrease when moved from air to in the biological media. Bio-Oss[®] presented relatively weak EFs due to the irregular deposition of Au nanoparticles on the surface, and, hence also a high standard deviation when measured in air. EFs of ZTA are relative stable in the range between $2.4 \cdot 10^5$ to $4.3 \cdot 10^5$. In general, the high standard deviation of the Raman EFs can be explained by the randomness of the measuring spot. The measuring spot on a large and dense Au nanoparticle agglomeration, or on a single Au nanoparticle, or even on a plasmonic hotspot can make an exponential difference on the Raman EF value [23].

Table 6.3.3.1 Raman EFs of plasmonic porous Bioglass, Bio-Oss[®] and ZTA substrates measured under different conditions. Adapted with permission from [3]. Copyright (2023), Wiley.

Enhancement factor (10^4)	air	In FBS	In SBF
Bioglass	5.4 ± 1.1	1.9 ± 1.0	1.6 ± 0.7
Bio-Oss [®]	1.1 ± 1.9	1.0 ± 0.4	1.7 ± 0.7
ZTA	23.6 ± 17.4	35.8 ± 11.0	42.6 ± 24.8

It is worth mentioning that the visibility of the Bioglass samples upon submission in the biological media was impeded, which complicated focusing on the sample surface during the Raman measurement. For an actual application of the plasmonic porous Bioglass for real-time molecule detection via SERS, especially *in vivo* or even through tissue, the measuring technique should be further developed, for instance, via SESORS [71–74].

6.3.4 Stability of plasmonic porous Bioglass in biological media

To test the stability in physiological conditions, plasmonic porous Bioglass was incubated in simulated body fluid at 37 °C. For comparison, Bio-Oss[®] and bioinert ZTA substrates were incubated under the identical condition. Figure 6.3.4.1 shows the weight change in relation to the initial weight of the three plasmonic porous ceramics after incubation in SBF. The weight of Bioglass reduced by 14 % after 7 days and by 57 % after 28 days of incubation. The dissolution and mineralization process of Bioglass is well-documented [364,365]. Blaker *et al.* recorded *in vitro* degradation of highly porous poly (D, L-lactide) (PDLLA) / Bioglass-filled composite foams in SBF up to 600 days. Their 30 wt.% Bioglass sample presented an immediate weight loss of 12 % during the first 24 h and stabilized at 15 % up to 365 days, while the sample contained 70 wt. % of PDLLA, whose weight remained relatively constant after the incubation [366]. The 100 wt. % Bioglass sample in this work demonstrated a remarkable higher weight loss after incubation in SBF. Since the simulated body fluid used in the reference was not changed, while in this work the SBF was exchanged three times a week to maintain the pH at the initial value of 7.4, which could lead to an accelerated process of the Bioglass degradation.

In Figure 6.3.4.1, Bio-Oss[®] presented a slight weight gain of 8.9 % after 14 days and 14 % after 28 days of incubation. Bio-Oss[®] is a natural biomaterial sourced from bovine bone and can be resorbed by the body albeit at much lower speed than Bioglass. Bio-Oss[®] was reported still remaining in the body for three to four years after the implantation [367–369]. The observed weight gain in Figure 6.3.4.1 can be explained by the deposition of amorphous calcium phosphate and the formation of crystalline hydroxyapatite on the sample surface [370]. ZTA sample had barely weight change, since it is bioinert.

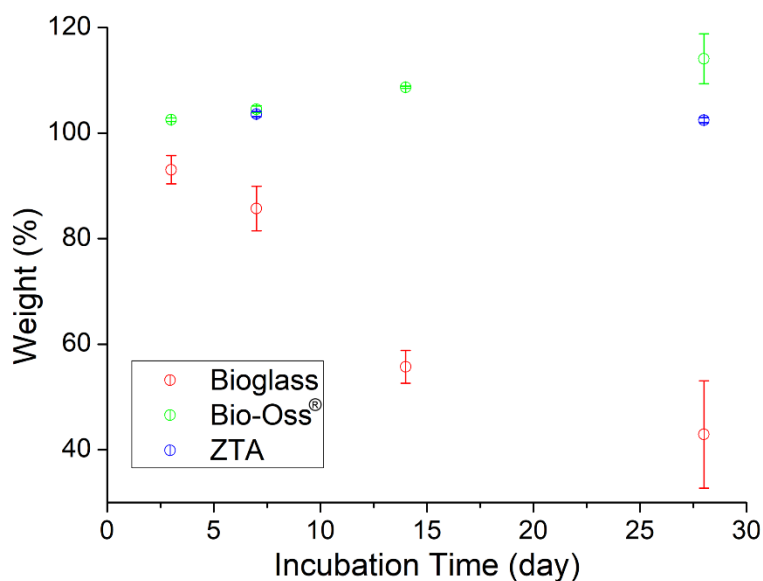


Figure 6.3.4.1 Weight change of plasmonic porous Bioglass (red), Bio-Oss® (green) and ZTA (blue) after incubation at 37 °C in SBF. Adapted with permission from [3]. Copyright (2023), Wiley.

To investigate whether the Au nanoparticle deposition has an influence on the Bioglass-bioactivity, bare Bioglass without Au nanoparticle coating and Bioglass functionalized with Au nanoparticles were analyzed upon incubation in SBF, respectively. Table 6.3.4.1 presents the weight change in percentage of bare Bioglass and Au NP coated Bioglass after incubation, while Figure 6.3.4.2 shows selected SEM images of both materials. No significant differences could be observed, indicating a comparable bioactivity after deposition of Au nanoparticles.

Table 6.3.4.1 Weight change of Bioglass 45S5 before and after Au NP coating upon incubation in SBF, compared to initial weight before incubation in percentage (%). Adapted with permission from [3]. Copyright (2023), Wiley.

Incubation time (day)	3	7	14	28
Bioglass	90.73 ± 1.91	75.42 ± 1.9	54.74 ± 1.9	40.41 ± 13.2
Au NP coated Bioglass	93.06 ± 2.68	85.7 ± 4.23	55.72 ± 3.11	42.91 ± 10.17

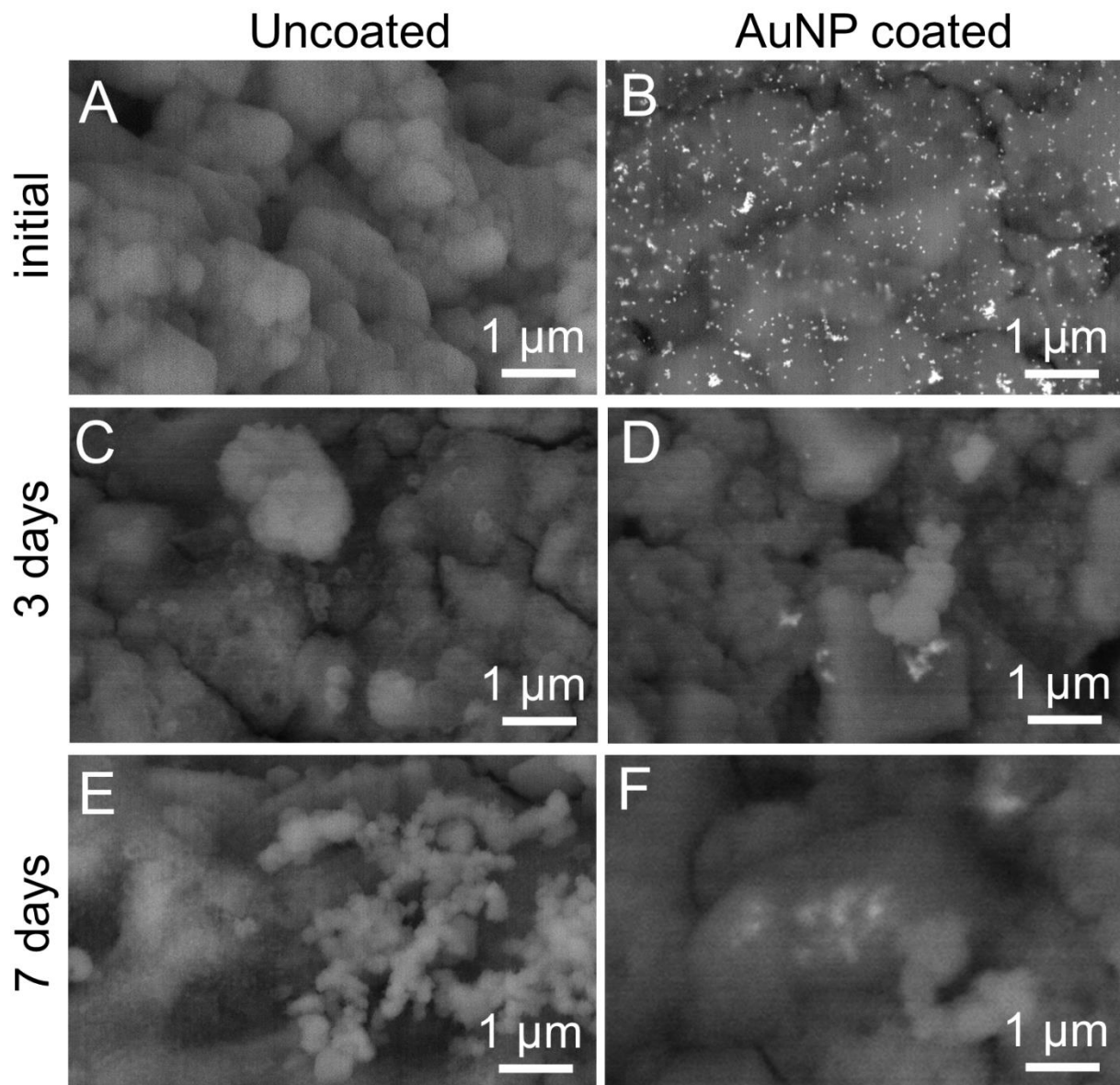


Figure 6.3.4.2 SEM images of Bioglass before (A, C and E) and after Au NP coating (B, D and F) at initial state and after incubation in SBF. Adapted with permission from [3]. Copyright (2023), Wiley.

Figure 6.3.4.3 shows SEM images of plasmonic porous Bioglass, Bio-Oss® and ZTA surface after 7 days and 28 days of incubation respectively. shows SEM images of plasmonic porous Bioglass, Bio-Oss® and ZTA surface after 7 days and 28 days of incubation respectively. A thin hydroxyapatite layer formed on the Bioglass surface after 7 days of incubation (Figure 6.3.4.3 (a)). The deposited Au nanoparticles were covered by the formed hydroxyapatite layer, but still visible through the thin layer. After 28 days of incubation, the hydroxyapatite layer became denser. Needle-like crystals can be observed in Figure 6.3.4.3 (b), indicating the growth of a crystallized hydroxyapatite layer [371]. The amount of the visible Au nanoparticles reduced accordingly.

Different from Bioglass, on Bio-Oss[®] surface there were only limited freshly formed layer visible after 7 days of incubation in SBF, which agrees with the references reporting the mineralization of hydroxyapatite on a hydroxyapatite surface is much slower than that on a Bioglass surface [148,370]. After 28 days, remarkably higher amount of the freshly formed layer can be observed on the Bio-Oss[®] surface, corresponding to the weight gain of 14 %, which resulted in a dense covering of the Au nanoparticles. As expected, the ZTA surface showed hardly any deposits or freshly formed layer after the incubation, although the Au nanoparticle surface coverage reduced slight after 7 days of incubation (Figure 6.3.4.3 (e)), due to possible wash-away of some Au nanoparticles on the surface.

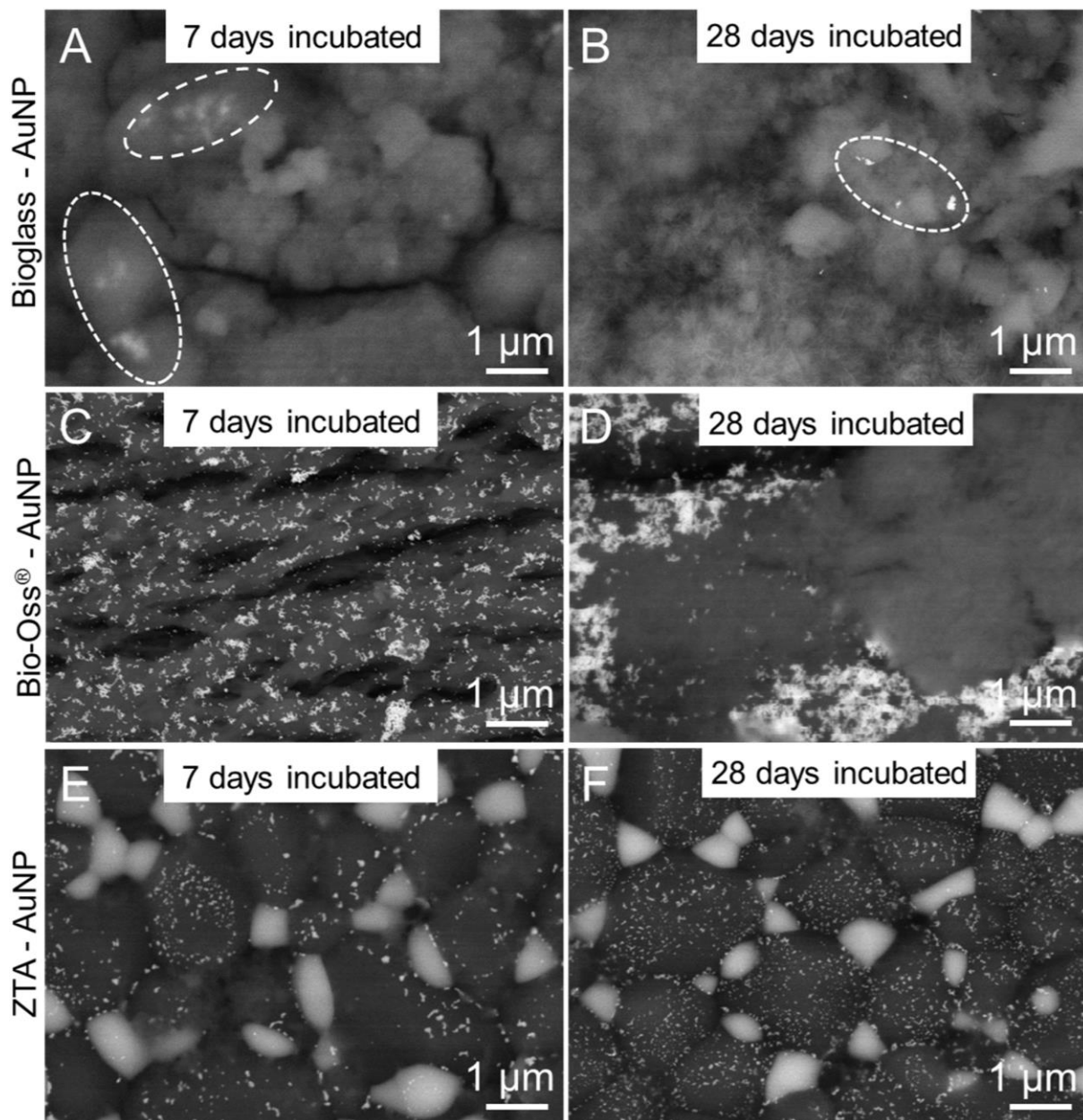


Figure 6.3.4.3 SEM-BSE images of plasmonic porous Bioglass after 7 days (a) and 28 days (b) of incubation with marked area referring to the Au nanoparticles covered by hydroxyapatite, Bio-Oss[®] after

7 days (c) and 28 days (d) of incubation and ZTA after 7 days (e) and 28 days (f) of incubation. Adapted with permission from [3]. Copyright (2023), Wiley.

Figure 6.3.4.4 (a) shows the Raman spectra of pyridine on plasmonic 60 ppi Bioglass as SERS substrate after incubation in SBF. The Raman EFs of the three different materials are summarized in Figure 6.3.4.4 (b). Plasmonic porous Bioglass shows an initial strong decrease of 65.9 % in the Raman enhancement effect after 3 days of incubation followed by a slower pace within the investigated period. In total, the EF decreased from $5.4 \cdot 10^4$ before incubation to $7.2 \cdot 10^3$ after 28 days of incubation, which is still remarkably high considering the ongoing dissolution of the Bioglass matrix to 42.9 % of its initial weight. Relating to the SEM result shown in Figure 6.3.4.3 (b), there were still Au NPs visible on the surface of the material, despite the dissolution of the Bioglass structure and deposition of a porous calcium phosphate layer on the Bioglass surface.

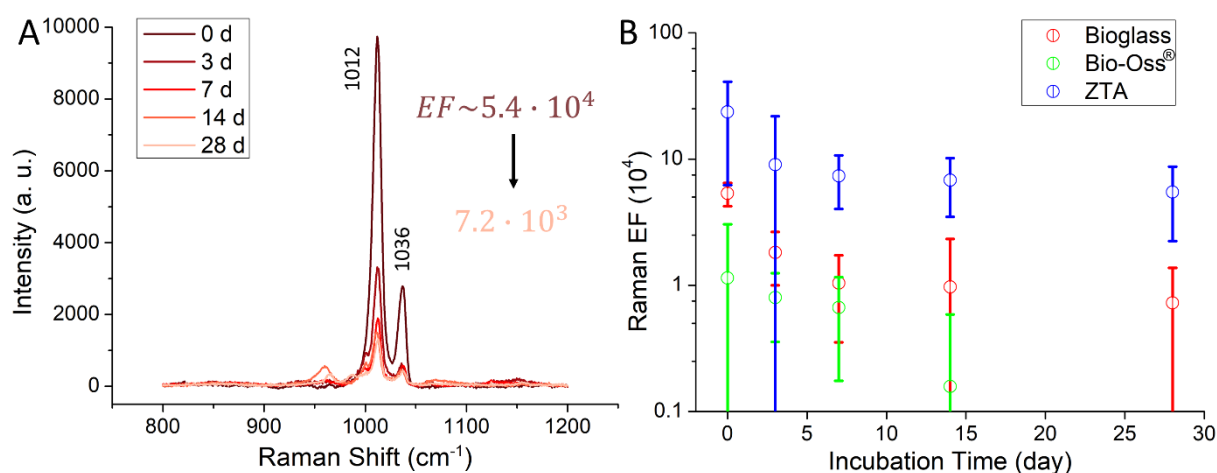


Figure 6.3.4.4 (a) Raman spectra of pyridine adsorbed on plasmonic porous Bioglass after incubation in SBF; (b) Raman enhancement factors of plasmonic porous Bioglass, Bio-Oss® and ZTA substrates after different incubation periods in SBF. Adapted with permission from [3]. Copyright (2023), Wiley.

Conversely, Bio-Oss® gained 2.5 % in weight after 3 days incubation, while the Raman EF was decreased to 69.9 % of the initial value. A sharp reduction of the initial EF to 13.8 % occurred after 14 days of incubation, which was accompanied by a total weight gain of only 8.7 %. The EF decreased from $6.7 \cdot 10^3$ to $1.6 \cdot 10^3$, when the incubation time period was prolonged from 7 to 14 days. The enhancement effect of plasmonic Bio-Oss® was no longer present after 28 days of incubation. This corresponds to the SEM results (Figure 6.3.4.3 (d)), where it was difficult to find individual Au NPs on the surface. Instead, only larger agglomerates and covering materials could be observed, which explains the loss of the enhancement effect. Plasmonic porous ZTA had a rapid decrease (61.8 %) in Raman EF after three days of incubation. The EFs stabilized after 3 days and remained at around 30 % of the initial value.

Knowing the ZTA is bioinert and showed hardly weight change upon incubation, the loss in Raman EFs could arise from the immersion in liquid, which could have removed some less firmly deposited Au NPs on the ZTA surface. Overall, useable Raman enhancement is maintained even after extended incubation in SBF in this case.

6.4 Conclusions

In this chapter, the three Au nanoparticles-coated porous bioceramics Bioglass, Bio-Oss[®] and ZTA were investigated for their ability to detect molecules via SERS. The plasmonic porous Bioglass delivered a higher Raman EF than the functionalized commercial bone replacement material Bio-Oss[®]. Meanwhile, Raman enhancement of the plasmonic porous Bioglass substrates did not depend on pore size, with Raman EFs between $3 \cdot 10^4$ - $5.6 \cdot 10^4$. On the contrary, the plasmonic porous ZTA showed significantly higher Raman EFs ($2.4 \cdot 10^5$ - $8.3 \cdot 10^5$) than the comparable dense pellet ($4.9 \cdot 10^4$). Moreover, the feasibility of the plasmonic porous bioceramics was tested in different conditions that simulate a biological environment. In the presence of the biological medium FBS, the Raman enhancement only very moderately decreased, e.g., from $5.4 \cdot 10^4$ to $1.9 \cdot 10^4$ for Bioglass. Moreover, the spectra showed no signals from the surrounding medium, even when the substrate was completely submerged in FBS with abundant proteins. When measured in SBF, the Raman EFs were slightly reduced, but remained in the same order of magnitude, indicating the feasibility of the plasmonic porous bioceramics for molecule detection via SERS under biological conditions.

The long-term stability of the SERS functionality of the three materials was tested through incubation in simulated body fluid. Although the Bioglass substrates showed the highest weight change after the incubation due to reaction on the surface, the Bioglass substrates still showed Raman EFs of 7.2×10^3 after 28 days of incubation in SBF, indicating the possibility of plasmonic porous Bioglass as bone substitute with molecule detection ability. The bioinert ZTA ceramic also only showed moderate decrease of the SERS enhancement over time, while the enhancement of Bio-Oss[®] disappeared after around 14 days of incubation.

7. Conclusion

The main purpose of this thesis was to introduce the concept of the 3D plasmonic open-cell foam ceramic and investigate its potential applications in different directions. Initially, ZTA based macro-porous ceramics were processed with polymer replica method and functionalized with silver nanoparticles.

Initially, the concept of plasmonic porous ceramics was introduced. Proof-of-principle was conducted using zirconia-toughened-alumina with an open-cell foam structure. The open porous ZTA ceramic was functionalized with Ag nanoparticles. The Ag nanoparticles were synthesized via a simple chemical reduction method and deposited on the ZTA ceramic surface through heterogeneous nucleation. The molecule detection ability of plasmonic porous ceramics in this work was examined through surface-enhanced Raman scattering. The Raman enhancement effect of the plasmonic porous ceramics can be tuned by adjusting the plasmonic nanostructure coverage on the ceramic surface. Meanwhile, the pore size of the open-cell porous ceramic foam has a relatively weak influence on the Raman enhancement factor. Furthermore, it was found out that the open porous ceramic structure was able to provide additional enhancement effect through light-trapping / multiple light scattering within the porous structure.

After Proof-of-principle, the application possibilities of plasmonic porous ceramics were investigated in two different directions, namely for *in situ* reaction monitoring and for biomedical applications. Through the functionalization with bimetallic core-shell nanoparticles, multifunction can be introduced in plasmonic porous ceramics. Au@Pd and Au@Pt core-shell nanoparticles with an Au core and Pd / Pt shell, realizing real-time *in situ* catalytic reaction monitoring. The substrates functionalized with Au@Pd nanoparticles showed Raman EFs of around 10^4 , while the samples deposited with Au@Pt nanoparticles reached Raman EFs up to 10^6 . The balance between SERS efficiency and catalytic activity of the substrates can be tailored through adjusting the shell thickness, due to the dominant character of the damped plasmon oscillations in the Pd / Pt shell. Moreover, the porous substrates showed not only higher Raman enhancement effect than the dense substrates, but also higher catalytic efficiency due to higher specific surface area.

Furthermore, plasmonic porous ceramics were developed for biomedical applications by employing bioceramics as support substrate. Au nanoparticles were introduced on Bioglass, Bio-Oss[®] and bio-inert ZTA surface. The plasmonic porous Bioglass showed no obvious change in bioactivity after the plasmonic nanoparticle functionalization. The Raman enhancing capability of the plasmonic porous Bioglass was examined and compared with the commercial product Bio-Oss[®] and bio-inert ZTA. The Raman enhancement effect of the bioceramic pore

size was observed. The Bioglass substrate showed relatively stable Raman EFs around 10^4 , regardless the pore sizes. While, the ZTA substrates functionalized with Au nanoparticles presented a similar trend as the substrates coated with Ag nanoparticles, that the Raman EFs of the porous samples were significantly higher than that of the dense pellet. Meanwhile, the Raman enhancement of the plasmonic porous Bioglass showed an only very limited decrease, when measured in the presence of biological medium FBS and SBF. Moreover, the stability of the molecule detection ability of the bioceramics as SERS substrates was tested upon incubation in SBF. Among the tested substrates, the Bioglass showed the highest weight change rate after the incubation in SBF. However, the Bioglass sample still achieved a Raman EF of $7.2 \cdot 10^3$ after 28 days of incubation. The Au nanoparticles could still be observed and were only partially covered by the formed apatite layer on the Bioglass surface. On the Bio-Oss[®] surface, only clusters of large nanoparticles could be observed after 28 days of incubation, which resulted in the loss of the SERS-activity. Meanwhile, the bioinert ZTA presented a moderate decrease of the Raman EFs upon incubation in SBF, probably caused by the possible removal of the deposited Au nanoparticles in liquid.

To conclude, this work focused on the conceptualization, design and develop of the plasmonic porous ceramics. This substrate was examined for real-time and sensitive molecule detection via SERS. The application of the plasmonic porous ceramics were exemplarily investigated in different directions, for instance, for *in situ* catalytic reaction monitoring by employing multifunctional core-shell metallic nanoparticles, and for molecule detection in simulated biological conditions even after extended time period. In consequence, the results in this work introduced the novel concept of plasmonic porous ceramics and revealed the application possibilities of this substrate as a milestone for potential further development. This work contributes significantly to the field of advanced ceramics as SERS substrate, combining the advantages of ceramics with the optical properties of plasmonic materials.

8. Outlook

The research of rapid and sensitive molecule detection has always been a popular and challenging topic, especially in life science and chemical, materials science [19,372–374]. Due to fingerprint recognition ability and high sensitivity, surface-enhanced Raman scattering has become one of the most powerful tools. Accordingly, the research on SERS substrates has been conducted and discussed widely [208,375,376].

The concept of plasmonic porous ceramics broadened SERS substrates from conventionally 2D substrates to 3D substrates with high accessibility, along with the advantages of advanced ceramics. Besides the two application directions studied in this work, plasmonic porous ceramics can be further adapted for applications in different fields, for instance, for high-temperature reaction monitoring up to 600 °C [308,377,378].

Through simply employing bioceramics as substrate, applications in biological fields can be realized. For detection of specific biomarkers, the plasmonic porous bioceramics could be developed by functionalizing the Au nanoparticles with targeting moieties, for instance to detect bone alkaline phosphatase as biomarker of osteotropic cancers [379]. Furthermore, examination in deeper tissue layers including bone can be achieved by combination with related techniques, such as SESORS [72,74,75]. Considering research on Au nanoparticles for biomedical applications is well-established [340,380–385], additional features of the Au nanoparticle-coated porous bioceramics could be investigated, such as antibacterial activity or hyperthermia based on plasmonic heating [386–389].

Meanwhile, plasmonic porous ceramics can be applied, because of their photothermal properties. Compared to conventional photothermal therapy method using lasers, the plasmonic photothermal therapy introduces a much more selective and efficient cancer therapy, due to highly enhanced photo-absorbing properties of the plasmonic porous ceramic substrate [15]. Also, plasmonic porous ceramics can be utilized for green energy conversion, such as solar-to-fuel conversion, which could reduce the reliance on fossil fuels and promotes the development of sustainable energy sources [390].

Furthermore, this material concept could be developed for biotechnological applications featuring in situ monitoring of molecule turn-over rates within reactors, e.g., monitoring of bioproduction processes involving antibodies, enzymes or cells in continuous flow set-ups, or green energy conversion and related applications [391–393].

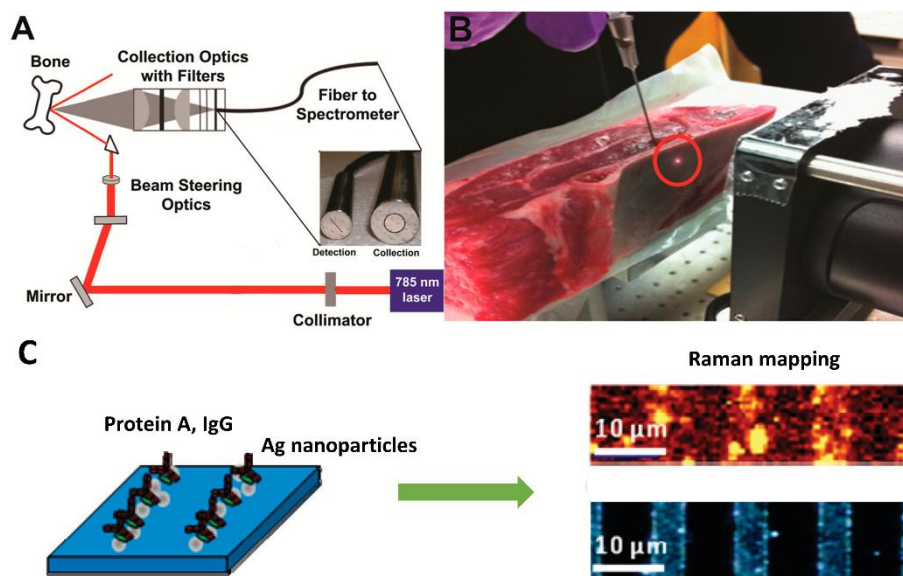


Figure 8.1 (a) Schematic illustration of SESORS instrumentation with collection and detection; (b) 785 nm laser spot (circled in red) on ovine shoulder bone with tissue attached, SESORS spectra were collected through the bone; (c) Schematic presentation of monitoring protein A and human immunoglobulin G (IgG) via SERS. (a, b) adapted with permission from [72]. Copyright (2013), *Journal of the American Chemical Society*. (c) adapted with permission from [391]. Copyright (2011), *Langmuir*.

Moreover, it is meaningful to investigate and simulate the complex light-trapping within the porous ceramic matrix, especially ceramics with different refractive indexes. Optical properties, especially the Raman enhancement effect of plasmonic porous ceramics based on different ceramic materials with various porous structures could be studied experimentally and compared with computational simulation results. This investigation might lead to a better understanding of the significantly improved Raman enhancement effect of the porous substrates.

9. References

- [1] T. Guo, M.N. Karim, K. Ghosh, M.M. Murshed, K. Rezwan, M. Maas, Plasmonic porous ceramics based on zirconia-toughened alumina functionalized with silver nanoparticles for surface-enhanced Raman scattering, *Open Ceram.* 9 (2022) 100228. <https://doi.org/10.1016/j.oceram.2022.100228>.
- [2] T. Guo, M.M. Murshed, K. Rezwan, M. Maas, Ceramic Open Cell Foams Featuring Plasmonic Hybrid Metal Nanoparticles for In Situ SERS Monitoring of Catalytic Reactions, *Adv. Mater. Interfaces* n/a (n.d.) 2300207. <https://doi.org/10.1002/admi.202300207>.
- [3] T. Guo, J. Schmidt, M.M. Murshed, K. Rezwan, M. Maas, Gold Nanoparticle-Coated Bioceramics for Plasmonically Enhanced Molecule Detection via Surface-Enhanced Raman Scattering, *Adv. Eng. Mater.* 25 (2023) 2300942. <https://doi.org/10.1002/adem.202300942>.
- [4] A. Campion, P. Kambhampati, Surface-enhanced Raman scattering, *Chem. Soc. Rev.* 27 (1998) 241–250. <https://doi.org/10.1039/A827241Z>.
- [5] T. Klar, M. Perner, S. Grosse, G. von Plessen, W. Spirkl, J. Feldmann, Surface-Plasmon Resonances in Single Metallic Nanoparticles, *Phys. Rev. Lett.* 80 (1998) 4249–4252. <https://doi.org/10.1103/PhysRevLett.80.4249>.
- [6] W.A. Murray, W.L. Barnes, Plasmonic Materials, *Adv. Mater.* 19 (2007) 3771–3782. <https://doi.org/10.1002/adma.200700678>.
- [7] G. Albrecht, M. Ubl, S. Kaiser, H. Giessen, M. Hentschel, Comprehensive Study of Plasmonic Materials in the Visible and Near-Infrared: Linear, Refractory, and Nonlinear Optical Properties, *ACS Photonics* 5 (2018) 1058–1067. <https://doi.org/10.1021/acsp Photonics.7b01346>.
- [8] P. r. West, S. Ishii, G. v. Naik, N. k. Emani, V. m. Shalaev, A. Boltasseva, Searching for better plasmonic materials, *Laser Photonics Rev.* 4 (2010) 795–808. <https://doi.org/10.1002/lpor.200900055>.
- [9] J. Yao, A.-P. Le, S.K. Gray, J.S. Moore, J.A. Rogers, R.G. Nuzzo, Functional Nanostructured Plasmonic Materials, *Adv. Mater.* 22 (2010) 1102–1110. <https://doi.org/10.1002/adma.200904097>.
- [10] I. Tokarev, I. Tokareva, S. Minko, Gold-Nanoparticle-Enhanced Plasmonic Effects in a Responsive Polymer Gel, *Adv. Mater.* 20 (2008) 2730–2734. <https://doi.org/10.1002/adma.200702885>.
- [11] W. Zou, X. Wang, Y. Yang, Y. Wu, G. Zu, L. Zou, J. Shen, Porous alumina aerogel with tunable pore structure for facile, ultrasensitive, and reproducible SERS platform, *J. Raman Spectrosc.* 50 (2019) 1429–1437. <https://doi.org/10.1002/jrs.5663>.
- [12] K.S. Giesfeldt, R.M. Connatser, M.A. De Jesús, P. Dutta, M.J. Sepaniak, Gold-polymer nanocomposites: studies of their optical properties and their potential as SERS substrates, *J. Raman Spectrosc.* 36 (2005) 1134–1142. <https://doi.org/10.1002/jrs.1418>.
- [13] M.A. Mackey, M.R.K. Ali, L.A. Austin, R.D. Near, M.A. El-Sayed, The Most Effective Gold Nanorod Size for Plasmonic Photothermal Therapy: Theory and In Vitro Experiments, *J. Phys. Chem. B* 118 (2014) 1319–1326. <https://doi.org/10.1021/jp409298f>.
- [14] Y.-J. Oh, M. Kang, M. Park, K.-H. Jeong, Engineering hot spots on plasmonic nanopillar arrays for SERS: A review, *BioChip J.* 10 (2016) 297–309. <https://doi.org/10.1007/s13206-016-0406-2>.
- [15] X. Huang, P.K. Jain, I.H. El-Sayed, M.A. El-Sayed, Plasmonic photothermal therapy (PPTT) using gold nanoparticles, *Lasers Med. Sci.* 23 (2007) 217. <https://doi.org/10.1007/s10103-007-0470-x>.
- [16] M. Fleischmann, P.J. Hendra, A.J. McQuillan, Raman spectra of pyridine adsorbed at a silver electrode, *Chem. Phys. Lett.* 26 (1974) 163–166. [https://doi.org/10.1016/0009-2614\(74\)85388-1](https://doi.org/10.1016/0009-2614(74)85388-1).
- [17] W.R. Premasiri, D.T. Moir, M.S. Klemperner, N. Krieger, G. Jones, L.D. Ziegler, Characterization of the Surface Enhanced Raman Scattering (SERS) of Bacteria, *J. Phys. Chem. B* 109 (2005) 312–320. <https://doi.org/10.1021/jp040442n>.
- [18] R.A. Halvorson, P.J. Vikesland, Surface-Enhanced Raman Spectroscopy (SERS) for Environmental Analyses, *Environ. Sci. Technol.* 44 (2010) 7749–7755. <https://doi.org/10.1021/es101228z>.

- [19] K. Kneipp, Y. Wang, H. Kneipp, L.T. Perelman, I. Itzkan, R.R. Dasari, M.S. Feld, Single Molecule Detection Using Surface-Enhanced Raman Scattering (SERS), *Phys. Rev. Lett.* 78 (1997) 1667–1670. <https://doi.org/10.1103/PhysRevLett.78.1667>.
- [20] L. Wu, X. Qu, Cancer biomarker detection: recent achievements and challenges, *Chem. Soc. Rev.* 44 (2015) 2963–2997. <https://doi.org/10.1039/C4CS00370E>.
- [21] E. Stern, A. Vacic, N.K. Rajan, J.M. Criscione, J. Park, B.R. Ilic, D.J. Mooney, M.A. Reed, T.M. Fahmy, Label-free biomarker detection from whole blood, *Nat. Nanotechnol.* 5 (2010) 138–142. <https://doi.org/10.1038/nnano.2009.353>.
- [22] M. Swierczewska, G. Liu, S. Lee, X. Chen, High-sensitivity nanosensors for biomarker detection, *Chem. Soc. Rev.* 41 (2012) 2641–2655. <https://doi.org/10.1039/C1CS15238F>.
- [23] R. Pilot, R. Signorini, C. Durante, L. Orian, M. Bhamidipati, L. Fabris, A Review on Surface-Enhanced Raman Scattering, *Biosensors* 9 (2019) 57. <https://doi.org/10.3390/bios9020057>.
- [24] R.L. Paul, A.J. McQuillan, P.J. Hendra, M. Fleischmann, Laser Raman spectroscopy at the surface of a copper electrode, *J. Electroanal. Chem. Interfacial Electrochem.* 66 (1975) 248–249. [https://doi.org/10.1016/S0022-0728\(75\)80007-6](https://doi.org/10.1016/S0022-0728(75)80007-6).
- [25] D.L. Jeanmaire, R.P. Van Duyne, Surface raman spectroelectrochemistry: Part I. Heterocyclic, aromatic, and aliphatic amines adsorbed on the anodized silver electrode, *J. Electroanal. Chem. Interfacial Electrochem.* 84 (1977) 1–20. [https://doi.org/10.1016/S0022-0728\(77\)80224-6](https://doi.org/10.1016/S0022-0728(77)80224-6).
- [26] B. Pettinger, H. Wetzel, Surface Enhanced Raman Scattering from Pyridine, Water, and Halide Ions on Au, Ag, and Cu Electrodes, *Berichte Bunsenges. Für Phys. Chem.* 85 (1981) 473–481. <https://doi.org/10.1002/bbpc.19810850604>.
- [27] M. Duval Malinsky, K.L. Kelly, G.C. Schatz, R.P. Van Duyne, Nanosphere Lithography: Effect of Substrate on the Localized Surface Plasmon Resonance Spectrum of Silver Nanoparticles, *J. Phys. Chem. B* 105 (2001) 2343–2350. <https://doi.org/10.1021/jp002906x>.
- [28] J.J. Mock, M. Barbic, D.R. Smith, D.A. Schultz, S. Schultz, Shape effects in plasmon resonance of individual colloidal silver nanoparticles, *J. Chem. Phys.* 116 (2002) 6755–6759. <https://doi.org/10.1063/1.1462610>.
- [29] L.J. Sherry, S.-H. Chang, G.C. Schatz, R.P. Van Duyne, B.J. Wiley, Y. Xia, Localized Surface Plasmon Resonance Spectroscopy of Single Silver Nanocubes, *Nano Lett.* 5 (2005) 2034–2038. <https://doi.org/10.1021/nl0515753>.
- [30] L.J. Sherry, R. Jin, C.A. Mirkin, G.C. Schatz, R.P. Van Duyne, Localized Surface Plasmon Resonance Spectroscopy of Single Silver Triangular Nanoprisms, *Nano Lett.* 6 (2006) 2060–2065. <https://doi.org/10.1021/nl061286u>.
- [31] A. Liang, Q. Liu, G. Wen, Z. Jiang, The surface-plasmon-resonance effect of nanogold/silver and its analytical applications, *TrAC Trends Anal. Chem.* 37 (2012) 32–47. <https://doi.org/10.1016/j.trac.2012.03.015>.
- [32] B.J. Wiley, S.H. Im, Z.-Y. Li, J. McLellan, A. Siekkinen, Y. Xia, Maneuvering the Surface Plasmon Resonance of Silver Nanostructures through Shape-Controlled Synthesis, *J. Phys. Chem. B* 110 (2006) 15666–15675. <https://doi.org/10.1021/jp0608628>.
- [33] G.J. Kovacs, R.O. Loutfy, P.S. Vincett, C. Jennings, R. Aroca, Distance dependence of SERS enhancement factor from Langmuir-Blodgett monolayers on metal island films: evidence for the electromagnetic mechanism, *Langmuir* 2 (1986) 689–694. <https://doi.org/10.1021/la00072a001>.
- [34] S.S. Masango, R.A. Hackler, N. Large, A.-I. Henry, M.O. McAnally, G.C. Schatz, P.C. Stair, R.P. Van Duyne, High-Resolution Distance Dependence Study of Surface-Enhanced Raman Scattering Enabled by Atomic Layer Deposition, *Nano Lett.* 16 (2016) 4251–4259. <https://doi.org/10.1021/acs.nanolett.6b01276>.
- [35] P. G. Etchegoin, E.C.L. Ru, A perspective on single molecule SERS : current status and future challenges, *Phys. Chem. Chem. Phys.* 10 (2008) 6079–6089. <https://doi.org/10.1039/B809196J>.
- [36] S.-Y. Ding, E.-M. You, Z.-Q. Tian, M. Moskovits, Electromagnetic theories of surface-enhanced Raman spectroscopy, *Chem. Soc. Rev.* 46 (2017) 4042–4076. <https://doi.org/10.1039/C7CS00238F>.

- [37] S. L. Kleinman, R. R. Frontiera, A.-I. Henry, J. A. Dieringer, R.P.V. Duyne, Creating, characterizing, and controlling chemistry with SERS hot spots, *Phys. Chem. Chem. Phys.* 15 (2013) 21–36. <https://doi.org/10.1039/C2CP42598J>.
- [38] E.C. Le Ru, J. Grand, I. Sow, W.R.C. Somerville, P.G. Etchegoin, M. Treguer-Delapierre, G. Charron, N. Félidj, G. Lévi, J. Aubard, A Scheme for Detecting Every Single Target Molecule with Surface-Enhanced Raman Spectroscopy, *Nano Lett.* 11 (2011) 5013–5019. <https://doi.org/10.1021/nl2030344>.
- [39] S.-Y. Ding, J. Yi, J.-F. Li, B. Ren, D.-Y. Wu, R. Panneerselvam, Z.-Q. Tian, Nanostructure-based plasmon-enhanced Raman spectroscopy for surface analysis of materials, *Nat. Rev. Mater.* 1 (2016) 1–16. <https://doi.org/10.1038/natrevmats.2016.21>.
- [40] L. Tong, H. Xu, M. Käll, Nanogaps for SERS applications, *MRS Bull.* 39 (2014) 163–168. <https://doi.org/10.1557/mrs.2014.2>.
- [41] E.G. Gillan, R.B. Kaner, Synthesis of Refractory Ceramics via Rapid Metathesis Reactions between Solid-State Precursors, *Chem. Mater.* 8 (1996) 333–343. <https://doi.org/10.1021/cm950232a>.
- [42] E. Sani, L. Mercatelli, F. Francini, J.-L. Sans, D. Sciti, Ultra-refractory ceramics for high-temperature solar absorbers, *Scr. Mater.* 65 (2011) 775–778. <https://doi.org/10.1016/j.scriptamat.2011.07.033>.
- [43] E.A. Ekimov, A.G. Gavriluk, B. Palosz, S. Gierlotka, P. Dluzewski, E. Tatianin, Yu. Kluev, A.M. Naletov, A. Presz, High-pressure, high-temperature synthesis of SiC–diamond nanocrystalline ceramics, *Appl. Phys. Lett.* 77 (2000) 954–956. <https://doi.org/10.1063/1.1288602>.
- [44] D.F.K. Hennings, B. Schreinemacher, H. Schreinemacher, High-permittivity dielectric ceramics with high endurance, *J. Eur. Ceram. Soc.* 13 (1994) 81–88. [https://doi.org/10.1016/0955-2219\(94\)90062-0](https://doi.org/10.1016/0955-2219(94)90062-0).
- [45] I.M. Reaney, D. Iddles, Microwave Dielectric Ceramics for Resonators and Filters in Mobile Phone Networks, *J. Am. Ceram. Soc.* 89 (2006) 2063–2072. <https://doi.org/10.1111/j.1551-2916.2006.01025.x>.
- [46] M.M. Hoog Antink, T. Sewczyk, S. Kroll, P. Árki, S. Beutel, K. Rezwani, M. Maas, Proteolytic ceramic capillary membranes for the production of peptides under flow, *Biochem. Eng. J.* 147 (2019) 89–99. <https://doi.org/10.1016/j.bej.2019.04.005>.
- [47] A. Julbe, D. Farrusseng, C. Guizard, Porous ceramic membranes for catalytic reactors — overview and new ideas, *J. Membr. Sci.* 181 (2001) 3–20. [https://doi.org/10.1016/S0376-7388\(00\)00375-6](https://doi.org/10.1016/S0376-7388(00)00375-6).
- [48] I. Nettleship, Applications of Porous Ceramics, *Key Eng. Mater.* 122–124 (1996) 305–324. <https://doi.org/10.4028/www.scientific.net/KEM.122-124.305>.
- [49] E.C. Hammel, O.L.-R. Ighodaro, O.I. Okoli, Processing and properties of advanced porous ceramics: An application based review, *Ceram. Int.* 40 (2014) 15351–15370. <https://doi.org/10.1016/j.ceramint.2014.06.095>.
- [50] M.-Y. Li, M. Yu, S. Jiang, S. Liu, H. Liu, H. Xu, D. Su, G. Zhang, Y. Chen, J. Wu, Controllable 3D plasmonic nanostructures for high-quantum-efficiency UV photodetectors based on 2D and 0D materials, *Mater. Horiz.* 7 (2020) 905–911. <https://doi.org/10.1039/C9MH01660K>.
- [51] C. Li, J. Yu, S. Xu, S. Jiang, X. Xiu, C. Chen, A. Liu, T. Wu, B. Man, C. Zhang, Constructing 3D and Flexible Plasmonic Structure for High-Performance SERS Application, *Adv. Mater. Technol.* 3 (2018) 1800174. <https://doi.org/10.1002/admt.201800174>.
- [52] G. Chen, D. Wang, W. Hong, L. Sun, Y. Zhu, X. Chen, Fluorescence Enhancement on Large Area Self-Assembled Plasmonic-3D Photonic Crystals, *Small* 13 (2017) 1602612. <https://doi.org/10.1002/sml.201602612>.
- [53] M. Dipalo, G. C. Messina, H. Amin, R.L. Rocca, V. Shalabaeva, A. Simi, A. Maccione, P. Zilio, L. Berdondini, F.D. Angelis, 3D plasmonic nanoantennas integrated with MEA biosensors, *Nanoscale* 7 (2015) 3703–3711. <https://doi.org/10.1039/C4NR05578K>.
- [54] A. Araújo, A. Pimentel, M.J. Oliveira, M.J. Mendes, R. Franco, E. Fortunato, H. Águas, R. Martins, Direct growth of plasmonic nanorod forests on paper substrates for low-cost flexible 3D SERS

- platforms, *Flex. Print. Electron.* 2 (2017) 014001. <https://doi.org/10.1088/2058-8585/2/1/014001>.
- [55] X. Feng, Z. Liu, G. Zhang, S. Zhang, S. Huang, Z. He, G. Wei, S. Yang, Y. Zhu, C. Ye, C.-T. Lin, G. Ding, G. Wang, Natural Graphene Plasmonic Nano-Resonators for Highly Active Surface-Enhanced Raman Scattering Platforms, *ENERGY Environ. Mater.* n/a (n.d.). <https://doi.org/10.1002/eem2.12394>.
- [56] M.T. Aguilar-Gama, E. Ramírez-Morales, Z. Montiel-González, A. Mendoza-Galván, M. Sotelo-Lerma, P.K. Nair, H. Hu, Structure and refractive index of thin alumina films grown by atomic layer deposition, *J. Mater. Sci. Mater. Electron.* 26 (2015) 5546–5552. <https://doi.org/10.1007/s10854-014-2111-z>.
- [57] R. Shahmiri, O.C. Standard, J.N. Hart, C.C. Sorrell, Optical properties of zirconia ceramics for esthetic dental restorations: A systematic review, *J. Prosthet. Dent.* 119 (2018) 36–46. <https://doi.org/10.1016/j.prosdent.2017.07.009>.
- [58] D. Vollath, D.V. Szabó, J. Haußelt, Synthesis and properties of ceramic nanoparticles and nanocomposites, *J. Eur. Ceram. Soc.* 17 (1997) 1317–1324. [https://doi.org/10.1016/S0955-2219\(96\)00224-5](https://doi.org/10.1016/S0955-2219(96)00224-5).
- [59] K.E. Torrance, E.M. Sparrow, R.C. Birkebak, Polarization, Directional Distribution, and Off-Specular Peak Phenomena in Light Reflected from Roughened Surfaces, *JOSA* 56 (1966) 916–925. <https://doi.org/10.1364/JOSA.56.000916>.
- [60] T. Svensson, E. Adolfsson, M. Lewander, C.T. Xu, S. Svanberg, Disordered, Strongly Scattering Porous Materials as Miniature Multipass Gas Cells, *Phys. Rev. Lett.* 107 (2011) 143901. <https://doi.org/10.1103/PhysRevLett.107.143901>.
- [61] W.L. Xu, H. Chen, M.J. Zheng, G.Q. Ding, W.Z. Shen, Optical transmission spectra of ordered porous alumina membranes with different thicknesses and porosities, *Opt. Mater.* 28 (2006) 1160–1165. <https://doi.org/10.1016/j.optmat.2005.07.003>.
- [62] K. Huang, L. Pu, Y. Shi, P. Han, R. Zhang, Y.D. Zheng, Photoluminescence oscillations in porous alumina films, *Appl. Phys. Lett.* 89 (2006) 201118. <https://doi.org/10.1063/1.2390645>.
- [63] T.J. Hendricks, J.R. Howell, Absorption/Scattering Coefficients and Scattering Phase Functions in Reticulated Porous Ceramics, *J. Heat Transf.* 118 (1996) 79–87. <https://doi.org/10.1115/1.2824071>.
- [64] J. Wang, C. Fan, J. He, P. Ding, E. Liang, Q. Xue, Double Fano resonances due to interplay of electric and magnetic plasmon modes in planar plasmonic structure with high sensing sensitivity, *Opt. Express* 21 (2013) 2236–2244. <https://doi.org/10.1364/OE.21.002236>.
- [65] B. Hvolbæk, T.V.W. Janssens, B.S. Clausen, H. Falsig, C.H. Christensen, J.K. Nørskov, Catalytic activity of Au nanoparticles, *Nano Today* 2 (2007) 14–18. [https://doi.org/10.1016/S1748-0132\(07\)70113-5](https://doi.org/10.1016/S1748-0132(07)70113-5).
- [66] W. Xie, S. Schlücker, Surface-enhanced Raman spectroscopic detection of molecular chemo- and plasmocatalysis on noble metal nanoparticles, *Chem. Commun.* 54 (2018) 2326–2336. <https://doi.org/10.1039/C7CC07951F>.
- [67] M. Muhammad, Q. Huang, A review of aptamer-based SERS biosensors: Design strategies and applications, *Talanta* 227 (2021) 122188. <https://doi.org/10.1016/j.talanta.2021.122188>.
- [68] M.T. Yarak, A. Tukova, Y. Wang, Emerging SERS biosensors for the analysis of cells and extracellular vesicles, *Nanoscale* 14 (2022) 15242–15268. <https://doi.org/10.1039/D2NR03005E>.
- [69] T.J. Moore, A.S. Moody, T.D. Payne, G.M. Sarabia, A.R. Daniel, B. Sharma, In Vitro and In Vivo SERS Biosensing for Disease Diagnosis, *Biosensors* 8 (2018) 46. <https://doi.org/10.3390/bios8020046>.
- [70] C. Fan, N. Zhao, K. Cui, G. Chen, Y. Chen, W. Wu, Q. Li, Y. Cui, R. Li, Z. Xiao, Ultrasensitive Exosome Detection by Modularized SERS Labeling for Postoperative Recurrence Surveillance, *ACS Sens.* 6 (2021) 3234–3241. <https://doi.org/10.1021/acssensors.1c00890>.

- [71] K. Eberhardt, C. Stiebing, C. Matthäus, M. Schmitt, J. Popp, Advantages and limitations of Raman spectroscopy for molecular diagnostics: an update, *Expert Rev. Mol. Diagn.* 15 (2015) 773–787. <https://doi.org/10.1586/14737159.2015.1036744>.
- [72] B. Sharma, K. Ma, M.R. Glucksberg, R.P. Van Duyne, Seeing through Bone with Surface-Enhanced Spatially Offset Raman Spectroscopy, *J. Am. Chem. Soc.* 135 (2013) 17290–17293. <https://doi.org/10.1021/ja409378f>.
- [73] H. Cui, A. Glidle, J.M. Cooper, Highly Efficient Spatially Offset Raman Spectroscopy to Profile Molecular Composition in Bone, *IEEE Access* 8 (2020) 62905–62911. <https://doi.org/10.1109/ACCESS.2020.2984170>.
- [74] N. Stone, M. Kerssens, G.R. Lloyd, K. Faulds, D. Graham, P. Matousek, Surface enhanced spatially offset Raman spectroscopic (SESORS) imaging – the next dimension, *Chem. Sci.* 2 (2011) 776. <https://doi.org/10.1039/c0sc00570c>.
- [75] J.M. Yuen, N.C. Shah, J.T.Jr. Walsh, M.R. Glucksberg, R.P. Van Duyne, Transcutaneous Glucose Sensing by Surface-Enhanced Spatially Offset Raman Spectroscopy in a Rat Model, *Anal. Chem.* 82 (2010) 8382–8385. <https://doi.org/10.1021/ac101951j>.
- [76] S. Kasani, K. Curtin, N. Wu, A review of 2D and 3D plasmonic nanostructure array patterns: fabrication, light management and sensing applications, *Nanophotonics* 8 (2019) 2065–2089. <https://doi.org/10.1515/nanoph-2019-0158>.
- [77] S. Lee, I. Choi, Fabrication Strategies of 3D Plasmonic Structures for SERS, *BioChip J.* 13 (2019) 30–42. <https://doi.org/10.1007/s13206-019-3105-y>.
- [78] F.P. Miller, A.F. Vandome, M. John, *Fresnel Equations*, VDM Publishing, 2010.
- [79] A. Gonis, W.H. Butler, *Multiple Scattering in Solids*, Springer Science & Business Media, 1999.
- [80] Lord Rayleigh, X. On the electromagnetic theory of light, *Lond. Edinb. Dublin Philos. Mag. J. Sci.* 12 (1881) 81–101. <https://doi.org/10.1080/14786448108627074>.
- [81] Lord Rayleigh, XXXIV. On the transmission of light through an atmosphere containing small particles in suspension, and on the origin of the blue of the sky, *Lond. Edinb. Dublin Philos. Mag. J. Sci.* 47 (1899) 375–384. <https://doi.org/10.1080/14786449908621276>.
- [82] C.V. Raman, A New Radiation, (1927). <http://arxiv.iacs.res.in:8080/jspui/handle/10821/377> (accessed December 8, 2022).
- [83] R. Aroca, *Surface-Enhanced Vibrational Spectroscopy*, John Wiley & Sons, 2006.
- [84] K.C. Bantz, A.F. Meyer, N.J. Wittenberg, H. Im, Ö. Kurtuluş, S.H. Lee, N.C. Lindquist, S.-H. Oh, C.L. Haynes, Recent progress in SERS biosensing, *Phys. Chem. Chem. Phys.* 13 (2011) 11551–11567. <https://doi.org/10.1039/C0CP01841D>.
- [85] E.L. Ru, P. Etchegoin, *Principles of Surface-Enhanced Raman Spectroscopy: and Related Plasmonic Effects*, Elsevier, 2008.
- [86] R. Pilot, R. Signorini, L. Fabris, *Surface-Enhanced Raman Spectroscopy: Principles, Substrates, and Applications*, in: F.L. Deepak (Ed.), *Met. Nanoparticles Clust. Adv. Synth. Prop. Appl.*, Springer International Publishing, Cham, 2018: pp. 89–164. https://doi.org/10.1007/978-3-319-68053-8_4.
- [87] M. Bovand, S. Rashidi, J.A. Esfahani, Heat transfer enhancement and pressure drop penalty in porous solar heaters: Numerical simulations, *Sol. Energy* 123 (2016) 145–159. <https://doi.org/10.1016/j.solener.2015.10.054>.
- [88] L. Li, H. Yu, Y. Li, Y.-L. He, Characteristics of the transient thermal load and deformation of the evacuated receiver in solar parabolic trough collector, *Sci. China Technol. Sci.* 63 (2020) 1188–1201. <https://doi.org/10.1007/s11431-019-1508-y>.
- [89] B. Yang, L. Fang, L. Zan, J. Cai, Y. Feng, X. Li, Hydrogenation of cyclohexene catalyzed by nanoporous SPE-PtNi/C membrane electrode, *Int. J. Hydrog. Energy* 47 (2022) 2500–2510. <https://doi.org/10.1016/j.ijhydene.2021.10.179>.
- [90] M. Dehghan, M.S. Valipour, S. Saedodin, Temperature-dependent conductivity in forced convection of heat exchangers filled with porous media: A perturbation solution, *Energy Convers. Manag.* 91 (2015) 259–266. <https://doi.org/10.1016/j.enconman.2014.12.011>.

- [91] Z.A.S. Raizah, S.E. Ahmed, A.M. Aly, ISPH simulations of natural convection flow in E-enclosure filled with a nanofluid including homogeneous/heterogeneous porous media and solid particles, *Int. J. Heat Mass Transf.* 160 (2020) 120153. <https://doi.org/10.1016/j.ijheatmasstransfer.2020.120153>.
- [92] S. Azizifar, M. Ameri, I. Behroyan, Subcooled flow boiling of water in a metal-foam tube: An experimental study, *Int. Commun. Heat Mass Transf.* 118 (2020) 104897. <https://doi.org/10.1016/j.icheatmasstransfer.2020.104897>.
- [93] W. Fuqiang, Z. Xinping, D. Yan, Y. Hongliang, X. Shi, L. Yang, C. Ziming, Progress in radiative transfer in porous medium: A review from macro scale to pore scale with experimental test, *Appl. Therm. Eng.* 210 (2022) 118331. <https://doi.org/10.1016/j.applthermaleng.2022.118331>.
- [94] H. Qi, Z.-Z. He, F.-Z. Zhao, L.-M. Ruan, Determination of the spectral complex refractive indices of microalgae cells by light reflectance-transmittance measurement, *Int. J. Hydrog. Energy* 41 (2016) 4941–4956. <https://doi.org/10.1016/j.ijhydene.2016.01.112>.
- [95] J.-Y. Zhang, H. Qi, Y.-T. Ren, L.-M. Ruan, Simultaneous identification of optical constants and PSD of spherical particles by multi-wavelength scattering–transmittance measurement, *Opt. Commun.* 413 (2018) 317–328. <https://doi.org/10.1016/j.optcom.2017.12.089>.
- [96] P. Boulet, G. Jeandel, G. Morlot, Model of radiative transfer in fibrous media—matrix method, *Int. J. Heat Mass Transf.* 36 (1993) 4287–4297. [https://doi.org/10.1016/0017-9310\(93\)90113-K](https://doi.org/10.1016/0017-9310(93)90113-K).
- [97] X. Huang, H. Qi, C. Niu, L. Ruan, H. Tan, J. Sun, C. Xu, Simultaneous reconstruction of 3D temperature distribution and radiative properties of participating media based on the multi-spectral light-field imaging technique, *Appl. Therm. Eng.* 115 (2017) 1337–1347. <https://doi.org/10.1016/j.applthermaleng.2016.12.029>.
- [98] S.-Z. Tian, Y. Shuai, Y.-M. Guo, B.-S. Jiang, G.-H. Zhang, H.-P. Tan, Simple and fast approach to exploit the spectral reflection properties of liquid media, *Appl. Opt.* 57 (2018) 9046–9052. <https://doi.org/10.1364/AO.57.009046>.
- [99] Y. Li, X.-L. Xia, C. Sun, J. Wang, H.-P. Tan, Tomography-based radiative transfer analysis of an open-cell foam made of semitransparent alumina ceramics, *Sol. Energy Mater. Sol. Cells* 188 (2018) 164–176. <https://doi.org/10.1016/j.solmat.2018.09.005>.
- [100] J.R. Howell, M.P. Menguc, R. Siegel, *Thermal Radiation Heat Transfer*, 5th ed., CRC Press, Boca Raton, 2010. <https://doi.org/10.1201/9781439894552>.
- [101] B. Qiu, M. Xing, Q. Yi, J. Zhang, Chiral Carbonaceous Nanotubes Modified with Titania Nanocrystals: Plasmon-Free and Recyclable SERS Sensitivity, *Angew. Chem. Int. Ed.* 54 (2015) 10643–10647. <https://doi.org/10.1002/anie.201505319>.
- [102] Y. Wang, H. Hu, S. Jing, Y. Wang, Z. Sun, B. Zhao, C. Zhao, J.R. Lombardi, Enhanced Raman Scattering as a Probe for 4-Mercaptopyridine Surface-modified Copper Oxide Nanocrystals, *Anal. Sci.* 23 (2007) 787–791. <https://doi.org/10.2116/analsci.23.787>.
- [103] Q. Zhang, X. Li, W. Yi, W. Li, H. Bai, J. Liu, G. Xi, Plasmonic MoO₂ Nanospheres as a Highly Sensitive and Stable Non-Noble Metal Substrate for Multicomponent Surface-Enhanced Raman Analysis, *Anal. Chem.* 89 (2017) 11765–11771. <https://doi.org/10.1021/acs.analchem.7b03385>.
- [104] K. Manthiram, A.P. Alivisatos, Tunable Localized Surface Plasmon Resonances in Tungsten Oxide Nanocrystals, *J. Am. Chem. Soc.* 134 (2012) 3995–3998. <https://doi.org/10.1021/ja211363w>.
- [105] P. Patsalas, N. Kalfagiannis, S. Kassavetis, Optical Properties and Plasmonic Performance of Titanium Nitride, *Materials* 8 (2015) 3128–3154. <https://doi.org/10.3390/ma8063128>.
- [106] G.V. Naik, J. Kim, A. Boltasseva, Oxides and nitrides as alternative plasmonic materials in the optical range [Invited], *Opt. Mater. Express* 1 (2011) 1090–1099. <https://doi.org/10.1364/OME.1.001090>.
- [107] P. Biagioni, J.-S. Huang, B. Hecht, Nanoantennas for visible and infrared radiation, *Rep. Prog. Phys.* 75 (2012) 024402. <https://doi.org/10.1088/0034-4885/75/2/024402>.
- [108] M.G. Blaber, M.D. Arnold, M.J. Ford, A review of the optical properties of alloys and intermetallics for plasmonics, *J. Phys. Condens. Matter* 22 (2010) 143201. <https://doi.org/10.1088/0953-8984/22/14/143201>.

- [109] M.G. Blaber, M.D. Arnold, M.J. Ford, Designing materials for plasmonic systems: the alkali-noble intermetallics, *J. Phys. Condens. Matter* 22 (2010) 095501. <https://doi.org/10.1088/0953-8984/22/9/095501>.
- [110] B.J. Messinger, K.U. von Raben, R.K. Chang, P.W. Barber, Local fields at the surface of noble-metal microspheres, *Phys. Rev. B* 24 (1981) 649–657. <https://doi.org/10.1103/PhysRevB.24.649>.
- [111] E. Cottancin, G. Celep, J. Lermé, M. Pellarin, J.R. Huntzinger, J.L. Vialle, M. Broyer, Optical Properties of Noble Metal Clusters as a Function of the Size: Comparison between Experiments and a Semi-Quantal Theory, *Theor. Chem. Acc.* 116 (2006) 514–523. <https://doi.org/10.1007/s00214-006-0089-1>.
- [112] A. Liebsch, Surface plasmon dispersion of Ag, *Phys. Rev. Lett.* 71 (1993) 145–148. <https://doi.org/10.1103/PhysRevLett.71.145>.
- [113] J. Lermé, B. Palpant, B. Prével, M. Pellarin, M. Treilleux, J.L. Vialle, A. Perez, M. Broyer, Quenching of the Size Effects in Free and Matrix-Embedded Silver Clusters, *Phys. Rev. Lett.* 80 (1998) 5105–5108. <https://doi.org/10.1103/PhysRevLett.80.5105>.
- [114] P.B. Johnson, R.W. Christy, Optical Constants of the Noble Metals, *Phys. Rev. B* 6 (1972) 4370–4379. <https://doi.org/10.1103/PhysRevB.6.4370>.
- [115] A. Kunzmann, B. Andersson, T. Thurnherr, H. Krug, A. Scheynius, B. Fadeel, Toxicology of engineered nanomaterials: Focus on biocompatibility, biodistribution and biodegradation, *Biochim. Biophys. Acta BBA - Gen. Subj.* 1810 (2011) 361–373. <https://doi.org/10.1016/j.bbagen.2010.04.007>.
- [116] R. Shukla, V. Bansal, M. Chaudhary, A. Basu, R.R. Bhonde, M. Sastry, Biocompatibility of Gold Nanoparticles and Their Endocytotic Fate Inside the Cellular Compartment: A Microscopic Overview, *Langmuir* 21 (2005) 10644–10654. <https://doi.org/10.1021/la0513712>.
- [117] O. Bondarenko, K. Juganson, A. Ivask, K. Kasemets, M. Mortimer, A. Kahru, Toxicity of Ag, CuO and ZnO nanoparticles to selected environmentally relevant test organisms and mammalian cells in vitro: a critical review, *Arch. Toxicol.* 87 (2013) 1181–1200. <https://doi.org/10.1007/s00204-013-1079-4>.
- [118] M. Ahamed, M. Karns, M. Goodson, J. Rowe, S.M. Hussain, J.J. Schlager, Y. Hong, DNA damage response to different surface chemistry of silver nanoparticles in mammalian cells, *Toxicol. Appl. Pharmacol.* 233 (2008) 404–410. <https://doi.org/10.1016/j.taap.2008.09.015>.
- [119] M.D. McMahon, R. Lopez, H.M. Meyer, L.C. Feldman, R.F. Haglund, Rapid tarnishing of silver nanoparticles in ambient laboratory air, *Appl. Phys. B* 80 (2005) 915–921. <https://doi.org/10.1007/s00340-005-1793-6>.
- [120] H.E. Bennett, R.L. Peck, D.K. Burge, J.M. Bennett, Formation and Growth of Tarnish on Evaporated Silver Films, *J. Appl. Phys.* 40 (1969) 3351–3360. <https://doi.org/10.1063/1.1658187>.
- [121] M. Erol, Y. Han, S.K. Stanley, C.M. Stafford, H. Du, S. Sukhishvili, SERS Not To Be Taken for Granted in the Presence of Oxygen, *J. Am. Chem. Soc.* 131 (2009) 7480–7481. <https://doi.org/10.1021/ja807458x>.
- [122] Y. Han, R. Lupitskyy, T.-M. Chou, C.M. Stafford, H. Du, S. Sukhishvili, Effect of Oxidation on Surface-Enhanced Raman Scattering Activity of Silver Nanoparticles: A Quantitative Correlation, *Anal. Chem.* 83 (2011) 5873–5880. <https://doi.org/10.1021/ac2005839>.
- [123] G.H. Chan, J. Zhao, E.M. Hicks, G.C. Schatz, R.P. Van Duyne, Plasmonic Properties of Copper Nanoparticles Fabricated by Nanosphere Lithography, *Nano Lett.* 7 (2007) 1947–1952. <https://doi.org/10.1021/nl070648a>.
- [124] D. Gérard, S.K. Gray, Aluminium plasmonics, *J. Phys. Appl. Phys.* 48 (2014) 184001. <https://doi.org/10.1088/0022-3727/48/18/184001>.
- [125] H. Jeong, J. Kim, Electrodeposition of Nanoflake Pd Structures: Structure-Dependent Wettability and SERS Activity, *ACS Appl. Mater. Interfaces* 7 (2015) 7129–7135. <https://doi.org/10.1021/acsami.5b02113>.

- [126] T. Bhuvana, G.U. Kulkarni, A SERS-Active Nanocrystalline Pd Substrate and its Nanopatterning Leading to Biochip Fabrication, *Small* 4 (2008) 670–676. <https://doi.org/10.1002/sml.200701075>.
- [127] S. Choi, H. Jeong, K. Choi, J.Y. Song, J. Kim, Electrodeposition of Triangular Pd Rod Nanostructures and Their Electrocatalytic and SERS Activities, *ACS Appl. Mater. Interfaces* 6 (2014) 3002–3007. <https://doi.org/10.1021/am405601g>.
- [128] L. Cui, S. Mahajan, R. M. Cole, B. Soares, P. N. Bartlett, J. J. Baumberg, I. P. Hayward, B. Ren, A. E. Russell, Z. Q. Tian, UV SERS at well ordered Pd sphere segment void (SSV) nanostructures, *Phys. Chem. Chem. Phys.* 11 (2009) 1023–1026. <https://doi.org/10.1039/B817803H>.
- [129] F.J. Vidal-Iglesias, J. Solla-Gullón, J.M. Pérez, A. Aldaz, Evidence by SERS of azide anion participation in ammonia electrooxidation in alkaline medium on nanostructured Pt electrodes, *Electrochem. Commun.* 8 (2006) 102–106. <https://doi.org/10.1016/j.elecom.2005.11.002>.
- [130] S. Sam Sankar, K. Sangeetha, K. Karthick, S. Anantharaj, S. Rao Ede, S. Kundu, Pt nanoparticle tethered DNA assemblies for enhanced catalysis and SERS applications, *New J. Chem.* 42 (2018) 15784–15792. <https://doi.org/10.1039/C8NJ03940B>.
- [131] V. Amendola, M. Meneghetti, O.M. Bakr, P. Riello, S. Polizzi, D.H. Anjum, S. Fiameni, P. Arosio, T. Orlando, C. de J. Fernandez, F. Pineider, C. Sangregorio, A. Lascialfari, Coexistence of plasmonic and magnetic properties in Au₈₉Fe₁₁ nanoalloys, *Nanoscale* 5 (2013) 5611–5619. <https://doi.org/10.1039/C3NR01119D>.
- [132] V. Amendola, S. Scaramuzza, L. Litti, M. Meneghetti, G. Zuccolotto, A. Rosato, E. Nicolato, P. Marzola, G. Fracasso, C. Anselmi, M. Pinto, M. Colombatti, Magneto-Plasmonic Au-Fe Alloy Nanoparticles Designed for Multimodal SERS-MRI-CT Imaging, *Small* 10 (2014) 2476–2486. <https://doi.org/10.1002/sml.201303372>.
- [133] V. Amendola, R. Pilot, M. Frasconi, O.M. Maragò, M.A. Iatì, Surface plasmon resonance in gold nanoparticles: a review, *J. Phys. Condens. Matter* 29 (2017) 203002. <https://doi.org/10.1088/1361-648X/aa60f3>.
- [134] V. Amendola, S. Scaramuzza, S. Agnoli, S. Polizzi, M. Meneghetti, Strong dependence of surface plasmon resonance and surface enhanced Raman scattering on the composition of Au–Fe nanoalloys, *Nanoscale* 6 (2014) 1423–1433. <https://doi.org/10.1039/C3NR04995G>.
- [135] Q. Cui, G. Shen, X. Yan, L. Li, H. Möhwald, M. Bargheer, Fabrication of Au@Pt Multibranching Nanoparticles and Their Application to In Situ SERS Monitoring, *ACS Appl. Mater. Interfaces* 6 (2014) 17075–17081. <https://doi.org/10.1021/am504709a>.
- [136] R. Liu, J.-F. Liu, Z.-M. Zhang, L.-Q. Zhang, J.-F. Sun, M.-T. Sun, G.-B. Jiang, Submonolayer-Pt-Coated Ultrathin Au Nanowires and Their Self-Organized Nanoporous Film: SERS and Catalysis Active Substrates for Operando SERS Monitoring of Catalytic Reactions, *J. Phys. Chem. Lett.* 5 (2014) 969–975. <https://doi.org/10.1021/jz500238z>.
- [137] J.-W. Hu, Y. Zhang, J.-F. Li, Z. Liu, B. Ren, S.-G. Sun, Z.-Q. Tian, T. Lian, Synthesis of Au@Pd core-shell nanoparticles with controllable size and their application in surface-enhanced Raman spectroscopy, *Chem. Phys. Lett.* 408 (2005) 354–359. <https://doi.org/10.1016/j.cplett.2005.04.071>.
- [138] W. Xie, C. Herrmann, K. Kömpe, M. Haase, S. Schlücker, Synthesis of Bifunctional Au/Pt/Au Core/Shell Nanoraspberries for in Situ SERS Monitoring of Platinum-Catalyzed Reactions, *J. Am. Chem. Soc.* 133 (2011) 19302–19305. <https://doi.org/10.1021/ja208298q>.
- [139] Z.Y. Bao, D.Y. Lei, R. Jiang, X. Liu, J. Dai, J. Wang, H.L.W. Chan, Y.H. Tsang, Bifunctional Au@Pt core-shell nanostructures for in situ monitoring of catalytic reactions by surface-enhanced Raman scattering spectroscopy, *Nanoscale* 6 (2014) 9063–9070. <https://doi.org/10.1039/C4NR00770K>.
- [140] L. Jensen, C.M. Aikens, G.C. Schatz, Electronic structure methods for studying surface-enhanced Raman scattering, *Chem. Soc. Rev.* 37 (2008) 1061–1073. <https://doi.org/10.1039/B706023H>.
- [141] L.L. Hench, *Bioceramics*, *J. Am. Ceram. Soc.* 81 (1998) 1705–1728. <https://doi.org/10.1111/j.1151-2916.1998.tb02540.x>.

- [142] J.W. Arner, R.D. Santrock, A Historical Review of Common Bone Graft Materials in Foot and Ankle Surgery, *Foot Ankle Spec.* 7 (2014) 143–151. <https://doi.org/10.1177/1938640013516358>.
- [143] S.M. Best, A.E. Porter, E.S. Thian, J. Huang, Bioceramics: Past, present and for the future, *J. Eur. Ceram. Soc.* 28 (2008) 1319–1327. <https://doi.org/10.1016/j.jeurceramsoc.2007.12.001>.
- [144] V. Campana, G. Milano, E. Pagano, M. Barba, C. Cicione, G. Salonna, W. Lattanzi, G. Logroscino, Bone substitutes in orthopaedic surgery: from basic science to clinical practice, *J. Mater. Sci. Mater. Med.* 25 (2014) 2445–2461. <https://doi.org/10.1007/s10856-014-5240-2>.
- [145] Q.Z. Chen, I.D. Thompson, A.R. Boccaccini, 45S5 Bioglass®-derived glass–ceramic scaffolds for bone tissue engineering, *Biomaterials* 27 (2006) 2414–2425. <https://doi.org/10.1016/j.biomaterials.2005.11.025>.
- [146] Q. Fu, E. Saiz, M.N. Rahaman, A.P. Tomsia, Bioactive glass scaffolds for bone tissue engineering: state of the art and future perspectives, *Mater. Sci. Eng. C* 31 (2011) 1245–1256. <https://doi.org/10.1016/j.msec.2011.04.022>.
- [147] L.L. Hench, The story of Bioglass®, *J. Mater. Sci. Mater. Med.* 17 (2006) 967–978. <https://doi.org/10.1007/s10856-006-0432-z>.
- [148] L.L. Hench, J. Wilson, Bioceramics, *MRS Bull.* 16 (1991) 62–74. <https://doi.org/10.1557/S0883769400056086>.
- [149] L.L. Hench, J.M. Polak, Third-Generation Biomedical Materials, *Science* 295 (2002) 1014–1017. <https://doi.org/10.1126/science.1067404>.
- [150] K. Rezwani, Q.Z. Chen, J.J. Blaker, A.R. Boccaccini, Biodegradable and bioactive porous polymer/inorganic composite scaffolds for bone tissue engineering, *Biomaterials* 27 (2006) 3413–3431. <https://doi.org/10.1016/j.biomaterials.2006.01.039>.
- [151] Q. Fu, E. Saiz, A.P. Tomsia, Bioinspired Strong and Highly Porous Glass Scaffolds, *Adv. Funct. Mater.* 21 (2011) 1058–1063. <https://doi.org/10.1002/adfm.201002030>.
- [152] M.N. Rahaman, D.E. Day, B. Sonny Bal, Q. Fu, S.B. Jung, L.F. Bonewald, A.P. Tomsia, Bioactive glass in tissue engineering, *Acta Biomater.* 7 (2011) 2355–2373. <https://doi.org/10.1016/j.actbio.2011.03.016>.
- [153] M.S. Bahniuk, H. Pirayesh, H.D. Singh, J.A. Nychka, L.D. Unsworth, Bioactive Glass 45S5 Powders: Effect of Synthesis Route and Resultant Surface Chemistry and Crystallinity on Protein Adsorption from Human Plasma, *Biointerphases* 7 (2012) 41. <https://doi.org/10.1007/s13758-012-0041-y>.
- [154] F. Baines, E. Fiume, J. Barberi, S. Kargozar, J. Marchi, J. Massera, E. Verné, Processing methods for making porous bioactive glass-based scaffolds—A state-of-the-art review, *Int. J. Appl. Ceram. Technol.* 16 (2019) 1762–1796. <https://doi.org/10.1111/ijac.13195>.
- [155] Q.-M. Jin, H. Takita, T. Kohgo, K. Atsumi, H. Itoh, Y. Kuboki, Effects of geometry of hydroxyapatite as a cell substratum in BMP-induced ectopic bone formation, *J. Biomed. Mater. Res.* 51 (2000) 491–499. [https://doi.org/10.1002/1097-4636\(20000905\)51:3<491::AID-JBM25>3.0.CO;2-1](https://doi.org/10.1002/1097-4636(20000905)51:3<491::AID-JBM25>3.0.CO;2-1).
- [156] A. Bignon, J. Chouteau, J. Chevalier, G. Fantozzi, J. -p Carret, P. Chavassieux, G. Boivin, M. Melin, D. Hartmann, Effect of micro- and macroporosity of bone substitutes on their mechanical properties and cellular response, *J. Mater. Sci. Mater. Med.* 14 (2003) 1089–97. <https://doi.org/10.1023/B:JMSM.0000004006.90399.b4>.
- [157] L.A. Cyster, D.M. Grant, S.M. Howdle, F.R.A.J. Rose, D.J. Irvine, D. Freeman, C.A. Scotchford, K.M. Shakesheff, The influence of dispersant concentration on the pore morphology of hydroxyapatite ceramics for bone tissue engineering, *Biomaterials* 26 (2005) 697–702. <https://doi.org/10.1016/j.biomaterials.2004.03.017>.
- [158] L.-C. Gerhardt, A.R. Boccaccini, Bioactive Glass and Glass-Ceramic Scaffolds for Bone Tissue Engineering, *Materials* 3 (2010) 3867–3910. <https://doi.org/10.3390/ma3073867>.
- [159] F.A. Akin, H. Zreiqat, S. Jordan, M.B.J. Wijesundara, L. Hanley, Preparation and analysis of macroporous TiO₂ films on Ti surfaces for bone–tissue implants, *J. Biomed. Mater. Res.* 57

- (2001) 588–596. [https://doi.org/10.1002/1097-4636\(20011215\)57:4<588::AID-JBM1206>3.0.CO;2-Y](https://doi.org/10.1002/1097-4636(20011215)57:4<588::AID-JBM1206>3.0.CO;2-Y).
- [160] B. Thavornnyutikarn, N. Chantarapanich, K. Sitthiseripratip, G.A. Thouas, Q. Chen, Bone tissue engineering scaffolding: computer-aided scaffolding techniques, *Prog. Biomater.* 3 (2014) 61–102. <https://doi.org/10.1007/s40204-014-0026-7>.
- [161] J. Jones, A. Clare, *Bio-Glasses: An Introduction*, John Wiley & Sons, 2012.
- [162] A.R. Studart, U.T. Gonzenbach, E. Tervoort, L.J. Gauckler, Processing Routes to Macroporous Ceramics: A Review, *J. Am. Ceram. Soc.* 89 (2006) 1771–1789. <https://doi.org/10.1111/j.1551-2916.2006.01044.x>.
- [163] S.A.M. Ealia, M.P. Saravanakumar, A review on the classification, characterisation, synthesis of nanoparticles and their application, *IOP Conf. Ser. Mater. Sci. Eng.* 263 (2017) 032019. <https://doi.org/10.1088/1757-899X/263/3/032019>.
- [164] R. Indiarto, L.P.A. Indriana, R. Andoyo, E. Subroto, B. Nurhadi, Bottom–up nanoparticle synthesis: a review of techniques, polyphenol-based core materials, and their properties, *Eur. Food Res. Technol.* 248 (2022) 1–24. <https://doi.org/10.1007/s00217-021-03867-y>.
- [165] W. Chen, W. Cai, L. Zhang, G. Wang, L. Zhang, Sonochemical Processes and Formation of Gold Nanoparticles within Pores of Mesoporous Silica, *J. Colloid Interface Sci.* 238 (2001) 291–295. <https://doi.org/10.1006/jcis.2001.7525>.
- [166] R. Geethalakshmi, D.V.L. Sarada, Gold and silver nanoparticles from *Trianthema decandra*: Synthesis, characterization, and antimicrobial properties, *Int. J. Nanomedicine* 7 (2012) 5375–5384. <https://doi.org/10.2147/IJN.S36516>.
- [167] M. Vijayakumar, K. Priya, F.T. Nancy, A. Noorlidah, A.B.A. Ahmed, Biosynthesis, characterisation and anti-bacterial effect of plant-mediated silver nanoparticles using *Artemisia nilagirica*, *Ind. Crops Prod.* 41 (2013) 235–240. <https://doi.org/10.1016/j.indcrop.2012.04.017>.
- [168] N.L. Pacioni, C.D. Borsarelli, V. Rey, A.V. Veglia, Synthetic Routes for the Preparation of Silver Nanoparticles, in: E.I. Alarcon, M. Griffith, K.I. Udekwu (Eds.), *Silver Nanoparticle Appl. Fabr. Des. Med. Biosensing Devices*, Springer International Publishing, Cham, 2015: pp. 13–46. https://doi.org/10.1007/978-3-319-11262-6_2.
- [169] P.G. Jamkhande, N.W. Ghule, A.H. Bamer, M.G. Kalaskar, Metal nanoparticles synthesis: An overview on methods of preparation, advantages and disadvantages, and applications, *J. Drug Deliv. Sci. Technol.* 53 (2019) 101174. <https://doi.org/10.1016/j.jddst.2019.101174>.
- [170] P.A. Pandey, G.R. Bell, J.P. Rourke, A.M. Sanchez, M.D. Elkin, B.J. Hickey, N.R. Wilson, Physical Vapor Deposition of Metal Nanoparticles on Chemically Modified Graphene: Observations on Metal–Graphene Interactions, *Small* 7 (2011) 3202–3210. <https://doi.org/10.1002/sml.201101430>.
- [171] S.-C. Chen, D.-H. Hsieh, H. Jiang, Y.-K. Liao, F.-I. Lai, C.-H. Chen, C.W. Luo, J.-Y. Juang, Y.-L. Chueh, K.-H. Wu, H.-C. Kuo, Growth and characterization of Cu(In,Ga)Se₂ thin films by nanosecond and femtosecond pulsed laser deposition, *Nanoscale Res. Lett.* 9 (2014) 280. <https://doi.org/10.1186/1556-276X-9-280>.
- [172] M. Parashar, V.K. Shukla, R. Singh, Metal oxides nanoparticles via sol–gel method: a review on synthesis, characterization and applications, *J. Mater. Sci. Mater. Electron.* 31 (2020) 3729–3749. <https://doi.org/10.1007/s10854-020-02994-8>.
- [173] N. Lkhagvajav, I. Ya, E. Çel, M. Koizhaiganova, Ö. Sari, ANTIMICROBIAL ACTIVITY OF COLLOIDAL SILVER NANOPARTICLES PREPARED BY SOL-GEL METHOD, (n.d.).
- [174] A. Chatterjee, D. Chakravorty, Electrical conductivity of sol-gel derived metal nanoparticles, *J. Mater. Sci.* 27 (1992) 4115–4119. <https://doi.org/10.1007/BF01105113>.
- [175] M. Epifani, C. Giannini, L. Tapfer, L. Vasanelli, Sol–Gel Synthesis and Characterization of Ag and Au Nanoparticles in SiO₂, TiO₂, and ZrO₂ Thin Films, *J. Am. Ceram. Soc.* 83 (2000) 2385–2393. <https://doi.org/10.1111/j.1151-2916.2000.tb01566.x>.
- [176] M.G. Guzmán, J. Dille, S. Godet, Synthesis of silver nanoparticles by chemical reduction method and their antibacterial activity, (2009).

- [177] J. Kimling, M. Maier, B. Okenve, V. Kotaidis, H. Ballot, A. Plech, Turkevich Method for Gold Nanoparticle Synthesis Revisited, *J. Phys. Chem. B* 110 (2006) 15700–15707. <https://doi.org/10.1021/jp061667w>.
- [178] P. Zhao, N. Li, D. Astruc, State of the art in gold nanoparticle synthesis, *Coord. Chem. Rev.* 257 (2013) 638–665. <https://doi.org/10.1016/j.ccr.2012.09.002>.
- [179] A. Henglein, B.G. Ershov, M. Malow, Absorption Spectrum and Some Chemical Reactions of Colloidal Platinum in Aqueous Solution, *J. Phys. Chem.* 99 (1995) 14129–14136. <https://doi.org/10.1021/j100038a053>.
- [180] J. Turkevich, G. Kim, Palladium: Preparation and Catalytic Properties of Particles of Uniform Size, *Science* 169 (1970) 873–879.
- [181] J. Turkevich, R.S. Miner, L. Babenkova, Further studies on the synthesis of finely divided platinum, *J. Phys. Chem.* 90 (1986) 4765–4767. <https://doi.org/10.1021/j100411a011>.
- [182] V.K. LaMer, A.S. Kenyon, Kinetics of the formation of monodispersed sulfur sols from thiosulfate and acid, *J. Colloid Sci.* 2 (1947) 257–264. [https://doi.org/10.1016/0095-8522\(47\)90026-3](https://doi.org/10.1016/0095-8522(47)90026-3).
- [183] J. Turkevich, P.C. Stevenson, J. Hillier, A study of the nucleation and growth processes in the synthesis of colloidal gold, *Discuss. Faraday Soc.* 11 (1951) 55–75. <https://doi.org/10.1039/DF9511100055>.
- [184] J. Turkevich, P.C. Stevenson, J. Hillier, The Formation of Colloidal Gold, *J. Phys. Chem.* 57 (1953) 670–673. <https://doi.org/10.1021/j150508a015>.
- [185] G. Frens, Controlled Nucleation for the Regulation of the Particle Size in Monodisperse Gold Suspensions, *Nat. Phys. Sci.* 241 (1973) 20–22. <https://doi.org/10.1038/phyci241020a0>.
- [186] Y. Mikhlin, A. Karacharov, M. Likhatski, T. Podlipskaya, Y. Zubavichus, A. Veligzhanin, V. Zaikovski, Submicrometer intermediates in the citrate synthesis of gold nanoparticles: New insights into the nucleation and crystal growth mechanisms, *J. Colloid Interface Sci.* 362 (2011) 330–336. <https://doi.org/10.1016/j.jcis.2011.06.077>.
- [187] M.K. Chow, C.F. Zukoski, Gold Sol Formation Mechanisms: Role of Colloidal Stability, *J. Colloid Interface Sci.* 165 (1994) 97–109. <https://doi.org/10.1006/jcis.1994.1210>.
- [188] B.-K. Pong, H.I. Elim, J.-X. Chong, W. Ji, B.L. Trout, J.-Y. Lee, New Insights on the Nanoparticle Growth Mechanism in the Citrate Reduction of Gold(III) Salt: Formation of the Au Nanowire Intermediate and Its Nonlinear Optical Properties, *J. Phys. Chem. C* 111 (2007) 6281–6287. <https://doi.org/10.1021/jp068666o>.
- [189] X. Ji, X. Song, J. Li, Y. Bai, W. Yang, X. Peng, Size Control of Gold Nanocrystals in Citrate Reduction: The Third Role of Citrate, *J. Am. Chem. Soc.* 129 (2007) 13939–13948. <https://doi.org/10.1021/ja074447k>.
- [190] M. Wuthschick, A. Birnbaum, S. Witte, M. Sztucki, U. Vainio, N. Pinna, K. Rademann, F. Emmerling, R. Kraehnert, J. Polte, Turkevich in New Robes: Key Questions Answered for the Most Common Gold Nanoparticle Synthesis, *ACS Nano* 9 (2015) 7052–7071. <https://doi.org/10.1021/acsnano.5b01579>.
- [191] Y. Gao, L. Torrente-Murciano, Mechanistic insights of the reduction of gold salts in the Turkevich protocol, *Nanoscale* 12 (2020) 2740–2751. <https://doi.org/10.1039/C9NR08877F>.
- [192] K. Okuyama, I. Wuled Lenggoro, Preparation of nanoparticles via spray route, *Chem. Eng. Sci.* 58 (2003) 537–547. [https://doi.org/10.1016/S0009-2509\(02\)00578-X](https://doi.org/10.1016/S0009-2509(02)00578-X).
- [193] M.T. Swihart, Vapor-phase synthesis of nanoparticles, *Curr. Opin. Colloid Interface Sci.* 8 (2003) 127–133. [https://doi.org/10.1016/S1359-0294\(03\)00007-4](https://doi.org/10.1016/S1359-0294(03)00007-4).
- [194] X. Xia, Y. Wang, A. Ruditskiy, Y. Xia, 25th Anniversary Article: Galvanic Replacement: A Simple and Versatile Route to Hollow Nanostructures with Tunable and Well-Controlled Properties, *Adv. Mater.* 25 (2013) 6313–6333. <https://doi.org/10.1002/adma.201302820>.
- [195] A.G.M. da Silva, T.S. Rodrigues, S.J. Haigh, P.H.C. Camargo, Galvanic replacement reaction: recent developments for engineering metal nanostructures towards catalytic applications, *Chem. Commun.* 53 (2017) 7135–7148. <https://doi.org/10.1039/C7CC02352A>.

- [196] Y. Xia, K.D. Gilroy, H.-C. Peng, X. Xia, Seed-Mediated Growth of Colloidal Metal Nanocrystals, *Angew. Chem. Int. Ed.* 56 (2017) 60–95. <https://doi.org/10.1002/anie.201604731>.
- [197] E. Bauer, J.H. van der Merwe, Structure and growth of crystalline superlattices: From monolayer to superlattice, *Phys. Rev. B* 33 (1986) 3657–3671. <https://doi.org/10.1103/PhysRevB.33.3657>.
- [198] P.T. Sprunger, E. Lægsgaard, F. Besenbacher, Growth of Ag on Cu(100) studied by STM: From surface alloying to Ag superstructures, *Phys. Rev. B* 54 (1996) 8163–8171. <https://doi.org/10.1103/PhysRevB.54.8163>.
- [199] C. Langlois, D. Alloyeau, Y.L. Bouar, A. Loiseau, T. Oikawa, C. Mottet, C. Ricolleau, Growth and structural properties of CuAg and CoPt bimetallic nanoparticles, *Faraday Discuss.* 138 (2008) 375–391. <https://doi.org/10.1039/B705912B>.
- [200] H. Hao, H. Li, S. Wang, Z. Cheng, Y. Fang, Epitaxial growth of Ag-Cu bimetallic nanoparticles via thermal evaporation deposition, *Appl. Surf. Sci.* 505 (2020) 143871. <https://doi.org/10.1016/j.apsusc.2019.143871>.
- [201] J.R. Lombardi, R.L. Birke, A Unified View of Surface-Enhanced Raman Scattering, *Acc. Chem. Res.* 42 (2009) 734–742. <https://doi.org/10.1021/ar800249y>.
- [202] A. Otto, The ‘chemical’ (electronic) contribution to surface-enhanced Raman scattering, *J. Raman Spectrosc.* 36 (2005) 497–509. <https://doi.org/10.1002/jrs.1355>.
- [203] E.C. Le Ru, P.G. Etchegoin, Quantifying SERS enhancements, *MRS Bull.* 38 (2013) 631–640. <https://doi.org/10.1557/mrs.2013.158>.
- [204] E.C. Le Ru, M. Meyer, E. Blackie, P.G. Etchegoin, Advanced aspects of electromagnetic SERS enhancement factors at a hot spot, *J. Raman Spectrosc.* 39 (2008) 1127–1134. <https://doi.org/10.1002/jrs.1945>.
- [205] W. Zhu, R. Esteban, A.G. Borisov, J.J. Baumberg, P. Nordlander, H.J. Lezec, J. Aizpurua, K.B. Crozier, Quantum mechanical effects in plasmonic structures with subnanometre gaps, *Nat. Commun.* 7 (2016) 11495. <https://doi.org/10.1038/ncomms11495>.
- [206] A.B. Zrimsek, N.L. Wong, R.P. Van Duyne, Single Molecule Surface-Enhanced Raman Spectroscopy: A Critical Analysis of the Biantalyte versus Isotopologue Proof, *J. Phys. Chem. C* 120 (2016) 5133–5142. <https://doi.org/10.1021/acs.jpcc.6b00606>.
- [207] S. Nie, S.R. Emory, Probing Single Molecules and Single Nanoparticles by Surface-Enhanced Raman Scattering, *Science* 275 (1997) 1102–1106. <https://doi.org/10.1126/science.275.5303.1102>.
- [208] P.A. Mosier-Boss, Review of SERS Substrates for Chemical Sensing, *Nanomaterials* 7 (2017) 142. <https://doi.org/10.3390/nano7060142>.
- [209] M. Fan, G.F.S. Andrade, A.G. Brolo, A review on the fabrication of substrates for surface enhanced Raman spectroscopy and their applications in analytical chemistry, *Anal. Chim. Acta* 693 (2011) 7–25. <https://doi.org/10.1016/j.aca.2011.03.002>.
- [210] X.-M. Lin, Y. Cui, Y.-H. Xu, B. Ren, Z.-Q. Tian, Surface-enhanced Raman spectroscopy: substrate-related issues, *Anal. Bioanal. Chem.* 394 (2009) 1729–1745. <https://doi.org/10.1007/s00216-009-2761-5>.
- [211] L. Fabris, SERS Tags: The Next Promising Tool for Personalized Cancer Detection?, *ChemNanoMat* 2 (2016) 249–258. <https://doi.org/10.1002/cnma.201500221>.
- [212] M.R. Jones, K.D. Osberg, R.J. Macfarlane, M.R. Langille, C.A. Mirkin, Templated Techniques for the Synthesis and Assembly of Plasmonic Nanostructures, *Chem. Rev.* 111 (2011) 3736–3827. <https://doi.org/10.1021/cr1004452>.
- [213] J.M. McMahon, S. Li, L.K. Ausman, G.C. Schatz, Modeling the Effect of Small Gaps in Surface-Enhanced Raman Spectroscopy, *J. Phys. Chem. C* 116 (2012) 1627–1637. <https://doi.org/10.1021/jp207661y>.
- [214] J.M. McMahon, S.K. Gray, G.C. Schatz, Fundamental behavior of electric field enhancements in the gaps between closely spaced nanostructures, *Phys. Rev. B* 83 (2011) 115428. <https://doi.org/10.1103/PhysRevB.83.115428>.

- [215] Y. Huang, Q. Zhou, M. Hou, L. Ma, Z. Zhang, Nanogap effects on near- and far-field plasmonic behaviors of metallic nanoparticle dimers, *Phys. Chem. Chem. Phys.* 17 (2015) 29293–29298. <https://doi.org/10.1039/C5CP04460J>.
- [216] G. Hajisalem, M.S. Nezami, R. Gordon, Probing the Quantum Tunneling Limit of Plasmonic Enhancement by Third Harmonic Generation, *Nano Lett.* 14 (2014) 6651–6654. <https://doi.org/10.1021/nl503324g>.
- [217] R.L. McCreery, *Raman Spectroscopy for Chemical Analysis*, John Wiley & Sons, 2005.
- [218] E. Hemmer, N. Venkatachalam, H. Hyodo, A. Hattori, Y. Ebina, H. Kishimoto, K. Soga, Upconverting and NIR emitting rare earth based nanostructures for NIR-bioimaging, *Nanoscale* 5 (2013) 11339–11361. <https://doi.org/10.1039/C3NR02286B>.
- [219] S.L. Kleinman, B. Sharma, M.G. Blaber, A.-I. Henry, N. Valley, R.G. Freeman, M.J. Natan, G.C. Schatz, R.P. Van Duyne, Structure Enhancement Factor Relationships in Single Gold Nanoantennas by Surface-Enhanced Raman Excitation Spectroscopy, *J. Am. Chem. Soc.* 135 (2013) 301–308. <https://doi.org/10.1021/ja309300d>.
- [220] M.J. Natan, Concluding Remarks, *Faraday Discuss.* 132 (2006) 321–328. <https://doi.org/10.1039/B601494C>.
- [221] R.J.C. Brown, M.J.T. Milton, Nanostructures and nanostructured substrates for surface-enhanced Raman scattering (SERS), *J. Raman Spectrosc.* 39 (2008) 1313–1326. <https://doi.org/10.1002/jrs.2030>.
- [222] M. Manheller, S. Trelenkamp, R. Waser, S. Karthäuser, Reliable fabrication of 3 nm gaps between nanoelectrodes by electron-beam lithography, *Nanotechnology* 23 (2012) 125302. <https://doi.org/10.1088/0957-4484/23/12/125302>.
- [223] F. Hua, Y. Sun, A. Gaur, M.A. Meitl, L. Bilhaut, L. Rotkina, J. Wang, P. Geil, M. Shim, J.A. Rogers, A. Shim, Polymer Imprint Lithography with Molecular-Scale Resolution, *Nano Lett.* 4 (2004) 2467–2471. <https://doi.org/10.1021/nl048355u>.
- [224] V.R. Manfrinato, A. Stein, L. Zhang, C.-Y. Nam, K.G. Yager, E.A. Stach, C.T. Black, Aberration-Corrected Electron Beam Lithography at the One Nanometer Length Scale, *Nano Lett.* 17 (2017) 4562–4567. <https://doi.org/10.1021/acs.nanolett.7b00514>.
- [225] A. Hakonen, P.O. Andersson, M. Stenbæk Schmidt, T. Rindzevicius, M. Käll, Explosive and chemical threat detection by surface-enhanced Raman scattering: A review, *Anal. Chim. Acta* 893 (2015) 1–13. <https://doi.org/10.1016/j.aca.2015.04.010>.
- [226] J. Zheng, L. He, Surface-Enhanced Raman Spectroscopy for the Chemical Analysis of Food, *Compr. Rev. Food Sci. Food Saf.* 13 (2014) 317–328. <https://doi.org/10.1111/1541-4337.12062>.
- [227] R. Pilot, SERS detection of food contaminants by means of portable Raman instruments, *J. Raman Spectrosc.* 49 (2018) 954–981. <https://doi.org/10.1002/jrs.5400>.
- [228] A. Hakonen, T. Rindzevicius, M.S. Schmidt, P.O. Andersson, L. Juhlin, M. Svedendahl, A. Boisen, M. Käll, Detection of nerve gases using surface-enhanced Raman scattering substrates with high droplet adhesion, *Nanoscale* 8 (2016) 1305–1308. <https://doi.org/10.1039/C5NR06524K>.
- [229] R. Tantra, R.J.C. Brown, M.J.T. Milton, Strategy to improve the reproducibility of colloidal SERS, *J. Raman Spectrosc.* 38 (2007) 1469–1479. <https://doi.org/10.1002/jrs.1797>.
- [230] M. Meyer, E.C. Le Ru, P.G. Etchegoin, Self-Limiting Aggregation Leads to Long-Lived Metastable Clusters in Colloidal Solutions, *J. Phys. Chem. B* 110 (2006) 6040–6047. <https://doi.org/10.1021/jp055866b>.
- [231] B. Vlčková, M. Moskovits, I. Pavel, K. Šišková, M. Sládková, M. Šlouf, Single-molecule surface-enhanced Raman spectroscopy from a molecularly-bridged silver nanoparticle dimer, *Chem. Phys. Lett.* 455 (2008) 131–134. <https://doi.org/10.1016/j.cplett.2008.02.078>.
- [232] D. Graham, D.G. Thompson, W.E. Smith, K. Faulds, Control of enhanced Raman scattering using a DNA-based assembly process of dye-coded nanoparticles, *Nat. Nanotechnol.* 3 (2008) 548–551. <https://doi.org/10.1038/nnano.2008.189>.
- [233] L. Guerrini, D. Graham, Molecularly-mediated assemblies of plasmonic nanoparticles for Surface-Enhanced Raman Spectroscopy applications, *Chem. Soc. Rev.* 41 (2012) 7085–7107. <https://doi.org/10.1039/C2CS35118H>.

- [234] A. Lehmuskero, P. Johansson, H. Rubinsztein-Dunlop, L. Tong, M. Käll, Laser Trapping of Colloidal Metal Nanoparticles, *ACS Nano* 9 (2015) 3453–3469. <https://doi.org/10.1021/acsnano.5b00286>.
- [235] A. Foti, C. D'Andrea, V. Villari, N. Micali, M.G. Donato, B. Fazio, O.M. Maragò, R. Gillibert, M. Lamy de la Chapelle, P.G. Gucciardi, Optical Aggregation of Gold Nanoparticles for SERS Detection of Proteins and Toxins in Liquid Environment: Towards Ultrasensitive and Selective Detection, *Materials* 11 (2018) 440. <https://doi.org/10.3390/ma11030440>.
- [236] C. Durante, V. Perazzolo, A.A. Isse, M. Favaro, G. Granozzi, A. Gennaro, Electrochemical Activation of Carbon–Halogen Bonds: Electrocatalysis at Palladium–Copper Nanoparticles, *ChemElectroChem* 1 (2014) 1370–1381. <https://doi.org/10.1002/celec.201402032>.
- [237] G. Giallongo, R. Pilot, C. Durante, G.A. Rizzi, R. Signorini, R. Bozio, A. Gennaro, G. Granozzi, Silver Nanoparticle Arrays on a DVD-Derived Template: An easy&cheap SERS Substrate, *Plasmonics* 6 (2011) 725–733. <https://doi.org/10.1007/s11468-011-9256-x>.
- [238] W. Ju, M. Favaro, C. Durante, L. Perini, S. Agnoli, O. Schneider, U. Stimming, G. Granozzi, Pd Nanoparticles deposited on nitrogen-doped HOPG: New Insights into the Pd-catalyzed Oxygen Reduction Reaction, *Electrochimica Acta* 141 (2014) 89–101. <https://doi.org/10.1016/j.electacta.2014.06.141>.
- [239] S.E. Ward Jones, F.W. Campbell, R. Baron, L. Xiao, R.G. Compton, Particle Size and Surface Coverage Effects in the Stripping Voltammetry of Silver Nanoparticles: Theory and Experiment, *J. Phys. Chem. C* 112 (2008) 17820–17827. <https://doi.org/10.1021/jp807093q>.
- [240] P. He, H. Liu, Z. Li, Y. Liu, X. Xu, J. Li, Electrochemical Deposition of Silver in Room-Temperature Ionic Liquids and Its Surface-Enhanced Raman Scattering Effect, *Langmuir* 20 (2004) 10260–10267. <https://doi.org/10.1021/la048480l>.
- [241] A.T. Dimitrov, S.H. Jordanov, K.I. Popov, M.G. Pavlovic, V. Radmilovic, Electrodeposition of Ag from nitrate solutions: Part I. Effect of phosphate ions on morphology, *J. Appl. Electrochem.* 28 (1998) 791–796. <https://doi.org/10.1023/A:1003462924591>.
- [242] A.P. Abbott, K.E. Ttaib, G. Frisch, K.S. Ryder, D. Weston, The electrodeposition of silver composites using deep eutectic solvents, *Phys. Chem. Chem. Phys.* 14 (2012) 2443–2449. <https://doi.org/10.1039/C2CP23712A>.
- [243] B.H.R. Suryanto, C.A. Gunawan, X. Lu, C. Zhao, Tuning the electrodeposition parameters of silver to yield micro/nano structures from room temperature protic ionic liquids, *Electrochimica Acta* 81 (2012) 98–105. <https://doi.org/10.1016/j.electacta.2012.07.066>.
- [244] K.C. Grabar, R.Griffith. Freeman, M.B. Hommer, M.J. Natan, Preparation and Characterization of Au Colloid Monolayers, *Anal. Chem.* 67 (1995) 735–743. <https://doi.org/10.1021/ac00100a008>.
- [245] A. Walcarius, E. Sibottier, M. Etienne, J. Ghanbaja, Electrochemically assisted self-assembly of mesoporous silica thin films, *Nat. Mater.* 6 (2007) 602–608. <https://doi.org/10.1038/nmat1951>.
- [246] V.M. Volgin, V.V. Lyubimov, I.V. Gnidina, A.D. Davydov, Modeling of Formation of Nanostructured Metal Surfaces by Electrodeposition through a Monolayer Colloidal Crystal Mask, *Procedia CIRP* 37 (2015) 89–94. <https://doi.org/10.1016/j.procir.2015.08.095>.
- [247] H. Masuda, K. Fukuda, Ordered Metal Nanohole Arrays Made by a Two-Step Replication of Honeycomb Structures of Anodic Alumina, *Science* 268 (1995) 1466–1468. <https://doi.org/10.1126/science.268.5216.1466>.
- [248] H.-H. Wang, C.-Y. Liu, S.-B. Wu, N.-W. Liu, C.-Y. Peng, T.-H. Chan, C.-F. Hsu, J.-K. Wang, Y.-L. Wang, Highly Raman-Enhancing Substrates Based on Silver Nanoparticle Arrays with Tunable Sub-10 nm Gaps, *Adv. Mater.* 18 (2006) 491–495. <https://doi.org/10.1002/adma.200501875>.
- [249] M. Kahl, E. Voges, S. Kostrewa, C. Viets, W. Hill, Periodically structured metallic substrates for SERS, *Sens. Actuators B Chem.* 51 (1998) 285–291. [https://doi.org/10.1016/S0925-4005\(98\)00219-6](https://doi.org/10.1016/S0925-4005(98)00219-6).
- [250] A. Sarangan, *Nanofabrication: Principles to Laboratory Practice*, CRC Press, 2016.
- [251] C. Lu, R. h. Lipson, Interference lithography: a powerful tool for fabricating periodic structures, *Laser Photonics Rev.* 4 (2010) 568–580. <https://doi.org/10.1002/lpor.200810061>.

- [252] J.A. Rogers, R.G. Nuzzo, Recent progress in soft lithography, *Mater. Today* 8 (2005) 50–56. [https://doi.org/10.1016/S1369-7021\(05\)00702-9](https://doi.org/10.1016/S1369-7021(05)00702-9).
- [253] D. Qin, Y. Xia, G.M. Whitesides, Soft lithography for micro- and nanoscale patterning, *Nat. Protoc.* 5 (2010) 491–502. <https://doi.org/10.1038/nprot.2009.234>.
- [254] Y. Xia, G.M. Whitesides, Soft Lithography, *Annu. Rev. Mater. Sci.* 28 (1998) 153–184. <https://doi.org/10.1146/annurev.matsci.28.1.153>.
- [255] L.A. Lane, X. Qian, S. Nie, SERS Nanoparticles in Medicine: From Label-Free Detection to Spectroscopic Tagging, *Chem. Rev.* 115 (2015) 10489–10529. <https://doi.org/10.1021/acs.chemrev.5b00265>.
- [256] G. McNay, D. Eustace, W.E. Smith, K. Faulds, D. Graham, Surface-Enhanced Raman Scattering (SERS) and Surface-Enhanced Resonance Raman Scattering (SERRS): A Review of Applications, *Appl. Spectrosc.* 65 (2011) 825–837. <https://doi.org/10.1366/11-06365>.
- [257] E. Engel, R.M. Dreizler, *Density Functional Theory: An Advanced Course*, Springer, Berlin, Heidelberg, 2011. <https://doi.org/10.1007/978-3-642-14090-7>.
- [258] R.G. Parr, Density Functional Theory, *Annu. Rev. Phys. Chem.* 34 (1983) 631–656. <https://doi.org/10.1146/annurev.pc.34.100183.003215>.
- [259] D.-Y. Wu, B. Ren, Z.-Q. Tian, A Theoretical Study on SERS Intensity of Pyridine Adsorbed on Transition Metal Electrodes, *Isr. J. Chem.* 46 (2006) 317–327. https://doi.org/10.1560/IJC_46_3_317.
- [260] C. Lee, W. Yang, R.G. Parr, Development of the Colle-Salvetti correlation-energy formula into a functional of the electron density, *Phys. Rev. B* 37 (1988) 785–789. <https://doi.org/10.1103/PhysRevB.37.785>.
- [261] P. Johansson, Illustrative direct ab initio calculations of surface Raman spectra, *Phys. Chem. Chem. Phys.* 7 (2005) 475–482. <https://doi.org/10.1039/B415535A>.
- [262] D.-Y. Wu, B. Ren, Y.-X. Jiang, X. Xu, Z.-Q. Tian, Density Functional Study and Normal-Mode Analysis of the Bindings and Vibrational Frequency Shifts of the Pyridine–M (M = Cu, Ag, Au, Cu⁺, Ag⁺, Au⁺, and Pt) Complexes, *J. Phys. Chem. A* 106 (2002) 9042–9052. <https://doi.org/10.1021/jp025970i>.
- [263] D.-Y. Wu, B. Ren, X. Xu, G.-K. Liu, Z.-L. Yang, Z.-Q. Tian, Periodic trends in the bonding and vibrational coupling: Pyridine interacting with transition metals and noble metals studied by surface-enhanced Raman spectroscopy and density-functional theory, *J. Chem. Phys.* 119 (2003) 1701–1709. <https://doi.org/10.1063/1.1580102>.
- [264] D.Y. Wu, M. Hayashi, Y.J. Shiu, K.K. Liang, C.H. Chang, Y.L. Yeh, S.H. Lin, A Quantum Chemical Study of Bonding Interaction, Vibrational Frequencies, Force Constants, and Vibrational Coupling of Pyridine–Mn (M = Cu, Ag, Au; n = 2–4), *J. Phys. Chem. A* 107 (2003) 9658–9667. <https://doi.org/10.1021/jp034951l>.
- [265] T.D. Klots, Raman vapor spectrum and vibrational assignment for pyridine¹Contribution number 370 from the Bartlesville Thermodynamics Group.1, *Spectrochim. Acta. A. Mol. Biomol. Spectrosc.* 54 (1998) 1481–1498. [https://doi.org/10.1016/S1386-1425\(98\)00054-7](https://doi.org/10.1016/S1386-1425(98)00054-7).
- [266] M. Picollo, M. Aceto, T. Vitorino, UV-Vis spectroscopy, *Phys. Sci. Rev.* 4 (2019). <https://doi.org/10.1515/psr-2018-0008>.
- [267] Beer, *Annalen der Physik und Chemie*, J.A. Barth, 1852.
- [268] D.G. Goebel, Generalized Integrating-Sphere Theory, *Appl. Opt.* 6 (1967) 125–128. <https://doi.org/10.1364/AO.6.000125>.
- [269] J.A. Jacquez, H.F. Kuppenheim, Theory of the Integrating Sphere, *JOSA* 45 (1955) 460–470. <https://doi.org/10.1364/JOSA.45.000460>.
- [270] J. Mertz, *Introduction to Optical Microscopy*, Cambridge University Press, 2019.
- [271] L. Reimer, *Transmission Electron Microscopy: Physics of Image Formation and Microanalysis*, Springer, 2013.
- [272] D.B. Williams, C.B. Carter, The Transmission Electron Microscope, in: D.B. Williams, C.B. Carter (Eds.), *Transm. Electron Microsc. Textb. Mater. Sci.*, Springer US, Boston, MA, 1996: pp. 3–17. https://doi.org/10.1007/978-1-4757-2519-3_1.

- [273] P.J. Goodhew, J. Humphreys, R. Beanland, *Electron Microscopy and Analysis*, Third Edition, CRC Press, 2000.
- [274] J.C.H. Spence, *High-Resolution Electron Microscopy*, OUP Oxford, 2013.
- [275] R.E. Gordon, *Electron Microscopy: A Brief History and Review of Current Clinical Application*, in: C.E. Day (Ed.), *Histopathol. Methods Protoc.*, Springer, New York, NY, 2014: pp. 119–135. https://doi.org/10.1007/978-1-4939-1050-2_7.
- [276] A. Koster, J. Klumperman, *Electron microscopy in cell biology: Integrating structure and function*, *Nat. Rev. Mol. Cell Biol. Suppl* (2003) SS6-10. <https://doi.org/10.1038/nrm1194>.
- [277] E.L. Ritman, *Micro-Computed Tomography—Current Status and Developments*, *Annu. Rev. Biomed. Eng.* 6 (2004) 185–208. <https://doi.org/10.1146/annurev.bioeng.6.040803.140130>.
- [278] L. Vásárhelyi, Z. Kónya, Á. Kukovecz, R. Vajtai, *Microcomputed tomography–based characterization of advanced materials: a review*, *Mater. Today Adv.* 8 (2020) 100084. <https://doi.org/10.1016/j.mtadv.2020.100084>.
- [279] E. Maire, P.J. Withers, *Quantitative X-ray tomography*, *Int. Mater. Rev.* 59 (2014) 1–43. <https://doi.org/10.1179/1743280413Y.0000000023>.
- [280] D.L. Wood, K. Nassau, T.Y. Kometani, *Refractive index of Y 2O 3 stabilized cubic zirconia: variation with composition and wavelength*, *Appl. Opt.* 29 (1990) 2485–2488.
- [281] X. Chen, U. Betke, S. Rannabauer, P.C. Peters, G.M. Söffker, M. Scheffler, *Improving the Strength of ZTA Foams with Different Strategies: Immersion Infiltration and Recoating*, *Materials* 10 (2017) 735. <https://doi.org/10.3390/ma10070735>.
- [282] S. Kroll, L. Treccani, K. Rezwan, G. Grathwohl, *Development and characterisation of functionalised ceramic microtubes for bacteria filtration*, *J. Membr. Sci.* 365 (2010) 447–455. <https://doi.org/10.1016/j.memsci.2010.09.045>.
- [283] A. Katsevich, *Theoretically Exact Filtered Backprojection-Type Inversion Algorithm for Spiral CT*, *SIAM J. Appl. Math.* 62 (2002) 2012–2026. <https://doi.org/10.1137/S0036139901387186>.
- [284] *3D Slicer: A Platform for Subject-Specific Image Analysis, Visualization, and Clinical Support* | SpringerLink, (n.d.). https://link.springer.com/chapter/10.1007/978-1-4614-7657-3_19 (accessed January 7, 2022).
- [285] J. Schindelin, I. Arganda-Carreras, E. Frise, V. Kaynig, M. Longair, T. Pietzsch, S. Preibisch, C. Rueden, S. Saalfeld, B. Schmid, J.-Y. Tinevez, D.J. White, V. Hartenstein, K. Eliceiri, P. Tomancak, A. Cardona, *Fiji: an open-source platform for biological-image analysis*, *Nat. Methods* 9 (2012) 676–682. <https://doi.org/10.1038/nmeth.2019>.
- [286] G. Laurent, N. Félidj, J. Aubard, G. Lévi, J.R. Krenn, A. Hohenau, G. Schider, A. Leitner, F.R. Aussenegg, *Evidence of multipolar excitations in surface enhanced Raman scattering*, *Phys. Rev. B* 71 (2005) 045430. <https://doi.org/10.1103/PhysRevB.71.045430>.
- [287] M. Green, F.M. Liu, *SERS Substrates Fabricated by Island Lithography: The Silver/Pyridine System*, *J. Phys. Chem. B* 107 (2003) 13015–13021. <https://doi.org/10.1021/jp030751y>.
- [288] A.D. McFarland, M.A. Young, J.A. Dieringer, R.P. Van Duyne, *Wavelength-Scanned Surface-Enhanced Raman Excitation Spectroscopy*, *J. Phys. Chem. B* 109 (2005) 11279–11285. <https://doi.org/10.1021/jp050508u>.
- [289] T. Ohji, M. Fukushima, *Macro-porous ceramics: processing and properties*, *Int. Mater. Rev.* 57 (2012) 115–131. <https://doi.org/10.1179/1743280411Y.0000000006>.
- [290] J. Luyten, S. Mullens, J. Coymans, A.M. De Wilde, I. Thijs, R. Kemps, *Different methods to synthesize ceramic foams*, *J. Eur. Ceram. Soc.* 29 (2009) 829–832. <https://doi.org/10.1016/j.jeurceramsoc.2008.07.039>.
- [291] S. Agnihotri, S. Mukherji, S. Mukherji, *Size-controlled silver nanoparticles synthesized over the range 5–100 nm using the same protocol and their antibacterial efficacy*, *RSC Adv.* 4 (2014) 3974–3983. <https://doi.org/10.1039/C3RA44507K>.
- [292] V.-B. Jose, G. Stephanie Marin, R. Ericka Rodriguez, M. Veronica Vega, *Synthesis and characterization of silver nanoparticles and their application as an antibacterial agent*, *Int. J. Biosens. Bioelectron. Volume 5* (2019). <https://doi.org/10.15406/ijbsbe.2019.05.00172>.

- [293] A. Sharonova, M. Surmeneva, K. Loza, O. Prymak, M. Epple, R. Surmenev, Surface functionalization of titanium with silver nanoparticles, *J. Phys. Conf. Ser.* 1145 (2019) 012032. <https://doi.org/10.1088/1742-6596/1145/1/012032>.
- [294] N.G. Bastús, F. Merkoçi, J. Piella, V. Puntes, Synthesis of Highly Monodisperse Citrate-Stabilized Silver Nanoparticles of up to 200 nm: Kinetic Control and Catalytic Properties, *Chem. Mater.* 26 (2014) 2836–2846. <https://doi.org/10.1021/cm500316k>.
- [295] X. Dong, X. Ji, H. Wu, L. Zhao, J. Li, W. Yang, Shape Control of Silver Nanoparticles by Stepwise Citrate Reduction, *J. Phys. Chem. C* 113 (2009) 6573–6576. <https://doi.org/10.1021/jp900775b>.
- [296] Z.S. Pillai, P.V. Kamat, What Factors Control the Size and Shape of Silver Nanoparticles in the Citrate Ion Reduction Method?, *J. Phys. Chem. B* 108 (2004) 945–951. <https://doi.org/10.1021/jp037018r>.
- [297] K. Ranoszek-Soliwoda, E. Tomaszewska, E. Socha, P. Krzyczmonik, A. Ignaczak, P. Orłowski, M. Krzyczowska, G. Celichowski, J. Grobelny, The role of tannic acid and sodium citrate in the synthesis of silver nanoparticles, *J. Nanoparticle Res.* 19 (2017) 273. <https://doi.org/10.1007/s11051-017-3973-9>.
- [298] M. Tejamaya, I. Römer, R.C. Merrifield, J.R. Lead, Stability of Citrate, PVP, and PEG Coated Silver Nanoparticles in Ecotoxicology Media, *Environ. Sci. Technol.* 46 (2012) 7011–7017. <https://doi.org/10.1021/es2038596>.
- [299] X.Y. Liu, Heterogeneous nucleation or homogeneous nucleation?, *J. Chem. Phys.* 112 (2000) 9949–9955. <https://doi.org/10.1063/1.481644>.
- [300] W. Liu, Z. Song, Y. Zhao, Y. Liu, X. He, S. Cui, Flexible porous aerogels decorated with Ag nanoparticles as an effective SERS substrate for label-free trace explosives detection, *Anal. Methods* 12 (2020) 4123–4129. <https://doi.org/10.1039/D0AY00771D>.
- [301] L. Yang, Z. Ren, M. Zhang, Y. Song, P. Li, Y. Qiu, P. Deng, Z. Li, Three-dimensional porous SERS powder for sensitive liquid and gas detections fabricated by engineering dense “hot spots” on silica aerogel, *Nanoscale Adv.* 3 (2021) 1012–1018. <https://doi.org/10.1039/D0NA00849D>.
- [302] Y.-J. Oh, M. Kang, M. Park, K.-H. Jeong, Engineering hot spots on plasmonic nanopillar arrays for SERS: A review, *BioChip J.* 10 (2016) 297–309. <https://doi.org/10.1007/s13206-016-0406-2>.
- [303] D. Shan, L. Huang, X. Li, W. Zhang, J. Wang, L. Cheng, X. Feng, Y. Liu, J. Zhu, Y. Zhang, Surface Plasmon Resonance and Interference Coenhanced SERS Substrate of AAO/Al-Based Ag Nanostructure Arrays, *J. Phys. Chem. C* 118 (2014) 23930–23936. <https://doi.org/10.1021/jp5026152>.
- [304] D. Choi, Y. Choi, S. Hong, T. Kang, L.P. Lee, Self-Organized Hexagonal-Nanopore SERS Array, *Small* 6 (2010) 1741–1744. <https://doi.org/10.1002/smll.200901937>.
- [305] S. Damm, F. Lordan, A. Murphy, M. McMillen, R. Pollard, J.H. Rice, Application of AAO Matrix in Aligned Gold Nanorod Array Substrates for Surface-Enhanced Fluorescence and Raman Scattering, *Plasmonics* 9 (2014) 1371–1376. <https://doi.org/10.1007/s11468-014-9751-y>.
- [306] J. P. Singh, H. Chu, J. Abell, R. A. Tripp, Y. Zhao, Flexible and mechanical strain resistant large area SERS active substrates, *Nanoscale* 4 (2012) 3410–3414. <https://doi.org/10.1039/C2NR00020B>.
- [307] U. Guler, A. Botasheva, V.M. Shalaev, Refractory Plasmonics, *Science* 344 (2014) 263–264. <https://doi.org/10.1126/science.1252722>.
- [308] M.P. Wells, R. Bower, R. Kilmurray, B. Zou, A.P. Mihai, G. Gobalakrishnan, N.M. Alford, R.F.M. Oulton, L.F. Cohen, S.A. Maier, A.V. Zayats, P.K. Petrov, Temperature stability of thin film refractory plasmonic materials, *Opt. Express* 26 (2018) 15726–15744. <https://doi.org/10.1364/OE.26.015726>.
- [309] A.S. de Dios, M.E. Díaz-García, Multifunctional nanoparticles: Analytical prospects, *Anal. Chim. Acta* 666 (2010) 1–22. <https://doi.org/10.1016/j.aca.2010.03.038>.
- [310] D.-E. Lee, H. Koo, I.-C. Sun, J. Hee Ryu, K. Kim, I. Chan Kwon, Multifunctional nanoparticles for multimodal imaging and theragnosis, *Chem. Soc. Rev.* 41 (2012) 2656–2672. <https://doi.org/10.1039/C2CS15261D>.

- [311] N. Sanvicens, M.P. Marco, Multifunctional nanoparticles – properties and prospects for their use in human medicine, *Trends Biotechnol.* 26 (2008) 425–433. <https://doi.org/10.1016/j.tibtech.2008.04.005>.
- [312] S.M. dePaula, M.F.G. Huila, K. Araki, H.E. Toma, Confocal Raman and electronic microscopy studies on the topotactic conversion of calcium carbonate from *Pomacea lineata* shells into hydroxyapatite bioceramic materials in phosphate media, *Micron* 41 (2010) 983–989. <https://doi.org/10.1016/j.micron.2010.06.014>.
- [313] H. Aguiar, S. Chiussi, M. López-Álvarez, P. González, J. Serra, Structural characterization of bioceramics and mineralized tissues based on Raman and XRD techniques, *Ceram. Int.* 44 (2018) 495–504. <https://doi.org/10.1016/j.ceramint.2017.09.203>.
- [314] G. Pezzotti, R. M. Bock, B. J. McEntire, T. Adachi, E. Marin, F. Boschetto, W. Zhu, O. Mazda, S. B. Bal, In vitro antibacterial activity of oxide and non-oxide bioceramics for arthroplastic devices: I. In situ time-lapse Raman spectroscopy, *Analyst* 143 (2018) 3708–3721. <https://doi.org/10.1039/C8AN00233A>.
- [315] D. Liu, P. Jiang, X. Li, J. Liu, L. Zhou, X. Wang, F. Zhou, 3D printing of metal-organic frameworks decorated hierarchical porous ceramics for high-efficiency catalytic degradation, *Chem. Eng. J.* 397 (2020) 125392. <https://doi.org/10.1016/j.cej.2020.125392>.
- [316] B.R. Johnson, N.L. Canfield, D.N. Tran, R.A. Dagle, X.S. Li, J.D. Holladay, Y. Wang, Engineered SMR catalysts based on hydrothermally stable, porous, ceramic supports for microchannel reactors, *Catal. Today* 120 (2007) 54–62. <https://doi.org/10.1016/j.cattod.2006.07.056>.
- [317] Z. Li, S. Liu, S. Song, W. Xu, Y. Sun, Y. Dai, Porous ceramic nanofibers as new catalysts toward heterogeneous reactions, *Compos. Commun.* 15 (2019) 168–178. <https://doi.org/10.1016/j.coco.2019.07.004>.
- [318] M. Liao, C. Guo, W. Guo, T. Hu, H. Qin, P. Gao, H. Xiao, Hydrogen production in microreactor using porous SiC ceramic with a pore-in-pore hierarchical structure as catalyst support, *Int. J. Hydrog. Energy* 45 (2020) 20922–20932. <https://doi.org/10.1016/j.ijhydene.2020.05.244>.
- [319] C.H. Song, M. Zakia, G.S. Lee, S.I. Yoo, Scattering-mediated photothermal heating in plasmonic PES/Au membranes for heterogeneous catalysis, *Mater. Chem. Front.* 5 (2021) 2425–2433. <https://doi.org/10.1039/D0QM00746C>.
- [320] H. Pines, W.O. Haag, Alumina: Catalyst and Support. I. Alumina, its Intrinsic Acidity and Catalytic Activity¹, *J. Am. Chem. Soc.* 82 (1960) 2471–2483. <https://doi.org/10.1021/ja01495a021>.
- [321] K.Y. Paranjpe, Alpha, Beta and Gamma Alumina as a catalyst -A Review, (n.d.).
- [322] L. Lu, G. Sun, H. Zhang, H. Wang, S. Xi, J. Hu, Z. Tian, R. Chen, Fabrication of core-shell Au-Pt nanoparticle film and its potential application as catalysis and SERS substrate, *J. Mater. Chem.* 14 (2004) 1005–1009. <https://doi.org/10.1039/B314868H>.
- [323] J. Li, Y. Zheng, J. Zeng, Y. Xia, Controlling the Size and Morphology of Au@Pd Core-Shell Nanocrystals by Manipulating the Kinetics of Seeded Growth, *Chem. – Eur. J.* 18 (2012) 8150–8156. <https://doi.org/10.1002/chem.201200823>.
- [324] J. Han, Z. Zhou, Y. Yin, X. Luo, J. Li, H. Zhang, B. Yang, One-pot, seedless synthesis of flowerlike Au-Pd bimetallic nanoparticles with core-shell-like structure via sodium citrate coreduction of metal ions, *CrystEngComm* 14 (2012) 7036–7042. <https://doi.org/10.1039/C2CE25824B>.
- [325] L. Lu, H. Wang, S. Xi, H. Zhang, Improved size control of large palladium nanoparticles by a seeding growth method, *J. Mater. Chem.* 12 (2002) 156–158. <https://doi.org/10.1039/B109797K>.
- [326] J. Wang, R. Stevens, Zirconia-toughened alumina (ZTA) ceramics, *J. Mater. Sci.* 24 (1989) 3421–3440. <https://doi.org/10.1007/BF02385721>.
- [327] L. Feng, X. Wu, L. Ren, Y. Xiang, W. He, K. Zhang, W. Zhou, S. Xie, Well-Controlled Synthesis of Au@Pt Nanostructures by Gold-Nanorod-Seeded Growth, *Chem. – Eur. J.* 14 (2008) 9764–9771. <https://doi.org/10.1002/chem.200800544>.
- [328] Z.-Q. Tian, B. Ren, D.-Y. Wu, Surface-Enhanced Raman Scattering: From Noble to Transition Metals and from Rough Surfaces to Ordered Nanostructures, *J. Phys. Chem. B* 106 (2002) 9463–9483. <https://doi.org/10.1021/jp0257449>.

- [329] D.-Y. Wu, B. Ren, X. Xu, G.-K. Liu, Z.-L. Yang, Z.-Q. Tian, Periodic trends in the bonding and vibrational coupling: Pyridine interacting with transition metals and noble metals studied by surface-enhanced Raman spectroscopy and density-functional theory, *J. Chem. Phys.* 119 (2003) 1701–1709. <https://doi.org/10.1063/1.1580102>.
- [330] D.-Y. Wu, S. Duan, B. Ren, Z.-Q. Tian, Density functional theory study of surface-enhanced Raman scattering spectra of pyridine adsorbed on noble and transition metal surfaces, *J. Raman Spectrosc.* 36 (2005) 533–540. <https://doi.org/10.1002/jrs.1353>.
- [331] G. Mizutani, S. Ushioda, Normal mode analysis of surface adsorbed and coordinated pyridine molecule, *J. Chem. Phys.* 91 (1989) 598–602. <https://doi.org/10.1063/1.457661>.
- [332] L.-W.H. Leung, M.J. Weaver, Extending the metal interface generality of surface-enhanced Raman spectroscopy: Underpotential deposited layers of mercury, thallium, and lead on gold electrodes, *J. Electroanal. Chem. Interfacial Electrochem.* 217 (1987) 367–384. [https://doi.org/10.1016/0022-0728\(87\)80229-2](https://doi.org/10.1016/0022-0728(87)80229-2).
- [333] L.W.H. Leung, M.J. Weaver, Extending surface-enhanced raman spectroscopy to transition-metal surfaces: carbon monoxide adsorption and electrooxidation on platinum- and palladium-coated gold electrodes, *J. Am. Chem. Soc.* 109 (1987) 5113–5119. <https://doi.org/10.1021/ja00251a011>.
- [334] L.W.H. Leung, M.J. Weaver, Adsorption and electrooxidation of carbon monoxide on rhodium- and ruthenium-coated gold electrodes as probed by surface-enhanced Raman spectroscopy, *Langmuir* 4 (1988) 1076–1083. <https://doi.org/10.1021/la00083a002>.
- [335] M. Fleischmann, Z.Q. Tian, The induction of SERS on smooth Ag by the deposition of Ni and Co, *J. Electroanal. Chem. Interfacial Electrochem.* 217 (1987) 411–416. [https://doi.org/10.1016/0022-0728\(87\)80232-2](https://doi.org/10.1016/0022-0728(87)80232-2).
- [336] K. Abshagen, I. Schrodi, T. Gerber, B. Vollmar, In vivo analysis of biocompatibility and vascularization of the synthetic bone grafting substitute NanoBone®, *J. Biomed. Mater. Res. A* 91A (2009) 557–566. <https://doi.org/10.1002/jbm.a.32237>.
- [337] F.M. Klenke, Y. Liu, H. Yuan, E.B. Hunziker, K.A. Siebenrock, W. Hofstetter, Impact of pore size on the vascularization and osseointegration of ceramic bone substitutes in vivo, *J. Biomed. Mater. Res. A* 85A (2008) 777–786. <https://doi.org/10.1002/jbm.a.31559>.
- [338] M.W. Laschke, K. Witt, T. Pohlemann, M.D. Menger, Injectable nanocrystalline hydroxyapatite paste for bone substitution: In vivo analysis of biocompatibility and vascularization, *J. Biomed. Mater. Res. B Appl. Biomater.* 82B (2007) 494–505. <https://doi.org/10.1002/jbm.b.30755>.
- [339] L.C. Kennedy, L.R. Bickford, N.A. Lewinski, A.J. Coughlin, Y. Hu, E.S. Day, J.L. West, R.A. Drezek, A New Era for Cancer Treatment: Gold-Nanoparticle-Mediated Thermal Therapies, *Small* 7 (2011) 169–183. <https://doi.org/10.1002/smll.201000134>.
- [340] R. A. Sperling, P.R. Gil, F. Zhang, M. Zanella, W. J. Parak, Biological applications of gold nanoparticles, *Chem. Soc. Rev.* 37 (2008) 1896–1908. <https://doi.org/10.1039/B712170A>.
- [341] M. De, P.S. Ghosh, V.M. Rotello, Applications of Nanoparticles in Biology, *Adv. Mater.* 20 (2008) 4225–4241. <https://doi.org/10.1002/adma.200703183>.
- [342] M. Sun, J. Lee, Y. Chen, K. Hoshino, Studies of nanoparticle delivery with in vitro bio-engineered microtissues, *Bioact. Mater.* 5 (2020) 924–937. <https://doi.org/10.1016/j.bioactmat.2020.06.016>.
- [343] T. Bollhorst, K. Rezwan, M. Maas, Colloidal capsules: nano- and microcapsules with colloidal particle shells, *Chem. Soc. Rev.* 46 (2017) 2091–2126. <https://doi.org/10.1039/C6CS00632A>.
- [344] D. Graham, W.E. Smith, A.M.T. Linacre, C.H. Munro, N.D. Watson, P.C. White, Selective Detection of Deoxyribonucleic Acid at Ultralow Concentrations by SERRS, *Anal. Chem.* 69 (1997) 4703–4707. <https://doi.org/10.1021/ac970657b>.
- [345] G. Sabatté, R. Keir, M. Lawlor, M. Black, D. Graham, W.E. Smith, Comparison of Surface-Enhanced Resonance Raman Scattering and Fluorescence for Detection of a Labeled Antibody, *Anal. Chem.* 80 (2008) 2351–2356. <https://doi.org/10.1021/ac071343j>.

- [346] A. Pal, N. R. Isola, J. P. Alarie, D. L. Stokes, T. Vo-Dinh, Synthesis and characterization of SERS gene probe for BRCA-1 (breast cancer), *Faraday Discuss.* 132 (2006) 293–301. <https://doi.org/10.1039/B506341H>.
- [347] S. Keren, C. Zavaleta, Z. Cheng, A. de la Zerda, O. Gheysens, S.S. Gambhir, Noninvasive molecular imaging of small living subjects using Raman spectroscopy, *Proc. Natl. Acad. Sci.* 105 (2008) 5844–5849. <https://doi.org/10.1073/pnas.0710575105>.
- [348] M.S. Saveleva, A.N. Ivanov, E.S. Prikhozhenko, A.M. Yashchenok, B.V. Parakhonskiy, A.G. Skirtach, Y.I. Svenskaya, Hybrid functional materials for tissue engineering: synthesis, in vivo drug release and SERS effect, *J. Phys. Conf. Ser.* 1461 (2020) 012150. <https://doi.org/10.1088/1742-6596/1461/1/012150>.
- [349] M. Saveleva, E. Prikhozhenko, D. Gorin, A.G. Skirtach, A. Yashchenok, B. Parakhonskiy, Polycaprolactone-Based, Porous CaCO₃ and Ag Nanoparticle Modified Scaffolds as a SERS Platform With Molecule-Specific Adsorption, *Front. Chem.* 7 (2020). <https://www.frontiersin.org/articles/10.3389/fchem.2019.00888> (accessed March 11, 2023).
- [350] Y. Yang, M. Li, B. Zhou, X. Jiang, D. Zhang, H. Luo, S. Lei, Novel Therapeutic Strategy for Bacteria-Contaminated Bone Defects: Reconstruction with Multi-Biofunctional GO/Cu-Incorporated 3D Scaffolds, *Adv. Ther.* 5 (2022) 2200043. <https://doi.org/10.1002/adtp.202200043>.
- [351] Y. Liu, T. Li, H. Ma, D. Zhai, C. Deng, J. Wang, S. Zhuo, J. Chang, C. Wu, 3D-printed scaffolds with bioactive elements-induced photothermal effect for bone tumor therapy, *Acta Biomater.* 73 (2018) 531–546. <https://doi.org/10.1016/j.actbio.2018.04.014>.
- [352] H. Ma, T. Li, Z. Huan, M. Zhang, Z. Yang, J. Wang, J. Chang, C. Wu, 3D printing of high-strength bioscaffolds for the synergistic treatment of bone cancer, *NPG Asia Mater.* 10 (2018) 31–44. <https://doi.org/10.1038/s41427-018-0015-8>.
- [353] P. Pei, H. Hu, Y. Chen, S. Wang, J. Chen, J. Ming, Y. Yang, C. Sun, S. Zhao, F. Zhang, NIR-II Ratiometric Lanthanide-Dye Hybrid Nanoprobes Doped Bioscaffolds for In Situ Bone Repair Monitoring, *Nano Lett.* 22 (2022) 783–791. <https://doi.org/10.1021/acs.nanolett.1c04356>.
- [354] A. Baranowska, M. Kochanowicz, A. Wajda, M. Leśniak, J.M. Żmojda, P. Miluski, I. Zglobicka, K.J. Kurzydłowski, D. Dorosz, Luminescence Sensing Method for Degradation Analysis of Bioactive Glass Fibers, *Sensors* 21 (2021) 2054. <https://doi.org/10.3390/s21062054>.
- [355] P. Colombo, Conventional and novel processing methods for cellular ceramics, *Philos. Trans. R. Soc. Math. Phys. Eng. Sci.* 364 (2005) 109–124. <https://doi.org/10.1098/rsta.2005.1683>.
- [356] H. Okamoto, K. Imura, Visualizing the Optical Field Structures in Metal Nanostructures, *J. Phys. Chem. Lett.* 4 (2013) 2230–2241. <https://doi.org/10.1021/jz401023d>.
- [357] P. González, J. Serra, S. Liste, S. Chiussi, B. León, M. Pérez-Amor, Raman spectroscopic study of bioactive silica based glasses, *J. Non-Cryst. Solids* 320 (2003) 92–99. [https://doi.org/10.1016/S0022-3093\(03\)00013-9](https://doi.org/10.1016/S0022-3093(03)00013-9).
- [358] I. Notinger, A.R. Boccaccini, J. Jones, V. Maquet, L.L. Hench, Application of Raman microspectroscopy to the characterisation of bioactive materials, *Mater. Charact.* 49 (2002) 255–260. [https://doi.org/10.1016/S1044-5803\(03\)00029-9](https://doi.org/10.1016/S1044-5803(03)00029-9).
- [359] E.C. Ziemath, M.A. Aegerter, Raman and infrared investigations of glass and glass-ceramics with composition 2Na₂O · 1CaO · 3SiO₂, *J. Mater. Res.* 9 (1994) 216–225. <https://doi.org/10.1557/JMR.1994.0216>.
- [360] M.A. Walters, Y.C. Leung, N.C. Blumenthal, K.A. Konsker, R.Z. LeGeros, A Raman and infrared spectroscopic investigation of biological hydroxyapatite, *J. Inorg. Biochem.* 39 (1990) 193–200. [https://doi.org/10.1016/0162-0134\(90\)84002-7](https://doi.org/10.1016/0162-0134(90)84002-7).
- [361] R.S. Krishnan, Raman spectrum of alumina and the luminescence of ruby, *Proc. Indian Acad. Sci. - Sect. A* 26 (1947) 450. <https://doi.org/10.1007/BF03170901>.
- [362] H.-K. Hyun, J.L. Ferracane, Influence of biofilm formation on the optical properties of novel bioactive glass-containing composites, *Dent. Mater.* 32 (2016) 1144–1151. <https://doi.org/10.1016/j.dental.2016.06.011>.
- [363] M. Li, W. Liu, J. Nie, C. Wang, W. Li, Z. Xing, Influence of yttria-stabilized zirconia content on rheological behavior and mechanical properties of zirconia-toughened alumina fabricated by

- paste-based stereolithography, *J. Mater. Sci.* 56 (2021) 2887–2899. <https://doi.org/10.1007/s10853-020-05494-6>.
- [364] R.G. Ribas, V.M. Schatkoski, T.L. do A. Montanheiro, B.R.C. de Menezes, C. Stegemann, D.M.G. Leite, G.P. Thim, Current advances in bone tissue engineering concerning ceramic and bioglass scaffolds: A review, *Ceram. Int.* 45 (2019) 21051–21061. <https://doi.org/10.1016/j.ceramint.2019.07.096>.
- [365] J.R. Jones, Review of bioactive glass: From Hench to hybrids, *Acta Biomater.* 9 (2013) 4457–4486. <https://doi.org/10.1016/j.actbio.2012.08.023>.
- [366] J.J. Blaker, S.N. Nazhat, V. Maquet, A.R. Boccaccini, Long-term in vitro degradation of PDLLA/Bioglass® bone scaffolds in acellular simulated body fluid, *Acta Biomater.* 7 (2011) 829–840. <https://doi.org/10.1016/j.actbio.2010.09.013>.
- [367] M.G. Araújo, D. Carmagnola, T. Berglundh, B. Thilander, J. Lindhe, Orthodontic movement in bone defects augmented with Bio-Oss®, *J. Clin. Periodontol.* 28 (2001) 73–80. <https://doi.org/10.1111/j.1600-051X.2001.280111.x>.
- [368] N.U. Zitzmann, P. Schärer, Sinus elevation procedures in the resorbed posterior maxilla: Comparison of the crestal and lateral approaches, *Oral Surg. Oral Med. Oral Pathol. Oral Radiol. Endodontology* 85 (1998) 8–17. [https://doi.org/10.1016/S1079-2104\(98\)90391-2](https://doi.org/10.1016/S1079-2104(98)90391-2).
- [369] M.B. Hürzeler, C.R. Quiñones, A. Kirsch, C. Gloker, P. Schübachs, J.R. Strub, R.G. Caffesse, Maxillary sinus augmentation using different grafting materials and dental implants in monkeys, *Clin. Oral Implants Res.* 8 (1997) 476–486. <https://doi.org/10.1034/j.1600-0501.1997.080606.x>.
- [370] H.-M. Kim, T. Himeno, M. Kawashita, T. Kokubo, T. Nakamura, The mechanism of biomineralization of bone-like apatite on synthetic hydroxyapatite: an in vitro assessment, *J. R. Soc. Interface* 1 (2004) 17–22. <https://doi.org/10.1098/rsif.2004.0003>.
- [371] F. Bains, S. Yamaguchi, The Use of Simulated Body Fluid (SBF) for Assessing Materials Bioactivity in the Context of Tissue Engineering: Review and Challenges, *Biomimetics* 5 (2020) 57. <https://doi.org/10.3390/biomimetics5040057>.
- [372] D.R. Walt, Optical Methods for Single Molecule Detection and Analysis, *Anal. Chem.* 85 (2013) 1258–1263. <https://doi.org/10.1021/ac3027178>.
- [373] A.M. Armani, R.P. Kulkarni, S.E. Fraser, R.C. Flagan, K.J. Vahala, Label-Free, Single-Molecule Detection with Optical Microcavities, *Science* 317 (2007) 783–787. <https://doi.org/10.1126/science.1145002>.
- [374] Y. Ishii, T. Yanagida, Single Molecule Detection in Life Sciences, *Single Mol.* 1 (2000) 5–16. [https://doi.org/10.1002/\(SICI\)1438-5171\(200004\)1:1<5::AID-SIMO5>3.0.CO;2-A](https://doi.org/10.1002/(SICI)1438-5171(200004)1:1<5::AID-SIMO5>3.0.CO;2-A).
- [375] L. Ouyang, W. Ren, L. Zhu, J. Irudayaraj, Prosperity to challenges: recent approaches in SERS substrate fabrication, *Rev. Anal. Chem.* 36 (2017). <https://doi.org/10.1515/revac-2016-0027>.
- [376] B. Sharma, R.R. Frontiera, A.-I. Henry, E. Ringe, R.P. Van Duyne, SERS: Materials, applications, and the future, *Mater. Today* 15 (2012) 16–25. [https://doi.org/10.1016/S1369-7021\(12\)70017-2](https://doi.org/10.1016/S1369-7021(12)70017-2).
- [377] A.M. Venezia, V. La Parola, G. Deganello, B. Pawelec, J.L.G. Fierro, Synergetic effect of gold in Au/Pd catalysts during hydrodesulfurization reactions of model compounds, *J. Catal.* 215 (2003) 317–325. [https://doi.org/10.1016/S0021-9517\(03\)00005-8](https://doi.org/10.1016/S0021-9517(03)00005-8).
- [378] A. Cybula, J.B. Priebe, M.-M. Pohl, J.W. Sobczak, M. Schneider, A. Zielińska-Jurek, A. Brückner, A. Zaleska, The effect of calcination temperature on structure and photocatalytic properties of Au/Pd nanoparticles supported on TiO₂, *Appl. Catal. B Environ.* 152–153 (2014) 202–211. <https://doi.org/10.1016/j.apcatb.2014.01.042>.
- [379] S. D’Oronzo, J. Brown, R. Coleman, The value of biomarkers in bone metastasis, *Eur. J. Cancer Care (Engl.)* 26 (2017) e12725. <https://doi.org/10.1111/ecc.12725>.
- [380] R. Sardar, A.M. Funston, P. Mulvaney, R.W. Murray, Gold Nanoparticles: Past, Present, and Future, *Langmuir* 25 (2009) 13840–13851. <https://doi.org/10.1021/la9019475>.

- [381] D.A. Giljohann, D.S. Seferos, W.L. Daniel, M.D. Massich, P.C. Patel, C.A. Mirkin, Gold Nanoparticles for Biology and Medicine, in: *Spherical Nucleic Acids*, Jenny Stanford Publishing, 2020.
- [382] P. Ghosh, G. Han, M. De, C.K. Kim, V.M. Rotello, Gold nanoparticles in delivery applications, *Adv. Drug Deliv. Rev.* 60 (2008) 1307–1315. <https://doi.org/10.1016/j.addr.2008.03.016>.
- [383] E. C. Dreaden, A. M. Alkilany, X. Huang, C. J. Murphy, M. A. El-Sayed, The golden age: gold nanoparticles for biomedicine, *Chem. Soc. Rev.* 41 (2012) 2740–2779. <https://doi.org/10.1039/C1CS15237H>.
- [384] M. Brust, J. Fink, D. Bethell, D. J. Schiffrin, C. Kiely, Synthesis and reactions of functionalised gold nanoparticles, *J. Chem. Soc. Chem. Commun.* 0 (1995) 1655–1656. <https://doi.org/10.1039/C39950001655>.
- [385] K. Saha, S.S. Agasti, C. Kim, X. Li, V.M. Rotello, Gold Nanoparticles in Chemical and Biological Sensing, *Chem. Rev.* 112 (2012) 2739–2779. <https://doi.org/10.1021/cr2001178>.
- [386] A.F. Aly, A.S. Eldesouky, K.A.M. Eid, Evaluation, Characterization and Cell Viability of Ceramic Scaffold and Nano-gold loaded Ceramic Scaffold for Bone Tissue Engineering, *Am. J. Biomed. Sci.* (2012) 316–326. <https://doi.org/10.5099/aj120400316>.
- [387] S. Grandi, V. Cassinelli, M. Bini, E. Saino, P. Mustarelli, C.R. Arciola, M. Imbriani, L. Visai, Bone Reconstruction: Au Nanocomposite Bioglasses with Antibacterial Properties, *Int. J. Artif. Organs* 34 (2011) 920–928. <https://doi.org/10.5301/ijao.5000059>.
- [388] G.S. Terentyuk, G.N. Maslyakova, L.V. Suleymanova, N.G. Khlebtsov, B.N. Khlebtsov, G.G. Akchurin, I.L. Maksimova, V.V. Tuchin, Laser-induced tissue hyperthermia mediated by gold nanoparticles: toward cancer phototherapy, *J. Biomed. Opt.* 14 (2009) 021016. <https://doi.org/10.1117/1.3122371>.
- [389] A.N. Yakunin, Y.A. Avetisyan, V.V. Tuchin, Quantification of laser local hyperthermia induced by gold plasmonic nanoparticles, *J. Biomed. Opt.* 20 (2015) 051030. <https://doi.org/10.1117/1.JBO.20.5.051030>.
- [390] S. Luo, X. Ren, H. Lin, H. Song, J. Ye, Plasmonic photothermal catalysis for solar-to-fuel conversion: current status and prospects, *Chem. Sci.* 12 (2021) 5701–5719. <https://doi.org/10.1039/D1SC00064K>.
- [391] Z.A. Combs, S. Chang, T. Clark, S. Singamaneni, K.D. Anderson, V.V. Tsukruk, Label-Free Raman Mapping of Surface Distribution of Protein A and IgG Biomolecules, *Langmuir* 27 (2011) 3198–3205. <https://doi.org/10.1021/la104787w>.
- [392] Y.-T. Li, D.-W. Li, Y. Cao, Y.-T. Long, Label-free in-situ monitoring of protein tyrosine nitration in blood by surface-enhanced Raman spectroscopy, *Biosens. Bioelectron.* 69 (2015) 1–7. <https://doi.org/10.1016/j.bios.2015.01.011>.
- [393] V. Vojinović, J.M.S. Cabral, L.P. Fonseca, Real-time bioprocess monitoring: Part I: In situ sensors, *Sens. Actuators B Chem.* 114 (2006) 1083–1091. <https://doi.org/10.1016/j.snb.2005.07.059>.

Curriculum vitae

Personal information

Name Tongwei Guo
E-mail guotongwei29@gmail.com

Education

10.2019-2023 PhD student
Advanced Ceramics group, University of Bremen,
Bremen, Germany
Topic: Plasmonic porous ceramics

04.2015-01.2019 M. Sc. Chemistry
University of Duisburg-Essen, Essen, Germany

10.2009-07.2013 B. Eng. Applied Chemistry
University of Electronic Science and Technology of
China, Chengdu, China

Professional/Research experience

10.2019-03.2023 PhD researcher, Advanced Ceramics Institute
Member of research training group Micro-, meso-
and macroporous non-metallic Materials:
Fundamentals and Applications (MIMENIMA),
University of Bremen, Bremen, Germany

06.2018-12.2018 Master Thesis: Transport- and storage-stability of
albumin-nanocapsule, Physical chemistry
department, University of Duisburg-Essen, Essen,
Germany

03.2018-06.2018 Internship: Synthesis and characterization of
polystyrene nanoparticles, Physical chemistry
department, University of Duisburg-Essen, Essen,
Germany

01.2013-06.2013 Bachelor Thesis: Synthesis and characterization of
LiFePO₄ coin battery, Electrochemistry department,
University of Electronic Science and Technology of
China, Chengdu, China

04.2012-12.2012 Internship: Design and synthesis of LiFePO₄ coin
battery with Si as anode material, Electrochemistry
department, University of Electronic Science and
Technology of China, Chengdu, China

List of publications and oral presentations

Publications

L. Messner, M. H. Antink, T. Guo, M. Maas, S. Beutel, Enzymatische Hydrolyseprozesse im kontinuierlich betriebenen Keramikkapillarreaktor. In: *Chemie Ingenieur Technik* **2020**, 9, DOI:10.1002/cite.202055316

L. Messner, M. H. Antink, T. Guo, M. Maas, S. Beutel, A versatile ceramic capillary membrane reactor system for continuous enzyme-catalyzed hydrolysis. In: *Engineering in Life Sciences* **2021**, 21, DOI: 10.1002/elsc.202100027

T. Guo, M. N. Karim, K. Ghosh, M. M. Murshed, K. Rezwani, M. Maas, Plasmonic porous ceramics based on zirconia-toughened-alumina functionalized with silver nanoparticles for surface-enhanced Raman scattering. In: *Open Ceramics* **2022**, 9, 100228. DOI: 10.1016/j.oceram.2022.100228.

T. Guo, M. M. Murshed, K. Rezwani, M. Maas, Ceramic open cell foams featuring plasmonic hybrid metal nanoparticles for *in situ* SERS monitoring of catalytic reactions. Submitted by Advanced Materials Interfaces.

T. Guo, J. Schmidt, M. M. Murshed, K. Rezwani, M. Maas, Gold nanoparticle-coated bioceramics for plasmonically-enhanced molecule detection via surface-enhanced Raman scattering. Submitted by Advanced Healthcare Materials.

Poster/oral presentations

T. Guo, K. Rezwani, M. Maas, Plasmonic Porous Ceramics, CellMAT2020, 2020, Online (Oral presentation)

T. Guo, M. N. Karim, K. Ghosh, M. M. Murshed, K. Rezwani, M. Maas, Plasmonic Porous Ceramics for Surface-enhanced Raman Scattering, European Material Research Society 2022 Fall Meeting, Warsaw, Poland (Oral presentation)

T. Guo, M. N. Karim, K. Ghosh, M. M. Murshed, K. Rezwani, M. Maas, Plasmonic Porous Ceramics, 51st General Assembly of the German Colloid Society, Berlin, Germany (Poster)

List of student projects

This thesis contains results that have been derived during the supervision of the following projects.

Umut Güngördü	Deposition and characterization of Ag nanoparticles on hydroxyapatite surface
Jonas Schmidt	Synthesis and analysis of plasmonic porous ceramics for biomedical application